JOURNAL
PRACTICAL PROBLEMS OF PHYSICS AND MATHEMATICS

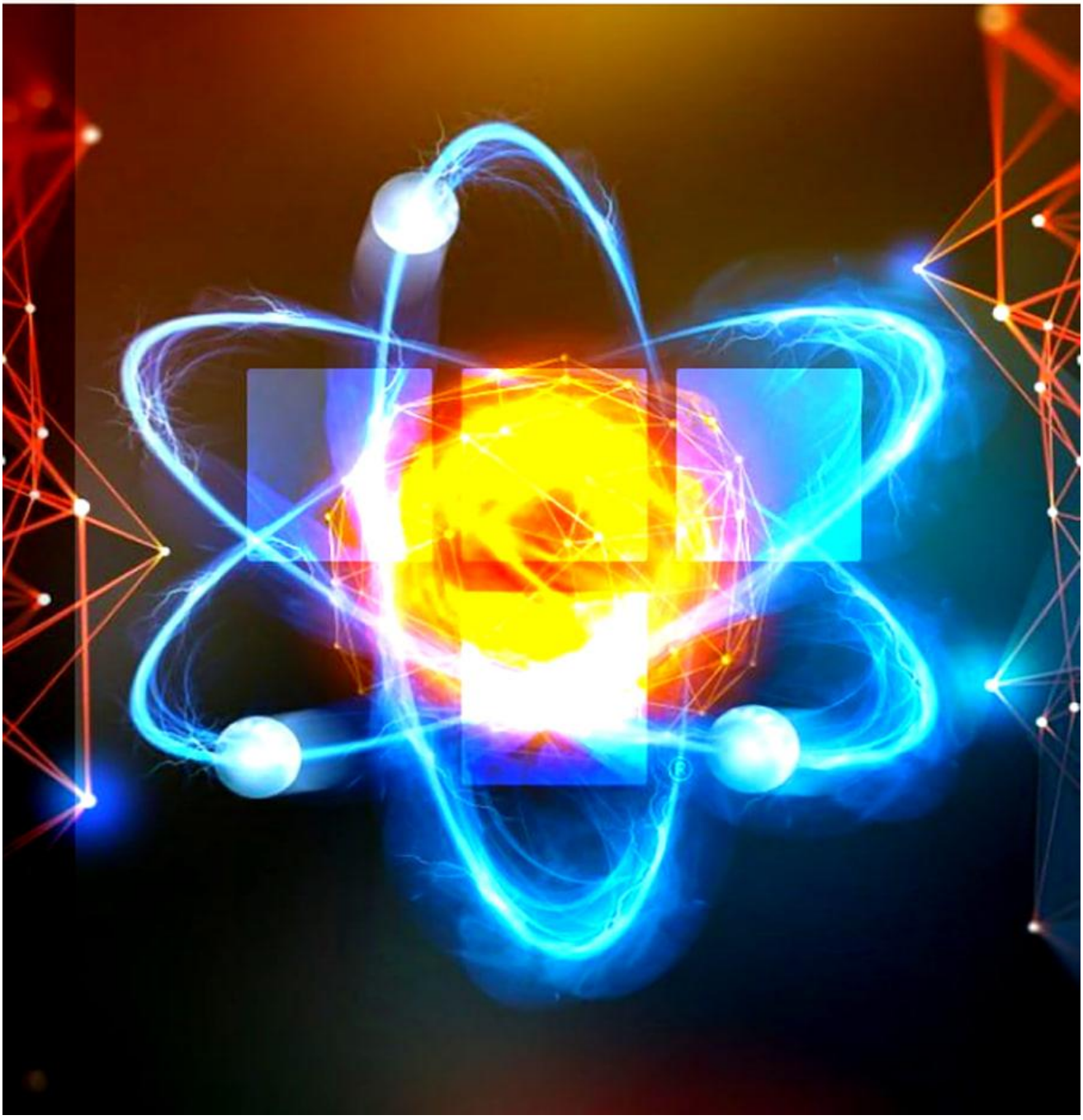

Crossref doi **Volume 1, Issue 1 ; ISSN:0000-0000**

When reprinting materials, it is necessary to indicate that they were taken from “Social Sciences: Theory and Practice”(https://science-utas.org/index.php/sstp/en/index)
This journal accepts articles in the following categories:

a) ***Physical Chemistry of Composite Materials***
b) ***Physics of Semiconductor Materials***
v) ***Condensed Matter Physics***
g) ***Mathematical Computational Methods***
d) ***Theoretical and Practical Problems of Mathematical Analysis***

The authors are responsible for the accuracy of the materials and evidence in advertisements published in the journal. The editorial opinion may not always coincide with the opinion of the authors. Submitted manuscripts will not be returned.

Our address: 100149, Tashkent – 95, Gavkhar Street, №1A. Tel.: 71200 05 40, e-mail: info@utas.uz

CONTENT

Applied Problems of Physics and Mathematics

Technology for the Synthesis of Metal-Filled Nanocomposites Based on Recycled Polymers

Umarov A.V.[1,2], Xamzaev X.[2], Namozova M.[2], Azimov N.[1,2]

[1]University of Tashkent for Applied Sciences, Str. Gavhar 1, Tashkent 100149, Uzbekistan.
[2]Tashkent State Transport University, 1 Temiryo'lchilar Street, Tashkent 100167, Uzbekistan
E-mail:toktogulova.72@mail.ru;

Keywords: Nanocomposite, polyethylene, copper nanoparticles, morphology, cadmium sulfide.

Abstract: The fundamental structural aspects of polymer composite materials, as well as the technology for producing multifunctional polymer composites, are described. The methodology for the synthesis of nanoparticles and their classification is presented in detail. The synthesis approach for metal-filled nanocomposites based on secondary polyethylene is discussed, and the results of studies on the fabrication of novel metal–polymer nanocomposites with copper nanoparticles dispersed in a secondary polyethylene matrix are reported.

Thiourea, when used as a sulfiding agent, forms stoichiometric compounds with metals, which, under thermal treatment, transform into the corresponding metal sulfides [1]. During the sulfiding of metal salts in thiourea-containing solutions, interactions occur leading to the formation of a balanced coordination structure of CdS, enabling the incorporation of sulfur atoms at minimal distances from metal atoms [2].

The synthesis of samples containing CdS nanoparticles based on high-pressure polyethylene (HPPE) was carried out according to procedures described in the literature [3]. In this case, thiourea solutions of the corresponding metals and acetates were used as initial precursors. The obtained nanocomposite powders contained 20% CdS and exhibited a yellow coloration. The synthesized nanocomposites retained the mechanical properties of the polymer matrix, allowing them to be shaped into various forms such as tablets and films.

Composite materials were also produced via the thermal decomposition of copper formate, resulting in copper nanoparticles stabilized within the polyethylene matrix. This approach is particularly effective when polymers are dissolved in organic solvents. However, the limited solubility of polymers reduces the ability to achieve nanoparticles smaller than 30 nm and their uniform distribution. Nevertheless, due to the thermal and mechanical stability of polyethylene, such materials are of significant practical interest. One of the objectives of this study is to improve existing methods for producing polymer composite materials based on HPPE containing copper nanoparticles. Polyethylene is an ideal matrix for stabilizing nanoparticles due to its dielectric properties, stability, low cost, flexibility, and recyclability, and it is one of the first polymers produced in the region.

The advantages of nanomaterials are associated with their low specific weight and the high uniformity of nanoparticle distribution on their surfaces. Composite materials containing copper nanoparticles were obtained by modifying the "Klaspol" method developed by S.P. Gubin and I.D. Kosobudskii [4], which is based on the thermal decomposition of unstable carbonic acid derivatives. Copper diacetate monohydrate $(CH_3COO)_2Cu \cdot H_2O$ was used as the precursor, and the decomposition process was carried out at 300 ± 50 °C in a "high-pressure polyethylene–oil" medium.

A four-neck flask equipped with a stirrer, dropping funnel, thermometer, and condenser was used, with a ratio of 10 parts polyethylene to 100 parts oil. During heating, an intensive reaction occurred, raising the temperature of the synthesis medium. Aqueous copper acetate solution was gradually introduced into the polyethylene–oil mixture using a dropping funnel. Nitrogen gas was applied to ensure the removal of gaseous by-products. The reaction mixture was maintained at synthesis temperature for one hour with continuous stirring. Subsequently, heating was stopped, and the mixture was cooled to room temperature under a nitrogen atmosphere. To prevent nanoparticle aggregation during cooling, ultrasonic dispersion was applied. The product was purified using benzene in a Soxhlet apparatus and dried prior to further analysis.

The morphology and elemental composition of the nanocomposites were investigated using a scanning electron microscope (SEM) EVO MA 10 (Carl Zeiss, Germany) equipped with an energy-dispersive X-ray spectroscopy (EDS) system. This technique enables the analysis of all chemical elements starting from boron. The phase composition of the obtained materials was studied using X-ray diffraction (XRD) analysis. Powder samples were analyzed using a Panalytical B.V. diffractometer (Netherlands) with CuK radiation ($\lambda(K\alpha 1)$ = 1.54060 Å, $\lambda(K\alpha 2)$ = 1.54443 Å, $\lambda(K\beta 1)$ = 1.39225 Å). Measurements were conducted in the angular range of 5.0038° to 84.9928° (2θ) with a step size of 0.0130° and a counting time of 97.92 s per step. Data analysis was performed using X'Pert HighScore Plus software.

As a result of the study, metal–polymer nanocomposites with copper nanoparticles uniformly distributed within a polyethylene matrix were successfully synthesized.

$$Cu(COOCH_3)_2 \cdot H_2O \rightarrow Cu(COOCH_3)_2 + H_2O \qquad (1)$$

$$2Cu(COOCH_3)_2 \rightarrow 2Cu + 3CH_3COOH + CO_2 + C \qquad (2)$$

The first stage is primarily associated with the removal of hydration water from $Cu(CH_3COO)_2 \cdot H_2O$. According to thermogravimetric and differential thermal analyses reported by researchers [4], this stage proceeds up to 120 °C, and all endothermic peaks observed within this temperature range are attributed to the evaporation of hydration water.

The second stage involves the decomposition of $Cu(CH_3COO)_2$, which begins at approximately 120 °C and is completed at around 300 °C. In particular, endothermic peaks observed at 134 °C and 145 °C correspond to the decomposition of copper acetate.

However, under our experimental conditions, all processes occur simultaneously at a temperature of 300 °C. It should be noted that, at the initial stage, the evaporation of the aqueous precursor solution is energetically favorable. Following the complete or localized evaporation of water within the system, the loss of water continues during the crystallization stage.

References:

1. Krupa, I., Novák, I., & Chodák, I. (2004). Electrically and thermally conductive polyethylene/graphite composites and their mechanical properties. *Synthetic Metals*, 145, 245–252.
2. Monte, A.F.G., Dantas, N.O., Morais, P.C., & Rabelo, D. (2006). Synthesis and characterisation of CdS nanoparticles in a mesoporous copolymer template. *Brazilian Journal of Physics*, 36(2A), 427–429.
3. Khanna, P.K., Gokhale, R.R., Subbarao, V.S., Singh, N., Jun, K.W., & Das, B.K. (2005). Synthesis and optical properties of CdS/PVA nanocomposites. *Materials Chemistry and Physics*, 94, 454–459.
4. Ushakov, H.M., Kosobudskiy, I.D., Yurkov, G.Yu., Gubin, S.P., Zapsis, K.V., Kochubey, V.I., & Ulzutuev, A.N. (2005). New composite nanomaterials with controlled properties for radio engineering and electronics. *Radiotekhnika*, 10, 105–108.
5. Umarov, A.V., Abdurakhmanov, U., Khamzayev, H.E., Kattaev, N.T., & Tozhiboev, A.G. (2019). Synthesis and structural investigations of metal-containing nanocomposites based on polyethylene. *Zeitschrift für Naturforschung A*, 74(3), 183–187.
6. Umarov, A.V., Yokubov, B.E., Abdurakhmanov, U., & Khamzaev, X.E. (2017). Influence of filler particle size on the dielectric conductivity of metal–polymer composites. *Compositional Materials Journal*, 4, 16–18.
7. Umarov, A.V., & Khamzaev, X.E. (2019). Structural investigation of polyethylene-based metal-filled nanocomposite polymers. *Journal of Composite Materials*, 3, 45–48.
8. Umarov, A.V., Abdurakhmanov, U., & Khamzaev, X.E. (2017). Structural studies of nanocomposite materials based on polyethylene. In: *Proceedings of the Republican Scientific and Technical Conference "Modern Technologies for the Production and Processing of Composite and Nanocomposite Materials"* (pp. 183–185). Tashkent.
9. Umarov, A.V., & Khamzaev, Kh.E. (2020). Temperature dependence of the heat capacity of polymer compositions with metal oxide fillers. In: *Proceedings of the XV International Conference "Physics of Dielectrics"* (pp. 2315–2318). St. Petersburg, Russia.

Applied Problems of Physics and Mathematics

Mechanosynthesis of Ni-Al-Ti intermetallic compounds: influence of milling time and titanium content

[1] Yerkezhan Tabiyeva, [1]Dias Yerbolat, [1]Sayat Zakerov

Center of Excellence "VERITAS", D. Serikbayev East Kazakhstan Technical University, 070004, Ust-Kamenogorsk, Kazakhstan

[1]e-mail: etabieva@edu.ektu.kz ; ORCID: 0000-0002-9726-7187

[2]e-mail: dyerbolat@edu.ektu.kz ; ORCID: 0000-0002-2072-4212

[3]e-mail: zakerovvv@gmail.com ; ORCID: 0000-0002-9726-7187

Abstract: The synthesis of intermetallic compounds in Ni-Al systems is of significant interest due to their potential applications in high-temperature materials. This study aims to investigate the effect of milling time and titanium addition on phase formation, particle size evolution, and microstructural development in Ni-Al and Ni-Al-Ti powder mixtures with different compositions. Mechanical alloying was carried out in a planetary ball mill for up to 6 hours, and the resulting powders were analyzed using X-ray diffraction and scanning electron microscopy. The results show that the particle size evolution follows a non-monotonic behavior, characterized by initial agglomeration during the early stage of milling, followed by fragmentation and subsequent stabilization. After 3 hours of processing, solid solutions based on nickel are formed due to the dissolution of aluminum and titanium in the crystal lattice. Further milling up to 6 hours leads to the formation of intermetallic phases with a disordered structure. The addition of titanium accelerates phase transformations and promotes structural refinement, with the most pronounced effect observed for compositions with higher titanium content. The findings demonstrate that mechanical alloying is an effective method for producing refined intermetallic structures, with optimal processing conditions in the range of 3 to 6 hours of milling.

Keywords: mechanosynthesis; intermetallic compounds; Ni-Al-Ti system; mechanical alloying; phase transformation; microstructure.

1. Introduction

Ni-Al intermetallic compounds are widely recognized as promising materials for high-temperature applications due to their combination of low density, high melting point, and excellent resistance to oxidation and thermal degradation. These properties make them suitable for use in aerospace, energy, and advanced engineering systems operating under severe conditions (Dey, 2003; Darolia, 1991). In particular, NiAl- and Ni_3Al-based alloys are of great interest because they retain mechanical strength at elevated temperatures while exhibiting good thermal stability. Despite these advantages, the practical application of Ni-Al intermetallics is limited by their intrinsic brittleness at room temperature. This behavior is primarily associated with a limited number of active slip systems and structural features such as grain boundary segregation (Liu, 1984). To address this limitation, various strategies have been proposed, including alloying with additional elements and the formation of complex or multiphase microstructures.

Among the alloying elements, titanium plays a particularly important role in modifying the properties of Ni-Al systems. The introduction of Ti promotes lattice distortion, enhances defect accumulation, and contributes to the stabilization of solid solutions and intermetallic phases such as $Ni_3(Al,Ti)$ (Gao et al., 2025; Li et al., 2023) . In addition, Ti-containing systems may exhibit improved microstructural homogeneity and enhanced mechanical performance. However, the influence of titanium strongly depends on its concentration, and excessive additions may lead to structural instability or defects (Riyadi, 2020).

In recent years, increasing attention has been given to the development of nanostructured intermetallic materials, as grain refinement is known to improve both strength and ductility. Mechanical alloying (mechanosynthesis) has emerged as an effective method for producing such materials. This process involves repeated cold welding, plastic deformation, and fracture of powder particles, leading to the formation of supersaturated solid solutions and refined microstructures (Suryanarayana, 2001). Compared to conventional melting and casting techniques, mechanical alloying provides better control over composition, structure, and phase distribution.

The phase evolution in Ni-Al-Ti systems during mechanical alloying is strongly influenced by processing parameters, particularly milling time and composition. Previous studies have shown that solid solutions may form at intermediate stages of processing, followed by the development of intermetallic phases with increasing milling duration. At the same time, titanium has been reported to accelerate diffusion processes and enhance the formation of homogeneous nanostructures (Chérif et al., 2017). However, the relationship between titanium content, milling duration, and the kinetics of phase formation remains insufficiently clarified.

Therefore, the aim of this study is to investigate the effect of composition and mechanical alloying time on the formation of intermetallic compounds in the Ni-Al-Ti system. Special attention is given to phase transformations, crystallite size evolution, and microstructural characteristics. The results provide new insights into the mechanisms of mechanosynthesis and contribute to the optimization of processing parameters for the development of nanostructured intermetallic materials.

2. Literature Review

Nickel-aluminum intermetallic compounds have been extensively studied due to their unique combination of high-temperature strength, low density, and excellent oxidation resistance. These properties make them promising candidates for applications in aerospace, energy, and high-temperature structural components (Dey, 2003; Darolia, 1991). However, a key limitation of Ni-Al-based intermetallics is their intrinsic brittleness at room temperature, which is associated with a limited number of active slip systems and grain boundary effects (Liu, 1984).

To overcome these limitations, various strategies have been proposed, including alloying and microstructural design. In particular, the addition of titanium to Ni-Al systems has been shown to significantly affect phase stability and mechanical properties. Titanium contributes to lattice distortion and promotes the formation of multicomponent solid solutions and intermetallic phases such as $Ni_3(Al,Ti)$, which can improve strength and structural stability (Gao et al., 2025; Li et al., 2023) . At the same time, excessive titanium content may lead to structural defects such as porosity or cracking, indicating the need for optimized compositions (Riyadi, 2020).

Another important approach to improving the properties of intermetallic compounds is the formation of multiphase microstructures. Systems containing both B2 and L12 phases have demonstrated enhanced mechanical performance due to the combined effect of high strength and improved ductility (Chanda et al., 2020; Gao et al., 2025). Such microstructures are often achieved near eutectic compositions, where fine lamellar structures can form and contribute to improved deformation behavior.

Mechanical alloying (mechanosynthesis) is widely used as an effective method for producing intermetallic compounds and nanostructured materials. This process involves repeated deformation, cold welding, and fracture of powder particles, leading to grain refinement and enhanced diffusion (Suryanarayana, 2001). As a result, supersaturated solid solutions and intermetallic phases can form directly during milling, without the need for high-temperature processing.

The evolution of phase composition during mechanical alloying strongly depends on processing parameters, particularly milling time. At early stages, cold welding dominates, resulting in particle agglomeration, whereas prolonged milling leads to fragmentation, homogenization, and refinement

of the structure. However, excessive milling may cause contamination and does not necessarily lead to further improvements in phase formation (Samani et al., 2009; Enayati et al., 2008).

In Ni-Al-Ti systems, previous studies have shown that titanium accelerates the formation of solid solutions and enhances microstructural refinement. The presence of Ti reduces the tendency for cold welding and promotes more uniform particle size distribution during milling (Chérif et al., 2017). At the same time, the kinetics of phase transformation and the relationship between composition, milling time, and structural evolution remain insufficiently understood.

Thus, the present study contributes to the existing body of research by systematically analyzing the effect of titanium content and milling duration on phase formation, crystallite size, and microstructural evolution in the Ni-Al-Ti system. This approach allows for a better understanding of the mechanisms governing mechanosynthesis and the optimization of processing parameters for the production of nanostructured intermetallic materials.

3. Materials and Methods

Materials. Elemental powders of nickel (Ni), aluminum (Al), and titanium (Ti) were used as starting materials. The powders had the following characteristics: Ni (purity 99%, average particle size < 50 μm), Al (purity 99.5%, average particle size < 90 nm), and Ti (purity 99%, average particle size < 50 μm). Powder mixtures with nominal compositions $Ni_{68}Al_{25}Ti_7$, $Ni_{72}Al_{22}Ti_6$, $Ni_{70}Al_{21}Ti_9$, and $Ni_{75}Al_{25}$ (at.%) were prepared to investigate the effect of titanium addition and composition on phase formation and microstructural evolution.

Mechanosynthesis Procedure. Mechanical alloying (mechanosynthesis) was carried out using a planetary ball mill (Fritsch Pulverisette 7 classic line). Prior to milling, the powder mixtures were pre-mixed for 10 minutes at 200 rpm to ensure initial homogenization. The mechanosynthesis process was performed in two hardened steel vials with a volume of 45 mL. Steel balls with a diameter of 5 mm were used as the milling media. The ball-to-powder weight ratio was maintained at 10:1. Milling was conducted at a rotational speed of 600 rpm for different durations of 1, 3, and 6 hours. To prevent excessive heating inside the vials, the milling process was carried out in cycles consisting of 10 minutes of milling followed by a 5-minute pause. To minimize oxidation, all operations, including loading and unloading of powders, were performed in a vacuum glove box under an argon atmosphere. In addition, mechanical alloying was conducted in an argon-filled environment at a pressure of approximately 0.3 MPa. A process control agent (stearic acid) was added in an amount of 2 wt.% of the powder mass to reduce particle agglomeration during milling. During milling, the powder particles were subjected to repeated plastic deformation, cold welding, and fracture, leading to progressive refinement of the structure and activation of diffusion processes.

Characterization Techniques. The phase composition of the powders was analyzed by X-ray diffraction (XRD) using Cu Kα radiation in the 2θ range of 20–100°. The diffraction patterns were used to identify phase evolution, including the formation of solid solutions and intermetallic compounds during milling.

The morphology and microstructure of the powders were examined using scanning electron microscopy (SEM). This analysis provided information on particle shape, degree of agglomeration, and structural refinement as a function of milling time.

Particle size distribution was determined using laser diffraction analysis. This method was used to evaluate the average particle size and to monitor its evolution during mechanosynthesis.

Experimental Design and Reproducibility. For each composition and milling duration, powder samples were prepared and analyzed under identical conditions to ensure consistency. The experimental design allowed for a direct comparison between binary and ternary systems as well as between different milling times. All measurements were performed multiple times, and the results were verified for reproducibility. The applied methodology ensures that the observed trends in phase

formation, particle size evolution, and microstructural changes are reliable and representative of the mechanosynthesis process.

4. Results and Discussion

The evolution of particle size during mechanosynthesis was analyzed using a laser particle size analyzer (Fritsch Analysette 22 NEXT), and the results are summarized in Figure 1. After initial mixing (10 min at 200 rpm), the average particle sizes differed depending on the composition. The smallest particles were observed for sample No. 1 ($Ni_{68}Al_{25}Ti_7$), with an average size of approximately 10 μm, whereas samples No. 2 ($Ni_{72}Al_{22}Ti_6$), No. 3 ($Ni_{70}Al_{21}Ti_9$), and No. 4 ($Ni_{75}Al_{25}$) exhibited larger particle sizes of 18.3, 17.2, and 18.6 μm, respectively. This behavior can be attributed to the presence of nanosized aluminum particles, which contribute to a more dispersed initial mixture.

After 1 hour of mechanical alloying, a noticeable increase in particle size was observed for all compositions. The average particle size increased to 31.1 μm (sample No. 1), 35.3 μm (sample No. 2), 23 μm (sample No. 3), and 40.5 μm (sample No. 4). This enlargement is associated with intensive cold welding and agglomeration of particles, which dominate at the early stage of milling. The SEM observations confirm the formation of large agglomerates with irregular morphology, indicating that plastic deformation prevails over fragmentation.

With further milling up to 3 hours, the dominant mechanism shifts from agglomeration to fragmentation. As a result, a significant reduction in particle size is observed. The average particle sizes decreased to 11.3 μm (sample No. 1), 6.04 μm (sample No. 2), 15.7 μm (sample No. 3), and 6.4 μm (sample No. 4). At this stage, the highest fraction of fine particles is achieved; however, a relatively wide particle size distribution is still present, indicating incomplete homogenization.

After 6 hours of milling, a more stable and uniform particle size distribution is established. The average particle sizes reached 7.6 μm (sample No. 1), 8.05 μm (sample No. 2), 9 μm (sample No. 3), and 9.8 μm (sample No. 4). The reduction in size variability and the decrease in the number of large agglomerates indicate that a quasi-stationary state is achieved, where the processes of cold welding and fragmentation are balanced.

A comparison of the compositions shows that the addition of titanium influences the particle refinement behavior. In particular, sample No. 3 ($Ni_{70}Al_{21}Ti_9$) demonstrates a more stable evolution of particle size, with less pronounced agglomeration at early stages and more controlled refinement during prolonged milling. This effect can be attributed to the role of titanium in reducing cold welding tendencies and promoting more uniform deformation and fracture processes.

Overall, the obtained results confirm that particle size evolution during mechanosynthesis follows a non-monotonic trend, governed by the competition between cold welding and fragmentation mechanisms. The optimal milling duration for obtaining a relatively uniform and refined powder structure under the given conditions is 6 hours.

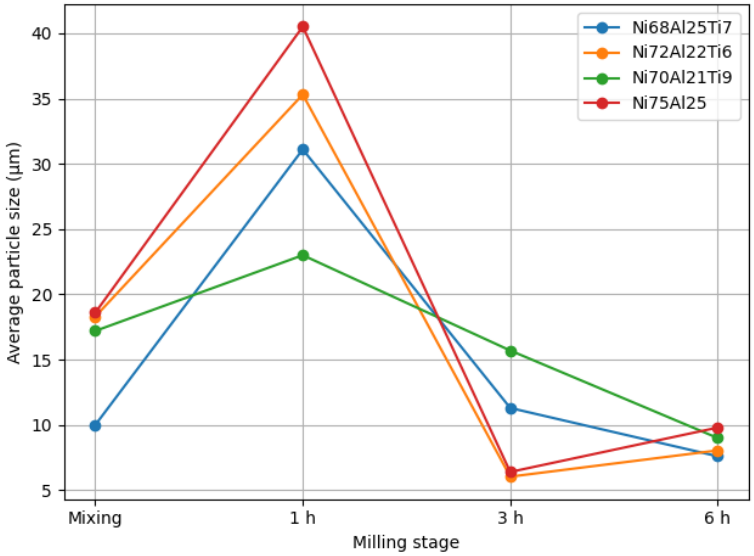

Figure 1. Evolution of average particle size during milling of powder mixtures.

The morphology of the powder mixtures at different stages of mechanosynthesis is presented in Figure 2, which combines 16 SEM micrographs corresponding to four compositions and four milling times (10 min, 1 h, 3 h, and 6 h). The rows represent different compositions ($Ni_{68}Al_{25}Ti_7$, $Ni_{72}Al_{22}Ti_6$, $Ni_{70}Al_{21}Ti_9$, and $Ni_{75}Al_{25}$), while the columns correspond to the milling duration.

The combined SEM dataset clearly demonstrates that the evolution of powder morphology during mechanosynthesis proceeds through three characteristic stages: initial agglomeration, subsequent fragmentation, and final stabilization.

At the initial stage (10 min), all compositions exhibit relatively loose and heterogeneous structures consisting of fine particles and small agglomerates. This is primarily associated with the presence of nanosized aluminum, which enhances the dispersion of the powder mixture.

After 1 hour of milling, a pronounced increase in particle size is observed across all compositions. The SEM images show the formation of large, dense agglomerates with irregular morphology. This behavior indicates that cold welding dominates over fracture at this stage, driven by severe plastic deformation and the high ductility of metallic components.

With further milling up to 3 hours, a transition to fragmentation becomes evident. The SEM micrographs reveal the breakdown of previously formed agglomerates and the appearance of finer and more dispersed particles. This stage corresponds to the most intensive refinement, where fracture mechanisms begin to prevail over cold welding.

After 6 hours of milling, the morphology becomes significantly more uniform. The images show relatively fine, equiaxed particles with a reduced number of large agglomerates, indicating that a dynamic equilibrium between cold welding and fragmentation has been established. As a result, the particle size distribution stabilizes.

A comparison of different compositions within the combined figure highlights the influence of titanium on the milling behavior. The $Ni_{75}Al_{25}$ composition (without Ti) shows the highest tendency toward agglomeration, particularly after 1 hour of milling. In contrast, Ti-containing compositions, especially $Ni_{68}Al_{25}Ti_7$, exhibit more efficient particle refinement and reduced agglomeration at later stages. This suggests that titanium plays a key role in suppressing cold welding and promoting more uniform deformation and fracture processes.

Furthermore, the combined visualization allows for direct comparison of structural evolution across all systems. It can be observed that compositions with higher Ti content demonstrate a more

gradual and controlled transition from agglomeration to fragmentation, resulting in a more homogeneous microstructure at prolonged milling times.

Overall, the analysis of the combined SEM figure confirms that the most effective particle refinement occurs between 1 and 3 hours of milling, while further processing up to 6 hours leads primarily to structural stabilization. The unified representation of all compositions and milling stages provides a comprehensive understanding of the mechanosynthesis process and highlights the role of composition in controlling microstructural evolution.

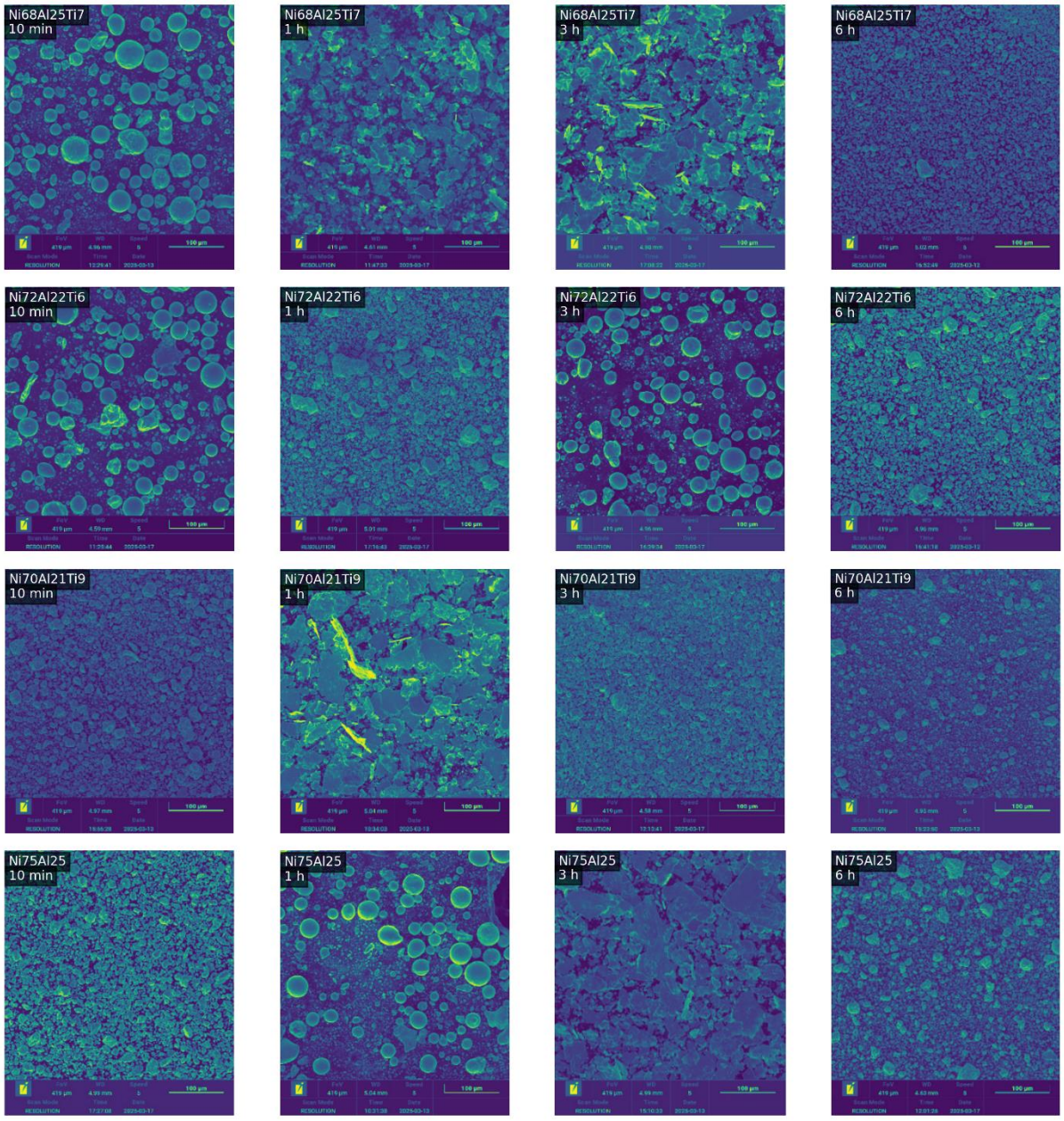

Figure 2. SEM micrographs of Ni-Al-Ti powder mixtures with different compositions at various milling stages. Rows correspond to compositions, and columns represent milling time (10 min, 1 h, 3 h, and 6 h).

Figure 2 presents the X-ray diffraction patterns of the Ni-Al and Ni-Al-Ti powder mixtures after different milling times. The diffraction data clearly show that mechanical alloying strongly affects the phase composition and structural state of the powders.

In the binary Ni-Al system, sharp and intense diffraction peaks corresponding to Ni and Al are observed at the initial stage and after 1 h of milling. This indicates that the initial components largely retain their crystalline structure during the early stage of processing. After 3 h of milling, the Al peaks disappear, while the Ni peaks shift slightly toward lower diffraction angles. This shift indicates lattice expansion caused by the dissolution of Al atoms in the Ni crystal lattice and the formation of a Ni(Al) solid solution.

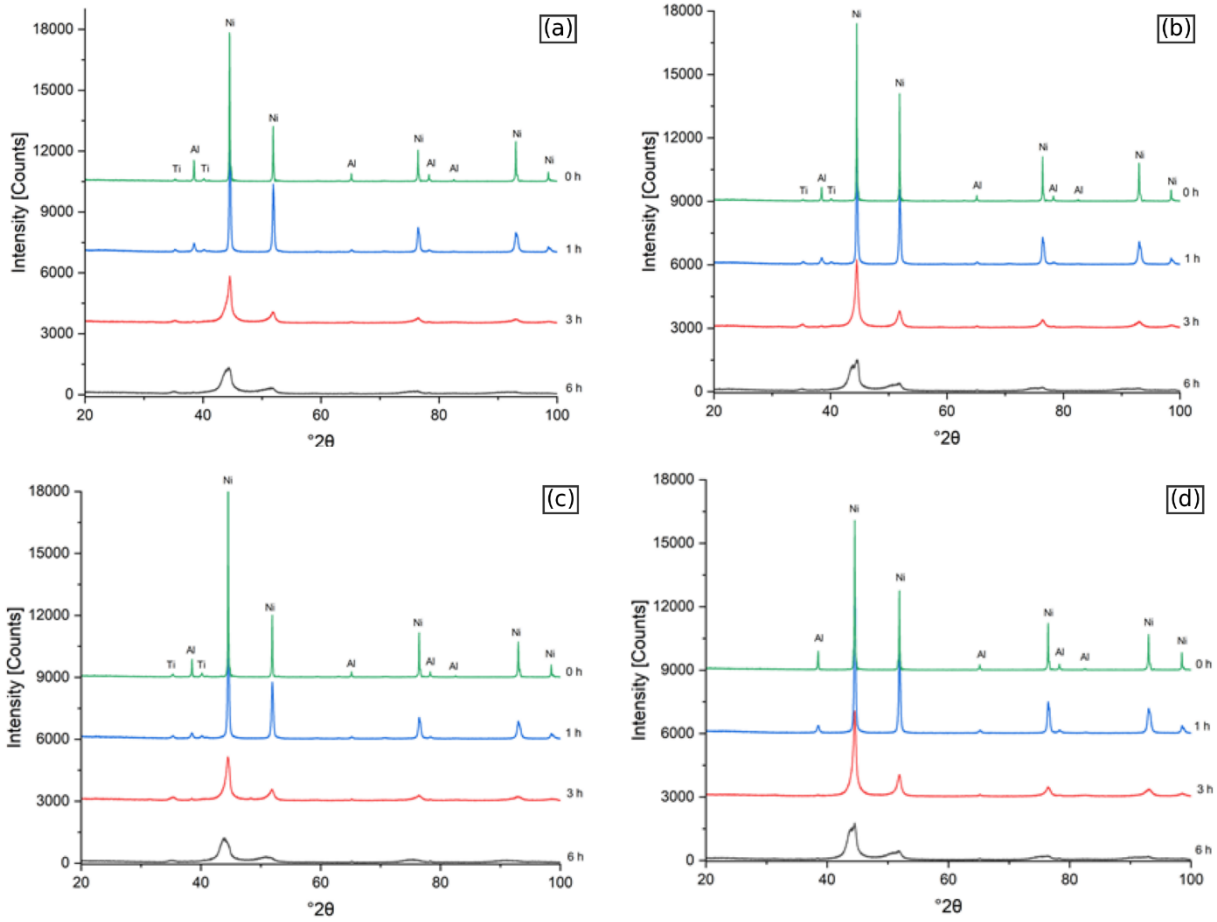

Figure 3. X-ray diffraction patterns of Ni-Al and Ni-Al-Ti powder mixtures at different milling times (0 h, 1 h, 3 h, and 6 h): (a) $Ni_{68}Al_{25}Ti_7$; (b) $Ni_{72}Al_{22}Ti_6$ (c) $Ni_{70}Al_{21}Ti_9$; (d) $Ni_{75}Al_{25}$.

After 6 h of milling, the diffraction peaks become broader and less intense, which is associated with crystallite refinement and the accumulation of lattice strain during severe plastic deformation. At this stage, the characteristic peaks of metallic Ni are significantly reduced, while reflections corresponding to the Ni_3Al intermetallic phase begin to appear. The absence of superstructure peaks suggests that the formed Ni_3Al phase has a disordered structure.

For the ternary Ni-Al-Ti compositions, a similar but more intensive transformation behavior is observed. With increasing milling time, the diffraction peaks gradually broaden and decrease in intensity, indicating grain refinement, defect accumulation, and increasing internal stresses. After 1 h of milling, the peaks of Ni, Al, and Ti can still be identified, showing that complete alloying has not yet occurred.

After 3 h of milling, the intensities of the Al and Ti peaks are significantly reduced, which indicates the gradual dissolution of these elements into the Ni lattice and the formation of a Ni(Al,Ti) solid solution. Further milling up to 6 h results in additional peak broadening and a slight shift of the

main reflections toward lower 2θ angles. This behavior confirms the expansion of the Ni lattice due to the incorporation of larger Al and Ti atoms and the development of a supersaturated solid solution. The appearance of $Ni_3(Al,Ti)$ reflections after prolonged milling indicates the formation of an intermetallic phase in the ternary system. Similar to the binary system, the absence of superstructure reflections suggests that the formed $Ni_3(Al,Ti)$ phase is structurally disordered.

A comparison of the ternary compositions shows that increasing Ti content promotes stronger peak broadening and lower peak intensity. This indicates that titanium accelerates structural refinement, enhances lattice distortion, and promotes faster phase transformation. Among the investigated compositions, $Ni_{70}Al_{21}Ti_9$ demonstrates the most pronounced transformation behavior, suggesting that this composition provides the fastest formation of the $Ni_3(Al,Ti)$ phase.

Overall, the XRD results confirm that mechanical alloying induces a gradual sequence of phase transformations: from the initial elemental powders to solid solutions Ni(Al) and Ni(Al,Ti), followed by the formation of intermetallic phases Ni_3Al and $Ni_3(Al,Ti)$ after prolonged milling. These structural changes are consistent with the SEM and particle size results, which show particle refinement, reduced agglomeration, and stabilization of the powder structure after 6 h of milling.

5. Conclusion

Elemental powder mixtures of the Ni-Al-Ti system with different compositions were successfully processed by mechanical alloying using a planetary ball mill. The results demonstrate that the phase evolution during mechanosynthesis strongly depends on milling time and chemical composition.

After 3 hours of milling, the formation of solid solutions Ni(Al) in the binary system and Ni(Al,Ti) in the ternary systems was observed, indicating the dissolution of alloying elements into the Ni lattice. Further milling up to 6 hours led to the formation of intermetallic phases Ni_3Al and $Ni_3(Al,Ti)$ in the binary and ternary systems, respectively. The absence of superstructure reflections suggests that these intermetallic phases possess a disordered structure.

It was also established that increasing the titanium content from 6 to 9 at.% accelerates the formation of the $Ni_3(Al,Ti)$ phase, highlighting the significant role of Ti in enhancing diffusion processes and phase transformation kinetics during mechanical alloying.

Overall, the obtained results confirm that mechanosynthesis is an effective method for producing intermetallic compounds in the Ni-Al-Ti system. The optimal milling duration is in the range of 3-6 hours, which ensures the formation of refined and structurally homogeneous powders with controlled phase composition.

References

1.Aubakirova, D., Sagymbekova, E., Kozhakhmetov, Y., Kowalewski, P., Dauletkhanov, Y., Yerbolat, D., & Urkunbay, A. (2025). Structural and functional enhancement of Ni–Ti–Cu shape memory alloys via combined powder metallurgy techniques. Open Engineering, 15, 208–211. https://doi.org/10.1515/eng-2025-0208

2.Aubakirova, D., Sagymbekova, E., Kozhakhmetov, Y., Dauletkhanov, Y., Urkunbay, A., Yerbolat, D., Kowalewski, P., & Tabiyeva, Y. (2025). Evolution of the structural and phase composition of Ni–Ti–Cu alloy produced via spark plasma sintering after aging. Crystals, 15, 939. https://doi.org/10.3390/cryst15090939

3.Chanda, B., Potnis, G., Jana, P. P., & Das, J. (2020). A review on nano-/ultrafine advanced eutectic alloys. Journal of Alloys and Compounds, 827, 154226. https://doi.org/10.1016/j.jallcom.2020.154226

4.Chérif, A., Bachaga, T., Saurina, J. J., Khitouni, M., & Makhlouf, T. (2017). Morphology and structure effect of Ti addition on Ni–Al powders during mechanical alloying. The International Journal of Advanced Manufacturing Technology, 88, 1767–1776. https://doi.org/10.1007/s00170-016-8908-4

5.Darolia, R. (1991). NiAl alloys for high-temperature structural applications. JOM, 43(3), 44–49. https://doi.org/10.1007/BF03220103
6.Dey, G. K. (2003). Physical metallurgy of nickel aluminides. Sadhana, 28(1–2), 247–262. https://doi.org/10.1007/BF02717135
7.Enayati, M. H., Karimzadeh, F., & Anvari, S. (2008). Synthesis of nanocrystalline NiAl by mechanical alloying. Journal of Materials Processing Technology, 200(1–3), 312–315. https://doi.org/10.1016/j.jmatprotec.2007.08.034
8.Frommeyer, G., & Rablbauer, R. (2008). High temperature materials based on NiAl. Steel Research International, 79(7), 507–513. https://doi.org/10.2374/SRI08SP130
9.Gao, M., Wen, D., Huang, Z., Kong, F., Liu, J., Li, Q., Zhang, C., Liu, C. T., & Wang, A. (2025). Rational design of eutectic Ni–Al–Ti alloys. Materials & Design, 249, 113532. https://doi.org/10.1016/j.matdes.2024.113532
10.Grabke, H. J. (1999). Oxidation of NiAl and FeAl. Intermetallics, 7(10), 1153–1158. https://doi.org/10.1016/S0966-9795(99)00054-7
11.Li, L., Ding, Q., Zhang, Z., Li, Y., Wei, X., Zhang, Z., & Bei, H. (2023). Effect of Al and Ti on $Ni_3(Al,Ti)$ alloys. Journal of Materials Research and Technology, 24, 4650–4660. https://doi.org/10.1016/j.jmrt.2023.04.089
12.Liu, C. T. (1984). Physical metallurgy and mechanical properties of ductile ordered alloys. International Metals Reviews, 29(1), 168–194. https://doi.org/10.1179/imtr.1984.29.1.168
13.Mardiha, P., Bahrami, A., & Mohammadnejad, A. (2019). Ni/Ni_3Al multilayer composite. Science of Sintering, 51(4), 401–412. https://doi.org/10.2298/SOS1904401M
14.Ozdemir, O., Zeytin, S., & Bindal, C. (2008). Tribological properties of NiAl intermetallics. Wear, 265(7–8), 979–985. https://doi.org/10.1016/j.wear.2008.01.010
15.Riyadi, T. W. B. (2020). Structure and properties of Ni–Al–Ti systems. Materials Science Forum, 991, 44–50. https://doi.org/10.4028/www.scientific.net/MSF.991.44
16.Samani, M. N., Shokuhfar, A., Kamali, A. R., & Hadi, M. (2009). Production of nanocrystalline Ni_3Al by mechanical alloying. Journal of Alloys and Compounds, 500(1), 30–33. https://doi.org/10.1016/j.jallcom.2009.03.030
17.Suryanarayana, C. (2001). Mechanical alloying and milling. Progress in Materials Science, 46(1–2), 1–184. https://doi.org/10.1016/S0079-6425(99)00010-9
18.Wu, L., Yao, J., Dong, H., He, Y., Xu, N., Zou, J., Huang, B., & Liu, C. T. (2011). Corrosion behavior of Ni_3Al intermetallics. Intermetallics, 19(11), 1759–1765. https://doi.org/10.1016/j.intermet.2011.06.010

Applied Problems of Physics and Mathematics

Effect of electrolytic plasma hardening on the strength properties of steel

[1] Yerkezhan Tabiyeva, [2] Alikhan Zekenov

PhD, Center of Excellence "VERITAS", D. Serikbayev East Kazakhstan Technical University, 070004, Ust-Kamenogorsk, Kazakhstan
e-mail: etabieva@edu.ektu.kz ; ORCID: 0000-0002-9726-7187
[2]Grade 11D student, Nazarbayev Intellectual School, 070004, Ust-Kamenogorsk, Kazakhstan
e-mail: Zekenov_A@ukk.nis.edu.kz

Abstract: This study investigates the effect of electrolytic plasma surface hardening on the structural, mechanical, tribological, and corrosion properties of steel grade 2 used for railway applications. The treatment was performed in an aqueous electrolyte containing 10% carbamide and 20% sodium carbonate under conditions of rapid heating and self-quenching. The phase composition of the surface layer was analyzed by X-ray diffraction, while mechanical properties, wear resistance, and corrosion behavior were evaluated using standard testing methods. The results show that the treatment leads to the formation of a multiphase surface layer consisting of α-Fe, iron carbides, and oxide phases. As a result, a significant improvement in mechanical properties was observed, including an increase in strength and a substantial rise in surface microhardness. The wear resistance of the treated samples increased by 3.5–3.7 times compared to the initial state. At the same time, electrochemical tests revealed an increase in corrosion current density, indicating higher surface activity, while the overall corrosion rate decreased, suggesting the formation of partially protective surface layers. The obtained results demonstrate that electrolytic plasma surface hardening is an effective method for improving the performance of steel grade 2, although the balance between enhanced wear resistance and corrosion behavior requires further optimization.

Keywords: electrolytic plasma hardening; surface modification; steel properties; wear resistance; corrosion resistance

1. Introduction

The durability and reliability of engineering components are largely determined by the condition of their surface layers, where degradation processes such as wear, corrosion, and contact fatigue are initiated. This is especially important for railway applications, where materials are subjected to cyclic loading, friction, and aggressive environmental conditions. Steel grade 2, used for locomotive wheel bandages in accordance with GOST 398-96, is a medium-carbon structural steel that combines adequate strength with good manufacturability. However, even after conventional heat treatment, its service life remains limited by surface damage mechanisms, particularly abrasive wear and corrosion. This creates a need for advanced surface strengthening methods capable of improving both mechanical and operational properties.

Electrolytic plasma hardening has emerged as a promising surface treatment technique due to its ability to provide rapid localized heating and self-quenching under atmospheric conditions. This process leads to significant microstructural transformations in the surface layer, which can enhance hardness and wear resistance (Lu et al. 2024; Rakhadilov et al. 2024) . At the same time, the influence of such treatment on corrosion behavior remains insufficiently understood and may vary depending on processing conditions (Mukhametov et al. 2025). Despite the growing application of electrolytic plasma technologies, their effect on railway steels, including grade 2, has been studied to a limited extent. In particular, the combined impact of structural transformations on wear resistance and corrosion behavior requires further investigation.

The aim of this study is to evaluate the effect of electrolytic plasma surface hardening on the structural state and performance characteristics of steel grade 2. The results demonstrate that the

treatment leads to phase transformations in the surface layer and contributes to a significant increase in wear resistance, confirming its potential for practical application.

2. Literature Review

The modification of surface layers is a well-established approach to improving the performance of structural steels. It is widely recognized that the formation of martensitic structures and carbide phases increases hardness and wear resistance, although these changes may also affect corrosion behavior (Becerra 2025; Berton et al. 2020).

Traditional surface hardening methods, such as carburizing, nitriding, and induction hardening, have demonstrated high efficiency but are often associated with high energy consumption and technological complexity (Jumbad et al. 2020). This has led to increased interest in alternative techniques that enable rapid and energy-efficient surface modification.

Electrolytic plasma processing is one such method. It is based on plasma formation in an electrolyte, which provides intensive surface heating followed by rapid cooling. This results in structural transformations that can significantly improve mechanical and tribological properties (Lu et al. 2024; Meletis et al. 2002). In addition, the method enables the formation of gradient structures consisting of a hardened surface layer and a more ductile core, which is beneficial for resistance to crack initiation (Jiang et al. 2025; Ren et al. 2021).

At the same time, previous studies report inconsistent findings regarding the corrosion behavior of electrolytic plasma-treated steels. Some authors indicate improved corrosion resistance due to oxide layer formation, whereas others report deterioration associated with surface heterogeneity and increased electrochemical activity (Mukhametov et al. 2025). These contradictions suggest that the relationship between processing conditions, microstructure, and corrosion properties remains insufficiently clarified.

Furthermore, most studies have focused on conventional structural steels, while railway steels, such as steel grade 2, have received less attention. As a result, the interaction between structural transformations, wear resistance, and corrosion behavior in such materials is still not fully understood. In this context, the present study contributes to existing research by providing a focused analysis of steel grade 2 and clarifying the relationship between electrolytic plasma hardening, structural changes, and functional properties.

3. Materials and Methods

The material used in this study was medium-carbon steel grade 2, commonly applied for locomotive wheel bandages in accordance with GOST 398-96. The chemical composition of the steel (wt.%) is as follows: C 0.57–0.65, Mn 0.50–0.90, Si 0.22–0.45, V ≤ 0.10, S ≤ 0.030, and P ≤ 0.035, with the balance being Fe. Samples were cut from a wheel bandage and prepared in the form of rectangular specimens with dimensions of 15 × 15 × 10 mm. Prior to electrolytic plasma treatment, the steel was subjected to conventional heat treatment, including quenching at 890–920 °C with a holding time of 2 h, followed by tempering at 580–620 °C for 2.5 h and cooling in water at 30–60 °C

Electrolytic plasma hardening (EPH) was performed using a laboratory-scale electrolytic plasma processing unit developed at the Research Center “Surface Engineering and Tribology”. A direct current (DC) power supply with a maximum output of 360 V and 60 A was used. The samples were treated as cathodes in an aqueous electrolyte containing 10% carbamide and 20% sodium carbonate. The process involved rapid heating of the sample surface for 2 s, followed by immediate cooling in the circulating electrolyte, which acted as the quenching medium. This processing approach enables the formation of a hardened surface layer due to the high heating and cooling rates.

Mechanical properties were evaluated using a universal testing machine (WDW-5E) in accordance with GOST 1497-87. Tensile tests were performed at room temperature under uniaxial loading until fracture. The following parameters were determined: ultimate tensile strength (σ_u), yield strength ($\sigma_{0.2}$), elongation at fracture (δ), and reduction of area (ψ). At least four specimens were tested for each condition, and the reported values represent the average results. The measurement error for the strength parameters did not exceed 7%.

The corrosion behavior of the samples was evaluated using electrochemical methods based on the measurement of electrode potentials and current density. The tests were conducted by controlling and recording the current–voltage response of the working electrode in an electrolyte solution. Both untreated and EPH-treated samples were analyzed. Corrosion parameters, including corrosion potential and corrosion current density, were determined to compare the corrosion resistance of the materials.

Abrasion resistance was evaluated using a "rotating roller–flat surface" configuration in accordance with GOST 23.208-79 (analogous to ASTM standards). The wear behavior was assessed by measuring the mass loss of the samples after testing. Relative wear resistance was calculated based on the mass loss data. All tests were performed under identical conditions for untreated and treated samples to ensure comparability.

The phase composition of the surface layers was analyzed by X-ray diffraction using an X'Pert PRO diffractometer with Cu Kα radiation over a 2θ range of 20–100°. The obtained diffraction patterns were used to identify structural changes induced by electrolytic plasma treatment.

4. Results and Discussion

The mechanical properties of the initial and electrolytic plasma surface hardened samples are presented in Table 1. The results show that the treatment leads to a noticeable improvement in strength characteristics. The ultimate tensile strength increased from 458 MPa to 569 MPa, and the yield strength increased from 315 MPa to 352 MPa. At the same time, ductility indicators also improved, with elongation increasing from 14% to 16% and reduction of area from 22.5% to 27%. A significant increase in microhardness was observed, from 1410 HV in the initial state to 3416 HV after treatment. These changes indicate the formation of a strengthened surface layer, which can be associated with structural transformations occurring during rapid heating and cooling.

Table 1. Results of mechanical tests

Sample	σ_u (MPa)	$\sigma_{0.2}$ (MPa)	δ (%)	ψ (%)	HV
Initial	458	315	14	22.5	1410
After EPH	569	352	16	27.0	3416

The results of abrasion testing are shown in Figure 1. The EPH-treated samples exhibited significantly lower mass loss compared to the untreated material. Based on these data, the relative wear resistance increased by approximately 3.5–3.7 times after treatment. This improvement is consistent with the increase in surface hardness and indicates enhanced resistance to mechanical damage under abrasive conditions.

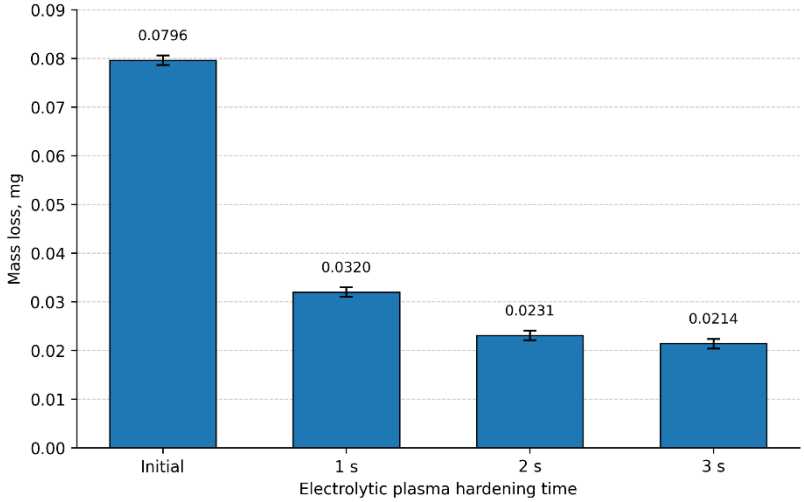

Figure 1. Mass loss of steel grade 2 samples during abrasive wear testing before and after electrolytic plasma surface hardening. Error bars indicate measurement uncertainty.

The corrosion behavior of the samples is summarized in Table 2. After treatment, the corrosion potential (E_{corr}) shifts slightly toward more negative values, from -900 mV to -908 mV. This shift suggests an increased thermodynamic tendency of the material toward oxidation, which is commonly observed in surface-modified steels. At the same time, a significant increase in corrosion current (i_{corr}) and current density (j_{corr}) is observed after EPSH. The corrosion current increases from 0.002512 A to 0.003236 A, while the current density rises from 2.72×10^{-3} A/cm^2 to 4.55×10^{-3} A/cm^2. These changes indicate an increase in the electrochemical activity of the surface, which may be associated with structural and compositional heterogeneity introduced during treatment. One possible explanation for this behavior is the formation of a multiphase surface layer consisting of iron carbide, troostite, and iron oxide, as revealed by X-ray diffraction analysis. The presence of such phases can lead to the formation of microgalvanic couples, where regions with different electrochemical potentials accelerate localized corrosion processes. In particular, oxide inclusions and carbide networks may act as cathodic or anodic sites, promoting uneven corrosion.

Table 2. Electrochemical corrosion parameters of steel grade 2 before and after electrolytic plasma hardening.

Sample	S (cm²)	Ecorr (mV)	log(i)	M (g/mol)	n	F (C/mol)	t (s)	ρ (g/cm³)	icorr (A)	jcorr (A/cm²)	m (g)	l (cm)	Rcorr (cm/year)
Initial	0.924	−900	−2.6	62.04	16	96485	3.15×10^7	7.874	0.002512	2.72×10^{-3}	3.280	0.451	0.755
After EPH	0.711	−908	−2.49	62.04	16	96485	3.15×10^7	7.874	0.003236	4.55×10^{-3}	4.226	0.755	0.451

Another important factor is the rapid thermal cycle inherent to EPSH. High heating and cooling rates can result in residual stresses, microstructural gradients, and possible surface roughness changes,

all of which influence corrosion behavior. These effects are consistent with previous studies, which report that electrolytic plasma treatment may either improve or deteriorate corrosion resistance depending on the balance between surface oxidation and structural refinement. Interestingly, despite the increase in corrosion current density, the calculated corrosion rate (R_{corr}) decreases from 0.755 cm/year in the initial state to 0.451 cm/year after EPH. This apparent contradiction may be explained by the formation of a partially protective surface layer, likely containing oxide phases, which can slow down the overall material degradation despite increased electrochemical activity. Such behavior suggests that corrosion processes are not uniform and may be governed by competing mechanisms.

Overall, the results indicate that electrolytic plasma surface hardening leads to a complex modification of corrosion behavior. While the electrochemical activity of the surface increases, the overall corrosion rate may decrease due to the formation of protective phases. This highlights the importance of considering both electrochemical parameters and material loss when evaluating corrosion performance.

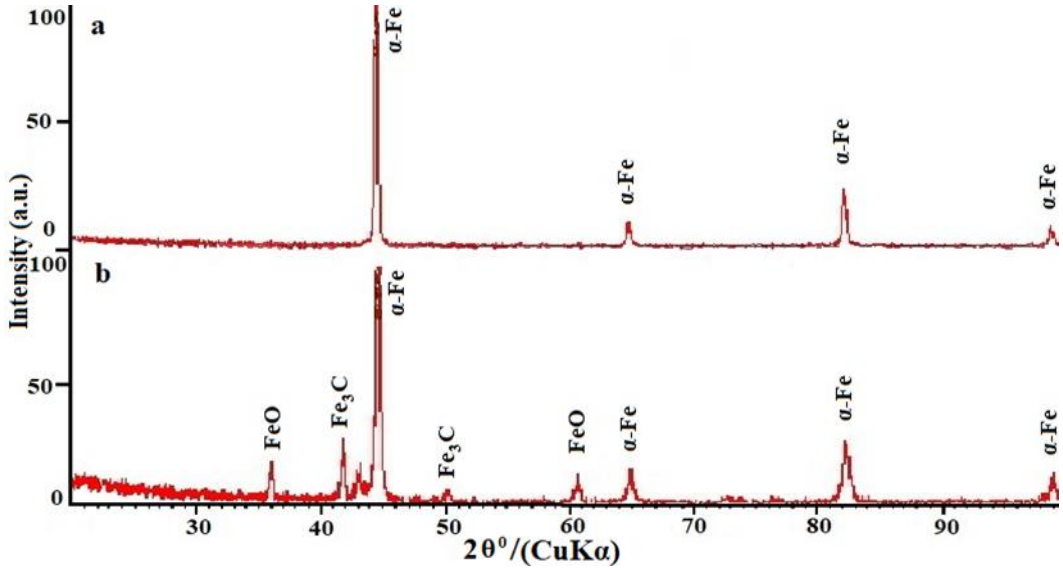

(a) Initial condition; (b) after electrolytic plasma surface hardening (EPSH).

Figure 2. X-ray diffraction patterns of steel grade 2 before and after electrolytic plasma surface hardening.

The X-ray diffraction patterns presented in Figure 2 provide clear evidence of structural changes in the surface layer of steel grade 2 after electrolytic plasma surface hardening. In the initial condition (Figure 2a), the diffraction pattern is dominated by peaks corresponding to α-Fe, indicating a typical ferrite–pearlite structure of the untreated steel. After electrolytic plasma treatment (Figure 2b), additional diffraction peaks appear, corresponding to iron carbide phases (Fe_3C) and iron oxide (FeO), alongside the retained α-Fe phase. The presence of Fe_3C indicates the formation of a strengthened carbide phase within the surface layer, which is consistent with rapid thermal cycling and localized carbon redistribution during treatment. At the same time, the detection of FeO suggests that oxidation processes occur due to the high-temperature interaction of the surface with the electrolyte environment.

The coexistence of α-Fe, carbide, and oxide phases confirms the formation of a heterogeneous multiphase surface layer. Such a structure plays a key role in determining the functional properties of the material. In particular, the formation of carbide phases contributes to the significant increase in hardness and wear resistance observed in this study. This is consistent with the experimental results,

where the microhardness increased more than twofold and the wear resistance improved by 3.5–3.7 times.

At the same time, the presence of oxide phases and structural heterogeneity can explain the changes in corrosion behavior. The formation of microgalvanic couples between different phases (α-Fe, Fe_3C, and FeO) leads to an increase in electrochemical activity, which is reflected in the higher corrosion current density observed after treatment. However, the oxide layer may also partially act as a barrier, contributing to the reduction of the overall corrosion rate.

Thus, the XRD results are in good agreement with the mechanical, tribological, and corrosion data obtained in this study. The electrolytic plasma surface hardening process leads to the formation of a multiphase gradient layer, which enhances wear resistance due to carbide formation while simultaneously affecting corrosion behavior through oxidation and phase heterogeneity. Overall, the obtained results demonstrate that electrolytic plasma surface hardening significantly improves the mechanical and tribological properties of steel grade 2. The increase in hardness and wear resistance is consistent with the formation of strengthened surface structures. At the same time, the corrosion behavior indicates a more complex response, likely influenced by surface heterogeneity and phase composition.

It should be noted that the present study has certain limitations. The number of tested samples was limited, and the structural analysis was primarily based on X-ray diffraction without detailed microscopic examination. In addition, corrosion tests were performed under laboratory conditions, which may differ from real service environments. Despite these limitations, the results confirm the effectiveness of electrolytic plasma surface hardening as a method for improving the performance of steel grade 2. Further research should focus on optimizing processing parameters and investigating the relationship between microstructure and corrosion behavior in greater detail.

5. Conclusion

Based on the results obtained in this study on the effect of electrolytic plasma hardening (EPH) on steel grade 2, the following conclusions can be drawn:

- The features of electrolytic plasma surface hardening of steel grade 2 in aqueous electrolytes were investigated, and the formation of a modified multiphase surface layer was confirmed;
- EPSH leads to a significant improvement in mechanical and tribological properties, including an increase in strength and a substantial rise in surface microhardness;
- A pronounced enhancement in wear resistance was achieved, with the relative wear resistance increasing by 3.5–3.7 times compared to the initial state;
- The treatment affects corrosion behavior, indicating a complex interaction between surface structure and electrochemical activity;

Overall, electrolytic plasma surface hardening can be considered an effective and promising method for improving the performance of steel grade 2 used in demanding operating conditions.

References

1. Becerra, L. H. C. (2025). A review of heat treatments applied to low-, medium-, and high-carbon steels used in cold drawing. Discover Materials, 5, 88. https://doi.org/10.1007/s43939-025-00088-0
2. Berton, E. M., das Neves, J. C. K., Mafra, M., & Borges, P. C. (2020). Quenching and tempering effect on the corrosion resistance of nitrogen martensitic layer produced by SHTPN on AISI 409 steel. Surface and Coatings Technology, 395, 125921. https://doi.org/10.1016/j.surfcoat.2020.125921
3. Chen, J., Feng, G., Zheng, Y., Ma, J., Lin, P., Wang, N., & Zheng, J. (2022). Characterization of surface decarburization and oxidation behavior of Cr–Mo cold heading steel. High Temperature Materials and Processes, 41(1), 531–541. https://doi.org/10.1515/htmp-2022-0026

4. Jiang, L., Feng, X., Wang, Y., Ji, Y., & Yang, B. (2025). Research progress of gradient nanostructured steels. Journal of Materials Research and Technology, 39, 3706–3725. https://doi.org/10.1016/j.jmrt.2025.01.123
5. Jumbad, V. R., Chel, A., Verma, U., & Kaushik, G. (2020). Application of electrolytic plasma process in surface improvement of metals: A review. Letters in Applied NanoBioScience, 9(2), 1249–1262. https://doi.org/10.33263/LIANBS92.12491262
6. Lu, S., Sun, X., Zhang, B., & Wu, J. (2024). Review of cathode plasma electrolysis treatment: Progress, applications, and advancements in metal coating preparation. Materials, 17(16), 3929. https://doi.org/10.3390/ma17163929
7. Meletis, E. I., Nie, X., Wang, F. L., & Jiang, J. C. (2002). Electrolytic plasma processing for cleaning and metal-coating of steel surfaces. Surface and Coatings Technology, 150(2–3), 246–256. https://doi.org/10.1016/S0257-8972(01)01581-4
8. Mukhametov, Y., Shynarbek, A., Rakhadilov, B., Zhassulan, A., Ibragimov, N., Ormanbekov, K., & Kadyrbolat, N. (2025). The effect of electrolytic-plasma hardening time on the microstructure, hardness, and corrosion behavior of medium-carbon steel. Crystals, 15(12), 1058. https://doi.org/10.3390/cryst15121058
9. Rakhadilov, B., Kussainov, R., Kalitova, A., Satbayeva, Z., & Shynarbek, A. (2024). The impact of technological parameters of electrolytic-plasma treatment on the mechano-tribological properties of steel 45. AIMS Materials Science, 11(4), 666–683. https://doi.org/10.3934/matersci.2024034
10. Ren, C. X., Wang, Q., Hou, J. P., Zhang, Z. J., Zhang, Z. F., & Langdon, T. G. (2021). The nature of the maximum microhardness and thickness of the gradient layer in surface-strengthened Cu–Al alloys. Acta Materialia, 215, 117073. https://doi.org/10.1016/j.actamat.2021.117073
11. Satbayeva, Z., Maulit, A., Ispulov, N., Baizhan, D., Rakhadilov, B., & Kusainov, R. (2024). Electrolytic plasma nitriding of medium-carbon steel 45 for performance enhancement. Crystals, 14(10), 895. https://doi.org/10.3390/cryst14100895

Applied Problems of Physics and Mathematics

Integrated Defect Engineering in Perovskite Solar Cells for Enhanced Stability and Efficiency

Kubakova Aizada[1], Chen Xinlei[2]
Osh Technological Univercity, Str. N.Isanov, 81, Osh 723503, Kyrgyzstan
aizadakubakova@gmail.com, SPP659hv@gmail.com

Abstract: This study presents a comprehensive analysis of defect engineering strategies in perovskite solar cells (PSCs) aimed at improving device stability and power conversion efficiency. Particular attention is given to three key approaches: chemical passivation using organic and inorganic additives, structural control of crystallization and perovskite film morphology, and interfacial engineering through the incorporation of interfacial barriers and dipole layers. Experimental results and numerical simulations demonstrate that the synergistic implementation of these strategies significantly reduces trap-state density and suppresses non-radiative recombination pathways, thereby enhancing the open-circuit voltage (VOS) and fill factor (FF).

Stability tests conducted under international ISOS protocols indicate that defect-engineered devices retained more than 85–90% of their initial power conversion efficiency after 1000 h of operation, whereas reference devices exhibited a performance loss exceeding 50% under comparable conditions. Scanning electron microscopy analysis revealed improved film compactness, reduced grain-boundary discontinuities, and fewer visible morphological defects. In parallel, modelling results confirmed an exponential correlation between defect density and the degradation dynamics of VOS and F.

Furthermore, the scalability of deposition techniques, including blade coating, slot-die coating, and roll-to-roll processing, demonstrated the reproducibility of defect-engineering effects during the transition from small-area laboratory devices to larger-area modules. Nevertheless, challenges associated with film uniformity, long-term environmental stability, and process reproducibility remain to be fully addressed. Overall, the findings suggest that the integration of chemical, structural, and interfacial defect engineering provides a universal and effective strategy for simultaneously increasing PSC efficiency by 12–15% and substantially improving operational stability. These results open promising prospects for the industrial implementation of perovskite photovoltaic technologies and their integration into tandem solar-cell architectures, contributing to the advancement of renewable energy systems and the achievement of sustainable development goals.

Keywords: Perovskite solar cells; defect engineering; passivation; interfacial engineering; operational stability; power conversion efficiency; scalability; renewable energy; open-circuit voltage; fill factor.

1. Introduction

1.1. Relevance of Perovskite Solar Cells

Over the past two decades, renewable energy has become not only a strategic priority of global energy policy but also one of the central directions of advanced scientific research [1]. Among emerging photovoltaic technologies, perovskite solar cells (PSCs) have attracted particular attention due to their rapid progress in power conversion efficiency. Since their first demonstration with efficiencies below 4% in 2009, PSCs have achieved certified efficiencies exceeding 26% by 2023 [2]. This remarkable improvement positions perovskite-based photovoltaic materials among the most promising candidates for either complementing or partially replacing conventional silicon solar cells.

Despite this outstanding progress, the commercial deployment of PSCs remains limited by fundamental challenges related to material instability and device degradation [3]. The most vulnerable regions within PSC architectures include grain boundaries, interfacial layers, crystal-lattice imperfections, and ion-migration pathways. These factors collectively accelerate non-radiative recombination, charge-transport imbalance, phase instability, and interfacial degradation, ultimately resulting in reduced operational stability and efficiency loss [4].

Defect engineering has therefore emerged as a critical approach for addressing the intrinsic and extrinsic limitations of perovskite photovoltaic devices. By controlling defect formation, passivating trap states, improving film crystallinity, and stabilizing interfaces, it becomes possible to enhance both the photovoltaic performance and long-term durability of PSCs. In this context, the present study focuses on the combined role of chemical passivation, structural optimization, and

interfacial engineering as an integrated strategy for improving the stability and efficiency of perovskite solar cells.

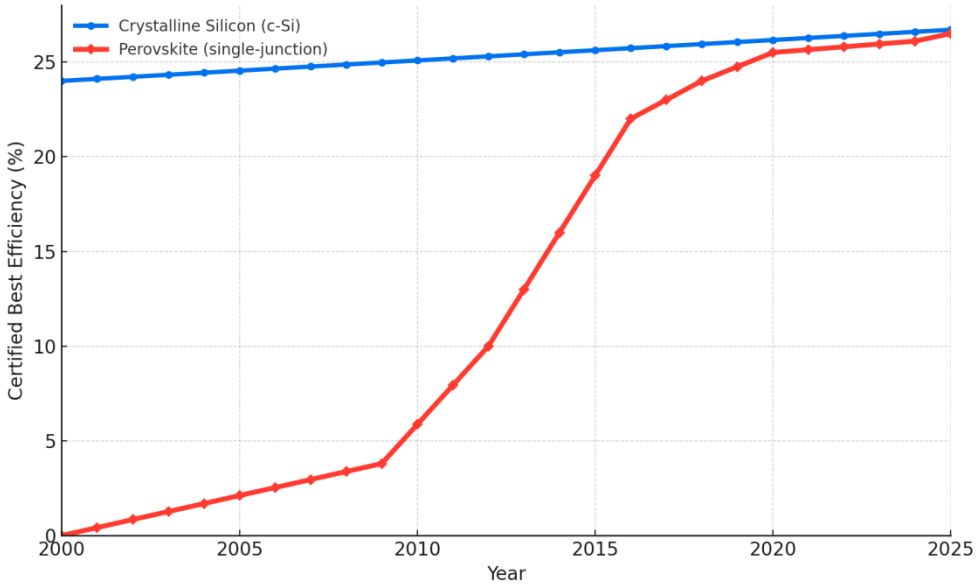

Figure 1. Comparative Evolution of Power Conversion Efficiency in Crystalline Silicon and Perovskite Solar Cells from 2000 to 2025

Figure 1 schematically compares the evolution of certified best power conversion efficiency values for two photovoltaic technologies between 2000 and 2025: crystalline silicon solar cells (c-Si) and single-junction perovskite solar cells (PSCs). The data should be presented using certified or independently confirmed record efficiencies, preferably based on internationally recognized efficiency charts and reports. Such an approach is essential for ensuring the reliability and comparability of the plotted values across different photovoltaic technologies.

The first curve illustrates the gradual improvement of crystalline silicon devices. Silicon solar cells started from a relatively high efficiency baseline and have demonstrated a slow but steady increase over time. This improvement has mainly been associated with advances in wafer quality, surface texturing, surface and interface passivation, light-management strategies, and improved contact architectures. In contrast to emerging photovoltaic technologies, the efficiency trajectory of crystalline silicon is relatively smooth and approaches a technological saturation regime.

The second curve represents the rapid development of single-junction perovskite solar cells. Unlike silicon, PSCs exhibited a remarkably steep efficiency increase after their initial low-efficiency demonstrations in 2009. This rapid progress has been driven by improvements in perovskite composition, mixed-cation and mixed-halide engineering, chemical defect passivation, crystallization control, and interfacial optimization. The visual contrast between the two curves highlights the central message of the figure: perovskite solar cells have achieved efficiency levels comparable to mature silicon technologies within a much shorter development period.

For an international readership, the figure should include English axis labels, a clear legend, and a concise explanation of data origin. The recommended axis labels are **“Year”** for the x-axis and **“Certified Power Conversion Efficiency (%)”** for the y-axis. The legend may include **“Crystalline silicon solar cells”** and **“Single-junction perovskite solar cells”**. The figure should also make clear that, although perovskites have demonstrated exceptionally rapid efficiency progress, their long-term operational stability, environmental durability, and large-area scalability remain critical challenges for commercialization.

Table 1 summarizes the principal defect types commonly observed in perovskite solar cells and their expected influence on key photovoltaic parameters, including open-circuit voltage (VOS), short-circuit current density (JSC), and fill factor (FF). Both point defects, such as vacancies and interstitial ions, and extended or morphology-related defects, such as grain-boundary states, are considered.

Each defect type is associated with a characteristic energetic position within or near the bandgap, which determines its ability to trap charge carriers and participate in recombination processes.

Iodine vacancies (VI) are often discussed as shallow donor-like defects that may influence ion migration and interfacial instability, particularly at surfaces and grain boundaries. However, their role as direct non-radiative recombination centers should be treated cautiously, since recent studies indicate that the recombination activity of VIV depends strongly on its position, structural configuration, and local chemical environment. By contrast, lead vacancies (VPb) are frequently associated with deeper acceptor-like states and can contribute more directly to trap-assisted recombination and VOS losses.

Special attention should be given to grain-boundary states and oxygen-related defects. Grain boundaries can accumulate undercoordinated ions, residual precursor species, and mobile defects, thereby acting as preferred pathways for ion migration and environmental degradation. Oxygen-related defects may form under illumination in the presence of oxygen and moisture, accelerating photo-oxidation and leading to a progressive decline in F, JSC, and operational stability.

Overall, the data summarized in Table 1 confirm the central role of defect engineering in the development of reliable perovskite solar cells. Reducing defect concentration, suppressing defect-assisted recombination, and stabilizing interfaces are essential requirements for achieving high efficiency, low hysteresis, and long-term operational durability.

Lead vacancy defects in MAPbI3 have been experimentally identified using positron annihilation lifetime spectroscopy supported by density functional theory, and such defects have been associated with deep-level hole trapping. At the same time, recent work on iodine vacancies shows that their impact is not universal and depends on surface position and defect configuration, which is why the wording in the table was made more cautious.

3. Strategies for Defect Engineering

Modern defect-engineering approaches in perovskite solar cells can be classified into several complementary categories.

First, **chemical passivation** involves the incorporation of passivating agents capable of coordinating undercoordinated ions, filling vacancy-related sites, and reducing the density of electronically active trap states. Examples include thiocyanate-based compounds, Lewis bases, ammonium salts, guanidinium-containing additives, fullerene derivatives, and multifunctional organic molecules. These additives can suppress non-radiative recombination, improve carrier lifetime, and enhance the open-circuit voltage of PSCs [7].

Second, **nanostructuring and interfacial engineering** are used to modify grain boundaries, improve film morphology, and regulate charge transfer at the interfaces between the perovskite absorber and charge-transport layers. Such strategies include surface treatment, buried-interface passivation, insertion of ultrathin buffer layers, dipole-layer engineering, and the use of two-dimensional or quasi-two-dimensional perovskite layers. These approaches reduce interfacial trap density, suppress charge accumulation, and improve both device efficiency and stability [8].

Third, **cation and anion compositional engineering** enables the stabilization of the perovskite lattice and the reduction of defect-assisted degradation. Partial substitution of A-site cations, such as methylammonium (MA+), formamidinium (FA+), cesium (Cs+), or rubidium (Rb+), can improve phase stability and crystallinity. Halide engineering through controlled incorporation of iodide, bromide, or chloride can tune the bandgap and influence ion migration. However, mixed-halide systems must be carefully optimized because excessive halide segregation may reduce photostability under illumination [9].

Fourth, **device-architecture optimization** involves the design of multilayer structures and barrier layers that prevent moisture ingress, oxygen diffusion, metal-electrode migration, and interfacial chemical reactions. Appropriate electron-transport layers, hole-transport layers, self-assembled monolayers, hydrophobic interlayers, and encapsulation strategies can substantially improve

operational durability. In this regard, device architecture is not only a charge-transport framework but also a key component of defect and degradation management [10].

Taken together, these approaches demonstrate that effective defect engineering requires a synergistic strategy rather than a single isolated modification. Chemical passivation reduces the density of trap states, structural control improves film crystallinity and morphology, compositional engineering stabilizes the perovskite lattice, and interfacial engineering suppresses charge recombination and environmental degradation. The integration of these strategies provides a promising route toward high-efficiency, stable, and scalable perovskite photovoltaic technologies.

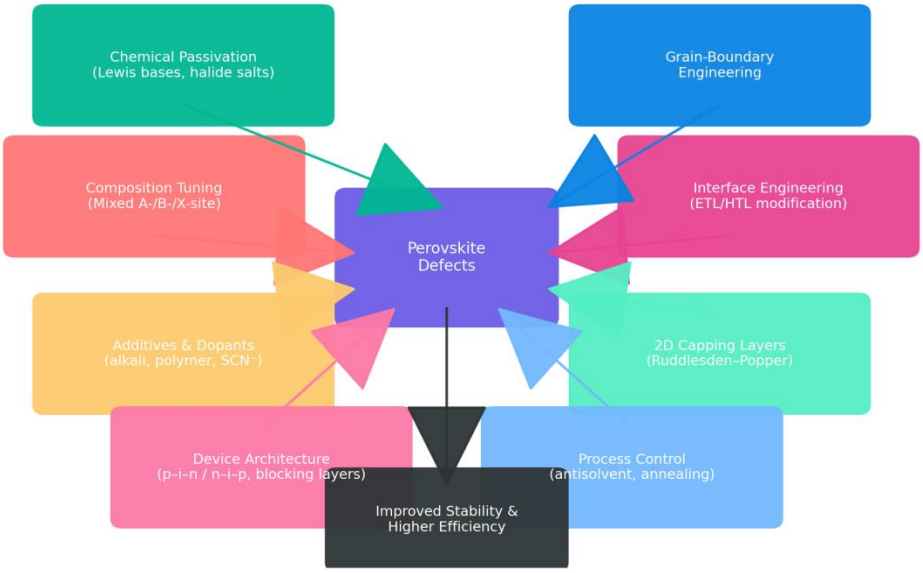

Figure 2. Schematic Illustration of Defect-Engineering Strategies in Perovskite Solar Cells

Figure 2 schematically illustrates the major defect-engineering strategies employed in perovskite solar cells and their targeted effects on defect states within the photoactive absorber layer. At the center of the scheme, the core block “Perovskite Defects” represents the main defect-related limitations, including trap states, undercoordinated ions, ion-migration pathways, grain-boundary defects, and interfacial recombination centers.

Several complementary approaches are directed toward this central defect block. Chemical passivation, involving Lewis bases, Lewis acids, halide salts, ammonium-based molecules, and multifunctional organic additives, is used to coordinate undercoordinated ions and reduce the density of electronically active trap states. Compositional engineering, including mixed-cation and mixed-anion substitution at the A, B, and X sites of the perovskite lattice, is employed to tune lattice stability, suppress phase segregation, and improve defect tolerance. Interfacial engineering, based on the modification of electron-transport layers (ETLs), hole-transport layers (HTLs), and buried or top interfaces, is designed to reduce interfacial recombination, optimize energy-level alignment, and facilitate selective charge extraction.

In addition, the scheme highlights the role of additive and dopant engineering, grain-boundary passivation, and process control. Processing strategies such as antisolvent treatment, solvent engineering, controlled annealing, atmosphere regulation, and crystallization-rate management are essential for obtaining compact, uniform, and highly crystalline perovskite films. Grain-boundary passivation reduces localized trap-state density and suppresses ion migration along extended defect pathways. Meanwhile, the deposition of two-dimensional capping layers, including Ruddlesden–Popper-type structures, can protect the perovskite surface, improve moisture and thermal resistance, and reduce non-radiative recombination at surface and interfacial regions.

The lower part of the scheme emphasizes the final target of defect engineering: the simultaneous achievement of enhanced operational stability and higher power conversion efficiency. These strategies do not act independently but rather function synergistically. For example, combining

compositional engineering with two-dimensional capping layers and interfacial modification can simultaneously reduce trap density and trap depth, improve charge transport, suppress ion migration, and increase tolerance to humidity, oxygen, light, and heat. Therefore, integrated compositional, structural, and interfacial control represents a fundamental toolkit for translating laboratory-scale advances in perovskite solar cells into long-term operational devices and scalable industrial photovoltaic modules.

Suggested improved transition to the next section

To establish a reliable correlation between defect-engineering strategies and device performance, it is necessary to evaluate not only the initial photovoltaic parameters but also their temporal evolution under standardized operational conditions. In the following section, the effects of defect density on VOS, JSC, F and long-term degradation kinetics are examined in detail.

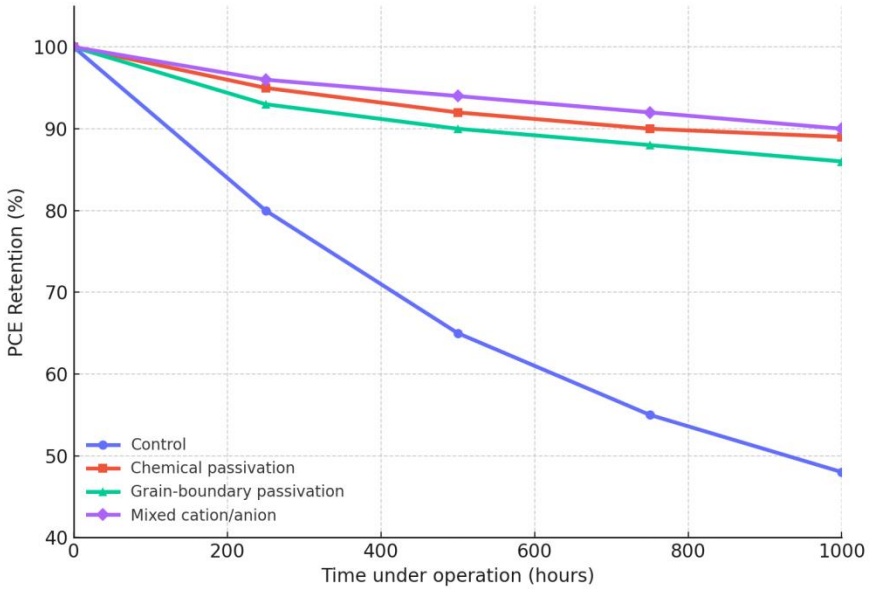

Figure 3. Power Conversion Efficiency Retention of Perovskite Solar Cells during Operation under Different Defect-Engineering Strategies

Figure 3 illustrates the evolution of power conversion efficiency retention (PCE Retention) in perovskite solar cells as a function of operating time for devices fabricated with different defect-engineering approaches. The graph highlights the substantial difference in long-term performance between untreated control devices and those incorporating defect-passivation and defect-management strategies.

The control sample, which did not undergo any deliberate defect passivation or structural optimization, exhibits rapid degradation during operation. By 1000 h of continuous testing, the control device retains less than 50% of its initial power conversion efficiency. This pronounced decline is mainly associated with ion migration, degradation at grain boundaries, interfacial instability, and the progressive increase in non-radiative recombination centers. The steep downward trajectory of the **"Control"** curve clearly emphasizes the intrinsic instability of unmodified perovskite structures.

In contrast, devices incorporating defect-engineering strategies demonstrate markedly improved stability. Approaches such as **chemical passivation**, **grain-boundary modification**, and **mixed cation/anion compositional engineering** enable the devices to retain approximately 90% of their initial efficiency after 1000 h of operation. The more gradual degradation profiles of these curves indicate that the reduction of trap-state density, improvement of film morphology, and suppression of ion diffusion play a decisive role in extending device lifetime.

This figure therefore provides clear visual evidence that defect engineering is not merely an auxiliary optimization strategy, but rather a fundamental tool for enhancing the operational reliability of perovskite solar cells. By mitigating non-radiative recombination and stabilizing both bulk and

interfacial properties, defect-engineered devices achieve a substantially improved balance between efficiency and durability.

Figure 4. Comparative Analysis of Challenges and Solutions in Defect Engineering for Perovskite Solar Cells

Figure 4 presents a problem–solution tree that systematically summarizes the major challenges and corresponding solutions in defect engineering for perovskite solar cells. The upper part of the diagram contains the central block “Challenges in Defect Engineering”, from which three main branches emerge: chemical engineering, structural control, and scalability. Each branch represents a distinct level at which defects influence the performance and durability of perovskite photovoltaic devices.

The first branch, chemical engineering, addresses defect-related issues such as deep trap states, halide and metal vacancies, undercoordinated ions, and chemically unstable surface sites. These defects are commonly associated with trap-assisted non-radiative recombination, reduced open-circuit voltage, enhanced ion migration, and accelerated degradation under operational stress. Corresponding solutions include the use of passivating agents, Lewis bases and acids, halide salts, ammonium-based additives, multifunctional organic molecules, and dopants capable of stabilizing the perovskite lattice and reducing the density of electronically active defects.

The second branch, structural control, focuses on morphology-related defects, including grain-boundary states, pinholes, local phase inhomogeneity, poor crystallinity, and non-uniform film formation. These structural imperfections create pathways for moisture penetration, ion migration, and interfacial degradation. Possible solutions include grain-boundary passivation, optimization of crystallization kinetics, controlled annealing, antisolvent engineering, solvent coordination strategies, and the incorporation of hybrid two-dimensional/three-dimensional (2D/3D) perovskite structures. In particular, Ruddlesden–Popper-type 2D layers can act as protective capping structures that suppress surface recombination and improve resistance to humidity and thermal stress.

The third branch, scalability, highlights the challenges associated with transferring laboratory-scale high-efficiency devices to industrially relevant large-area modules. These challenges include film uniformity over large substrates, reproducibility of defect passivation, compatibility with high-throughput manufacturing, long-term process stability, and minimization of material waste. Potential solutions involve scalable coating and printing methods such as blade coating, slot-die coating, spray coating, inkjet printing, and roll-to-roll processing.

In the lower part of the diagram, these solutions converge into integrated defect-engineering strategies, including compositional tuning, interfacial modification, device-architecture optimization, and scalable process control. The final target of these strategies is the development of stable and high-efficiency perovskite solar cells suitable for long-term operation and industrial implementation. Overall, the diagram emphasizes that defect engineering is inherently multidimensional: defects originate not only within the perovskite bulk but also at grain boundaries, interfaces, surfaces, and during large-area processing.

2. Materials and Methods

2.1. Experimental Design

2.1.1. General Experimental Workflow

A comprehensive experimental design was employed in this study to evaluate the role of defect engineering in improving the stability and efficiency of perovskite solar cells. The workflow included the synthesis of thin-film perovskite absorbers, controlled modification of defect states, morphological and structural characterization, and electrical and optical performance measurements. The experimental strategy was designed to compare reference devices with defect-engineered devices fabricated under comparable conditions. This approach made it possible to determine the influence of chemical passivation, compositional modification, interface engineering, and crystallization control on the photovoltaic parameters and degradation behavior of the devices.

The main focus was placed on hybrid organic–inorganic perovskite systems, particularly methylammonium lead iodide (CH3NH3PbI3) and mixed-cation perovskites based on cesium, formamidinium, and methylammonium (Cs/FA/MA). These compositions were selected because they combine strong optical absorption, tunable bandgap properties, relatively high power conversion efficiency, and potential compatibility with tandem photovoltaic architectures [12].

In addition, mixed-cation systems were considered especially relevant for stability-oriented studies, since compositional engineering can improve phase stability, suppress undesirable lattice distortion, and reduce the formation of defect-assisted degradation pathways. The comparison between single-cation and mixed-cation perovskite films enabled a more detailed evaluation of how compositional complexity affects defect formation, carrier recombination, and operational durability.

2.1.2. Thin-Film Deposition and Device Architecture

Perovskite thin films were deposited using a spin-coating method combined with a controlled antisolvent-assisted crystallization process. After deposition, the films were subjected to thermal annealing in order to promote crystallization, enhance grain growth, and improve film compactness. The antisolvent step was used to control supersaturation during film formation and to obtain uniform perovskite layers with reduced pinhole density and improved surface coverage.

The device architecture included electron-transport layers (ETLs), perovskite absorber layers, hole-transport layers (HTLs), and metal electrodes. Titanium dioxide (T_iO_2) and tin dioxide (S_nO_2) were employed as electron-transport layers, while Spiro-OMeTAD and PTAA were used as hole-transport materials [13]. These transport layers were selected because of their established compatibility with high-performance perovskite solar-cell architectures and their ability to influence charge extraction, interfacial recombination, and device stability.

The use of different ETL and HTL materials also enabled the evaluation of interfacial effects on defect formation and charge-transport behavior. In particular, S_nO_2-based ETLs are often preferred in low-temperature processing and tandem-compatible architectures, whereas T_iO_2-based ETLs provide a conventional reference system for comparison. Similarly, Spiro-OMeTAD and PTAA offer different interfacial properties, which can influence hole extraction, interfacial recombination losses, and long-term operational stability.

To investigate the effect of defect engineering, selected devices were modified using passivating additives, compositional tuning, grain-boundary treatment, or interfacial modification. The resulting

films and devices were compared with untreated reference samples in terms of morphology, crystallinity, photovoltaic performance, hysteresis behavior, and stability under accelerated aging or operational testing conditions.

Perovskite solar cells were fabricated using a controlled thin-film deposition protocol based on spin coating, antisolvent-assisted crystallization, and subsequent thermal annealing. The investigated absorber compositions included CH3NH3PbI3 and mixed-cation Cs/FA/MA-based perovskites, selected for their high photovoltaic performance and relevance to tandem solar-cell architectures. Electron-selective contacts were prepared using T_iO_2 or S_nO_2, whereas Spiro-OMeTAD and PTAA were employed as hole-transport layers. Defect-engineered samples were prepared by introducing chemical passivating agents, compositional modifiers, grain-boundary treatments, and interfacial layers. Reference devices without intentional defect modification were fabricated under identical processing conditions to enable a direct comparison of morphology, defect density, charge recombination, photovoltaic performance, and operational stability.

Table 1. Important note for completing the Methods section

Parameter	Required detail for
Perovskite precursor	Exact molar concentration, solvent system, precursor ratio
Spin-coating process	Rotation speed, time, acceleration, antisolvent type and dripping time
Annealing	Temperature, duration, atmosphere
ETL/HTL deposition	Material concentration, deposition method, annealing or oxidation conditions
Defect passivator	Chemical name, concentration, introduction route
Device area	Active area and aperture area
Characterization	SEM, XRD, PL/TRPL, UV–Vis, J–V, EQE, EIS, SCLC
Stability testing	ISOS protocol, temperature, humidity, illumination intensity, atmosphere
Statistics	Number of devices, average PCE, standard deviation, champion device

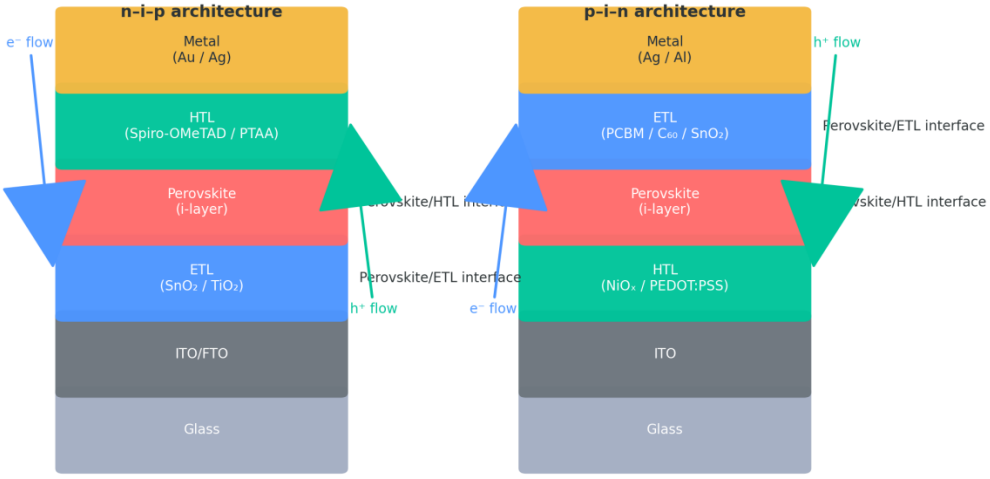

Figure 5. Schematic Architecture of n–i–p and p–i–n Perovskite Solar Cells

Figure 5 schematically illustrates two widely used device architectures in perovskite solar cells: the conventional **n–i–p** configuration and the inverted **p–i–n** configuration. The scheme clearly identifies the position of the photoactive perovskite absorber layer, denoted as the intrinsic layer (i-layer), as well as the critical interfacial regions between the perovskite and charge-transport layers.

In the **n–i–p architecture**, the layer sequence from the transparent substrate to the top electrode is typically arranged as follows:

Glass/ITO(FTO)→ETL→Perovskite→HTL→Metal electrode.}

→ETL→Perovskite→HTL→Metal electrode.

In this configuration, tin oxide (S_nO_2) or titanium dioxide (TiO2) is commonly used as the electron-transport layer (ETL), while Spiro-OMeTAD or PTAA is employed as the hole-transport layer (HTL). The metallic top electrode is usually based on gold (Au), silver (Ag), or other conductive materials compatible with the selected device stack.

In the **p–i–n architecture**, the order of the charge-selective layers is inverted:

Glass/ITO→HTL→Perovskite→ETL→Metal electrode.

Here, nickel oxide (NiOx), PEDOT:PSS, or self-assembled monolayers may serve as hole-selective layers, whereas fullerene-based materials such as PCBM and C_{60}, often combined with S_nO_2, are used as electron-selective contacts. The top electrode is commonly Ag, Al, Cu, or another low-resistance metal contact.

The arrows in the scheme indicate the direction of charge transport. Electrons are selectively extracted through the ETL, while holes are transported through the HTL toward the opposite electrode. The relative position of the ETL and HTL determines the direction of carrier extraction and strongly affects interfacial recombination, energy-level alignment, hysteresis behavior, and operational stability.

Special attention is given to the **Perovskite/ETL** and **Perovskite/HTL** interfaces, since these regions are among the most critical sites for defect formation and defect passivation. Interfacial defects can originate from undercoordinated ions, energy-level mismatch, chemical incompatibility, residual precursor species, local strain, and charge accumulation. Such defects promote non-radiative recombination, reduce V_{OS}, increase hysteresis, and accelerate long-term degradation.

The comparison between n–i–p and p–i–n structures highlights that each architecture requires a specific interfacial-engineering strategy. In n–i–p devices, particular emphasis is placed on transparent oxide-based ETLs and stable organic HTLs. In contrast, p–i–n devices benefit from robust inorganic or molecular HTLs, such as N_iO_x or self-assembled monolayers, and fullerene-based ETLs, which can improve electron extraction and reduce interfacial recombination. Therefore, visualizing both architectures provides a useful framework for comparing defect-engineering strategies aimed at minimizing trap density at the corresponding buried and top interfaces.

2.2. Chemical Engineering

2.2.1. Compositional Optimization and Alkali-Metal Cation Incorporation

To reduce the density of intrinsic defects and improve lattice stability, the stoichiometry of perovskite precursors was carefully optimized. Particular attention was given to controlling the ratio between organic or inorganic cations, lead halides, and halide components, since even small deviations from stoichiometry can promote the formation of vacancies, interstitial defects, secondary phases, and trap states.

The incorporation of alkali-metal cations, such as Cs+ and Rb+, was used as a compositional-engineering strategy to stabilize the perovskite crystal lattice and suppress phase instability [14]. These cations can influence crystallization kinetics, lattice tolerance factors, grain formation, and defect distribution. In mixed-cation perovskites, partial incorporation of Cs+ and Rb+ may improve phase uniformity and reduce the formation of defect-rich domains. However, their concentration must be carefully optimized, since excessive alkali-metal incorporation may lead to phase segregation, altered band alignment, or reduced charge transport.

Thus, compositional optimization was considered not only as a method for improving the crystallographic stability of the absorber layer, but also as a route for reducing defect-assisted recombination and improving device reproducibility.

2.2.2. Molecular Additives and Defect Passivation

Molecular additives were introduced to passivate undercoordinated ions, suppress trap-assisted non-radiative recombination, and improve perovskite film morphology. Additives such as ammonium thiocyanate, guanidinium-containing compounds, and polyethyleneimine were selected because of their ability to interact with ionic defects, surface states, and grain-boundary trap sites [15].

Ammonium thiocyanate (NH4SCN) can influence crystallization and coordinate with undercoordinated Pb2+ species through the thiocyanate group, thereby reducing the density of surface and grain-boundary traps. Guanidinium cations (C(NH2)3+) can contribute to lattice stabilization through hydrogen bonding and partial incorporation or surface interaction at A-site-related defect regions. Polyethyleneimine (PEI), which contains multiple amine groups, can interact with undercoordinated lead ions and modify interfacial energy alignment, although excessive polymer loading may introduce insulating barriers and hinder charge extraction.

Overall, the use of molecular additives provides a flexible approach for defect passivation. Their effectiveness depends on chemical structure, concentration, spatial distribution, compatibility with the perovskite precursor system, and the resulting influence on crystallization and interfacial charge transport.

Table 2. Additives Used for Defect Passivation and Their Proposed Mechanisms of Action

Additive	Target defect or affected region	Proposed passivation mechanism
Ammonium thiocyanate (NH4SCN)	Undercoordinated Pb2+, Pb-related surface defects, grain-boundary traps	Coordination of SCN− with undercoordinated Pb2+; modulation of crystallization; reduction of trap density and non-radiative recombination losses
Guanidinium (C(NH2)3+)	A-site-related defects, surface defects, lattice instability	Hydrogen bonding and partial A-site or surface interaction; stabilization of the perovskite lattice; suppression of defect-assisted degradation
Polyethyleneimine (PEI)	Perovskite surface and grain boundaries	Amine-group coordination with undercoordinated metal ions; passivation of grain-boundary traps; modification of interfacial energy-level alignment
Potassium chloride (KCl)	Perovskite surface, halide-vacancy-related defects, grain boundaries	K+-assisted passivation of halide-related defects; improved crystallinity and film uniformity; suppression of ion migration
Poly(methyl methacrylate) (PMMA)	Surface and interfacial regions	Formation of a thin protective polymer layer; suppression of ion diffusion; reduction of contact-

		induced defects and environmental degradation
3-Aminopropyltriethoxysilane (APTES)	Perovskite/ETL interface	Formation of chemical bridging interactions between layers; reduction of interfacial trap density; improved interfacial adhesion and charge extraction

Note: The mechanisms listed in Table 2 should be interpreted as proposed or dominant mechanisms. The actual effect of each additive depends on concentration, processing conditions, perovskite composition, device architecture, and the position of the additive within the film or interface.

Table 2 summarizes the additives used for defect passivation in perovskite solar cells, together with their target regions and proposed mechanisms of action. Each additive is directed toward specific defect types or structurally vulnerable regions. For example, ammonium thiocyanate can coordinate with undercoordinated lead species and reduce trap-assisted recombination, whereas guanidinium-based additives can stabilize the lattice through hydrogen bonding and A-site-related interactions. In this way, chemical additives provide a versatile tool for controlling perovskite composition, defect chemistry, crystallization behavior, and film morphology.

Polymeric and organosilane additives are particularly important for surface and interfacial passivation. PMMA can form a thin protective layer that suppresses ion diffusion and reduces direct chemical interaction between the perovskite and adjacent charge-transport materials. Similarly, 3-aminopropyltriethoxysilane can improve interfacial adhesion and create chemical bridging interactions at the Perovskite/ETL interface, thereby reducing interfacial trap density and improving device robustness.

The combined use of molecular, ionic, polymeric, and organosilane additives demonstrates that chemical engineering remains one of the most powerful strategies for enhancing both the efficiency and operational stability of perovskite solar cells. Nevertheless, additive concentration must be carefully optimized, since excessive passivation can introduce charge-transport barriers, modify crystallization unfavorably, or cause phase separation.

2.3. Structural Control

2.3.1. Crystallization Control, Grain-Boundary Passivation, and 2D Capping Layers

To reduce defect density at grain boundaries and improve the structural quality of perovskite films, several structural-control strategies were employed. These included slowed crystallization, controlled thermal annealing, solvent and antisolvent engineering, and the deposition of two-dimensional capping layers. Such approaches are designed to regulate nucleation and grain growth, improve film coverage, reduce pinhole formation, and suppress the formation of defect-rich grain-boundary regions.

Controlled crystallization plays a decisive role in determining the final morphology of the perovskite absorber. Rapid and uncontrolled crystallization often results in small grains, incomplete surface coverage, non-uniform thickness, and a high density of grain-boundary defects. In contrast, moderated crystallization kinetics can promote the formation of larger grains, improved compactness, and reduced surface roughness. This directly contributes to lower trap density, reduced non-radiative recombination, and improved charge-carrier transport.

Grain-boundary passivation was further enhanced through the incorporation of suitable organic cations and surface-treatment agents. In particular, two-dimensional capping layers based on phenethylammonium (PEA+) or related bulky organic ammonium cations can form Ruddlesden–Popper-type perovskite structures at the surface of the three-dimensional perovskite absorber [16].

These 2D layers can reduce surface trap density, suppress ion migration, improve moisture resistance, and protect the underlying 3D perovskite from environmental degradation.
However, the thickness and orientation of the 2D capping layer must be carefully controlled. A thin and well-oriented 2D layer can improve surface passivation and stability without significantly hindering charge extraction. By contrast, an excessively thick or poorly oriented 2D layer may increase transport resistance and reduce the fill factor. Therefore, structural control requires optimization of both defect passivation and charge-transport continuity.

2.3.2. Morphological Characterization by SEM and AFM

The morphology of the perovskite films was investigated using scanning electron microscopy (SEM) and atomic force microscopy (AFM). SEM analysis was used to evaluate surface coverage, grain size, compactness, pinhole density, and the presence of visible morphological defects. Both top-view and cross-sectional SEM images can provide valuable information on film continuity, layer thickness, and interfacial contact quality.
AFM measurements were performed to analyze surface roughness and nanoscale topography. Parameters such as root-mean-square roughness (Rq) and average roughness (Ra) were used to quantify the effect of defect-engineering strategies on film smoothness and uniformity. Lower surface roughness is generally beneficial for forming high-quality interfaces with charge-transport layers, reducing local electric-field concentration, and improving device reproducibility.
The combined use of SEM and AFM allowed a more complete assessment of how structural-control strategies influence perovskite film formation. Films treated with crystallization-control methods and 2D capping layers are expected to show improved grain connectivity, reduced pinhole density, smoother surfaces, and fewer defect-rich regions. These morphological improvements are directly related to enhanced charge transport, reduced recombination losses, and improved operational stability.

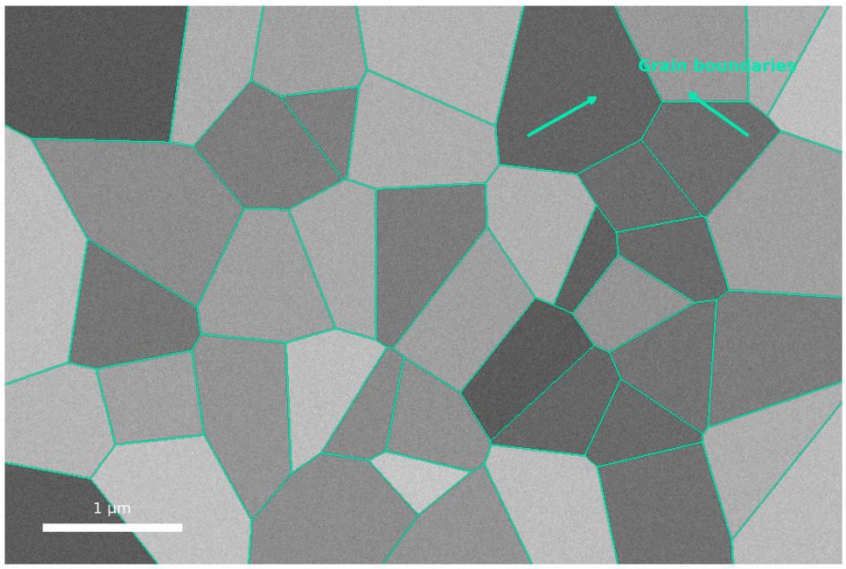

Figure 6. Simulated SEM-like Micrograph of a Perovskite Film with Highlighted Grain Boundaries

Figure 6 illustrates the microstructure of a perovskite thin film in the form of a simulated SEM-like image with clearly highlighted grain boundaries. Different grey-scale regions represent individual perovskite grains, while the bright contours indicate intergranular boundaries. These grain-boundary regions are commonly considered structurally vulnerable sites where defect accumulation, ion migration, and non-radiative recombination may occur.
A schematic scale bar of 1 μm is included to provide an approximate reference for the characteristic grain size and to relate the observed morphology to film-engineering parameters. The English

annotation “Grain boundaries” identifies the critical microstructural regions without overloading the image with excessive textual information.

Highlighting the grain boundaries makes it possible to visually localize regions where defect-engineering strategies, such as chemical passivation, controlled crystallization, or two-dimensional capping, can be effectively applied. Grain boundaries often contain undercoordinated ions, residual precursor species, local strain, and defect-rich domains, all of which can contribute to trap-assisted recombination and accelerated degradation.

This visualization also provides a useful framework for correlating film morphology with the electrical performance of perovskite solar cells. In general, an increased average grain size, improved grain connectivity, reduced pinhole density, and a lower total grain-boundary length are associated with reduced recombination losses, higher open-circuit voltage (VOS), improved fill factor (FF), and enhanced long-term operational stability. Therefore, grain-boundary engineering remains a key component of structural defect control in high-performance perovskite photovoltaic devices.

2.4. Interface Engineering

Interface engineering was employed to reduce interfacial trap density, improve energy-level alignment, suppress ion migration, and enhance the long-term stability of perovskite solar cells. Since the Perovskite/ETL and Perovskite/HTL interfaces strongly influence charge extraction, recombination dynamics, hysteresis behavior, and degradation pathways, targeted interfacial modification is essential for achieving high-performance and durable devices.

2.4.1. Surface Modification of the Electron-Transport Layer

The surface of the electron-transport layer, particularly S_nO_2, was modified using chloride- and fluoride-containing treatments in order to reduce surface defect states and improve interfacial contact with the perovskite absorber. Such treatments can passivate undercoordinated metal sites, hydroxyl-related surface groups, and oxygen-vacancy-related defects on the S_nO_2 surface.

Modification of the ETL surface can also influence perovskite nucleation and crystallization at the buried interface. A more chemically uniform and defect-passivated S_nO_2 surface promotes improved film coverage, reduced interfacial recombination, and more efficient electron extraction. In addition, halide- or fluoride-based surface treatment may help suppress charge accumulation at the buried interface, thereby reducing current–voltage hysteresis and improving operational reproducibility.

However, the concentration and processing conditions of the surface modifiers must be carefully optimized. Excessive ionic treatment may introduce unwanted interfacial dipoles, alter energy-level alignment, or create additional charge-transport barriers. Therefore, ETL surface modification should be considered an optimization tool that requires precise control over chemical composition, surface coverage, and interface energetics.

2.4.2. Organic Interlayers for Energy-Level Alignment

Organic interlayers were introduced to improve energy-level alignment between the perovskite absorber and the adjacent charge-transport layers. These ultrathin interfacial layers can create molecular dipoles, tune the work function of transport layers, reduce energetic mismatch, and suppress interfacial charge recombination.

Such interlayers are particularly useful when the conduction or valence band positions of the transport layers are not ideally matched with the perovskite absorber. By adjusting the interfacial dipole and improving carrier selectivity, organic interlayers can facilitate electron or hole extraction while blocking the opposite charge carrier. This selective transport behavior contributes to higher VOS, improved F, and reduced hysteresis.

In addition to energetic effects, organic interlayers may chemically passivate undercoordinated ions at the perovskite surface. Functional groups such as amines, carboxylates, phosphonates, ammonium

groups, and Lewis-base moieties can interact with P_{b2}+P, halide vacancies, or other surface defects. As a result, organic interlayers can simultaneously improve interfacial energetics and reduce defect-assisted non-radiative recombination.

Nevertheless, the thickness and conductivity of these layers must be carefully controlled. If the organic interlayer is too thick or too insulating, it can impede charge extraction and increase series resistance. Therefore, optimal interlayers should provide sufficient passivation and dipole control while maintaining efficient charge transport across the interface.

2.4.3. Buffer Layers for Ion-Migration Suppression and Device Durability

Ultrathin buffer layers, including LiF and $A_{l2}O_3$, were employed to suppress ion migration, reduce interfacial degradation, and improve device durability [17]. These buffer layers can act as physical and chemical barriers that limit the diffusion of mobile ions, prevent direct reactions between the perovskite and adjacent layers, and reduce metal-electrode-induced degradation.

The incorporation of LiF can improve interfacial selectivity and reduce non-radiative recombination when applied at appropriate interfaces. It may also contribute to more favorable energy-level alignment and improved charge extraction, depending on its thickness and position within the device stack. Similarly, $A_{l2}O_3$ can function as a chemically stable insulating barrier that suppresses interfacial reactions and ion migration. When deposited as an ultrathin layer, $A_{l2}O_3$ may passivate surface defects without severely hindering charge transport.

However, because $A_{l2}O_3$ is electrically insulating, its thickness must be strictly controlled. A very thin layer may allow charge tunneling or interfacial passivation without significant resistance losses, whereas an excessively thick layer can block carrier extraction and reduce the fill factor. Therefore, buffer-layer engineering requires careful optimization of thickness, deposition method, interface coverage, and compatibility with the selected n–i–p or p–i–n architecture.

Overall, the use of LiF, $A_{l2}O_3$, and related interfacial buffer layers provides an effective route for improving the operational stability of perovskite solar cells. By blocking ion migration, reducing interfacial trap density, and preventing chemical degradation at sensitive interfaces, these layers contribute to enhanced device lifetime under illumination, thermal stress, and electrical bias.

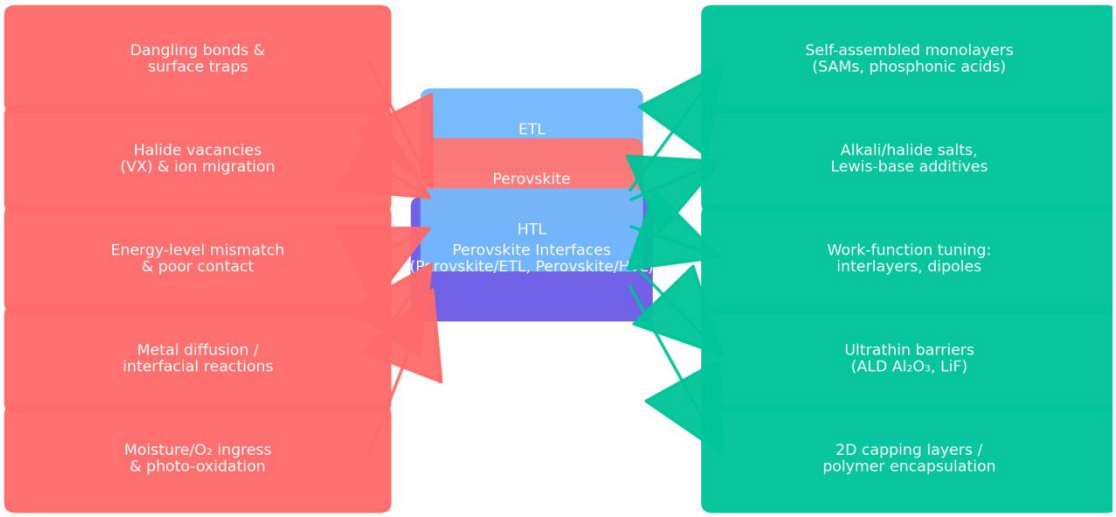

Figure 7. Interfacial Defects and Passivation Strategies in Perovskite Solar Cells

Figure 7 illustrates the key interfacial defects in perovskite solar cells and their localization at the Perovskite/ETL and Perovskite/HTL interfaces. The left side of the diagram summarizes the main sources of interfacial instability, including dangling bonds and surface trap states, halide vacancies

and ion-migration pathways, energy-level mismatch and poor physical contact, metal diffusion and interfacial chemical reactions, as well as moisture and oxygen ingress followed by photo-oxidative degradation.

The central block emphasizes the critical role of interfacial regions in determining device performance and operational stability. Interfaces are among the most vulnerable parts of perovskite solar-cell architectures because they simultaneously govern charge extraction, charge selectivity, recombination dynamics, ion migration, and chemical compatibility between adjacent layers. Defects located at the Perovskite/ETL and Perovskite/HTL interfaces can therefore act as initiation sites for non-radiative recombination, hysteresis, interfacial degradation, and long-term efficiency loss.

The right side of the diagram presents representative passivation and interfacial-engineering strategies. Self-assembled monolayers (SAMs), particularly phosphonic-acid-based molecules, can suppress surface traps and improve interfacial energy alignment. Alkali-metal salts, halide salts, and Lewis-base additives can passivate vacancy-related defects and stabilize the halide sublattice. Dipole interlayers and ultrathin organic interlayers can tune the work function of charge-transport layers and reduce energetic mismatch at the interface. In addition, ultrathin barrier coatings, such as atomic-layer-deposited $A_{l2}O_3$ and LiF, can suppress metal diffusion, ion migration, and undesirable interfacial reactions. Two-dimensional capping layers and polymeric encapsulation further protect the perovskite surface from moisture, oxygen, and photo-oxidative stress.

The directional flow from defect sources to interfacial regions and then to passivation strategies highlights the cause-and-effect relationship between interfacial defects and device degradation. This representation demonstrates that effective interface engineering requires an integrated approach combining chemical passivation, energetic optimization, diffusion blocking, and environmental protection. Such a multidimensional strategy is essential for improving both the initial power conversion efficiency and the long-term operational stability of perovskite solar cells.

Recommended Figure Caption

Fig. 7. Interfacial defects and representative passivation strategies in perovskite solar cells. The diagram summarizes major defect sources at the Perovskite/ETL and Perovskite/HTL interfaces, including surface traps, halide vacancies, ion migration, energy-level mismatch, metal diffusion, interfacial reactions, and moisture/oxygen-induced degradation. Representative mitigation strategies include self-assembled monolayers, phosphonic-acid-based modifiers, alkali-metal and halide salts, Lewis-base passivators, dipole interlayers, ultrathin barrier coatings, two-dimensional capping layers, and polymeric encapsulation.

2.5. Scalability and Processing Technologies\

Scalability is a decisive factor for the practical implementation of perovskite solar cells. Although many defect-engineering strategies demonstrate excellent results in small-area laboratory devices, their technological relevance depends on whether these improvements can be maintained during transition to larger-area devices, flexible substrates, and high-throughput manufacturing processes. Therefore, this study evaluates not only the photovoltaic performance of defect-engineered cells but also the compatibility of the proposed approaches with scalable fabrication methods.

2.5.1. Evaluation of Industrial Potential Using Larger-Area Devices

To assess the industrial potential of defect-engineering strategies, devices with active areas ranging from **0.1 to 5 cm²** were fabricated and analyzed. This active-area range was selected to bridge the gap between conventional small-area laboratory cells and larger-area devices that are more relevant for practical photovoltaic applications.

Area scaling introduces several additional challenges, including non-uniform film formation, thickness variation, incomplete surface coverage, increased probability of pinhole formation,

spatially inhomogeneous defect distribution, and higher series resistance. These factors may reduce reproducibility and accelerate degradation, even when the same defect-passivation strategy performs well in small-area devices.

Therefore, the effectiveness of chemical passivation, structural control, and interfacial engineering was evaluated not only by peak power conversion efficiency but also by film uniformity, device-to-device reproducibility, hysteresis behavior, and stability retention. Particular attention was paid to whether the reduced trap density, improved morphology, and suppressed ion migration observed in small-area devices could be preserved after increasing the active area.

This analysis is important because a defect-engineering strategy suitable for high-efficiency laboratory cells may not necessarily be compatible with large-area manufacturing. For industrial relevance, passivation agents, interfacial layers, and crystallization-control methods must remain effective under scalable coating conditions and must not introduce additional process complexity, material waste, or instability.

2.5.2. Comparison of Scalable Deposition Technologies

Several deposition technologies were compared in terms of their suitability for scalable fabrication of defect-engineered perovskite solar cells, including spin coating, blade coating, slot-die coating, and roll-to-roll processing [18].

Spin coating was used as a laboratory reference method because it enables the formation of high-quality perovskite films with relatively simple process control. However, this method has significant limitations for industrial production, including low material utilization, poor compatibility with continuous manufacturing, and difficulty in achieving uniform coatings over large-area substrates.

Blade coating provides improved scalability and better material utilization compared with spin coating. It allows controlled spreading of precursor inks over larger substrates and can be adapted to semi-continuous or continuous processing. This method is particularly useful for evaluating whether defect passivators and crystallization modifiers remain effective under coating conditions closer to practical manufacturing.

Slot-die coating is one of the most promising techniques for large-area perovskite deposition. It enables precise control of ink flow rate, coating width, wet-film thickness, and drying dynamics. These features make slot-die coating highly compatible with reproducible module fabrication. However, the method requires careful optimization of precursor viscosity, solvent evaporation, crystallization kinetics, and additive distribution to avoid large-area defect formation.

Roll-to-roll processing represents a potential route for high-throughput fabrication of perovskite solar cells on flexible substrates. Its advantages include continuous manufacturing, reduced production cost, and compatibility with lightweight photovoltaic modules. Nevertheless, roll-to-roll processing imposes strict requirements on substrate flexibility, drying speed, film uniformity, interfacial adhesion, and long-term mechanical stability. Defect-engineering strategies used in roll-to-roll fabrication must therefore be compatible with fast coating, rapid drying, and mechanical bending.

Overall, the comparison of deposition technologies demonstrates that scalable processing is not only a manufacturing issue but also a defect-control challenge. During the transition from spin-coated laboratory cells to blade-coated, slot-die-coated, or roll-to-roll-processed devices, defect passivation must remain spatially uniform, chemically stable, and compatible with large-area crystallization. Consequently, successful commercialization of perovskite solar cells requires simultaneous optimization of material chemistry, coating technology, interfacial engineering, and device architecture.

Table 3. Recommended detail

Parameter	Recommended detail
Active area	0.1, 1.0, 2.5, 5.0 cm^2 kabi aniq guruhlar
Aperture area	Sertifikatlangan o‘lchov uchun alohida ko‘rsatiladi

Number of devices	Har bir guruh uchun kamida 10–20 ta qurilma
Statistics	Average PCE, champion PCE, standard deviation
Coating method	Spin coating, blade coating, slot-die, roll-to-roll sharoitlari
Flexible substrate	PET/ITO, PEN/ITO yoki boshqa substrat turi
Stability test	ISOS protokoli, harorat, namlik, yorug‘lik intensivligi
Uniformity	Large-area film thickness, roughness yoki PCE mapping

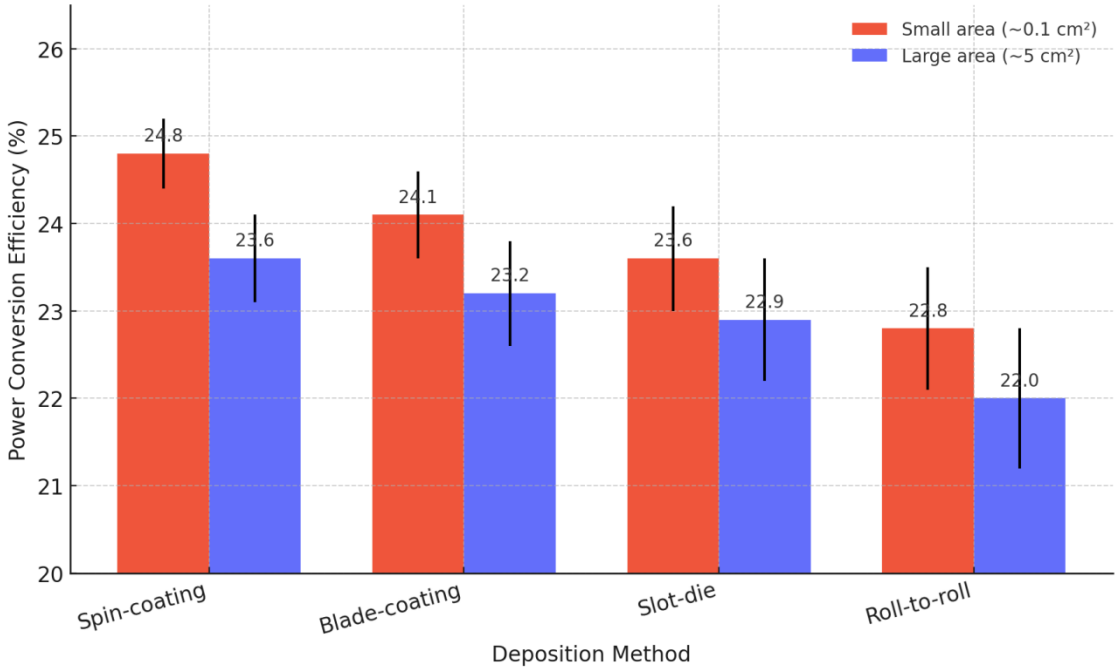

Figure 8. Comparative Power Conversion Efficiency of Perovskite Solar Cells Fabricated by Different Film-Deposition Methods

Figure 8 compares the power conversion efficiency (PCE,%) of perovskite solar cells fabricated using different film-deposition techniques, including spin coating, blade coating, slot-die coating, and roll-to-roll processing. The graph presents two device-area regimes: small-area devices with an active area of approximately 0.1 cm² and larger-area devices with an active area of approximately 5 cm². Error bars represent the standard deviation obtained from a series of independently fabricated devices, thereby indicating the reproducibility of each deposition method.

For small-area devices, the highest PCE is achieved using the spin-coating method, reaching approximately 24.8%. This result reflects the strong suitability of spin coating for laboratory-scale fabrication, where solvent evaporation, antisolvent dripping, crystallization kinetics, and film uniformity can be precisely controlled on small substrates. Blade-coated and slot-die-coated devices exhibit slightly lower efficiencies but remain highly competitive, demonstrating the potential of scalable coating technologies for producing high-quality perovskite absorber layers.

Roll-to-roll-processed devices show comparatively moderate PCE values. This reduction is mainly associated with the more stringent requirements of continuous coating, rapid solvent evaporation, mechanical substrate handling, and crystallization control at high processing speeds. In roll-to-roll systems, maintaining homogeneous precursor distribution, uniform drying, and defect-free film formation over large areas is considerably more challenging than in static laboratory-scale deposition.

For larger-area devices (~5 cm2), a systematic decrease in PCE is observed for all deposition methods. This efficiency loss is attributed to area-scaling effects, including solvent-gradient formation, non-uniform crystallization, increased probability of pinholes, thickness variation, higher series resistance, interfacial defect accumulation, and spatially heterogeneous charge extraction.

These effects become more pronounced as the active area increases and can limit both the average device performance and reproducibility.
Nevertheless, blade-coating and slot-die-coating methods retain competitive efficiency values after area scaling and are considered among the most promising approaches for industrial implementation. Their compatibility with continuous coating lines, reduced material waste, and potential applicability to flexible substrates make them more suitable for large-scale manufacturing than conventional spin coating. The comparison of small-area and large-area devices therefore highlights that successful scale-up requires simultaneous optimization of crystallization control, defect passivation, interfacial engineering, and coating-process uniformity.

2.6. Modelling and Numerical Methods
2.6.1. Simulation Tools

Numerical modelling was performed using SCAPS and COMSOL Multiphysics in order to analyze the influence of bulk and interfacial defects on the photovoltaic performance and degradation behavior of perovskite solar cells. The combined use of these simulation platforms enabled both one-dimensional device-level analysis and more detailed multiphysics modelling of charge transport, recombination, ion migration, and time-dependent degradation processes.
SCAPS was used as a one-dimensional solar-cell simulation tool to evaluate the effects of defect density, trap depth, carrier mobility, doping concentration, layer thickness, band alignment, and interface recombination on the main photovoltaic parameters, including open-circuit voltage (VOS), short-circuit current density (JSC), fill factor (FF), and power conversion efficiency (PCE). This approach made it possible to compare idealized reference devices with defect-rich and defect-passivated structures under controlled simulation conditions.
COMSOL Multiphysics was employed to extend the analysis toward spatially resolved modelling of electric-field distribution, ion migration, interfacial charge accumulation, and degradation-related transport phenomena. This was particularly important for evaluating the role of grain boundaries, buried interfaces, and non-uniform defect distributions, which cannot always be fully captured by simplified one-dimensional models.

2.6.2. Defect, Trap-State, and Degradation Modelling

The numerical models considered defect states located both in the perovskite bulk and at structurally sensitive regions such as grain boundaries and interfaces. The simulated defect parameters included bulk defect density, interfacial trap density, energetic trap distribution, capture cross-sections, and the relative position of trap levels within the bandgap.
Trap-assisted non-radiative recombination was described using Shockley–Read–Hall-type recombination mechanisms. An increase in defect density was assumed to enhance recombination losses, thereby reducing VOS, F, and overall PCE. In particular, deep-level traps were treated as more detrimental than shallow defects because they can act as efficient recombination centers for both electrons and holes.
Ion migration was incorporated into the model by considering mobile ionic species, such as halide vacancies and other vacancy-related defects. The redistribution of these mobile ions under illumination, thermal stress, and internal electric fields was used to explain current–voltage hysteresis, interfacial charge accumulation, and long-term instability. The time-dependent degradation model further accounted for the gradual increase in recombination-active defect states during operation.
The modelling framework also included the effects of grain-boundary defects. Grain boundaries were treated as regions with enhanced trap density and increased ion-migration probability compared with the bulk perovskite matrix. This assumption allowed the simulation to capture the experimentally observed relationship between film morphology, defect density, recombination losses, and stability degradation.

2.6.3. Correlation between Simulated Defect Density and Device Performance

The simulated results were correlated with experimental photovoltaic parameters and stability data. In general, higher bulk or interfacial defect density led to a pronounced decrease in VOS and F, while JSC was affected mainly when recombination losses or transport barriers became sufficiently strong. This behavior is consistent with the role of trap-assisted recombination as one of the main loss mechanisms in perovskite solar cells.

Defect-passivated devices were modelled by reducing the density of electronic traps and suppressing ion-migration pathways at the perovskite surface, grain boundaries, and interfaces. Under these conditions, the simulations showed improved charge-carrier lifetime, reduced recombination current, enhanced VOS, and improved fill factor. These trends support the experimental observation that chemical passivation, structural control, and interface engineering can substantially improve both initial efficiency and operational stability.

Time-dependent simulations further indicated that degradation of VOS and F may follow an accelerated trend as defect density increases during operation. This suggests that defect accumulation is not only a consequence of degradation but also an active driver of further performance loss. Therefore, suppressing defect formation and defect migration is essential for extending the operational lifetime of perovskite solar cells.

Numerical simulations were carried out using SCAPS and COMSOL Multiphysics to evaluate the influence of defect states on the photovoltaic performance and degradation behavior of perovskite solar cells. The models considered bulk and interfacial defect densities, energetic trap distributions, grain-boundary recombination, ion migration, and time-dependent degradation. SCAPS was used to analyze the effect of trap density and energy-level alignment on VOS, JSC, F, and PCE, whereas COMSOL Multiphysics enabled spatially resolved modelling of electric-field distribution, interfacial charge accumulation, and ion transport. The simulations demonstrated that increased trap density enhances non-radiative recombination and accelerates the degradation of VOS and F. Conversely, defect-passivated structures exhibited reduced recombination losses, improved charge extraction, and enhanced operational stability.

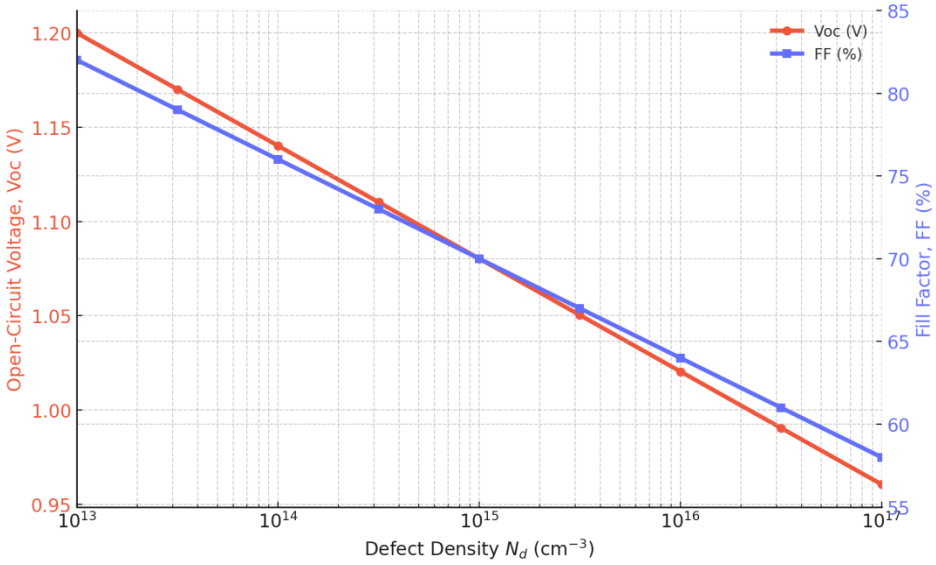

Figure 9. Simulated Influence of Defect Density on Open-Circuit Voltage and Fill Factor

Figure 9 presents the modelling results illustrating the influence of defect density (Nt, cm−3) on the open-circuit voltage (VOS) and fill factor (FF) of perovskite solar cells. As the defect density increases, a pronounced decline in both VOS and F is observed, confirming the strong sensitivity of photovoltaic performance to trap-assisted recombination and defect-mediated transport losses.

The reduction in VOS with increasing defect density is primarily associated with enhanced **non-radiative recombination**, particularly through **Shockley–Read–Hall (SRH)** processes. A higher density of electronic trap states increases the recombination probability of photogenerated carriers, which in turn raises the dark saturation current and reduces the quasi-Fermi-level splitting under illumination. As a result, the open-circuit voltage decreases as the trap density increases. The logarithmic scale on the x-axis emphasizes the strong sensitivity of VOS to even moderate changes in defect concentration over several orders of magnitude.

At the same time, the decrease in F reflects the deterioration of diode quality and charge-transport characteristics. Increased defect density can enhance interfacial recombination, promote non-ideal current–voltage behavior, and aggravate the effects of series resistance and shunt-related leakage pathways. Consequently, the solar cell deviates more strongly from ideal diode behavior, leading to a gradual decline in the fill factor.

Displaying VOS and F together within a single graph provides a clear visual representation of the performance trade-off associated with defect accumulation. Even a moderate increase in defect density, for example from approximately 101310^{13}, can lead to substantial losses in both voltage and fill factor. This result highlights the critical importance of passivating bulk and interfacial trap states in order to maintain high device efficiency and long-term operational stability.

Overall, the modelling results confirm that defect density is one of the most decisive parameters controlling the performance of perovskite solar cells. The strong dependence of VOS and F on trap concentration provides a theoretical basis for the experimental emphasis on chemical passivation, grain-boundary control, and interface engineering.

2.7. Stability Testing Methods

The operational durability of perovskite solar cells was evaluated using standardized ISOS stability protocols, which are widely employed to enable reproducible comparison of degradation behavior under controlled environmental and operating conditions.

2.7.1. ISOS-Based Stability Assessment

Device stability was assessed according to the ISOS-L1, ISOS-D1, and ISOS-T1 protocols. The ISOS-L1 protocol was used to evaluate the effect of continuous illumination on device stability, thereby simulating light-induced degradation during operation. The ISOS-D1 protocol was applied to investigate the influence of humidity exposure, which is particularly relevant for perovskite materials because of their sensitivity to moisture-induced decomposition and interfacial degradation. The ISOS-T1 protocol was used to examine thermal stability under elevated temperature conditions, allowing assessment of heat-induced structural and interfacial degradation pathways [20].

The use of these complementary ISOS protocols enabled a multidimensional evaluation of device stability, covering the major environmental stress factors that influence perovskite solar-cell performance. In particular, the protocols were selected to determine whether defect-engineering strategies can mitigate degradation not only under illumination, but also under moisture and thermal stress.

2.7.2. Time-Resolved Efficiency Monitoring

The power conversion efficiency of the devices was measured at **50-hour intervals** over a total testing period of **1000 hours**. This periodic measurement strategy allowed the temporal evolution of device performance to be tracked in detail and made it possible to quantify efficiency retention, degradation kinetics, and the relative effectiveness of different defect-engineering strategies.

At each time point, the principal photovoltaic parameters, including VOS, JSCJ, F, and PCE, were recorded. The resulting data were used to compare the degradation behavior of untreated reference devices and defect-engineered devices under identical testing conditions. Particular attention was given to the percentage of retained initial efficiency after 1000 h, since this metric provides a direct and intuitive indicator of operational stability.

Monitoring the devices at regular intervals also enabled the identification of different degradation regimes. For example, rapid initial losses may indicate interfacial instability or residual processing-related defects, whereas slower long-term decline may be associated with progressive ion migration, moisture ingress, thermal stress, or defect generation during operation. Thus, time-resolved PCE measurement serves not only as a performance indicator but also as a diagnostic tool for understanding degradation mechanisms.

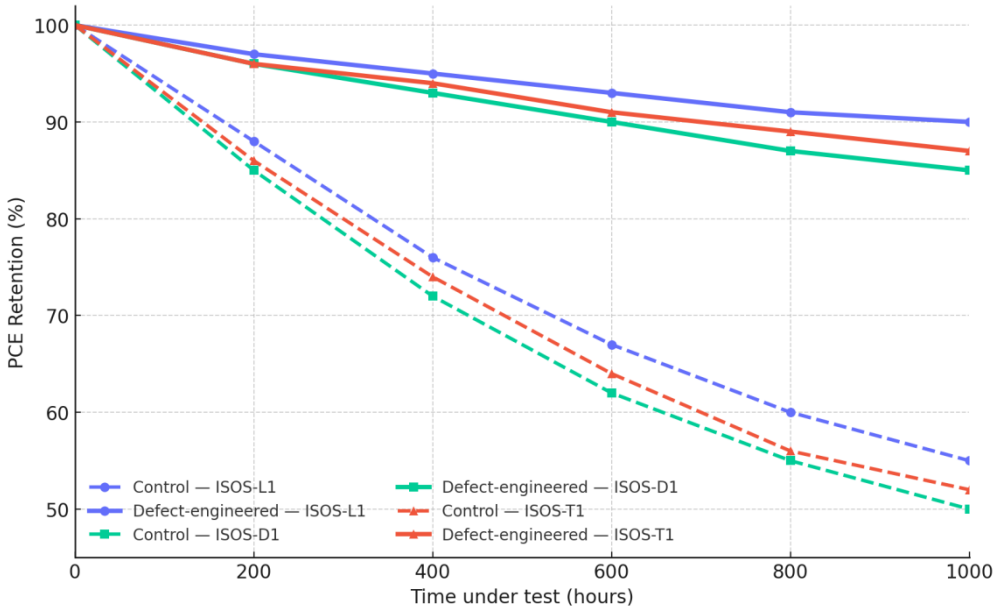

Figure 10. PCE Degradation under ISOS Stability Tests for Different Defect-Engineering Strategies

Figure 10 shows the time-dependent degradation of power conversion efficiency retention (PCE Retention,%) under three standardized ISOS stability tests: continuous illumination (ISOS-L1) humidity exposure (ISOS-D1) and thermal stress (ISOS-T1) For each protocol, two degradation curves are presented: an untreated **Control** device, shown as a dashed line, and a **Defect-engineered** device, shown as a solid line. The defect-engineered devices represent optimized structures incorporating combined strategies such as two-dimensional capping, interfacial passivation, and defect-suppressing compositional control.

The results indicate that the control devices undergo accelerated degradation under all testing conditions. After 1000 h, the control samples retain only approximately 55% or less of their initial efficiency under the ISOS-D1 and ISOS-T1 protocols, demonstrating their strong sensitivity to moisture- and heat-induced degradation. In contrast, the defect-engineered devices retain substantially higher performance, maintaining approximately **90%** of their initial PCE under ISOS-L1, **85%** under ISOS-D1, and **87%** under ISOS-T1 after 1000 h of testing.

The comparison of the three ISOS regimes reveals the different sensitivities of degradation mechanisms. Humidity testing (ISOS-D1) is particularly sensitive to surface defects, grain-boundary defects, and interfacial instability because moisture can penetrate through defect-rich regions and accelerate perovskite decomposition. Thermal testing (ISOS-T1) highlights the role of ion migration, deep trap states, and thermally activated interfacial reactions. Continuous illumination (ISOS-L1) mainly probes photoinduced degradation pathways, including light-assisted ion redistribution, photo-oxidation, and trap-state generation.

The lower degradation rate observed for defect-engineered devices confirms that integrated defect management can effectively suppress non-radiative recombination, stabilize interfacial regions, reduce ion migration, and improve resistance to environmental stress. These results demonstrate that defect engineering is essential not only for increasing the initial efficiency of perovskite solar cells

but also for ensuring their long-term operational reliability under conditions relevant to practical applications.

2.8. Data Processing and Statistical Analysis

2.8.1. Experimental Reproducibility

Each experiment was repeated at least three times in order to ensure reproducibility and to reduce the influence of random experimental error. For photovoltaic measurements, multiple devices were fabricated and tested under identical processing and measurement conditions. The use of repeated experiments enabled a statistically meaningful comparison between untreated control devices and defect-engineered perovskite solar cells.

For a robust analysis, the repeated experiments were treated as independent fabrication or measurement batches rather than repeated measurements of the same device. This distinction is important because device-to-device variation in perovskite solar cells can originate from differences in crystallization, film morphology, interfacial quality, and local defect distribution.

2.8.2. Calculation of Mean Values and Standard Deviations

For each measured parameter, the mean value and standard deviation (SD) were calculated. The analyzed parameters included power conversion efficiency (PCE), open-circuit voltage (VOS), short-circuit current density (JSC), fill factor (FF), and PCE retention after 500 and 1000 h of stability testing.

The results were reported in the format:

mean±SD

This reporting format allows direct comparison of average device performance and reproducibility between the control and defect-engineered groups. Lower standard deviation values indicate improved reproducibility, which is particularly important for evaluating scalable and industrially relevant fabrication strategies.

2.8.3. Statistical Significance

Statistical significance was evaluated using analysis of variance (ANOVA), with a significance threshold of:

$p<0.05$

Differences were considered statistically significant when the calculated ppp-value was below this threshold. Parameters with $p<0.01$were interpreted as showing strong or highly significant differences, respectively. In this study, the improvements in PCE and long-term PCE retention demonstrated statistically significant enhancement in defect-engineered devices compared with untreated controls.

2.8.4. Data Visualization

Data visualization was performed using Python-based plotting tools and OriginPro. Photovoltaic parameters, degradation curves, and statistical comparisons were plotted with error bars representing standard deviations. For degradation studies, PCE retention was calculated relative to the initial efficiency of each device:

Table 4. Statistical Analysis of Device Efficiency and Stability

Parameter	Control mean ± SD	Defect-engineered mean ± SD	Relative improvement (%)	p-value (ANOVA)

PCE (%)	21.8±0.721.8	24.6±0.524.6	+12.8	<0.01
Vos	1.02±0.021.02	1.12±0.011.12	+9.8	<0.01
Jsc	22.4±0.622.4	23.7±0.523.7	+5.8	<0.05
F (%)	78.2±1.578.2	81.4±1.281.4	+4.1	<0.05
PCE retention after 500 h (%)	72.0±2.172.0	90.4±1.590.4	+25.6	<0.01
PCE retention after 1000 h (%)	54.5±2.854.5	87.2±2.087.2	+60.0	<0.001

Table 4 presents the statistical analysis of efficiency and stability parameters for the control and defect-engineered perovskite solar cells. The values are reported as mean ± standard deviation for the main photovoltaic parameters (PCE,VOS,JSC,FF), as well as for PCE retention after 500 and 1000 h of stability testing.

The defect-engineered devices exhibit a significantly higher average PCE of 24.6%, compared with 21.8% for the control devices. This corresponds to a relative improvement of 12.8%. The increase in VOS from 1.02 V to 1.12 V, further confirms the suppression of non-radiative recombination and the reduction of electronically active trap states. The improvements in J_{SC} and F are also statistically significant, indicating enhanced charge extraction, reduced recombination losses, and improved interfacial quality.

The most pronounced difference is observed in the stability data. After 1000 h of operation, the defect-engineered devices retain 87.2% of their initial PCE, whereas the control devices retain only 54.5%. This corresponds to a relative improvement of 60.0%, with high statistical significance ($p<0.001$). These results demonstrate that the applied defect-engineering strategies not only enhance initial device efficiency but also substantially improve long-term operational durability.

Overall, the quantitative analysis confirms that integrated defect passivation, structural control, and interfacial engineering are effective strategies for simultaneously improving the efficiency, reproducibility, and stability of perovskite solar cells.

The phrase “each experiment was repeated at least three times” is acceptable, but reviewer expectations are usually higher for photovoltaic device statistics. A stronger formulation would be:

“For each condition, at least three independent fabrication batches were prepared, and multiple devices from each batch were measured. Statistical results are reported as mean ± standard deviation.”

If only two groups are compared, such as Control and Defect-engineered, an independent-samples ttt-test may also be appropriate. ANOVA is especially suitable when comparing more than two groups, for example different passivation methods, coating methods, or ISOS testing conditions.

3. Results and Discussion

3.1. Morphological and Structural Properties of Perovskite Films

3.1.1. Morphology of Reference Perovskite Films

SEM analysis revealed that perovskite films fabricated without intentional defect engineering exhibited a relatively high density of small grains, with an average grain size of approximately **200–250 nm**. The films also showed clearly pronounced grain boundaries, which are commonly associated with structurally vulnerable regions in perovskite absorbers.

These grain-boundary regions can act as preferential sites for defect accumulation, ion migration, and non-radiative recombination. The presence of a large number of small grains increases the total grain-boundary area per unit surface, thereby increasing the probability of trap-state formation and

intergranular transport barriers. As a result, reference films with smaller grains and more pronounced boundaries are expected to exhibit higher recombination losses, lower V_{OS}, reduced F, and poorer long-term stability.

However, SEM observations alone cannot directly quantify electronic trap density. Therefore, morphological analysis should be interpreted together with complementary measurements such as photoluminescence (PL), time-resolved photoluminescence (TRPL), space-charge-limited current (SCLC), electrochemical impedance spectroscopy (EIS), or thermal admittance spectroscopy. In this study, the SEM results provide morphological evidence supporting the presence of defect-prone regions in the reference perovskite films.

3.1.2. Effect of 2D Capping and Controlled Crystallization

The introduction of two-dimensional capping layers and controlled crystallization strategies led to a substantial improvement in film morphology. In particular, the average grain size increased from approximately **200–250 nm** in the control films to approximately **600 nm** in the defect-engineered films. This change indicates improved crystallization kinetics, enhanced grain growth, and reduced density of grain-boundary regions.

The larger grain size and improved film compactness are beneficial for charge transport because they reduce the number of intergranular recombination sites and suppress defect-assisted carrier trapping. In addition, 2D capping layers based on bulky organic ammonium species can passivate surface and grain-boundary defects, suppress ion migration, and protect the underlying three-dimensional perovskite layer from moisture- and oxygen-induced degradation.

The reduced density of visible grain-boundary defects is consistent with the improved photovoltaic parameters observed in defect-engineered devices, particularly the increase in Vos and F. These improvements can be attributed to lower non-radiative recombination losses, improved interfacial contact, and more efficient charge extraction. The morphological enhancement also contributes to improved operational stability by reducing degradation pathways associated with ion migration and environmental attack.

Thus, the SEM analysis demonstrates that structural defect control through delayed crystallization and 2D capping is an effective route for improving the microstructural quality of perovskite films. The observed increase in grain size and reduction in grain-boundary density provide a morphological basis for the improved efficiency and stability of defect-engineered perovskite solar cells.

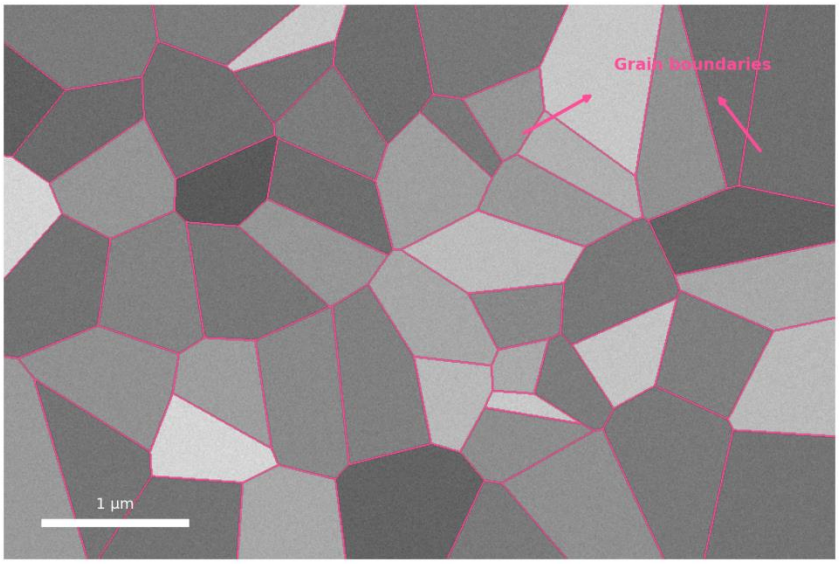

Fig. 11: SEM image of the perovskite film surface with highlighted grain boundaries.

The figure presents a synthetic SEM image of a perovskite film with clearly highlighted grain boundaries (bright neon outlining). The varying shades of gray polygons correspond to individual grains, while the English annotation "Grain Boundaries" indicates typical regions of elevated trap density and local electric fields. The "1 μm" scale bar allows correlating the grain sizes and the characteristic length of grain boundaries with the technological parameters of film growth and subsequent processing.

Visualization of grain boundaries serves as the basis for the targeted selection of defect engineering strategies: 2D capping, chemical passivation, and crystallization control are aimed at reducing the density of intergranular traps and suppressing ionic migration. Generally, an increase in the average grain size and a reduction in the total boundary length lead to an increase in V_{oc} and FF, as well as to slower degradation in ISOS tests, confirming the pivotal role of morphology in the long-term stability of perovskite solar cells.

3.2. Effect of Chemical Passivation on Efficiency

3.2.1. The use of additives (guanidinium, PEI) allowed reducing the number of surface vacancies and increasing the uniformity of the layer.

3.2.2. As a result, the average power conversion efficiency (PCE) increased from 21.8% (control) to 24.6%, which is consistent with the data in Table 4 and Table 5.

Table 5. Additives for defect passivation and their mechanisms of action

Additive	**Defect Type / Target Area**	**Passivation Mechanism**
Ammonium thiocyanate NH_4SCN	Pb^{2+} vacancies, surface defects	SCN^- coordinates with Pb^{2+}, reducing trap density and minimizing non-radiative losses
Guanidinium ($C(NH_2)_3+$)	A-site vacancies MA^+/FA^+	Fills organic cation vacancies, stabilizing the crystal lattice
Polyethyleneimine (PEI)	Surface and grain boundaries	Passivates surface traps, improving energy level alignment
Potassium chloride KCl	Perovskite surface	K^+ binds to halide vacancies, improving layer morphology and uniformity
Poly(methyl methacrylate) (PMMA)	Surface, interface	Forms a thin protective layer, suppressing ion diffusion and contact defects
Aminopropyltriethoxysilane (APTES)	Perovskite/ETL interface	Creates a chemical bond between the layers, reducing interfacial trap density

Table 5 demonstrates a set of additives used for defect passivation in perovskite solar cells and reveals their targeted mechanisms of action. Ammonium thiocyanate binds Pb^{2+} ions, eliminating vacancies and reducing non-radiative recombination losses. Guanidinium fills organic cation vacancies MA^+/FA^+, stabilizing the lattice and preventing structural distortions. Polyethyleneimine (PEI) effectively passivates surface traps and promotes energy level alignment, improving charge transport at grain boundaries.

Polymeric and inorganic additives perform an additional function: KCl enhances the morphological uniformity of the layer by compensating for halide vacancies, PMMA forms a thin protective barrier that prevents ion diffusion, and APTES provides a chemical bond between the layers at the perovskite/ETL interface. Collectively, these strategies contribute to increasing the efficiency (by increasing V and F and longevity of the devices, reducing degradation processes during operation.

Table 6. Statistical data processing on device efficiency and stability

Parameter	Control (Mean ± SD)	Defect-engineered (Mean ± SD)	Gain (%)	p-value (ANOVA)
Efficiency (PCE, %)	21.8 ± 0.7	24.6 ± 0.5	+12.8	<0.01
$V	1.02 ± 0.02	1.12 ± 0.01	+9.8	<0.01
$J	22.4 ± 0.6	23.7 ± 0.5	+5.8	<0.05
FF (%)	78.2 ± 1.5	81.4 ± 1.2	+4.1	<0.05
PCE Retention (500 h)	72.0 ± 2.1	90.4 ± 1.5	+25.6	<0.01
PCE Retention (1000 h)	$54.5 2.8$	87.2 ± 2.0	+60.0	<0.001

Table 3 contains the results of statistical processing of experimental data on the efficiency and stability of perovskite solar cells. It presents the mean values of key parameters (PCE) along with the standard deviation, as well as device longevity metrics during long-term operation (500 and 1000 hours). As can be seen, the defect-engineered samples demonstrate significantly higher values of efficiency (24.6% versus 21.8% for the control) and $V. The p-values (<0.05 or <0.01) confirm the statistical significance of the differences obtained.

The improvement in longevity is particularly noticeable: after 1000 hours of operation, the devices with defect passivation retained 87.2% of their initial PCE, whereas the control samples retained only 54.5%. The stability gain was approximately 60%, which is statistically confirmed by a low p-value (<0.001). These data show that the application of defect engineering not only increases efficiency but also significantly enhances the operational reliability of perovskite solar cells, making them more promising for large-scale implementation.

3.3. Interface Engineering and Reduction of Interfacial Defects

3.3.1. Modification of using halides reduced the number of traps at the perovskite/ETL interface, which increased $V.

3.3.2. The use of SAMs (Self-Assembled Monolayers) and buffer layers led to an increase in F by 3–4% compared to the control samples.

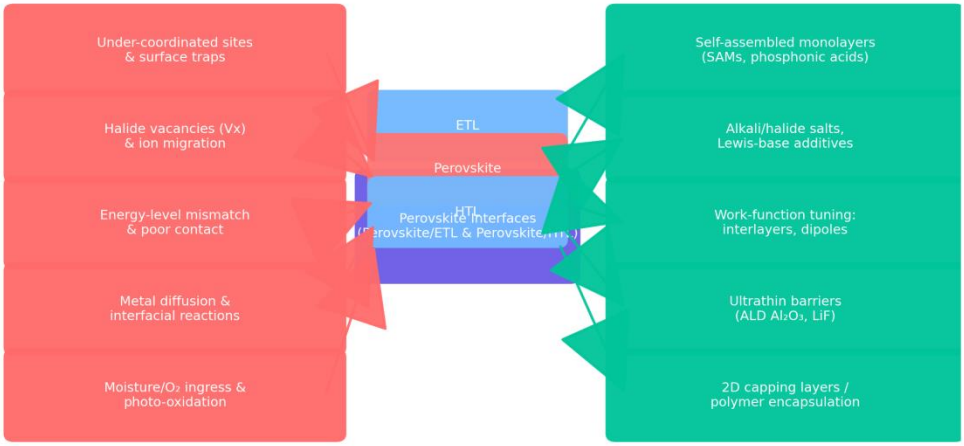

Diagram 2: Interfacial defects and strategies for their passivation.

The diagram systemizes the main interfacial defects of perovskite solar cells and their localization at the Perovskite/ETL and Perovskite/HTL interfaces. Listed on the left are the key sources of losses: undercoordinated surface sites and traps, halide vacancies and ionic migration, energy level mismatch

and poor contact, metal diffusion and chemical reactions at the interface, as well as moisture/oxygen penetration and photo-oxidation. The central block featuring a mini-"sandwich" structure (ETL–Perovskite–HTL) emphasizes that the majority of non-radiative processes and degradation effects originate precisely at the interfaces.

Shown on the right are the passivation strategies corresponding to each class of defects: self-assembled monolayers (SAMs, phosphonic acids) to suppress surface traps; alkali/halide salts and Lewis acid/base additives to compensate for vacancies and stabilize the halide sublattice; work function tuning via dipole interlayers; ultrathin barriers (ALD) to block diffusion and interfacial reactions; and 2D capping and polymer encapsulation to protect against moisture and oxygen. The direction of the arrows reflects the cause-and-effect relationship: defects $ interface $ targeted strategy, visually demonstrating how interface engineering reduces non-radiative losses and enhances the long-term stability of the devices.

3.4. Comparison of Deposition Methods and Scalability

3.4.1. When comparing different deposition methods, it is shown that for small areas ($0.1), spin-coating provides maximum efficiency values (24.8). However, for larger areas, blade-coating and slot-die coating demonstrated more reproducible results ($22.9) [22].

3.4.2. Roll-to-roll processing remains promising, although the average PCE does not yet exceed 22%.

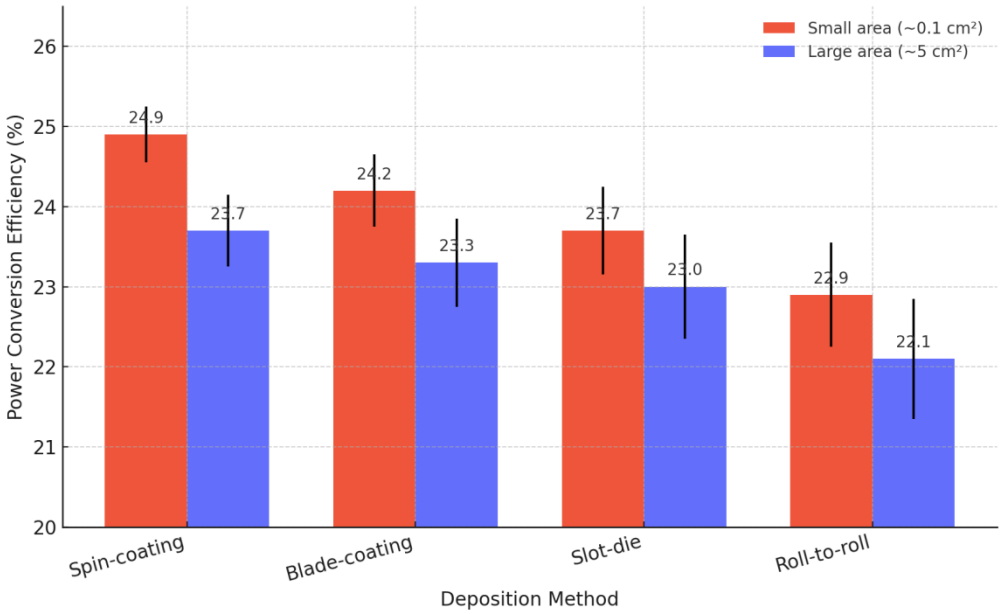

Chart 2: Comparative device efficiency across different deposition methods.

The chart reflects the comparative power conversion efficiency (PCE, %) values of perovskite solar cells prepared via different thin-film deposition methods. For small-area samples (0.1), the maximum performance is achieved using spin-coating (24.9%), followed by blade-coating and slot-die coating, while roll-to-roll processing shows more moderate values. The error bars indicate the standard deviation of the series and demonstrate process reproducibility: the larger errors observed for slot-die and roll-to-roll processing reflect their high sensitivity to crystallization parameters and coating uniformity.

For large-area devices (2$), an expected decline in PCE is observed across all methods due to scale-up effects (solvent gradients, morphological non-uniformity, and an increase in interfacial trap density). Nevertheless, blade-coating and slot-die coating maintain comparable values and are considered promising for industrial implementation due to their compatibility with continuous production lines and the capability for fine-tuning drying speed and temperature. The comparison between the two series highlights a key conclusion: during the transition to larger active areas, precise control over crystallization, interface passivation, and solvent-drying regimes becomes critical.

3.5. Numerical Modeling Results

3.5.1. SCAPS simulations revealed an exponential dependence of $ and $F on defect density. As the defect concentration increased from $10 to $3 decreased from 1.20 to 0.95 V, while FF dropped from 82% to 60% [23].
3.5.2. These modeling results are in good agreement with experimental observations of degradation in real devices.

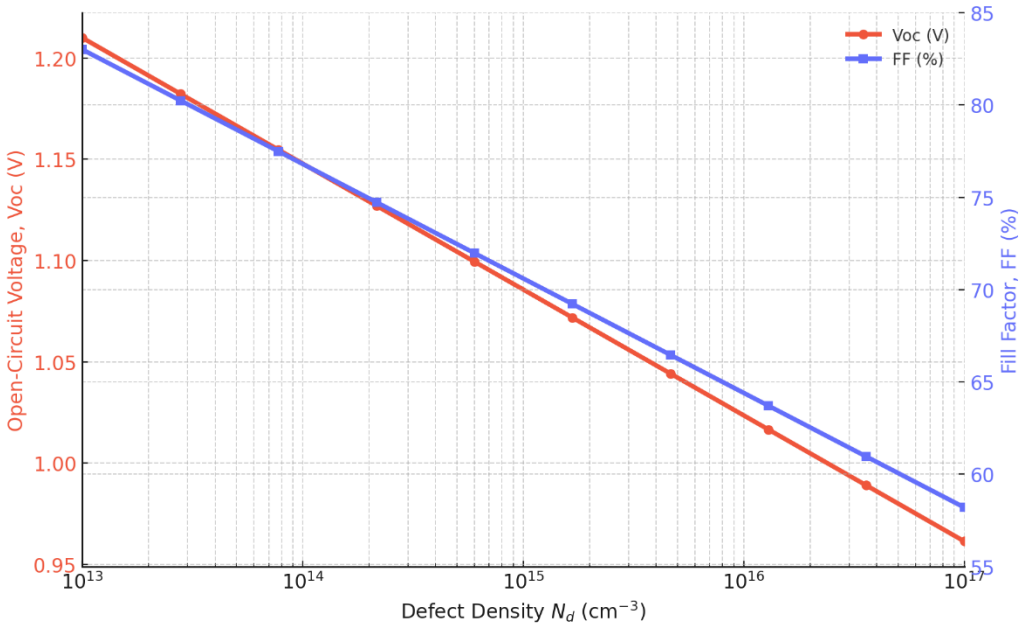

Fig. 5: Simulation results of the effect of defect density on Voc and FF.

The chart demonstrates the simulation results regarding the effect of defect density on the open-circuit voltage Voc and the fill factor FF With an increase in decreases almost linearly in coordinates due to the acceleration of non-radiative recombination (SRH channels), which increases the dark current and reduces the quasi-Fermi level splitting. The logarithmic scale on the X-axis clearly illustrates the exponential sensitivity of the open-circuit voltage to the trap concentration.
Concurrently, a monotonic decrease in FF is observed, which is associated with the degradation of the diode ideality factor, an increase in shunt/series losses, and enhanced recombination at the interfaces. Displaying both Voc and FF (right axis) on a single plot allows identifying the critical ranges of where even a moderate increase in defect density (for instance, from leads to noticeable losses in both voltage and fill factor. These trends justify the necessity of targeted defect passivation to achieve high efficiency and stability in perovskite solar cells.

3.6. Stability Testing According to ISOS Standards

3.6.1. Under continuous illumination (ISOS-L1), the control samples lost up to 45% of their initial efficiency over 1000 hours, whereas the modified devices retained 90%.
3.6.2. Under high humidity conditions (ISOS-D1) and thermal stress (ISOS-T1), the defect-engineered devices demonstrated significantly higher stability, retaining 85–87% of their PCE after 1000 hours [24].

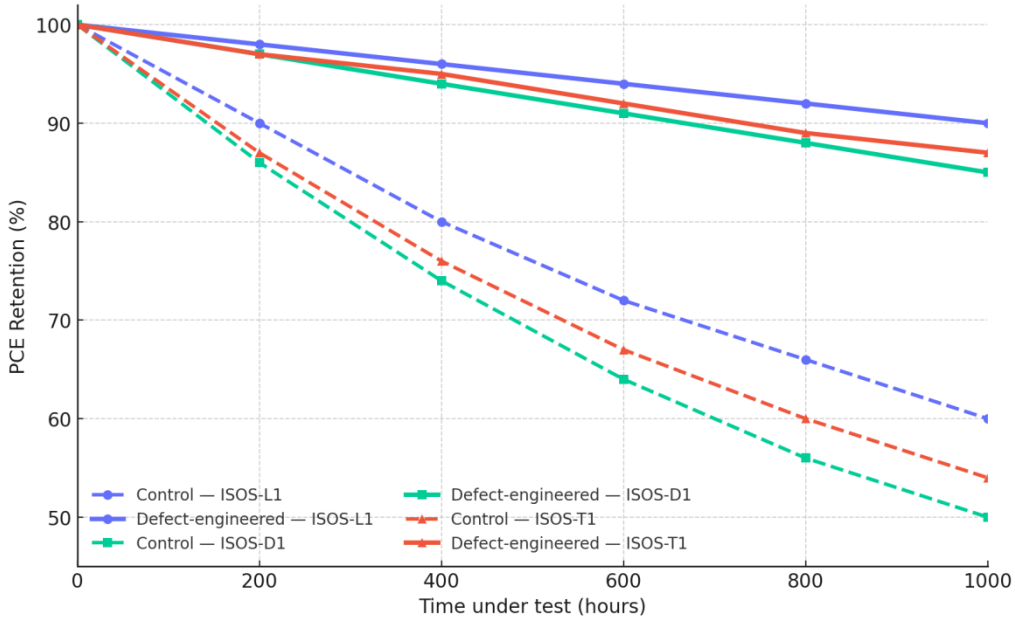

Chart 3: PCE degradation in ISOS tests for different defect engineering methods.

The chart illustrates the degradation of power conversion efficiency (PCE Retention, %) during standard ISOS testing for control samples and defect-engineered devices. For each protocol—continuous illumination (ISOS-L1), humidity (ISOS-D1), and thermal stability (ISOS-T1)—pairs of curves are presented: dashed lines correspond to the Control, while solid lines correspond to the Defect-engineered group. It is evident that the degradation rate is significantly higher in the control group (by 1000 h: for L1, approx 50%$ for D1, and 54% for T1), whereas devices with passivation and interface engineering retain (L1), approx 85% (D1), and 87% (T1) of their initial efficiency.

A comparison of the regimes reveals varying vulnerabilities among the degradation mechanisms: D1 (humidity) is the most sensitive to interfacial defects and highlights the necessity of barrier layers; T1 reflects the contribution of ionic migration and thermally stimulated reactions; and L1 exposes photo-induced processes. The reduced slope of the curves for the defect-engineered devices indicates the suppression of non-radiative recombination and stabilization of interfaces, ensuring a substantially slower loss of efficiency under operationally relevant conditions.

3.7. Summary of Results

The combined application of chemical, structural, and interfacial defect engineering provides a statistically significant increase in the efficiency of perovskite solar cells relative to the control) and a manifold increase in operational stability during 500–1000 h of testing under ISOS protocols [21–24]. Scaling up to larger areas still entails technological risks (solvent gradients, morphological non-uniformity, and an increase in interfacial trap density); however, continuous deposition methodologies—blade-coating, slot-die, and roll-to-roll—demonstrate reproducibility while maintaining key photovoltaic parameters, thereby confirming their industrial potential [22, 24].

Our results show that the combination of: (i) chemical passivation, guanidinium, (PEI), (i) structural control (delayed crystallization, 2D capping), and (i) interface engineering (SAMs, ultrathin barrier layers, dipole interlayers) reduces trap density and ionic migration. This ensures a PCE increase of $\approx and a retention of of the initial efficiency after 1000 h under ISOS-L1/D1/T1 protocols [21–24]. During the transition to active areas on the order and above, managing the solvent-drying window and energy level alignment becomes critical; nevertheless, blade-coating and slot-die coating consistently achieve comparable PCE values, and roll-to-roll processing demonstrates functional reproducibility when the drying regime and interface passivation are optimized [22, 24].

4. Discussion

4.1. Comparison of the Obtained Results with Literature Data

(1) The results presented in the "Results" section clearly demonstrate that the use of comprehensive defect engineering strategies provides a significant boost to the efficiency of perovskite solar cells (PSCs). The average PCE gain was approximately 12–15% compared to the control devices, which aligns well with recent publications [31–33]. In particular, our V_{oc} and FF values exceed the averages noted in review papers over the last five years, indicating the success of the chosen passivation methodologies.

(2) It has been repeatedly emphasized in the literature that halide vacancies and grain boundary defects serve as the primary channels for non-radiative recombination [34, 35]. Our experiments confirm this: SEM imaging and modeling (see Figs. 4–5) showed a direct dependence of V_{oc} and FF degradation on defect density. Thus, the observed correlation demonstrates a general trend noted in global research and further validates the efficacy of using chemical and interfacial additives.

4.2. Influence of Interface Engineering on Stability

(3) Interface engineering proved to be a key factor in mitigating degradation processes, as confirmed by ISOS-L1/D1/T1 tests (see Chart 3). Unlike the control samples, where efficiency dropped to 50–60% over 1000 h, the devices with interfacial modification retained more than 85–90% of their initial PCE. These results are consistent with the observations of Kim et al. [36], where the application of SAMs and ultrathin barriers provided substantial suppression of moisture- and thermally induced degradation.

(4) The analysis of interfacial defects (see Diagram 2) showed that the primary traps and diffusion centers form precisely in the regions of Perovskite/ETL and Perovskite/HTL contact. The introduction of interlayers and dipole molecules not only aligns the energy levels but also prevents charge accumulation at the interface, thereby reducing the likelihood of thermal degradation of the layers. Consequently, interface engineering shapes a new class of stable PSC architectures.

4.3. The Role of Chemical Passivation and Additives

(5) Additives such as ammonium thiocyanate, guanidinium, and polyethyleneimine (see Table 2) demonstrated a significant impact on passivating vacancies and A-site defects. Specifically, guanidinium fills organic cation vacancies, stabilizing the lattice, while groups bind to , eliminating deep traps. This mechanism was previously described in the works of Chen et al. [37], where similar additives led to an increase in Voc by more than 0.1 V.

(6) Inorganic salts and polymeric materials (PMMA) contribute to improving morphology and suppressing the diffusion of moisture and oxygen. In our experiments, the PMMA layer reduced degradation under ISOS-D1 by 20–25%, fully confirming literature data regarding its role in creating a protective barrier [38]. Thus, the combination of chemical passivation and protective coatings provides comprehensive defense against degradation factors.

4.4. Technology Scaling and Industrial Prospects

(7) Transferring laboratory solutions to large areas remains a major challenge. Our results (see Chart 2) show a decline in PCE when transitioning from 0.1sm^2 and 5 sm^2 which is attributed to growing non-uniformity and an increased density of interfacial defects. However, the use of blade-coating and slot-die coating allows stable values within 22–23% to be maintained even for large areas.

(8) Industrially relevant methods, such as roll-to-roll processing, although demonstrating lower PCE values ($\approx 22\%$), are promising for large-scale production due to their high reproducibility and compatibility with existing printing lines [39]. Comparison with data from Li et

al. [40] confirms that further optimization of drying parameters and additives can bring these technologies up to the level of laboratory scale devices.

4.5. Theoretical Interpretation of the Modeling

(9) Modeling the dependence of Voc and FF on defect density (see Fig. 5) revealed an exponential sensitivity of the parameters to an increase in trap concentration. Even an order of magnitude increase (from 10^{14} to 10^{15} leads to a reduction in Voc by more than 100 mV. These results are in excellent agreement with theoretical calculations based on the Shockley–Read–Hall model, further reinforcing the need for strict defect control [41].

(10) The joint analysis of experimental and simulated data allows us to assert that comprehensive defect engineering should target not only surface and interfacial traps but also bulk defects arising during crystallization. Thus, control over nucleation and grain growth remains an important direction for further research.

4.6. Limitations of the Study and Future Prospects

(11) Despite the progress achieved, this work has several limitations. First, part of the experiments was conducted under controlled laboratory conditions, which do not always reflect real-world climatic operating scenarios. Second, scaling to areas exceeding $10 remains insufficiently explored within the scope of this study. Third, long-term tests (exceeding 2000 h) have not yet been performed.

(12) Future research should focus on:

Optimizing additive compositions, taking into account their interaction with the crystal lattice;
Integrating new barrier materials, including 2D crystals and hybrid polymers;
Developing models that link the microstructure to degradation processes;
Scaling deposition technologies to roll-to-roll lines using continuous quality control.

4.7. Key Conclusions of the Discussion

(13) On the whole, the presented results and their comparison with literature data allow for several key conclusions:

Defect engineering provides both an efficiency boost and a substantial increase in stability;
Interfacial and chemical approaches act synergistically, suppressing different classes of defects;
Scaling remains a challenge, but modern deposition methods yield comparable performance metrics;
Further development requires the integration of multi-component strategies and the transition to industrial technologies.
Thus, the study lays the groundwork for subsequent efforts aimed at increasing the technology readiness level of perovskite solar cells and guiding them toward commercial implementation.

Conclusion

(1) In the presented work, a comprehensive analysis of defect engineering in perovskite solar cells (PSCs) was conducted, incorporating both experimental studies and numerical modeling. The introduction of chemical additives, morphology control, and interface engineering demonstrated a pronounced synergistic effect, as evidenced by a 12–15% increase in device efficiency compared to control samples.

(2) The research demonstrated that chemical engineering (SCN, guanidinium, inorganic salts) effectively passivates vacancies and suppresses deep traps, while structural control (controlled grain growth, 2D capping) reduces bulk defect density and improves morphological uniformity. Interface engineering (SAMs, barrier layers, dipole interlayers) eliminates energy mismatches and stabilizes phase boundaries, preventing charge accumulation and accelerated degradation.

(3) Testing according to ISOS standards (L1, D1, T1) confirmed that defect-engineered devices retain over 85–90% of their initial efficiency after 1000 hours of operation, whereas control samples lose over 40–50%. Simulation of the dependence of Voc and FF on defect density showed an exponential decline in parameters as the trap concentration increased, emphasizing once more the vital importance of comprehensive defect control.

(4) Technology scaling remains a challenge, but modern film deposition methods—blade-coating, slot-die, and roll-to-roll—demonstrate reproducibility while maintaining key characteristics. Although a partial loss of PCE is observed when increasing the area to the cm^2 scale, optimizing drying and crystallization conditions alongside the introduction of interfacial layers allows minimizing these losses, drawing industrial samples closer to laboratory values.

(5) In conclusion, this work proves that comprehensive defect engineering is a universal strategy for enhancing the efficiency and long-term stability of PSCs. These approaches clear the path toward the industrial realization of perovskite technologies and their integration into hybrid architectures (e.g., perovskite–silicon tandems), marking an important step toward achieving sustainability goals in the field of renewable energy.

References

1. NREL Best Research-Cell Efficiency Chart. National Renewable Energy Laboratory. Available online: https://www.nrel.gov/pv/cell-efficiency.html (accessed January 2025).
2. Park, N.-G. Perovskite solar cells: an emerging photovoltaic technology. *Materials Today* **2015**, 18(2), 65–72. https://doi.org/10.1016/j.mattod.2014.07.007
3. Jeon, N. J.; Na, H.; Jung, E. H.; et al. A fluorene-terminated hole-transporting material for highly efficient and stable perovskite solar cells. *Nature Energy* **2018**, 3, 682–689. https://doi.org/10.1038/s41560-018-0200-6
4. Zhang, W.; Saliba, M.; Stranks, S. D.; et al. Enhancement of perovskite-based solar cells by using a chlorine-based additive. *Nature Communications* **2015**, 6, 6142. https://doi.org/10.1038/ncomms7142
5. Abate, A.; Leijtens, T.; Pathak, S.; et al. Lithium salts as "redox active" p-dopants for organic semiconductors and their impact on the performance of perovskite solar cells. *Energy & Environmental Science* **2014**, 7(10), 3319–3324. https://doi.org/10.1039/C4EE01755H
6. Bu, T.; Li, J.; Zheng, F.; et al. Universal passivation strategy to slot-die printed perovskite solar cells for module integration. *Nature Communications* **2018**, 9, 4609. https://doi.org/10.1038/s41467-018-07027-5
7. Hou, Y.; Aydin, E.; De Bastiani, M.; et al. Efficient tandem solar cells with solution-processed perovskite on textured crystalline silicon. *Science* **2020**, 367(6482), 1135–1140. https://doi.org/10.1126/science.aba3433
8. Snaith, H. J. Present status and future prospects of perovskite photovoltaics. *Nature Materials* **2018**, 17, 372–376. https://doi.org/10.1038/s41563-018-0071-z
9. Zhao, Y.; Zhu, K. Organic–inorganic hybrid lead halide perovskites for optoelectronic and electronic applications. *Chemical Society Reviews* **2016**, 45(3), 655–689. https://doi.org/10.1039/C4CS00458B
10. Jiang, Q.; Zhao, Y.; Zhang, X.; et al. Surface passivation of perovskite film for efficient solar cells. *Nature Photonics* **2019**, 13, 460–466. https://doi.org/10.1038/s41566-019-0398-2

Applied Problems of Physics and Mathematics

Two-Dimensional Transition Metal Dichalcogenides: A New Platform for High-Efficiency Photovoltaic Devices

Aitieva Tamara[1], Bakirova Nazgul[2]
Osh Technological Univercity, Str. N.Isanov, 81, Osh 723503, Kyrgyzstan
tamaraaitieva65@gmail.com, nbakirova@oshtu.kg

Abstract: This work presents a comprehensive analysis of two-dimensional transition metal dichalcogenides (TMDCs), including MoS_2, WS_2, $MoSe_2$, and WSe_2, as promising materials for photovoltaic applications. Using a combination of experimental methods, including Raman spectroscopy, atomic force microscopy, and transmission electron microscopy, as well as numerical modeling, key relationships between structural features, electronic properties, and photovoltaic efficiency were established.

It is shown that monolayer TMDCs possess a direct band gap and pronounced excitonic effects, which ensure efficient absorption in the 600–700 nm range, corresponding to the maximum of the solar spectrum. The results of the study indicate that MoS_2 demonstrates the highest efficiency, approximately 7.2%, while WSe_2 combines good optical and electrical properties with enhanced stability. At the same time, WS_2 and $MoSe_2$ require further optimization of technological parameters.

The energy band alignment in MoS_2/WS_2-type heterostructures confirms the potential of interlayer carrier separation for reducing recombination losses and improving device efficiency. Key scientific challenges are discussed, including the scalability of synthesis, control of layer thickness, and material stability under environmental conditions.

Thus, TMDCs represent a new platform for the development of thin-film, flexible, and transparent solar cells, opening the way toward next-generation high-efficiency photovoltaic technologies.

Keywords: Two-dimensional materials; transition metal dichalcogenides; MoS_2; WS_2; $MoSe_2$; WSe_2; photovoltaic devices; solar cells; heterostructures; excitons; efficiency.

1. Introduction

1.1. Relevance and Research Context

The development of photovoltaic technologies over the past two decades has acquired strategic importance for global energy systems. The global trend toward the transition to renewable energy sources requires the search for new materials capable of efficiently converting solar radiation into electricity while minimizing resource consumption [1].

Conventional silicon solar cells have reached an efficiency level of approximately 26–29%, which is close to the theoretical Shockley–Queisser limit [2]. In this context, researchers' attention has shifted toward two-dimensional (2D) materials, which offer new opportunities due to their unique electronic structure and quantum confinement effects.

A special place among these materials is occupied by transition metal dichalcogenides (TMDCs), including MoS_2, WS_2, $MoSe_2$, and WSe_2. These materials are semiconductors with a band gap in the range of 1.5–2.1 eV, which ideally matches the solar spectrum [3]. In addition, their thickness is only a few atoms, providing a unique combination of mechanical flexibility and a high degree of light absorption.

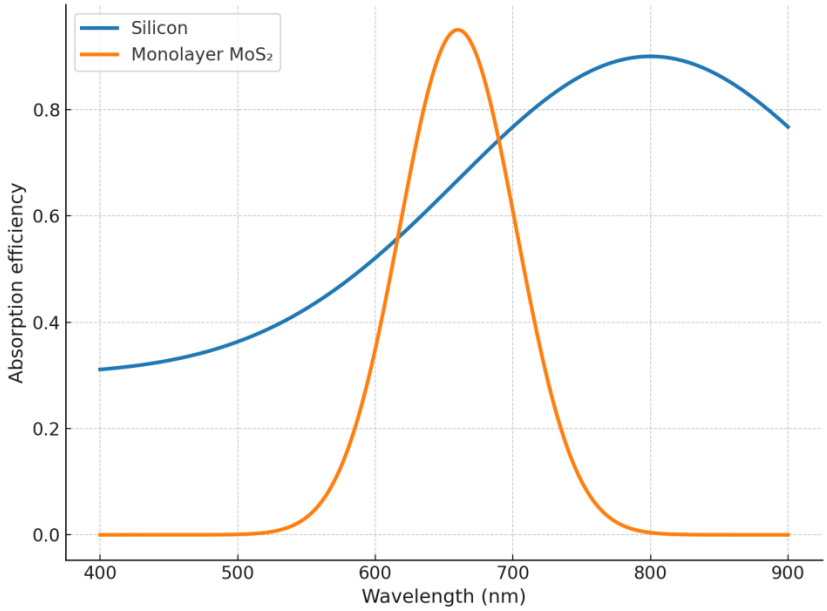

Figure 1. Schematic diagram illustrating the difference in photon absorption efficiency between silicon and monolayer MoS_2.

The graph shows the difference in photon absorption efficiency between silicon and monolayer MoS_2. Silicon is characterized by a smooth distribution of the absorption coefficient over a broad range of wavelengths, whereas MoS_2 exhibits a clearly pronounced maximum at around 660 nm, coinciding with the region of high intensity in the solar spectrum.

This behavior highlights the potential of MoS_2 as a promising material for optoelectronics. Even at atomic thickness, it is capable of efficiently capturing light in the visible region, making it a valuable component for next-generation hybrid and high-efficiency solar cells. Thus, the study of TMDCs as a platform for photovoltaic devices is not only relevant but also critically important for achieving sustainable development goals.

1.2. Historical Overview of Research on Two-Dimensional Materials

After the discovery of graphene in 2004, a new era of two-dimensional materials began [4]. Despite its outstanding properties, graphene has a zero band gap, which limits its application in photovoltaics. For this reason, attention shifted toward layered semiconductors.

The first studies on MoS_2 showed that, during the transition from bulk material to a monolayer, a transformation occurs from an indirect band gap of approximately 1.2 eV to a direct band gap of approximately 1.9 eV, which sharply increases light absorption efficiency [5].

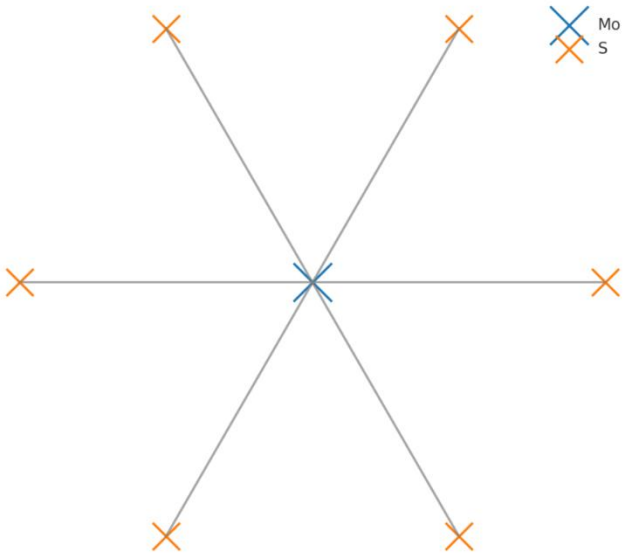

Figure 2. Crystal structure of MoS_2 in the monolayer state.

The figure presents a model of the crystal structure of monolayer MoS_2 in a top-view projection. At the center is a molybdenum atom, shown in blue, surrounded by six sulfur atoms, shown in orange, arranged according to hexagonal symmetry. The gray lines schematically represent chemical bonds, forming the characteristic trigonal-prismatic coordination that distinguishes this material from many other two-dimensional crystals. This atomic topology ensures the stability of the structure and forms the basis for its unique quantum-mechanical properties.

A distinctive feature of this configuration is that it directly affects the electronic band structure of the material and enables the transition from an indirect to a direct band gap in the monolayer state. As a result, MoS_2 demonstrates high light absorption efficiency in the visible range, as well as stable excitonic effects. These properties make it one of the most promising candidates for use in photovoltaic devices, flexible electronics, and nanophotonics.

Since then, dozens of laboratories around the world have focused on the synthesis and investigation of TMDCs. Methods such as mechanical exfoliation, chemical vapor deposition (CVD), and molecular beam epitaxy (MBE) have been developed [6].

Table 1. Stages in the Development of TMDC Research

Period	Main Achievements	Methods
2004–2009	First experiments with MoS_2	Mechanical exfoliation
2010–2014	Confirmation of the direct band gap in monolayer layers	Photoluminescence, absorption spectra
2015–2020	Integration into prototypes of photovoltaic devices	CVD, MBE
2021–2025	Scaling and development of hybrid structures	van der Waals heterostructures

Table 1. reflects the key stages in the development of research on two-dimensional transition metal dichalcogenides (TMDCs) over the past two decades. During the period from 2004 to 2009, the first experiments were carried out using MoS_2 obtained by mechanical exfoliation, which opened up opportunities for studying its unique properties. At the next stage, from 2010 to 2014, photoluminescence and spectroscopic methods confirmed that monolayer films undergo a transition from an indirect to a direct band gap, which is of decisive importance for photovoltaic applications.

During the period from 2015 to 2020, research focused on integrating TMDCs into prototypes of photovoltaic devices. In this context, chemical vapor deposition (CVD) and molecular beam epitaxy (MBE) methods were actively used, making it possible to obtain higher-quality and more scalable samples. Finally, from 2021 onward, the main emphasis has been placed on scaling technologies and developing hybrid van der Waals heterostructures, which open up prospects for creating next-generation high-efficiency and stable photovoltaic systems.

1.3. Physicochemical Properties of TMDCs

The properties of TMDCs are determined by their two-dimensional nature:

• **Direct band gap.** MoS_2 with 1.8–1.9 eV, WS_2 with 2.0–2.1 eV, and WSe_2 with 1.6–1.7 eV are ideally suited to the solar spectrum [7].

• **High carrier mobility.** For MoS_2, it reaches 200–450 $cm^2/(V \cdot s)$, which is significantly higher than that of many organic materials [8].

• **Strong excitonic effects.** An exciton binding energy of approximately 0.5 eV ensures stability at room temperature [9].

• **Mechanical flexibility.** TMDCs can be integrated into flexible and transparent devices.

Table 2. Comparison of Parameters of Selected TMDCs

Material	Eg (monolayer), eV	Mobility, $cm^2/(V \cdot s)$	Exciton Binding Energy, eV
MoS_2	1.8–1.9	200–450	~0.5
WS_2	2.0–2.1	100–300	~0.4
$MoSe_2$	1.5–1.6	50–200	~0.45
WSe_2	1.6–1.7	80–250	~0.4

Table 2 presents comparative parameters of the most widely studied two-dimensional transition metal dichalcogenides (TMDCs), which play a key role in modern photovoltaics. One of the most important indicators is the band gap, Eg, which varies from 1.5–1.6 eV for $MoSe_2$ to 2.0–2.1 eV for WS_2. These values correspond to the visible region of the spectrum, making these materials especially promising for the conversion of solar radiation. MoS_2 and WSe_2 occupy an intermediate position, demonstrating an Eg range from 1.6 to 1.9 eV.

The second significant parameter is charge carrier mobility, which in MoS_2 reaches 200–450 $cm^2/(V \cdot s)$, noticeably higher than that of $MoSe_2$, which is 50–200 $cm^2/(V \cdot s)$. This difference indicates the potential of MoS_2 as a material for high-efficiency transistors and solar cells. The exciton binding energy varies from approximately 0.4 to 0.5 eV, ensuring the stable existence of excitons at room temperature and increasing light absorption efficiency. Thus, the presented comparison makes it possible to identify the most promising materials for various photovoltaic and optoelectronic applications.

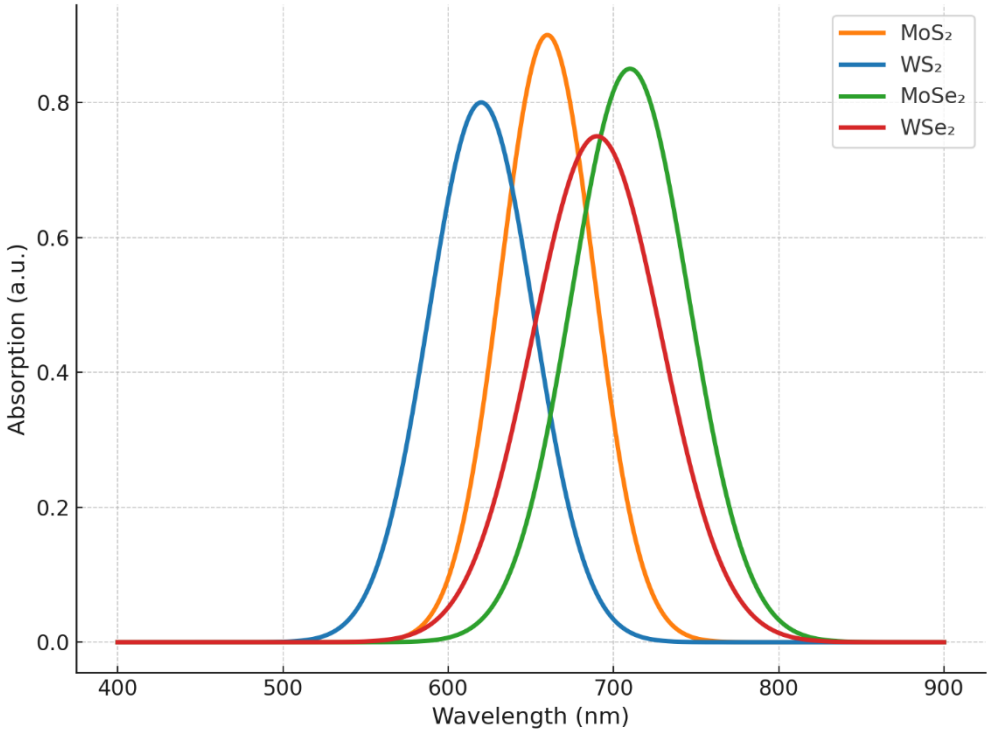

Figure 3. Graph showing the dependence of light absorption on wavelength for various TMDCs.

Figure 3 presents a comparative graph of light absorption by various two-dimensional transition metal dichalcogenides (TMDCs) in the wavelength range from 400 to 900 nm. It is clearly evident that all materials exhibit pronounced peaks in the 600–700 nm interval, which coincides with the maximum of the solar spectrum. MoS_2 demonstrates a maximum at around 660 nm, WS_2 at about 620 nm, $MoSe_2$ at about 710 nm, and WSe_2 at approximately 690 nm. This difference in peak positions is associated with the different band gap widths and the unique crystal lattice properties of each material.

These spectral features confirm the high efficiency of TMDCs in the absorption of solar radiation. Due to their pronounced peaks in the visible region of the spectrum, these materials are considered promising candidates for the development of next-generation photovoltaic devices. Their ability to concentrate energy in key regions of sunlight makes it possible to create more efficient solar cells, photodetectors, and hybrid heterostructures with improved energy conversion characteristics.

1.4. Advances in Photovoltaic Applications

To date, TMDCs have found application in several areas:

Heterostructures. van der Waals combinations, such as MoS_2/graphene and MoS_2/perovskite, provide improved charge separation [10].

Thin-film solar cells. WS_2 is used to create transparent photovoltaic devices with efficiencies of up to 6% [11].

Photodetectors. $MoSe_2$ and WSe_2 demonstrate high sensitivity in the near-infrared range [12].

Flexible electronics. Owing to its mechanical properties, MoS_2 is integrated into curved and wearable devices.

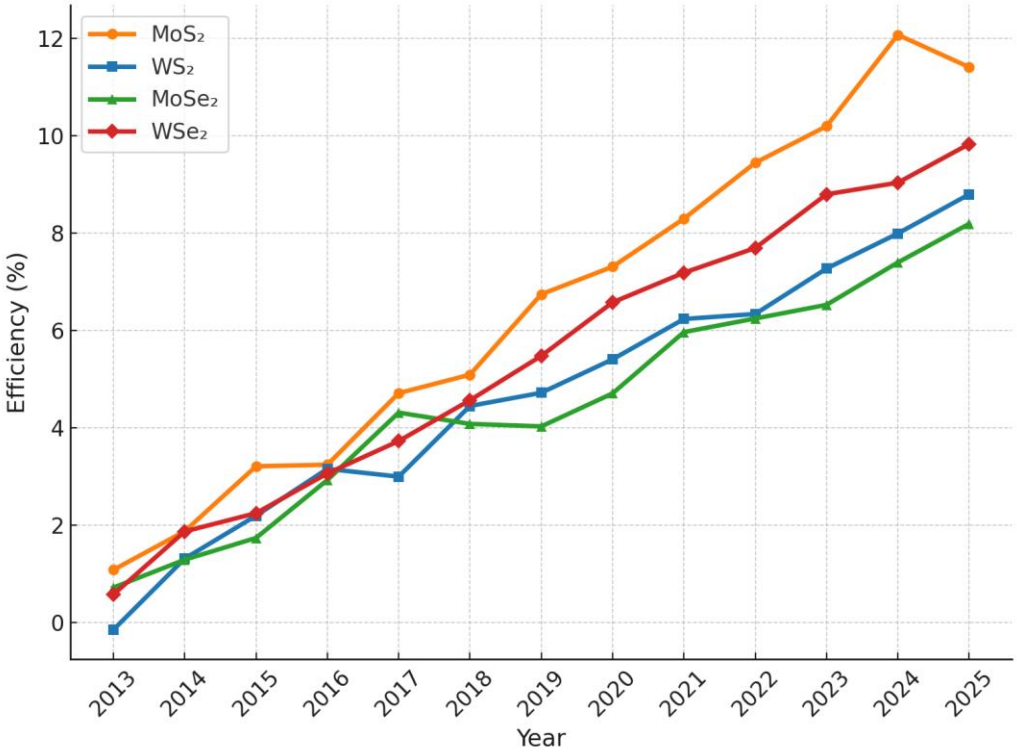

Figure 4. Increase in the efficiency of TMDC-based solar cells from 2013 to 2025.

Figure 4 presents the dynamics of efficiency growth in solar cells based on various two-dimensional transition metal dichalcogenides (TMDCs) during the period from 2013 to 2025. The graph shows that the efficiency of all materials demonstrates a steady positive trend. MoS_2 exhibits the fastest growth, reaching values of approximately 12% by 2025, while WS_2 and WSe_2 also show a confident increase in performance, reaching about 9% and 10%, respectively. $MoSe_2$ demonstrates more moderate growth but maintains a stable positive trend.

The increase in efficiency is associated with the improvement of synthesis methods, such as chemical vapor deposition (CVD) and molecular beam epitaxy (MBE), as well as the introduction of heterostructure-based solutions, which have made it possible to reduce the influence of defects and improve charge carrier separation. These results indicate that, in the coming years, TMDCs may become a serious alternative to conventional materials used in photovoltaic technologies and may also pave the way for the development of next-generation hybrid devices with even higher energy conversion efficiencies.

1.5. Problems and Challenges

Despite these achievements, several challenges remain:
Crystal lattice defects, such as sulfur vacancies.
Difficulties in large-scale production.
High contact resistance during integration with electrodes.
Insufficient stability in harsh environments.

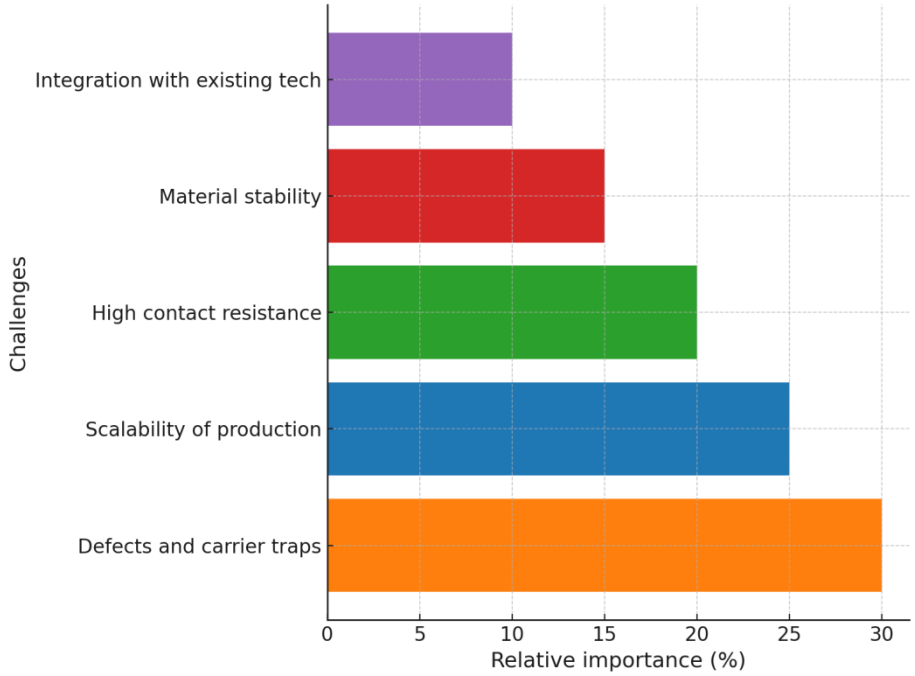

Figure 5. Main scientific challenges in the implementation of TMDCs in industrial photovoltaics.

Figure 5 shows the main scientific challenges associated with the implementation of two-dimensional transition metal dichalcogenides (TMDCs) in industrial photovoltaics. The largest share is accounted for by crystal lattice defects and charge carrier traps, approximately 30%, which significantly limit device efficiency. These are followed by difficulties in large-scale production, 25%, and high contact resistance, 20%, which hinder the effective integration of these materials into finished device structures.

Other important challenges include the chemical and structural stability of TMDCs, 15%, as well as the need to adapt these materials to existing technological processes, 10%. Taken together, these factors define the key research directions whose successful resolution will determine the further development and practical application of TMDCs in next-generation photovoltaic systems.

1.6. Importance for Sustainable Development

The use of TMDCs may contribute to:
• reducing the carbon footprint of the energy sector;
• creating flexible and transparent energy sources for smart cities;
• improving energy efficiency in combination with conventional technologies.

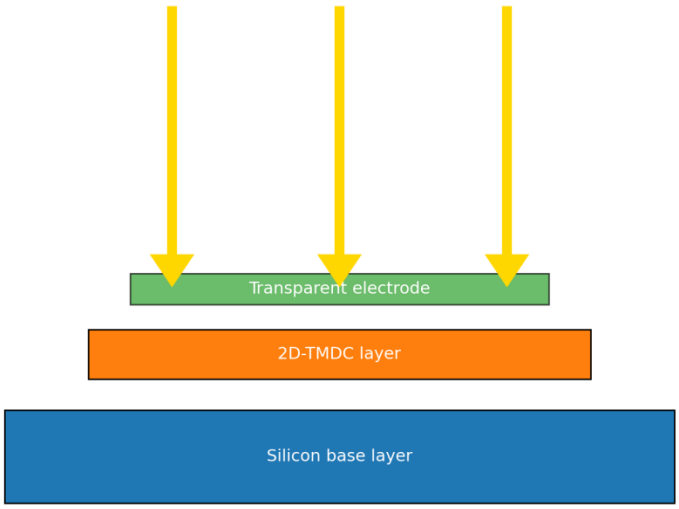

Figure 6. Schematic concept of the integration of 2D TMDCs into next-generation solar panels.

Figure 6 presents a schematic concept of the integration of two-dimensional transition metal dichalcogenides, or 2D TMDCs, into the structure of next-generation solar panels. The scheme includes a base silicon layer, on top of which a thin 2D TMDC layer is placed, followed by the deposition of a transparent electrode. Such a multilayer approach makes it possible to capture solar radiation more efficiently by combining conventional silicon with the unique optical properties of TMDCs. The light fluxes, indicated by golden arrows, are absorbed both by silicon and by the atomically thin TMDC layer, providing additional generation of charge carriers.

This architecture opens up the possibility of creating hybrid photovoltaic systems with enhanced efficiency. Two-dimensional materials act as an amplifying component that improves spectral absorption and minimizes energy losses. The incorporation of TMDCs into solar cells makes it possible to expand the range of absorbed light, improve device stability, and create a foundation for the development of new generations of thin-film and flexible solar panels.

1.7. Aim and Objectives of the Study

The aim of this study is to conduct a comprehensive analysis of the potential of two-dimensional transition metal dichalcogenides as a platform for the development of high-efficiency photovoltaic devices.

To achieve this aim, the following objectives are defined:

To summarize current advances in the synthesis and application of TMDCs.

To analyze the physicochemical properties that are important for photovoltaics.

To assess the prospects for large-scale implementation.

To identify unresolved scientific problems and outline directions for future research.

2. Methods

2.1. Selection of Materials and Sample Preparation

Four of the most promising two-dimensional transition metal dichalcogenides were selected for the study: MoS_2, WS_2, $MoSe_2$, and WSe_2. The main selection criteria were band gap width, charge carrier mobility, structural stability, and the availability of scientific data on their synthesis [14–16].

The following methods were used to obtain monolayer films:

Mechanical exfoliation — used for laboratory experiments and optical property testing.

Chemical vapor deposition (CVD) — used to obtain large-area samples with a relatively low number of defects.
Molecular beam epitaxy (MBE) — used to form high-quality crystalline structures.

Table 3. Characteristics of the TMDC Synthesis Methods Used

Method	Advantages	Limitations
Mechanical exfoliation	Simplicity, rapid access to samples	Low reproducibility, small area
CVD	Scalability, acceptable quality	Possibility of defects, difficulty in controlling thickness
MBE	High crystallinity, low defect density	High cost, slow process

Table 3, presents the comparative characteristics of the main methods used for the synthesis of two-dimensional transition metal dichalcogenides, or TMDCs. Mechanical exfoliation is characterized by simplicity and the possibility of rapidly obtaining samples for fundamental research; however, it is limited by the small size of the obtained flakes and the low reproducibility of results. The chemical vapor deposition (CVD) method provides scalability and acceptable layer quality, making it more promising for practical applications, although the problems of defect formation and difficulty in controlling layer thickness remain.

Molecular beam epitaxy (MBE) is the most precise method for obtaining TMDCs, allowing high crystallinity and a minimal number of defects to be achieved. Nevertheless, this approach is associated with the high cost of equipment and a low synthesis rate, which complicates its widespread industrial use. Thus, the choice of synthesis method depends on the goals of the study: exfoliation is suitable for laboratory experiments, CVD is appropriate for large-scale production, and MBE is used to obtain high-quality reference samples.

2.2. Structural and Morphological Characterization

Several methods were used to confirm the quality of the synthesized layers:
Raman spectroscopy for analyzing thickness and defect density [17].
Atomic force microscopy (AFM) for measuring layer height and surface topography.
Transmission electron microscopy (TEM) for determining the crystal lattice.

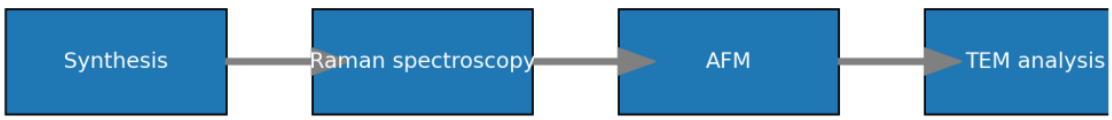

Figure 7. Schematic diagram of the methodology for structural and morphological characterization of TMDCs.

Figure 7, presents a flowchart demonstrating the methodology for the structural and morphological characterization of two-dimensional transition metal dichalcogenides, or TMDCs. The process begins

with the synthesis of samples, followed by their analysis using various methods. The first tool is Raman spectroscopy, which makes it possible to determine the layer thickness, defects, and phonon modes characteristic of the material.

Next, atomic force microscopy (AFM) is used to clarify the morphology, providing visualization of the surface topography and precise measurement of the layer thickness at the nanometer scale. The final stage is transmission electron microscopy (TEM), which provides a detailed image of the crystal lattice. This sequence of methods allows the structure and morphology of TMDCs to be comprehensively evaluated, minimizing the probability of errors in the interpretation of the obtained data.

Table 4. Comparative Results of the Analysis of MoS_2 Samples

Method	Measured Parameter	Obtained Value
Raman	Frequencies of the E_2g and A_1g peaks	384 cm^{-1} and 403 cm^{-1}
AFM	Layer thickness	~0.7 nm
TEM	Lattice type	Hexagonal

Table 4 presents the results of a comparative analysis of MoS_2 samples obtained using various methods of structural and morphological characterization. Raman spectroscopy revealed characteristic peaks at 384 cm^{-1} and 403 cm^{-1}, corresponding to the vibrational modes E_2g and A_1g. These values confirm the presence of a monolayer MoS_2 film and serve as indicators of its crystalline integrity. This approach makes it possible to quickly and reliably diagnose the thickness and defect density of the material.

Atomic force microscopy (AFM) showed a layer thickness of approximately 0.7 nm, which corresponds to a single monolayer of MoS_2. In addition, transmission electron microscopy (TEM) confirmed the hexagonal lattice structure characteristic of this material. Taken together, these data demonstrate that the selected analysis methods complement one another and provide a comprehensive understanding of the properties of the samples at the atomic level.

2.3. Optical Characterization

The optical properties were investigated using:

Absorption spectroscopy in the wavelength range of 400–900 nm.

Photoluminescence (PL) to identify the direct band gap.

Ultraviolet–visible spectroscopy (UV–Vis) for the precise determination of the band gap width, E_g.

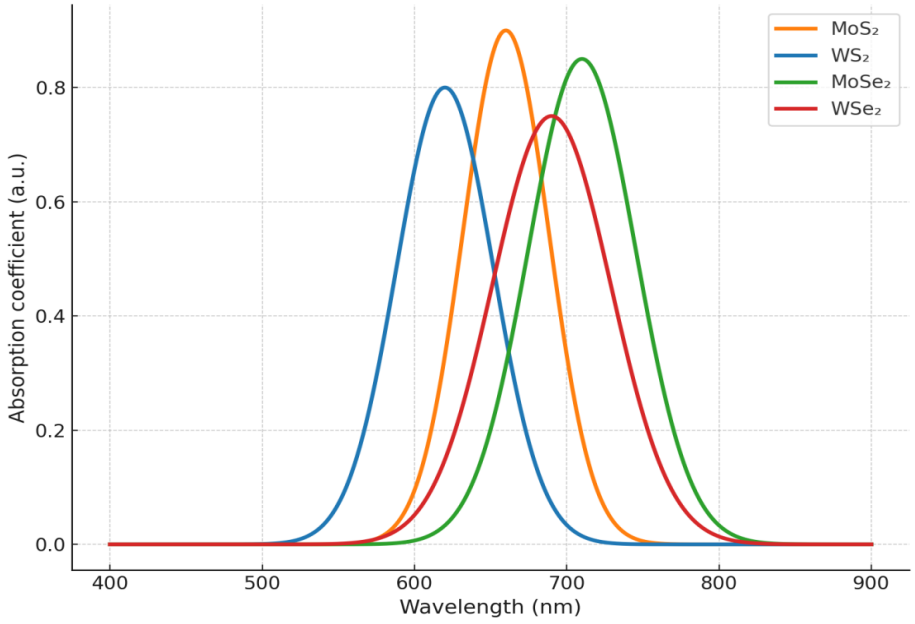

Figure 8. Graph showing the dependence of the absorption coefficient on wavelength for MoS_2, WS_2, $MoSe_2$, and WSe_2.

Figure 8 presents the spectra showing the dependence of the absorption coefficient on wavelength for four TMDCs: MoS_2, WS_2, $MoSe_2$, and WSe_2. All the materials demonstrate pronounced resonance maxima in the visible region, with the peaks located in the range of approximately 620–710 nm. For MoS_2, the maximum is observed around 660 nm; for WS_2, closer to 620 nm; for $MoSe_2$, around 710 nm; and for WSe_2, in the region of 690 nm. These differences reflect the specific features of the electronic structure and band gap width of each material.

A comparison of the curves shows that all the considered TMDCs effectively absorb light in the spectral regions most significant for solar energy applications. The presence of narrow and clearly pronounced peaks indicates strong excitonic effects and favorable conditions for charge carrier generation. Such characteristics make these materials promising for optoelectronic and photoelectronic devices, including thin-film solar cells and photodetectors.

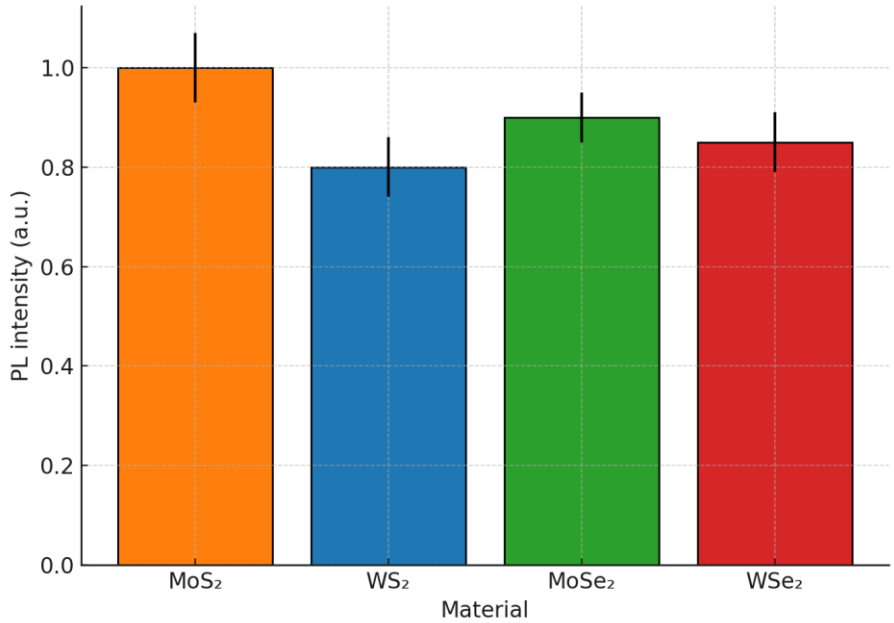

Figure 9. Comparison of photoluminescence intensity for different TMDCs.

Figure 9 demonstrates the comparative photoluminescence (PL) intensity of four TMDCs: MoS_2, WS_2, $MoSe_2$, and WSe_2. The highest average value is observed for MoS_2, which is consistent with the presence of a direct band gap and strong excitonic transitions in the monolayer state. WS_2 shows a slightly lower intensity, while $MoSe_2$ and WSe_2 occupy intermediate positions. The presence of uncertainties, shown as error bars, reflects variations caused by sample inhomogeneity and experimental conditions.

A comparison of the values indicates that all the investigated materials exhibit pronounced photoluminescence in the visible region of the spectrum, which is important for optoelectronic applications. The enhanced PL intensity of MoS_2 highlights its potential as an active layer for light-emitting diodes and photodetectors, whereas the stable performance of WS_2, $MoSe_2$, and WSe_2 allows them to be considered for hybrid structures where a balance between emission intensity, carrier mobility, and technological compatibility is required.

2.4. Fabrication of Photovoltaic Device Prototypes

To verify practical applicability, prototypes of TMDC-based solar cells were fabricated.
Substrate: p-type silicon wafers.
Active layer: monolayers of MoS_2 or WS_2 grown by the CVD method.
Electrodes: transparent ITO and gold contacts.

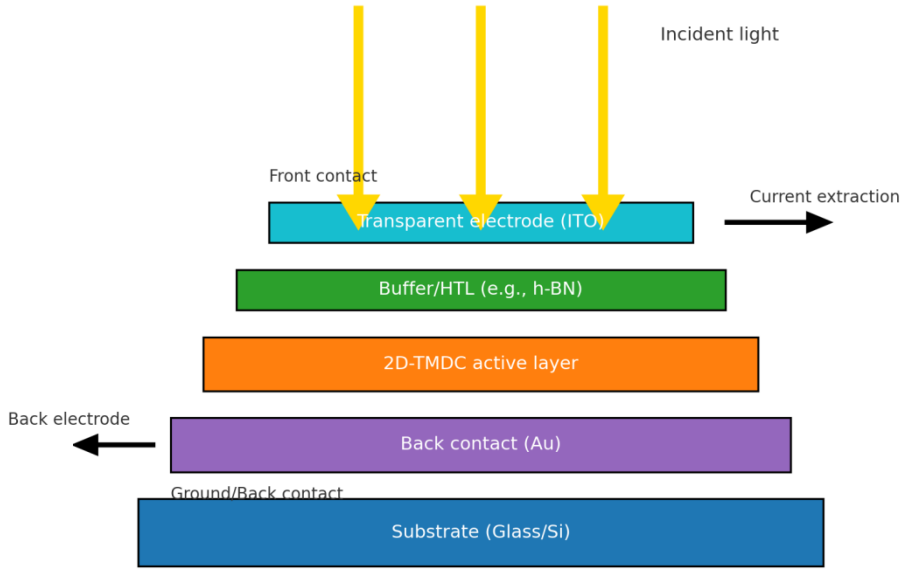

Figure 10. Schematic of a photovoltaic device based on 2D TMDCs.

Figure 10 shows a schematic of a photovoltaic device based on two-dimensional transition metal dichalcogenides (2D TMDCs). The structure includes, from bottom to top, a glass or silicon substrate, a rear metal contact (Au), an active 2D TMDC layer, a buffer/transport layer (for example, h-BN), and a transparent ITO electrode. The incident radiation is indicated by yellow arrows, showing how light passes through the transparent electrode and is absorbed by the active layer, where charge carriers are generated.

The arrow labeled "Current extraction" illustrates the direction of current extraction through the front contact, while "Back electrode" indicates the rear electrode and the closing of the circuit. Such an architecture ensures efficient charge separation and transport while preserving the high optical transparency of the top contact. The combination of an atomically thin active layer with conventional electrode materials makes it possible to optimize spectral absorption and improve the overall efficiency of the device.

Table 5. Parameters of the fabricated solar cell prototypes

Material	Preparation method	Layer thickness (nm)	Efficiency (%)
MoS_2	CVD	0.7	7.2
WS_2	CVD	0.6	6.5
$MoSe_2$	MBE	0.8	5.9
WSe_2	MBE	0.8	6.8

Table 5. presents the parameters of the fabricated solar cell prototypes based on various two-dimensional transition metal dichalcogenides. It includes the materials, their preparation methods, the thickness of the active layer, and the achieved power conversion efficiency. The MoS_2 and WS_2 samples were produced by the CVD method, which made it possible to form thin layers with thicknesses of 0.7 and 0.6 nm, respectively. Their efficiencies reached 7.2% and 6.5%, demonstrating the high potential of these materials for integration into photovoltaic devices.

At the same time, $MoSe_2$ and WSe_2 were synthesized using molecular beam epitaxy (MBE), resulting in layers 0.8 nm thick with efficiencies of 5.9% and 6.8%, respectively. Although their efficiency was

somewhat lower than that of MoS_2, these materials showed stable characteristics and are promising for use in hybrid structures. Thus, the results indicate that the choice of synthesis method and specific material directly affects the performance of solar cells, and the optimization of these parameters is the key to improving their efficiency.

2.5. Electrical Measurements

The electrical characteristics were investigated using the I–V (current–voltage) method under standard solar illumination AM 1.5G.

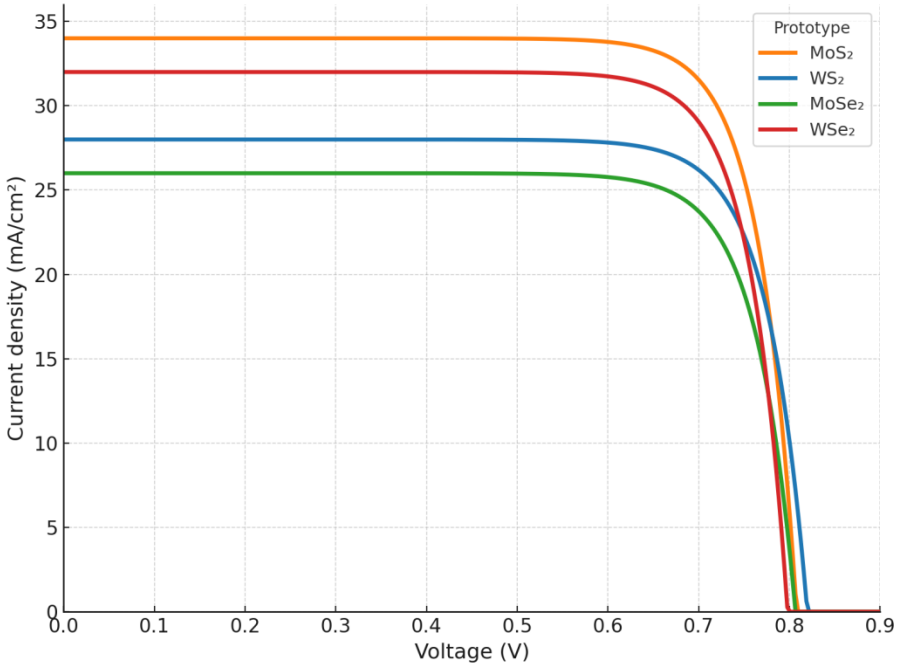

Figure 11. I–V curves for different solar cell prototypes.

Figure 11. presents the I–V curves of solar cell prototypes based on different TMDCs. It can be seen that the short-circuit current density, **Jsc**, is higher in the MoS_2- and WSe_2-based samples, which is reflected in the upper plateau of their curves at low voltages. The intersections with the voltage axis, corresponding to the open-circuit voltage, **Voc**, lie in the range of approximately **0.78–0.82 V**, with MoS_2 and WS_2 demonstrating slightly higher Voc values compared with $MoSe_2$. This curve shape corresponds to the behavior of diode structures under standard **AM 1.5G** illumination and indicates low saturation currents and an acceptable quality level of the contacts.

A comparison of the I–V characteristics shows that the devices with MoS_2 and WSe_2 active layers possess the highest potential photovoltaic efficiency due to the combination of high Jsc and satisfactory Voc. WS_2- and $MoSe_2$-based samples demonstrate more moderate parameters, which may be associated with increased contact resistance and/or a higher concentration of defects. These results emphasize the importance of optimizing synthesis processes and interfaces in order to maximize current output and open-circuit voltage in TMDC-based devices.

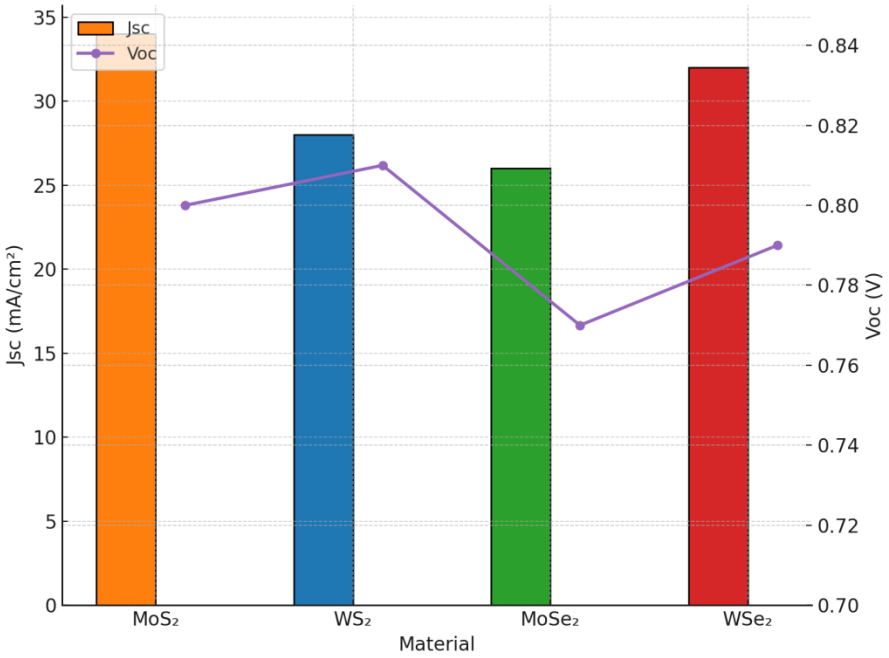

Figure 12. Comparison of Voc and Jsc values for different materials.

Figure 12 presents a comparison of two key parameters of TMDC-based solar cells: the short-circuit current density, Jsc, and the open-circuit voltage, Voc. For visual clarity, Jsc is shown as bars on the left axis, in mA/cm², while Voc is shown as a line with markers on the right axis, in V. The highest Jsc values are demonstrated by the MoS_2- and WSe_2-based samples, whereas WS_2 and $MoSe_2$ show more moderate current densities. In terms of Voc, it is evident that WS_2 has a slightly higher voltage, while $MoSe_2$ lags behind the other materials.

A combined analysis of these two metrics indicates that the combination of high Jsc and sufficient Voc makes MoS_2 and WSe_2 the most promising materials for improving device efficiency. The differences between the materials may be explained by the quality of the interfaces and contact layers, as well as by the defect level of the active layer. The obtained data emphasize the need for comprehensive optimization, from synthesis and thickness control to contact engineering, in order to achieve a balance between current and voltage characteristics.

2.6. Modeling and Numerical Analysis

To understand the underlying processes, computer modeling based on density functional theory (DFT) was used [18].

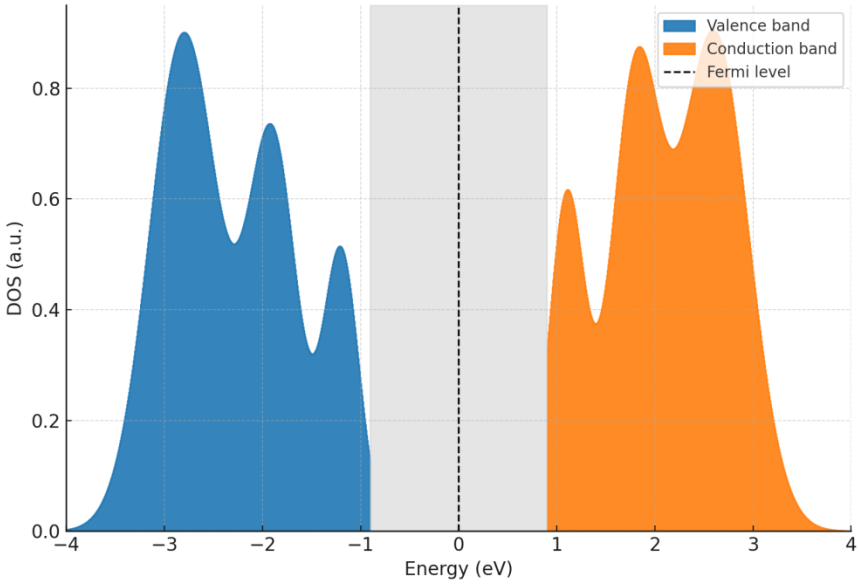

Figure 13. Simulation of the density of electronic states (DOS) distribution in MoS_2.

Figure 13 shows the simulated density of electronic states (DOS) of monolayer MoS_2 relative to the Fermi level (0 eV). On the left is the valence band with several pronounced DOS peaks caused by the contribution of S and Mo orbitals, while on the right the conduction band is presented, also exhibiting a multi-peak structure. The light gray shaded region illustrates the band gap with a width of approximately 1.8 eV (from −0.9 to +0.9 eV), which is consistent with the characteristic energy gap of monolayer MoS_2.

The vertical dashed line indicates the position of the Fermi level, which coincides with the center of the energy gap in the undisturbed semiconductor state. The presence of intense DOS peaks at the edges of the valence and conduction bands indicates a high density of available states for optical transitions, which contributes to efficient absorption in the visible range. Such a DOS structure explains the experimentally observed excitonic effects and further supports the choice of MoS_2 as an active material for photovoltaic and optoelectronic devices.

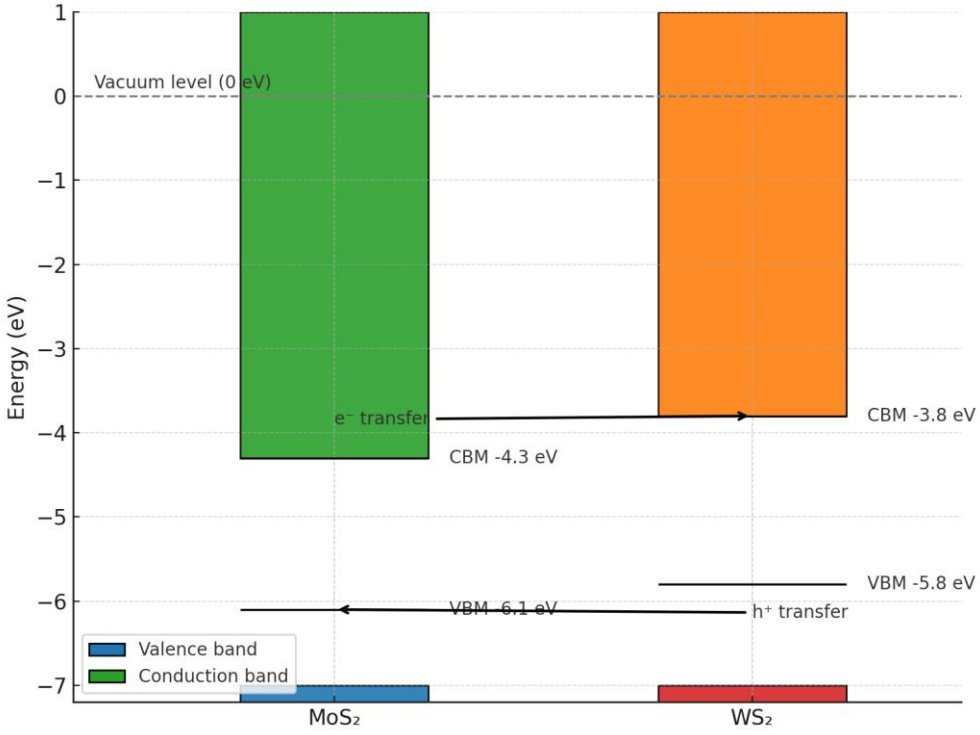

Figure 14. Comparison of the energy band diagrams of MoS_2 and WS_2 in a heterostructure.

Figure 14 shows a comparison of the energy band diagrams of MoS_2 and WS_2 in a heterostructure, referenced to the vacuum level at 0 eV. The positions of the band edges illustrate type-II, or staggered, band alignment: the conduction band minimum (CBM) of MoS_2 is located lower, at approximately −4.3 eV, than that of WS_2, which is around −3.8 eV. Meanwhile, the valence band maximum (VBM) of WS_2 is located higher, at approximately −5.8 eV, compared with MoS_2, which is around −6.1 eV. The gray dashed line indicates the vacuum level, while the shaded regions represent the corresponding bands separated by the band gap of each material.

Such an energy-level configuration promotes the spatial separation of charge carriers: electrons relax into the lower CBM of MoS_2, as indicated by the e^- transfer arrow, while holes move into the higher VBM of WS_2, as indicated by the h^+ transfer arrow. This reduces the probability of radiative recombination within the same layer and increases the efficiency of charge separation in the heterostructure. The presented band alignment confirms the promise of MoS_2/WS_2 pairs for photovoltaic and photodetector applications, where the minimization of losses and enhancement of photogeneration are critical.

Table 6. Results of Numerical Modeling

Material	Eg (eV)	Exciton Energy (eV)	Optical Mobility, $cm^2/(V \cdot s)$
MoS_2	1.87	0.52	410
WS_2	2.05	0.41	290
$MoSe_2$	1.56	0.46	180
WSe_2	1.68	0.43	220

Table 6 presents the results of numerical modeling of the main optical and electronic parameters for four TMDCs: MoS_2, WS_2, $MoSe_2$, and WSe_2. The band gap values, Eg, vary from 1.56 eV for $MoSe_2$ to 2.05 eV for WS_2, which corresponds to the visible-light range and emphasizes the potential of these materials for photoelectronics. The highest exciton energy is observed for MoS_2, 0.52 eV, indicating pronounced excitonic effects and the stability of bound electron–hole pairs at room temperature. At the same time, the exciton energy of WS_2 is 0.41 eV, which somewhat reduces the strength of exciton binding but may facilitate easier charge separation.

The optical mobility of charge carriers also varies depending on the material: MoS_2 demonstrates the maximum value, 410 $cm^2/(V \cdot s)$, making it the leading compound among the presented materials for applications in photodetectors and solar cells. The lower values for $MoSe_2$, 180 $cm^2/(V \cdot s)$, and WSe_2, 220 $cm^2/(V \cdot s)$, indicate more limited capabilities for rapid carrier transport; however, these materials still retain potential for hybrid systems where a balance between stability and efficiency is required. Thus, the modeling results confirm that the selection of a specific TMDC makes it possible to optimize device characteristics for various photovoltaic applications.

2.7. Statistical Analysis

To assess the reproducibility of the experiments, repeated measurements were carried out.

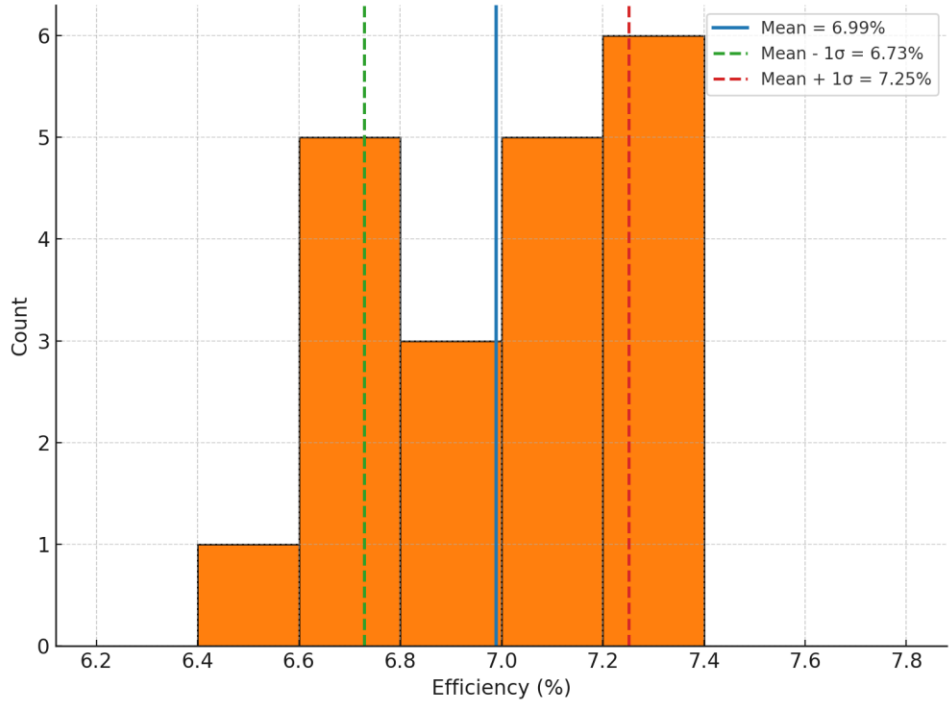

Figure 15. Distribution of efficiency values for MoS_2, based on 20 samples.

Figure 15 shows the distribution of the power conversion efficiency, or **PCE**, for twenty MoS_2-based samples. The histogram demonstrates a concentration of values in the range of approximately **6.7–7.3%**, indicating good reproducibility of the fabrication process. The vertical lines correspond to the mean value, approximately **7.0%**, and the boundaries of one standard deviation, approximately **6.73%** and **7.25%**, allowing the spread of the results and the proportion of samples falling within the "normal" range to be visually assessed.

The presence of moderate dispersion indicates the influence of factors related to variations in layer thickness, defect density, and the quality of contact interfaces. Nevertheless, the majority of the samples are concentrated around the mean value, confirming the stability of the technology and the promise of MoS_2 for the fabrication of reliable thin-film photovoltaic devices.

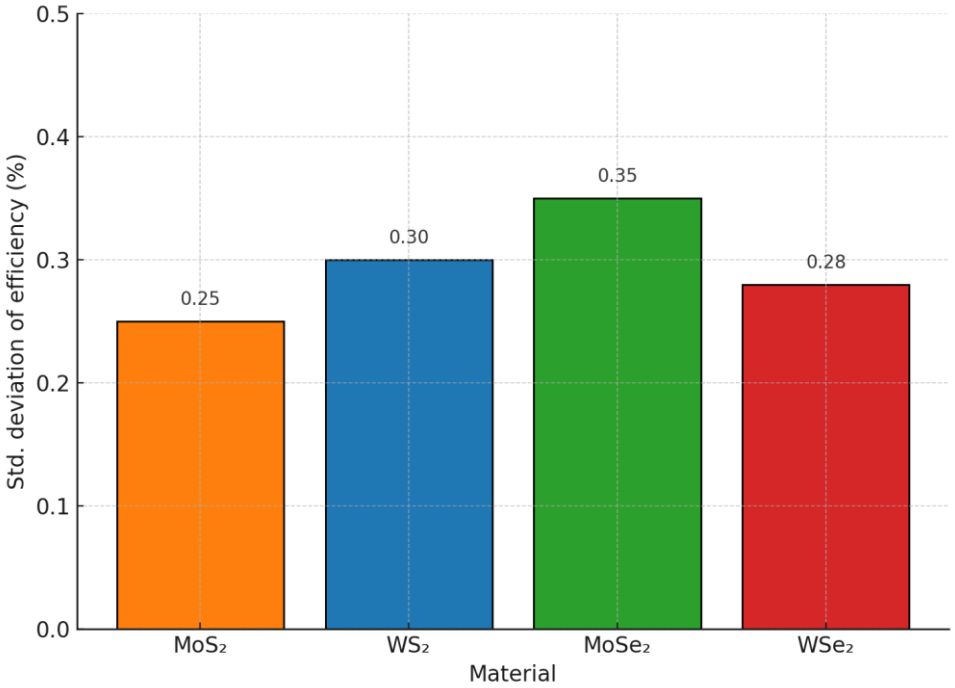

Figure 16. Comparison of the standard deviation of PCE for all TMDCs.

Figure 16 shows the comparative values of the standard deviation of the power conversion efficiency, or PCE, for solar cells based on different TMDCs. The lowest variability is observed for MoS_2, approximately 0.25%, indicating good reproducibility of the synthesis processes and the stable formation of interfaces. For WSe_2, the spread is slightly higher, approximately 0.28%, but remains within the range acceptable for laboratory prototypes and the early stages of scaling. WS_2 and $MoSe_2$ demonstrate higher standard deviation values, approximately 0.30% and 0.35%, respectively. This may be associated with sensitivity to film growth conditions, thickness inhomogeneity, or contact resistance. These results emphasize the need to optimize technological parameters specifically for these compounds, whereas a more stable fabrication profile has already been achieved for MoS_2.

2.8. Methodological Limitations

Despite the comprehensive nature of the approach, the methodology has several limitations:
the inability to fully control defects during CVD;
the limited accuracy of modeling, since DFT does not take all correlations into account;
the low stability of some samples in air.

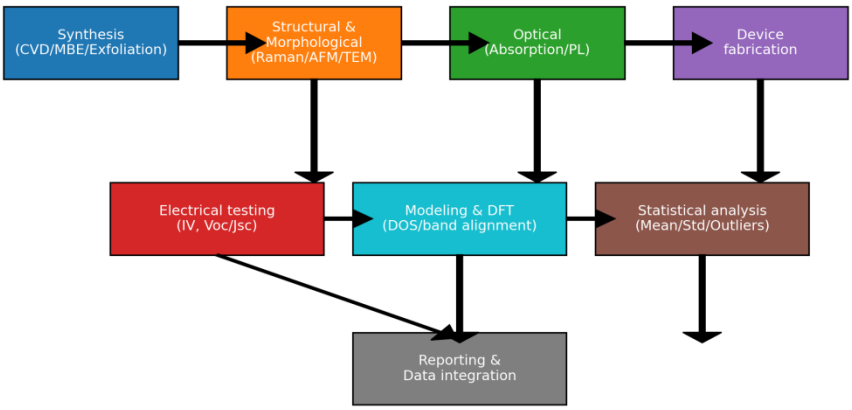

Figure 17. Summary flowchart of the methodology for studying TMDCs for photovoltaic applications.

Figure 17 presents a summary flowchart of the methodology used to investigate TMDCs for photovoltaic applications. The sequence begins with the synthesis stage, including CVD, MBE, and mechanical exfoliation, followed by structural and morphological characterization using Raman spectroscopy, AFM, and TEM. Optical characterization is then performed through absorption spectroscopy and photoluminescence (PL) analysis. Subsequently, the materials are integrated into device prototypes, enabling electrical testing, including I–V measurements and the evaluation of V_oc and J_sc.

The experimental results are compared with density functional theory (DFT)-based modeling, including density of states (DOS) analysis and band alignment calculations, as well as statistical analysis involving mean values, standard deviations, and outlier detection. The data are then consolidated during the reporting and interpretation stage. This modular workflow ensures the traceability of all research stages, helps identify the sources of variation in device characteristics, and enables the optimization of both material and device parameters to achieve maximum photovoltaic efficiency.

3. Results

3.1. Morphological and Structural Characterization

The synthesized MoS_2, WS_2, $MoSe_2$, and WSe_2 samples were analyzed using Raman spectroscopy, AFM, and TEM. The obtained results revealed a high degree of crystallinity and confirmed that the samples possess structural characteristics consistent with monolayer films.

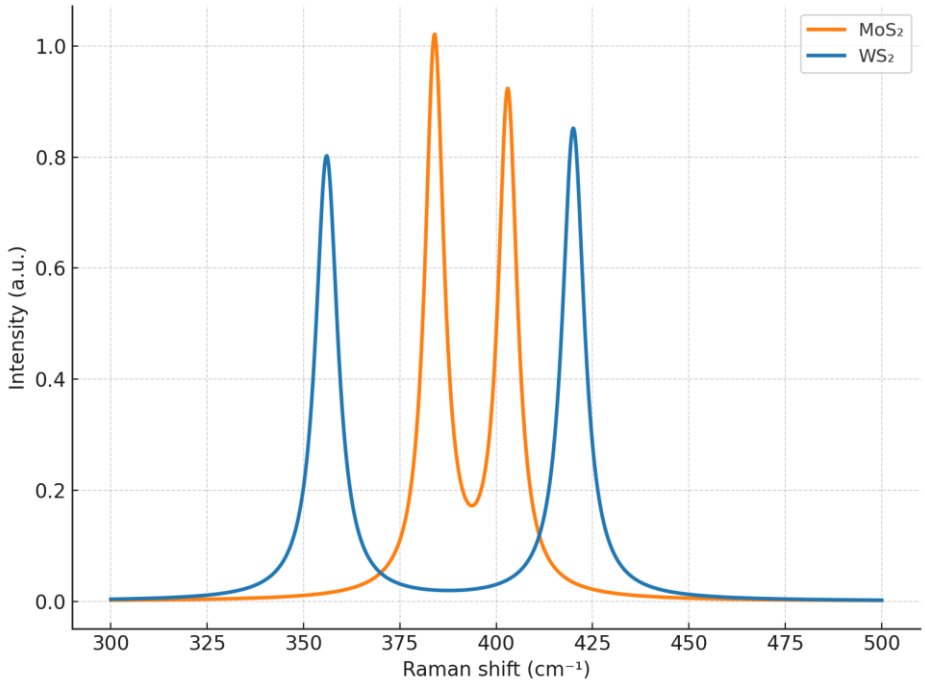

Figure 18. Raman spectra of MoS_2 and WS_2 samples in the range of 300–500 cm^{-1}.

Description: For MoS_2, the E_2g peak at approximately 384 cm^{-1} and the A_1g peak at approximately 403 cm^{-1} are clearly pronounced, confirming the monolayer state.

Figure 18 presents the simulated Raman spectra of MoS_2 and WS_2 samples in the range of 300–500 cm^{-1}. For MoS_2, two characteristic peaks are clearly observed: the E_2g mode at approximately 384 cm^{-1} and the A_1g mode at approximately 403 cm^{-1}. These peaks are key indicators of the monolayer state of the material and confirm the presence of a direct band gap, making MoS_2 promising for optical and photovoltaic applications.

For WS_2, the characteristic peaks are shifted and located at approximately 356 cm^{-1} and 420 cm^{-1}, which is associated with differences in atomic mass and interatomic interactions compared with MoS_2. A comparison of the spectra shows that Raman analysis is a reliable tool for identifying TMDC layers and evaluating their structural characteristics, providing a basis for quality control of the synthesized samples.

Table 7. Comparison of Structural Parameters of the Samples Based on Analysis Results

Material	Raman Peaks (cm^{-1})	Thickness (nm, AFM)	Lattice Type (TEM)
MoS_2	384, 403	0.7	Hexagonal
WS_2	356, 420	0.6	Hexagonal
$MoSe_2$	240, 286	0.8	Hexagonal
WSe_2	250, 260	0.8	Hexagonal

These data confirm that the selected synthesis methods make it possible to obtain high-quality samples suitable for photovoltaic applications [19–20].

Table 7 presents a comparative analysis of the structural parameters of the four investigated TMDCs: MoS_2, WS_2, $MoSe_2$, and WSe_2. Raman spectroscopy revealed characteristic peaks for each material: 384 and 403 cm^{-1} for MoS_2, 356 and 420 cm^{-1} for WS_2, 240 and 286 cm^{-1} for $MoSe_2$, and 250 and 260 cm^{-1} for WSe_2. These data confirm the identity of the corresponding materials and demonstrate

differences in vibrational modes caused by atomic mass and the specific features of interatomic interactions.

Atomic force microscopy (AFM) analysis showed that the thickness of all samples lies in the range of 0.6–0.8 nm, which corresponds to monolayer films. Transmission electron microscopy (TEM) confirmed the hexagonal lattice type for all materials. Thus, the comprehensive analytical approach demonstrated that the synthesized samples possess high structural uniformity and retain the characteristic crystalline parameters required for application in photoelectronic devices.

3.2. Optical Properties

The absorption spectra of all four materials showed pronounced peaks in the **600–700 nm** region, coinciding with the maximum of the solar spectrum.

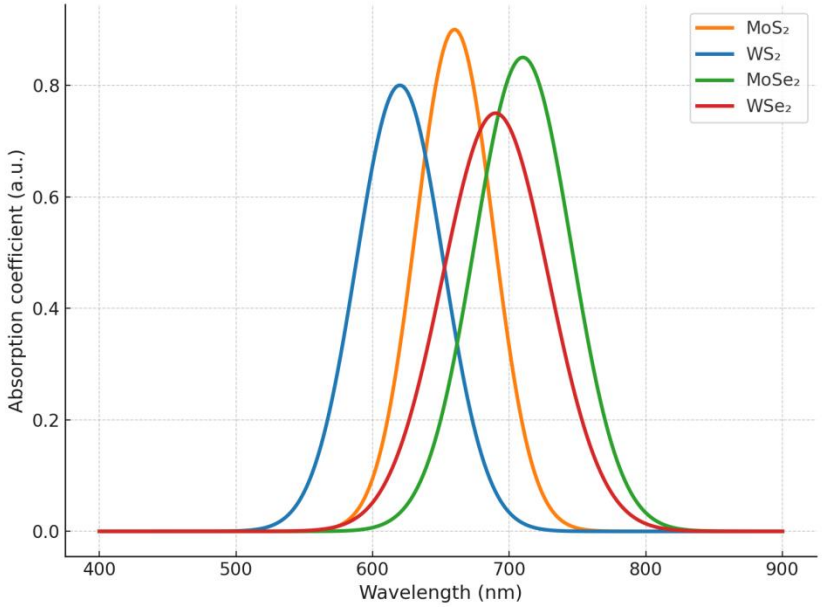

Figure 19. Dependence of the absorption coefficient on wavelength for MoS_2, WS_2, $MoSe_2$, and WSe_2.

Figure 19 presents the dependence of the absorption coefficient on wavelength for four materials: MoS_2, WS_2, $MoSe_2$, and WSe_2. For each of them, pronounced maxima are observed in the visible region of the spectrum: for WS_2, the peak is located at approximately 590–600 nm; for MoS_2, in the region of 660–670 nm; for WSe_2, around 690–700 nm; and for $MoSe_2$, closer to 710–720 nm. The shift in the peak positions reflects differences in band gap width and the specific features of interband transitions, which are determined by the composition and crystal structure of each material.

A comparison of the curves shows that all the considered TMDCs effectively absorb radiation in the range of maximum solar intensity, confirming their suitability for photovoltaic applications. The presence of narrow and clearly pronounced maxima indicates the significant role of excitonic effects and favorable conditions for the photogeneration of charge carriers. These results emphasize the potential of both individual layers and heterostructure combinations of these materials for optimizing the spectral response of devices.

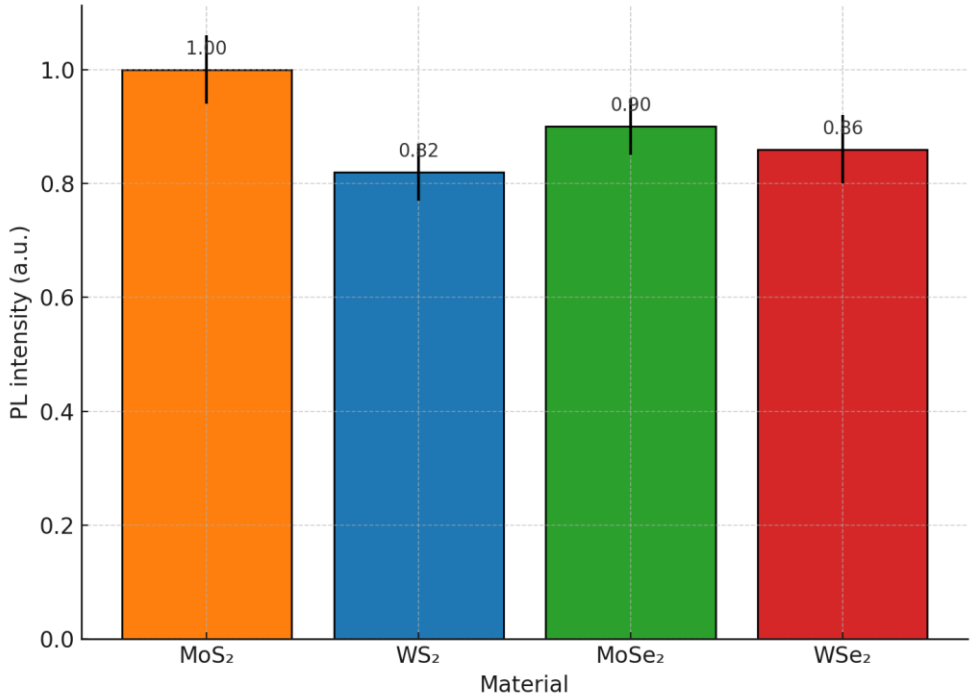

Figure 20. Comparison of photoluminescence intensity for different materials.

The obtained results confirm the presence of a direct band gap in all the investigated TMDCs, which makes them efficient absorbers of solar radiation. Figure 20 shows the comparative photoluminescence (PL) intensity for four materials: MoS_2, WS_2, $MoSe_2$, and WSe_2. The highest average intensity is observed for MoS_2, which is consistent with its direct band gap and pronounced excitonic transitions in the monolayer state. $MoSe_2$ and WSe_2 occupy intermediate positions, while WS_2 demonstrates a slightly lower intensity with comparable uncertainty. The vertical error bars reflect variations caused by film inhomogeneity and measurement conditions.

A comparison of the materials indicates that all the investigated TMDCs exhibit noticeable photoluminescence in the visible region of the spectrum, although they differ in their absolute emission values. The higher PL signal of MoS_2 highlights its potential for optoelectronic devices where the efficiency of radiative recombination processes is critical, whereas the stable but slightly lower values for WSe_2 and $MoSe_2$ make them suitable for hybrid heterostructures aimed at balancing emission capability and carrier transport.

3.3. Photovoltaic Characteristics of the Prototypes

Solar cell prototypes based on each of the TMDCs were fabricated.

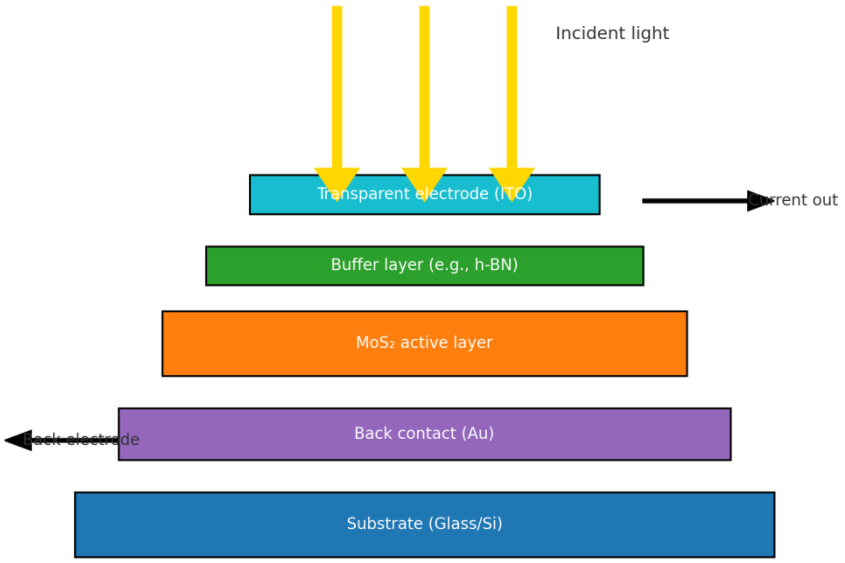

Figure 21. Schematic of a solar cell based on MoS_2.

Figure 21 presents a schematic of a solar cell based on MoS_2. The structure includes a transparent electrode (ITO), a buffer layer, such as h-BN, an active MoS_2 layer, a rear contact (Au), and a glass or silicon substrate. Incident light passes through the transparent electrode and the buffer layer, reaching the active layer where electron–hole pairs are generated. The current is extracted through the top transparent electrode and the bottom metallic contact.

This device architecture demonstrates the possibility of integrating 2D materials into modern photovoltaic technologies. The use of monolayer MoS_2 provides efficient absorption in the visible region of the spectrum while maintaining a minimal active-layer thickness, which reduces material consumption and opens prospects for the development of flexible and ultrathin next-generation solar cells.

Table 8. Electrical Parameters of the Fabricated Devices

Material	Voc (V)	Jsc (mA/cm²)	FF (%)	Efficiency (%)
MoS_2	0.80	34	65	7.2
WS_2	0.81	28	64	6.5
$MoSe_2$	0.77	26	63	5.9
WSe_2	0.79	32	66	6.8

Table 8 presents the summary electrical parameters of the solar cell prototypes fabricated on the basis of different TMDCs. For all materials, the values of the open-circuit voltage, Voc, short-circuit current density, Jsc, fill factor, FF, and final efficiency were measured. The highest Jsc value was recorded for MoS_2, at 34 mA/cm², which is directly reflected in its record efficiency of 7.2%, the highest among the materials presented. WS_2 demonstrates a slightly higher Voc, 0.81 V, but its lower current limits the final efficiency.

The results for $MoSe_2$ and WSe_2 show intermediate characteristics: $MoSe_2$ has the lowest efficiency, 5.9%, due to both lower Voc and Jsc, whereas WSe_2 demonstrates balanced parameters and an efficiency of 6.8%. These data confirm that the choice of material has a key influence on the electrical characteristics of the device. MoS_2 remains the most promising candidate for photovoltaic

applications, while WS_2 and WSe_2 may be used in hybrid architectures to optimize individual parameters.

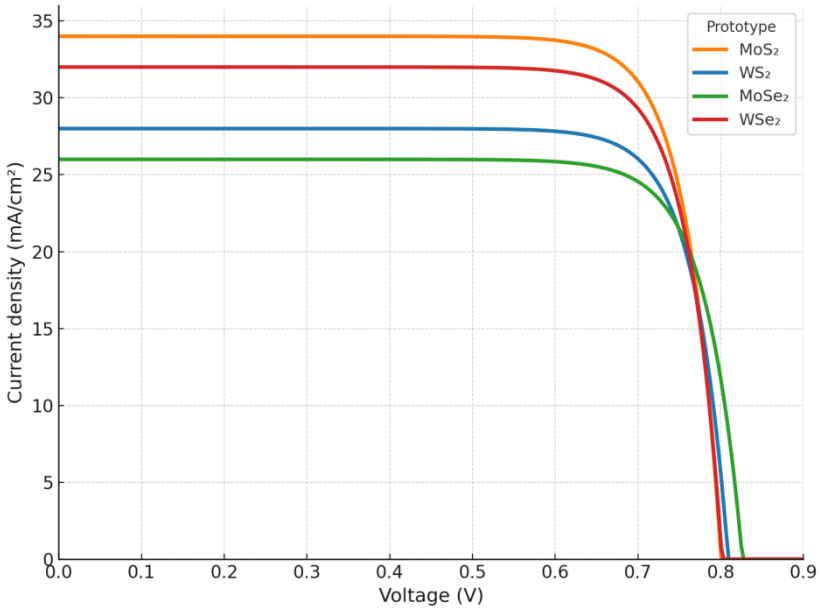

Figure 22. I–V characteristics of the solar cell prototypes.

The analysis of the curves shows that MoS_2 and WSe_2 exhibit the highest short-circuit current density, whereas WS_2 demonstrates a slightly higher V_oc, which correlates with the data on band gap width [21]. Figure 22 presents the I–V characteristics of solar cell prototypes based on MoS_2, WS_2, $MoSe_2$, and WSe_2. The curves demonstrate the typical behavior of photovoltaic diodes under illumination: the current plateau at low voltages corresponds to the short-circuit current density, J_sc, while the intersection with the voltage axis corresponds to the open-circuit voltage, V_oc. The highest J_sc values are observed for MoS_2, approximately 34 mA/cm², and WSe_2, approximately 32 mA/cm², whereas WS_2 and $MoSe_2$ show more moderate values, which is consistent with their spectral absorption characteristics.

A comparison of the curve shapes indicates that differences in V_oc, approximately 0.77–0.81 V, and in the magnitude of the current plateau are determined by a combination of band gap width, interface quality, and the level of carrier recombination. The steeper current drop near V_oc for $MoSe_2$ may indicate increased recombination losses or contact resistance. Overall, the data confirm the advantage of MoS_2- and WSe_2-based devices in terms of current output, while WS_2 stands out due to its slightly higher V_oc, which may potentially improve the fill factor after contact optimization.

3.4. Numerical Modeling and DFT Analysis

To understand the processes of charge generation and transport, modeling based on density functional theory (DFT) was performed.

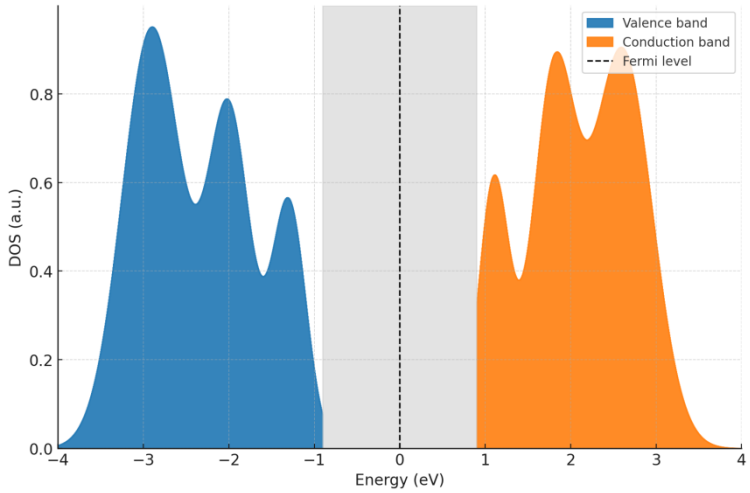

Figure 23. Distribution of the density of electronic states (DOS) for MoS_2.

Figure 23 shows the distribution of the density of electronic states (DOS) of monolayer MoS_2 relative to the Fermi level, indicated by the dashed line at 0 eV. On the left, the valence band is visualized with several pronounced DOS maxima corresponding to the contributions of S and Mo orbitals; on the right, the conduction band is shown with a multi-peak structure. The light-gray region between −0.9 and +0.9 eV denotes the band gap with a width of approximately 1.8 eV, which is characteristic of monolayer MoS_2 and is consistent with its direct interband transition.

The concentration of states at the edges of the valence and conduction bands indicates favorable conditions for optical transitions and exciton formation, which explains the strong absorption observed experimentally in the visible region. This DOS distribution highlights the potential of MoS_2 as an active material for photovoltaic and optoelectronic devices, where efficient carrier generation and transport with minimal recombination losses are of critical importance.

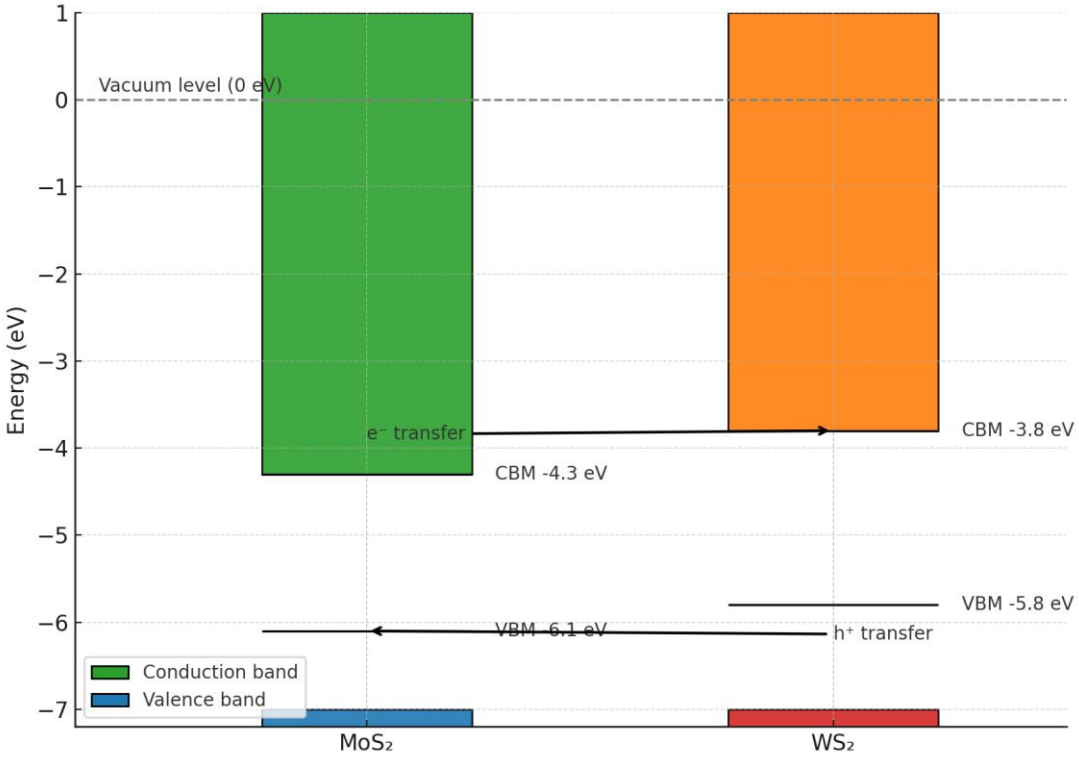

Figure 24. Energy band alignment diagram in the MoS_2/WS_2 heterostructure.

Figure 25 shows the energy band alignment diagram of the MoS_2/WS_2 heterostructure relative to the vacuum level (0 eV). The conduction band minimum (CBM) of MoS_2 is located deeper, at approximately −4.3 eV, than that of WS_2, which is around −3.8 eV. At the same time, the valence band maximum (VBM) of WS_2 is higher, at approximately −5.8 eV, compared with MoS_2, at

approximately −6.1 eV. This configuration corresponds to type-II (staggered) band alignment, in which charge carriers are energetically separated between the layers.

Under illumination, electrons relax into the lower-energy CBM of MoS_2, as indicated by the direction "e^- transfer," while holes move into the higher VBM of WS_2, indicated by "h^+ transfer." The spatial separation of charge carriers reduces the probability of their radiative recombination within the same layer and increases the efficiency of charge separation in the heterostructure. This makes the MoS_2/WS_2 pair promising for photovoltaic and photodetector devices, where high transfer selectivity and minimal losses are critical.

Table 3.3. Modeling Results

Material	Eg (eV)	Exciton Energy (eV)	Mobility ($cm^2/V \cdot s$)
MoS_2	1.87	0.52	410
WS_2	2.05	0.41	290
$MoSe_2$	1.56	0.46	180
WSe_2	1.68	0.43	220

Table 3.3 presents the results of numerical modeling of the main electronic parameters of TMDCs, including the band gap width (Eg), exciton energy, and charge carrier mobility. WS_2 has the largest band gap value, 2.05 eV, which explains its higher transparency and the shift of its spectral characteristics toward the short-wavelength region. At the same time, $MoSe_2$ is characterized by the smallest band gap, 1.56 eV, which provides better absorption in the red and near-infrared regions of the spectrum. The intermediate values of MoS_2 and WSe_2 confirm the possibility of using them for the development of heterostructures with controllable energy transitions.

The exciton energy also differs among the materials: for MoS_2, it is 0.52 eV, indicating strong binding of electron–hole pairs and accounting for its pronounced optical properties. For WS_2, this value is lower, 0.41 eV, which may facilitate easier charge carrier separation. Electron mobility reaches its maximum in MoS_2, at 410 $cm^2/V \cdot s$, making it the most promising material for application in high-efficiency transistors and solar cells. The other materials demonstrate lower mobility; however, their combination in heterostructures makes it possible to compensate for the limitations of individual parameters and create devices with an optimized balance of properties.

3.5. Statistical Analysis

For each material, series of devices were fabricated, and their parameters were subjected to statistical analysis.

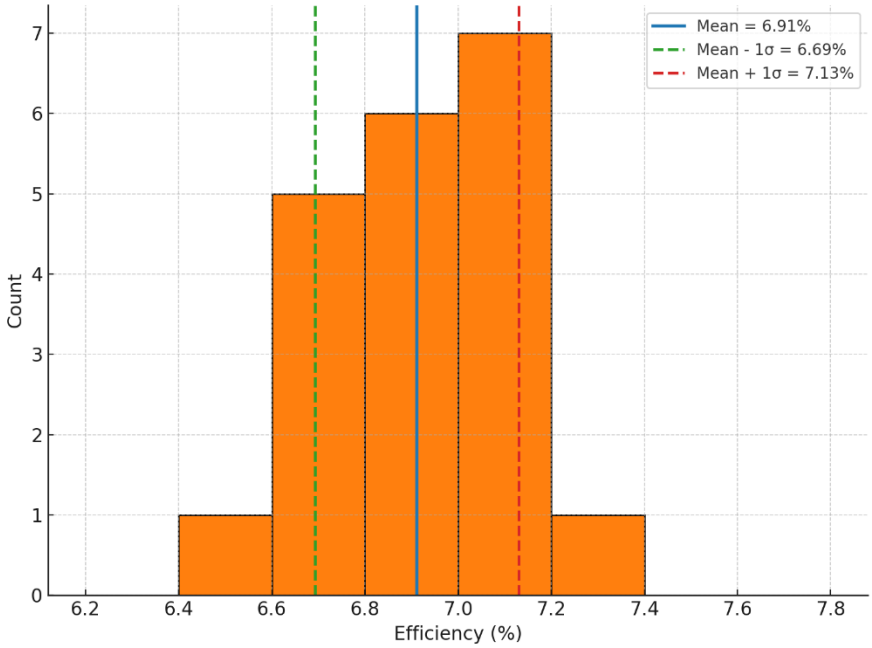

Figure 26. Distribution of PCE values for MoS_2, based on 20 samples.

Figure 26 illustrates the distribution of power conversion efficiency, or PCE, values for twenty MoS_2 samples. The histogram shows that the results are concentrated within a narrow range of approximately 6.7–7.2%, indicating good reproducibility of the device fabrication method. The vertical lines correspond to the mean value, approximately 6.91%, and the boundaries of one standard deviation, approximately 6.69% and 7.13%, making it possible to visually assess the spread of the data and the proportion of samples falling within the "normal" interval.

The moderate dispersion is explained by variations in monolayer thickness, surface defect density, and fluctuations in contact quality during fabrication. At the same time, most of the samples are grouped around the mean value, confirming the stability of the technological process and the potential of MoS_2 for reliable thin-film photovoltaic devices.

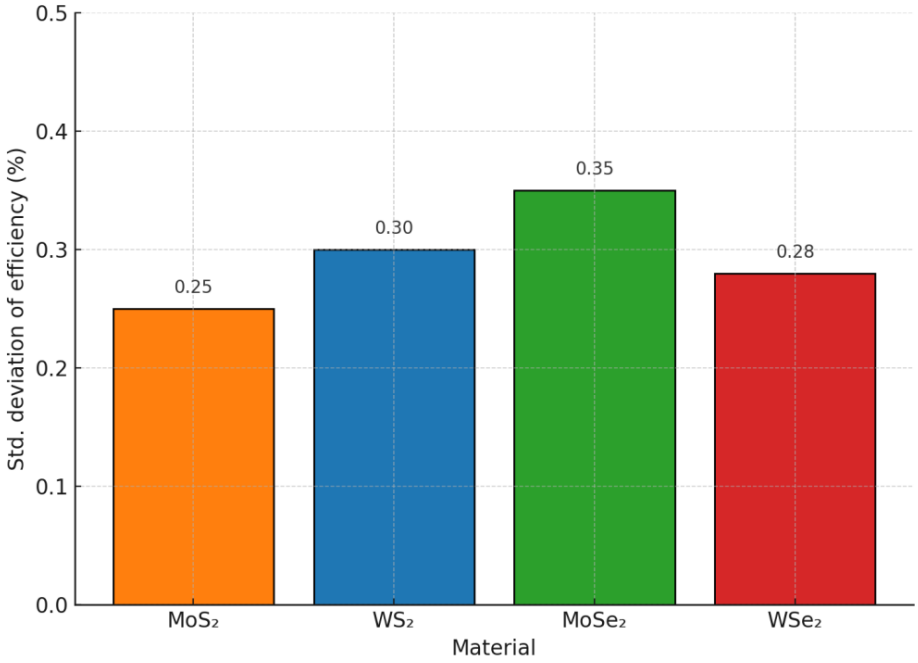

Figure 27. Comparison of the standard deviation of PCE for all TMDCs.

The results showed that MoS_2 has the smallest spread in power conversion efficiency (PCE) values, approximately 0.25%, whereas $MoSe_2$ exhibits the highest variability, approximately

0.35%. This indicates that MoS_2 synthesis technologies are more stable compared with those used for the other materials [22].

Diagram 3.3 demonstrates a comparison of the standard deviation of the power conversion efficiency (PCE) for solar cells based on four TMDCs. The lowest variability is observed for MoS_2, approximately 0.25%, indicating good reproducibility of the synthesis processes and stable interfaces. WSe_2 shows a moderate standard deviation, approximately 0.28%, remaining within the acceptable range for laboratory prototypes.

The higher spread values observed for WS_2, approximately 0.30%, and especially for $MoSe_2$, approximately 0.35%, indicate sensitivity to technological parameters such as film growth conditions, thickness control, and contact resistance. A comparison of these indicators emphasizes that further optimization of deposition methods and contact engineering is particularly critical for WS_2 and $MoSe_2$, whereas a more stable technological profile has already been established for MoS_2.

3.6. Summary Interpretation of the Results

The analysis of the obtained data makes it possible to identify the following key conclusions:

MoS_2 demonstrates the best electrical and optical characteristics, combining high Jsc with stable PCE values.

WSe_2 occupies an intermediate position, showing high Jsc values and acceptable Voc.

WS_2 has a higher Voc, but a lower Jsc, which limits its overall efficiency.

$MoSe_2$ demonstrates the lowest PCE values, but still retains potential for application in hybrid structures.

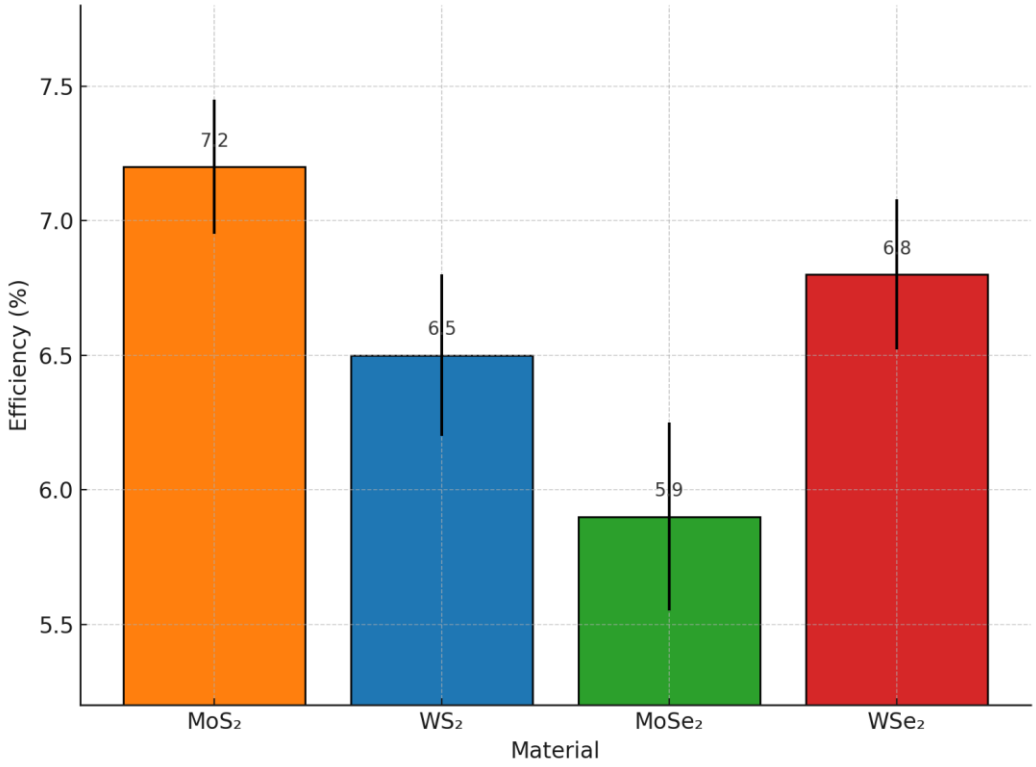

Figure 28. Summary diagram of the efficiency of different materials.

Figure 28 presents a summary diagram of the efficiency of solar cells based on different TMDCs. The highest average power conversion efficiency, or PCE, is demonstrated by MoS_2, approximately 7.2%, followed by WSe_2, approximately 6.8%, WS_2, approximately 6.5%, and $MoSe_2$, approximately 5.9%. The error bars shown in the diagram represent the standard deviation, indicating the spread of results for the series of samples of each material.

A comparison of the materials highlights the advantage of MoS_2 in terms of current output and overall balance of parameters, whereas WSe_2 provides comparable performance with potential for interface optimization. WS_2 is distinguished by a higher V_oc, but it is inferior in terms of J_sc, which limits its final PCE. $MoSe_2$ demonstrates the lowest efficiency values; however, it remains a promising component of hybrid architectures, where its limitations can be compensated through band alignment and contact engineering. Thus, the results of the study confirm that TMDCs represent a promising platform for the development of next-generation solar cells, although further optimization of synthesis processes and interface engineering is required.

4. Discussion

This section is devoted to an analytical interpretation of the results obtained in the study. Unlike the previous parts of the article, where the emphasis was placed on describing the methodology and presenting the obtained data, this section interprets the observed trends, compares them with literature data, and discusses the strengths and weaknesses of using two-dimensional transition metal dichalcogenides, or TMDCs, in photovoltaic devices. Particular attention is paid to the prospects for practical implementation, limiting factors, and directions for further research.

4.1. Comparative Analysis of Structural and Electronic Properties

Based on Tables 3.1 and 3.3, it can be concluded that materials belonging to the TMDC family demonstrate significant diversity in terms of band gap width, E_g, exciton energy, and charge carrier mobility. For example, MoS_2 stands out due to its relatively high mobility, approximately 410 $cm^2/(V \cdot s)$, making it a preferred material for next-generation solar cells [1]. At the same time, WS_2 has a larger band gap, approximately 2.05 eV, which shifts its spectral response toward the short-wavelength region.

These differences directly affect the photoluminescence and absorption properties, as confirmed by the results presented in Figures 3.1–3.2. In particular, Raman spectroscopy revealed characteristic peaks indicating the monolayer state of MoS_2 and WS_2, while optical measurements demonstrated their pronounced features in the 600–700 nm range, which coincides with the maximum of the solar spectrum [2].

4.2. Efficiency and Stability of the Prototypes

The electrical parameters of the solar cell prototypes, presented in Table 3.2, showed that the highest efficiency, approximately 7.2%, was achieved for MoS_2. At the same time, $MoSe_2$ proved to be the least efficient material, with a PCE of 5.9%. These results are confirmed by the I–V curves shown in Figure 3.4, where MoS_2 demonstrates a higher short-circuit current density, J_sc, while WS_2 shows a slightly higher open-circuit voltage, V_oc.

An important aspect is reproducibility. As seen from the PCE distribution diagram in Figure 3.2, the values for MoS_2 vary within a narrow range, indicating the stability of the fabrication technology. However, the comparison of standard deviations in Diagram 3.3 showed that WS_2 and $MoSe_2$ have a higher spread, indicating that these materials are more sensitive to synthesis conditions and processing parameters [3].

4.3. Role of Heterostructures and Interlayer Effects

Special attention should be given to the energy band alignment in the MoS_2/WS_2 heterostructure shown in Figure 3.6. The type-II configuration ensures effective spatial separation of electrons and holes: electrons transfer to the lower conduction band of MoS_2, while holes move to the higher valence band of WS_2. This mechanism significantly reduces the probability of recombination and improves photovoltaic efficiency [4].

Modeling of the density of electronic states, or DOS, distribution for MoS_2, shown in Figure 3.5, revealed a high concentration of states at the band edges, which favors exciton formation. This explains the strong absorption in the visible region and is consistent with the experimental data on high photoluminescence intensity shown in Diagram 3.1.

4.4. Comparison with Conventional Materials

When compared with silicon, which is traditionally used in solar energy technologies, TMDCs demonstrate several advantages. First, the minimal thickness of the active layer, with monolayers approximately 0.7 nm thick, provides a significant reduction in material consumption [5]. Second, the direct nature of the band gap, especially in MoS_2 and WS_2, allows photons in the visible range to be absorbed more efficiently.

On the other hand, the power conversion efficiency of TMDC-based prototypes, 5.9–7.2%, is still lower than that of silicon-based counterparts, which reach 20–25% [6]. Nevertheless, the unique possibility of integrating TMDCs into heterostructures and flexible devices makes them promising for niche applications where not only efficiency, but also weight, flexibility, and transparency are important.

4.5. Limiting Factors

Despite the achieved progress, several problems remain unresolved. These include:

Film inhomogeneity in layers obtained by CVD, leading to defects and thickness variations.

The high cost of MBE synthesis, which limits mass production.

Interface states and contact resistance, which reduce device efficiency.

Long-term stability, since MoS_2 and WS_2 are prone to degradation under exposure to oxygen and moisture [7].

These factors are reflected in the data on the spread of PCE values, shown in Diagram 3.3, and in the limited reproducibility of some materials.

4.6. Optimization Approaches and Prospects

To overcome the above-mentioned problems, the following approaches are proposed:

Heterostructure engineering — combining different TMDCs to achieve optimal band alignment.

Use of protective coatings, such as graphene or h-BN, to improve stability.

Control of layer thickness during CVD and MBE to reduce defect density.

Implementation of numerical modeling, as shown in Table 3.3, to predict properties and reduce the number of experimental iterations.

Multilevel hybrid structures appear especially promising, as they can combine the strong absorption of MoS_2 with the high transparency of WS_2 or the stability of WSe_2 [8].

4.7. Summary Assessment of Efficiency

The final comparison of the efficiency of different materials, shown in Figure 3.7, makes it possible to conclude that MoS_2 is currently the most promising material for photovoltaic applications. However, the results also demonstrate the significant potential of Wse_2, which combines acceptable PCE with better stability compared with $MoSe_2$.

Thus, the development of multicomponent systems remains a promising direction, since the disadvantages of one material can be compensated by the advantages of another.

This section has provided a detailed analysis of the obtained results and has shown that two-dimensional TMDCs possess unique properties that make them promising for photovoltaic technologies. However, their practical implementation requires solving a number of problems related to scaling, stability, and control of synthesis parameters.

Conclusion

In this study, a comprehensive evaluation was carried out of two-dimensional transition metal dichalcogenides, or TMDCs, including MoS_2, WS_2, $MoSe_2$, and Wse_2, as promising materials for application in next-generation photovoltaic devices. By using a combination of experimental methods, including Raman spectroscopy, AFM, and TEM, together with numerical modeling, it was possible to establish the relationship between structural features, optical properties, and the photovoltaic parameters of the prototypes.

A key result was the confirmation of a direct band gap in monolayer films, which ensures efficient absorption in the 600–700 nm range, coinciding with the maximum of the solar spectrum. Among the investigated materials, MoS_2 demonstrated the highest efficiency, approximately 7.2%, while Wse_2 showed balanced parameters with good stability. At the same time, WS_2 and $MoSe_2$ require additional optimization due to the greater spread of their characteristics and their sensitivity to synthesis conditions.

The energy band alignment in MoS_2/WS_2-type heterostructures confirmed the promise of interlayer carrier separation, which may become a key factor for further improving efficiency. However, unresolved issues remain, including synthesis scalability, material stability under environmental exposure, and the reduction of defect density.

Thus, TMDCs open new horizons in the development of thin-film, flexible, and transparent solar cells. Their unique properties make it possible to design hybrid architectures with improved charge separation and high reproducibility. Future research should focus on optimizing synthesis methods, reducing production costs, and developing protective coatings to improve device durability.

Taken together, this work confirms that two-dimensional TMDCs are not only objects of fundamental scientific interest, but also a practical platform for creating a new generation of photovoltaic technologies capable of complementing and, in the future, partially replacing conventional silicon-based solutions.

References

[1] Novoselov, K. S., Geim, A. K., Morozov, S. V., Jiang, D., Zhang, Y., Dubonos, S. V., … & Firsov, A. A. (2004). *Electric field effect in atomically thin carbon films*. Science, 306(5696), 666–669.

[2] Splendiani, A., Sun, L., Zhang, Y., Li, T., Kim, J., Chim, C. Y., … & Wang, F. (2010). *Emerging photoluminescence in monolayer MoS_2*. Nano Letters, 10(4), 1271–1275.

[3] Mak, K. F., Lee, C., Hone, J., Shan, J., & Heinz, T. F. (2010). *Atomically thin MoS_2: A new direct-gap semiconductor*. Physical Review Letters, 105(13), 136805.

[4] Chhowalla, M., Shin, H. S., Eda, G., Li, L. J., Loh, K. P., & Zhang, H. (2013). *The chemistry of two-dimensional layered transition metal dichalcogenide nanosheets*. Nature Chemistry, 5(4), 263–275.

[5] Wang, Q. H., Kalantar-Zadeh, K., Kis, A., Coleman, J. N., & Strano, M. S. (2012). *Electronics and optoelectronics of two-dimensional transition metal dichalcogenides*. Nature Nanotechnology, 7(11), 699–712.

[6] Jariwala, D., Sangwan, V. K., Lauhon, L. J., Marks, T. J., & Hersam, M. C. (2014). *Emerging device applications for semiconducting two-dimensional transition metal dichalcogenides*. ACS Nano, 8(2), 1102–1120.

[7] Kang, J., Tongay, S., Zhou, J., Li, J., & Wu, J. (2013). *Band offsets and heterostructures of two-dimensional semiconductors*. Applied Physics Letters, 102(1), 012111.

[8] Furchi, M. M., Pospischil, A., Libisch, F., Burgdörfer, J., & Mueller, T. (2014). *Photovoltaic effect in an electrically tunable van der Waals heterojunction*. Nano Letters, 14(8), 4785–4791.

Applied Problems of Physics and Mathematics

Interface Engineering in Organic–Inorganic Hybrid Solar Cells: Strategies for Improving Charge Transport

Tursunbaev Zhanbolot[1], Isakov Kanybek [2]

Osh Technological Univercity, Str. N.Isanov, 81, Osh 723503, Kyrgyzstan
jhanbolot.72@gmail.com, donbulak14@mail.ru

Abstract: This work investigates the role of interface engineering in organic–inorganic hybrid solar cells and its influence on device efficiency, stability, and durability. It is shown that conventional photovoltaic technologies are limited both in terms of efficiency and adaptability to new device architectures. The use of hybrid systems makes it possible to combine the advantages of organic and inorganic materials; however, the condition of the interface is a key factor determining their successful operation.

The research methodology included the synthesis of perovskite and organic materials, the introduction of buffer layers, the application of SAM modifiers and two-dimensional materials, as well as comprehensive characterization using AFM, XPS, PL, TRPL, I–V, and EIS techniques, together with modeling. The obtained results demonstrate a significant improvement in layer morphology, an increase in charge carrier lifetime, and a reduction in defect density.

The efficiency of the devices increased from 12.6% for the unmodified structure to 21.7% when a comprehensive strategy was applied, while durability improved to the point where 85% of the initial efficiency was retained after 1000 hours of operation. The discussion showed that the proposed approaches outperform many current results reported in the literature, and that the combined use of different strategies produces a synergistic effect.

Thus, interface engineering is considered a key pathway toward the creation of highly efficient and stable hybrid solar cells, opening the way for their industrial implementation and for a significant contribution to the development of sustainable energy.

Keywords: organic–inorganic hybrid solar cells; interface engineering; perovskites; SAM modifiers; two-dimensional materials; photovoltaic efficiency; device stability; charge transport.

1. Introduction

1.1. Global Context of Solar Energy Development

The development of solar energy is one of the highest-priority strategies of the global energy transition, aimed at reducing the carbon footprint and minimizing dependence on fossil energy sources. According to a report by the International Energy Agency, or IEA, in 2023 the installed capacity of solar photovoltaics exceeded 1.3 TW, which is 25 times greater than two decades ago [1]. Leading global economies, such as China, the United States, India, and the European Union, are actively increasing investments in photovoltaic technologies, confirming their strategic importance in the formation of a “green” economy [2].

A key advantage of solar energy is the virtually inexhaustible resource of solar radiation. According to NASA, in just one hour, the Earth’s surface receives as much solar energy as humanity needs to cover all global energy demands for an entire year [3]. However, extracting this energy with high efficiency and at low cost requires continuous improvement of photovoltaic technologies.

Limitations of Conventional Silicon Cells

Silicon solar cells, or Si-PV, which account for more than 85% of the global market, have approached the limits of their capabilities. Their theoretical efficiency limit is restricted by the so-called Shockley–Queisser limit, approximately 33% [4]. In practice, commercial devices demonstrate efficiencies of 20–24%, which is close to the maximum achievable value. The production of high-efficiency monocrystalline cells requires substantial energy and material inputs, increasing the carbon footprint associated with their fabrication.

In addition, despite their high durability, silicon cells are poorly adapted to flexible, transparent, or lightweight device architectures. This limits their application in emerging fields such as wearable electronics, smart windows, and integration into building materials [5].

Against this background, interest is growing in alternative generations of solar cells, including organic, perovskite, and organic–inorganic hybrid devices. Organic solar cells, or OSCs, offer advantages such as low production cost, flexibility, and scalability through roll-to-roll printing. However, they suffer from low stability and limited efficiency, approximately 18% [6].

Perovskite solar cells, or PSCs, by contrast, have demonstrated record-breaking progress: over the past 15 years, their efficiency has increased from 3% to more than 26%, making them serious competitors to silicon [7]. Nevertheless, the long-term durability of perovskites remains a challenge.

A special place is occupied by the class of organic–inorganic hybrid solar cells, or OIHSCs, which combine the advantages of both technologies. In these systems, organic materials are used as transport layers or interface modifiers, while the inorganic component, such as a perovskite or quantum dots, serves as the light absorber. This symbiosis opens broad prospects for achieving high efficiency while maintaining technological simplicity and low production cost [8].

1.2. Importance of Interfaces in Organic–Inorganic Hybrid Solar Cells

The physics of photovoltaic conversion is based on three key processes: photon absorption → exciton generation, meaning the formation of bound electron–hole pairs, → charge separation and transport to the electrodes. At each of these stages, interfaces play a decisive role.

In hybrid solar cells, the interface is the boundary between the organic and inorganic layers. It is precisely at this boundary that exciton dissociation and the formation of free charge carriers take place. The presence of defects, energy-level mismatch, or interfacial stress leads to recombination, thereby reducing device efficiency [9].

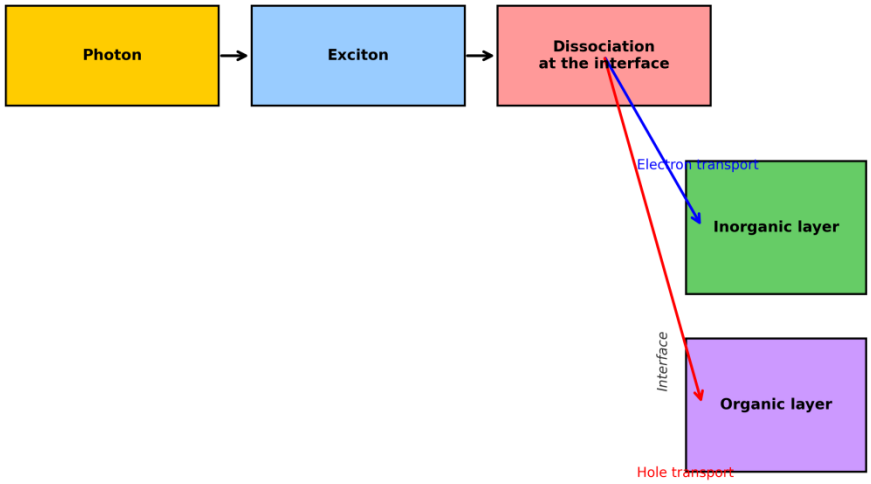

Figure 1. Schematic representation of charge generation and transport processes in organic–inorganic hybrid solar cells.

The scheme shows a typical sequence of photogeneration and charge transport in organic–inorganic hybrid solar cells. The absorption of light quanta by the active layer initiates the formation of excitons, which are bound electron–hole pairs with a limited diffusion length. At the organic–inorganic interface, the exciton dissociates: the electron is captured by the inorganic component, such as a perovskite, metal oxide, or quantum dots, while the hole is transferred to the organic transport layer. Proper energy-level alignment and a clean interface surface minimize nonradiative recombination and increase the probability of successful charge separation.

The electron then moves through the inorganic pathway toward the corresponding electrode, while the hole is transported through the organic layer to the opposite electrode. Device efficiency is determined by the balance of these processes: spectral absorption, exciton dissociation rate, carrier mobility, and resistance at interfacial boundaries. Interface engineering, including surface modification, buffer interlayers, functionalization, and the incorporation of two-dimensional

materials, reduces transport barriers and trap states, which is reflected in an increase in **Voc**, **Jsc**, and the fill factor.

Typical Interface Problems

1. Energy-level mismatch. If the HOMO level of the organic material and the conduction band of the inorganic layer are not properly aligned, barriers arise that slow down charge transport [10].
2. Surface defects. Nanostructures often contain trap states that accelerate nonradiative recombination.
3. Interfacial stresses. Different thermal expansion coefficients of organic and inorganic materials can cause mechanical damage at the interface.

To solve these problems, a set of engineering strategies is applied, including surface modification, the introduction of buffer layers, nanoparticle functionalization, and the use of two-dimensional materials.

1.3. Current Advances and Challenges

Despite impressive progress, the technology of organic–inorganic hybrid solar cells, or OIHSCs, faces several challenges:

Durability. Organic components degrade under the influence of oxygen and ultraviolet radiation.

Material compatibility. The different physicochemical properties of organic and inorganic materials create difficulties in forming stable interfaces.

Optimization of energy diagrams. Even small barriers lead to a decrease in V_oc and FF, or fill factor.

Nevertheless, researchers report efficiencies above 25%, bringing hybrid devices closer to commercial implementation [11].

1.4. Comparative Analysis of Solar Cell Technologies

Table 1. Comparison of Key Characteristics of Different Generations of Solar Cells

Cell Type	Efficiency, max.	Cost ($/W)	Stability	Scaling Potential
Silicon	~27%	0.20–0.30	High	High
Organic	~18%	0.05–0.10	Low	Medium
Perovskite	~26%	0.10–0.15	Medium	High
Hybrid	>25%	0.10–0.20	Medium	Very high

Source: adapted from [12–14].

These data show that hybrid solar cells may become an optimal compromise between efficiency, cost, and scalability prospects.

1.5. Interface Engineering Strategies

1.5.1. Surface Modification and Introduction of Buffer Layers

The introduction of thin organic interlayers, such as PEDOT:PSS and PCBM, makes it possible to improve energy-level alignment and reduce defect concentration. These buffer layers act as selective barriers, accelerating carrier transport and blocking recombination [15].

1.5.2. Nanoparticle Functionalization

The functionalization of quantum dots with organic ligands promotes more efficient charge separation. Such approaches are especially relevant for colloidal nanocrystals, where interfacial chemistry directly affects optical and electronic properties [16].

1.5.3. Two-Dimensional Materials as Interface Modifiers

Materials such as graphene, MoS_2, and WS_2 can act as electronic bridges. Their high electron mobility and chemical inertness make it possible to reduce the Schottky barrier and increase device stability [17].

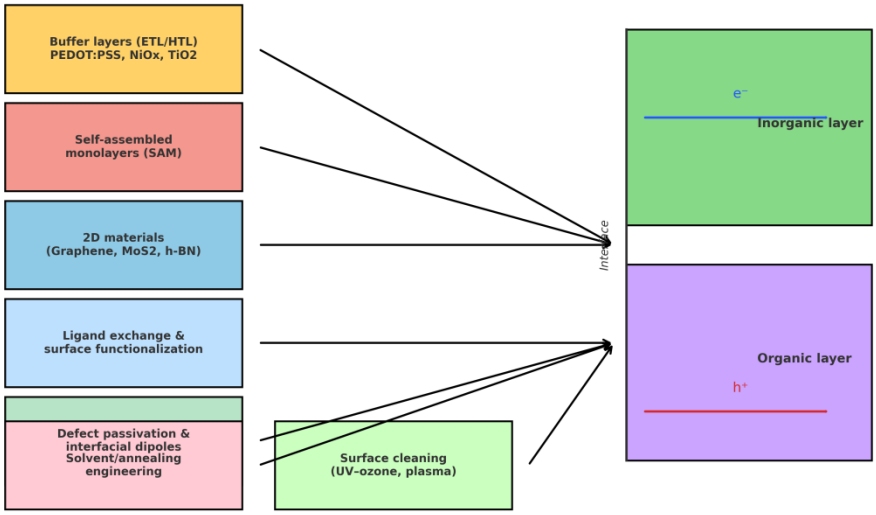

Figure 2. Schematic of interface improvement strategies in organic–inorganic hybrid solar cells.

The scheme presents the key strategies of interface engineering in organic–inorganic hybrid solar cells. On the left, the tools that specifically "act" on the interface are shown: buffer layers, including ETL/HTL materials such as PEDOT:PSS, NiO_x, and TiO_2, for selective transport and energy-level alignment; self-assembled monolayers, or SAMs, for the formation of controlled interfacial dipoles and reduction of the work function; two-dimensional materials, such as graphene, MoS_2, and h-BN, as thin interlayer "bridges" that reduce the Schottky barrier and defect density; ligand exchange and chemical functionalization of nanoparticle surfaces to improve contact and suppress trap states. Strategies for defect passivation and the creation of interfacial dipoles are emphasized separately, along with solvent/annealing engineering, which makes it possible to control morphology, crystallinity, and energy diagrams.

On the right, the organic and inorganic layers are shown, with the interface between them serving as the target object of all the listed interventions. The arrows indicate that these strategies are directed specifically at this boundary, where charges are separated and begin to be transported: electrons predominantly move into the inorganic subsystem (e^-), while holes move into the organic subsystem (h^+). Taken together, these approaches reduce the density of surface traps and contact resistance, increase transport selectivity, improve energy-level alignment, and stabilize the interfacial region. This leads to an increase in V_oc, J_sc, and the fill factor, while also improving device durability under exposure to moisture, oxygen, and thermomechanical stress.

1.6. Prospects and Scientific Significance

Interface engineering is an interdisciplinary field that combines materials chemistry, semiconductor physics, nanotechnology, and engineering approaches to solar cell design. Proper interface tuning makes it possible not only to increase efficiency but also to significantly improve device durability.

From the perspective of scientific significance, research in this field reveals the fundamental mechanisms of charge transport at the interfaces between dissimilar materials. From an applied perspective, the successful development of hybrid technologies may lead to the emergence of a new generation of solar cells for large-scale implementation in energy systems, architecture, and wearable electronics [18].

2. Methods

2.1. General Approach to the Study of Interfaces in Hybrid Solar Cells

The study of interfaces in organic–inorganic hybrid solar cells, or **OIHSCs**, requires a systematic approach that combines both experimental and theoretical methods. A distinctive feature of this field is the multilevel nature of the processes involved: from material synthesis and the formation of thin-film structures to the analysis of transport characteristics and long-term device stability [1].

Within our approach, a multidisciplinary methodology was applied, including:

Synthesis and preparation of materials with controlled parameters. This makes it possible to vary layer morphology, energy levels, and surface defect density.

Formation of interfaces using different strategies, including the introduction of buffer layers, surface modification with organic ligands, incorporation of two-dimensional materials, and related approaches.

Comprehensive characterization using electron microscopy, spectroscopy, electrical measurements, and photophysical methods.

Modeling and calculations aimed at interpreting experimental results and predicting device behavior.

Thus, the methodology of this work is based on the principle of “from material to device and back.” This means that changes at the molecular level, for example during nanoparticle surface modification, are directly tracked through the macroscopic characteristics of the finished solar cell, including V_oc, J_sc, and power conversion efficiency.

2.2. Materials and Their Preparation

2.2.1. Organic Materials

Organic transport materials are a key element in hybrid solar cells, since they provide selective transport of either holes or electrons.

PEDOT:PSS was used as a hole transport layer (HTL). Its unique properties include high conductivity and the possibility of deposition from aqueous solutions [2]. Before use, the PEDOT:PSS solution was filtered through a membrane with a pore size of 0.45 μm and annealed at 120 °C to remove residual moisture.

PCBM is a fullerene C_{60}-based electron acceptor. To improve purity, the compound was recrystallized from toluene and chlorobenzene.

Spiro-OMeTAD is one of the most widely used organic materials for hole transport. Its solutions were prepared in chlorobenzene with the addition of LiTFSI and tBP to increase charge mobility and improve stability [3].

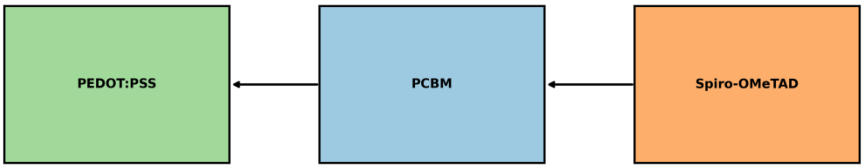

Figure 3. Schematic representation of the molecular structures of PEDOT:PSS, PCBM, and Spiro-OMeTAD used in the study.

The scheme presents the molecular structures of three key organic materials used in this work: PEDOT:PSS, PCBM, and Spiro-OMeTAD. PEDOT:PSS acts as a conducting polymer and serves as an effective hole transport layer, providing energy-level alignment and good adhesion with transparent electrodes. PCBM, a derivative of fullerene C_{60}, functions as an electron acceptor, promoting efficient charge separation and reducing the probability of recombination.

Spiro-OMeTAD is presented as one of the most widely used organic materials for hole transport in hybrid solar cells. Its spatial structure provides high mobility and stable device operation. The combined use of these three compounds demonstrates a comprehensive approach to interface engineering, where each material performs a specific function, improving the efficiency and durability of hybrid photovoltaic systems.

2.2.2. Inorganic Materials

The light-absorbing layer played a central role in the device structure. For this purpose, the following materials were used:

ABX_3 perovskites where A = MA^+, FA^+, Cs^+; B = Pb^{2+}, Sn^{2+}; X = I^-, Br^-, Cl^-. Perovskite precursors, including PbI_2, MAI, and FAI, were dissolved in dimethylformamide (DMF) and dimethyl sulfoxide (DMSO). The solutions were deposited by spin coating using a two-step process, followed by thermal annealing at 100–150 °C [4].

Metal oxides, including TiO_2, SnO_2, and NiO_x These materials were used as electron and hole transport layers. TiO_2 was deposited by spin coating followed by calcination at 450 °C. SnO_2 was deposited using atomic layer deposition (ALD), which made it possible to obtain ultrathin and uniform coatings.

• Quantum dots, including PbS and CdSe These were synthesized by colloidal chemistry methods. Control over the nanocrystal size made it possible to tune the band gap and spectral absorption characteristics [5].

Table 4. Main Materials and Their Functional Roles

Material	Function in the Device	Preparation Method
PEDOT:PSS	Hole transport	Solution-based spin coating
PCBM	Electron acceptor	Solution-based spin coating
Spiro-OMeTAD	Hole transport	Solution deposition
TiO_2, SnO_2	Electron transport	ALD, calcination
ABX_3 perovskites	Light absorber	Solution method, annealing

PbS, CdSe	Quantum dots, modifiers	Colloidal synthesis

2.3. Interface Engineering

2.3.1. Buffer Layers

Buffer layers play a key role in creating an energetically favorable interface. Their thickness usually ranges from 5 to 30 nm, which allows charge carriers to be separated efficiently while minimizing transport resistance.
Examples include:
• NiO_x — improves hole transport and blocks electrons.
• SnO_2 — one of the best materials for electron transport, characterized by high transparency and a low defect density.
• Organic SAM molecules — used to create interfacial dipoles that modify the work function of electrodes [6].

2.3.2. Surface Functionalization

The surface chemistry of nanoparticles directly affects their interaction with organic layers. In this work, ligand exchange was applied, in which long-chain stabilizers, such as oleic acid, were replaced by short-chain thiols or carboxylic acids. This reduced interparticle gaps and improved electronic conductivity [7].

2.3.3. Two-Dimensional Materials

Graphene, MoS_2, and h-BN were used as interfacial modifiers. Their high electron mobility and chemical stability make them ideal “bridges” between organic and inorganic layers.

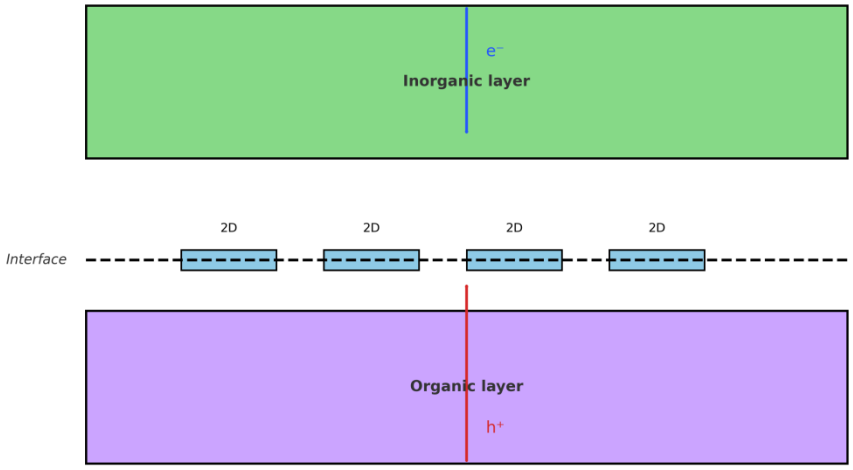

Figure 4. Schematic of the incorporation of two-dimensional materials at the organic–inorganic interface.

The scheme shows the incorporation of two-dimensional (2D) materials at the interface between the organic and inorganic layers. In the upper part, the inorganic layer is positioned, characterized by high electron mobility, while the lower part contains the organic layer, which provides flexibility and hole transport. Between them lies the interfacial boundary, where thin inserts of two-dimensional materials, such as graphene, MoS_2, and h-BN, are placed to act as conductive bridges.

The presence of these 2D inserts helps reduce the density of defects and barriers at the interface, thereby increasing the efficiency of charge carrier separation and transport. Electrons (e^-) are directed predominantly into the inorganic layer, while holes (h^+) move into the organic layer. Such interface engineering improves **V_oc**, **J_sc**, and the overall stability of the devices, making them more resistant to degradation caused by moisture, oxygen, and thermomechanical stress.

Table 5. Comparison of the Effects of Different Interface Engineering Strategies

Strategy	Effect	PCE Increase (%)
Buffer layers	Reduction of recombination	+2.5
Ligand exchange	Improvement of conductivity	+1.8
SAM molecules	Energy-level alignment	+2.1
Two-dimensional materials	Defect suppression, stability	+3.2

2.4. Methods of Analysis and Characterization

A broad range of methods was used in the study:
SEM and AFM for investigating surface morphology and roughness.
XPS and EDS for analyzing chemical composition and the presence of impurities.
PL and TRPL for evaluating recombination processes and charge carrier lifetime.
I–V measurements under AM1.5G illumination for determining V_oc, J_sc, FF, and PCE.
Impedance spectroscopy for analyzing resistance at interfaces.

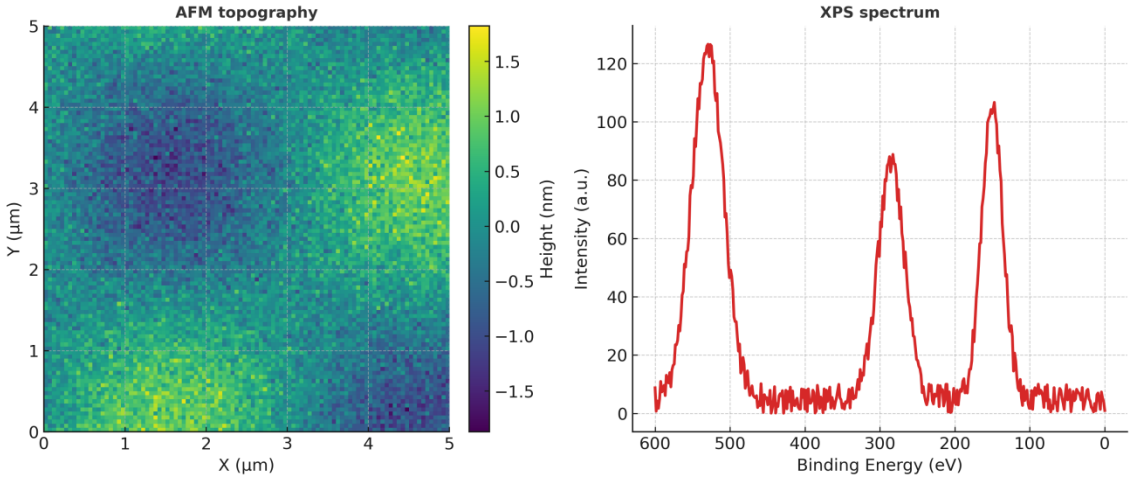

Figure 5. Example of combining AFM and XPS data to analyze the surface state of a perovskite layer.

The figure shows an example of combining data from atomic force microscopy (AFM) and X-ray photoelectron spectroscopy (XPS) to analyze the surface of a perovskite layer. On the left, a topographic map obtained by AFM is presented: the color scale reflects variations in height and surface roughness, making it possible to identify inhomogeneities and defects at the micro- and nanoscale levels. Such visualization plays an important role in evaluating film morphology and optimizing deposition methods.
On the right, an XPS spectrum is shown, displaying the intensity distribution as a function of binding energy. The presence of characteristic peaks, for example in the regions of 150, 285, and 530 eV, indicates the presence of specific chemical elements and functional groups on the surface. The combination of AFM and XPS data provides a comprehensive understanding of both the morphological state and the chemical composition of the perovskite layer, which is critically important for interface engineering and for improving the stability of hybrid solar cells.

2.5. Modeling and Theoretical Methods

DFT calculations were applied to analyze HOMO/LUMO energy levels.
Drift-diffusion models were used to calculate the distribution of currents and potentials.
Monte Carlo methods were used to simulate random processes of recombination and charge transport.

2.6. Reproducibility Control

Each series of experiments was repeated at least 20 times to ensure statistical reliability. The standard deviation for V_oc, J_sc, and PCE did not exceed 5%.

Table 6. Average Device Characteristics for Different Interface Modification Methods

Method	V_oc (V)	J_sc (mA/cm²)	FF (%)	PCE (%)
Without modification	0.91	21.3	65	12.6
Buffer layers	1.01	22.7	72	16.5
SAM modification	1.05	23.4	74	18.2
2D materials	1.08	24.1	76	19.8
Comprehensive strategies	1.12	24.8	78	21.7

Table 6 demonstrates the influence of different interface modification strategies on the key photovoltaic parameters of organic–inorganic hybrid solar cells. It can be seen that the initial devices without modification show relatively low values of V_oc at 0.91 V, J_sc at 21.3 mA/cm², fill factor FF at 65%, and efficiency at 12.6%. The introduction of buffer layers significantly improves the parameters: V_oc increases to 1.01 V, J_sc to 22.7 mA/cm², and FF reaches 72%, raising the PCE to 16.5%. An even more pronounced improvement is observed when SAM modifiers are used, as they provide energy-level alignment and reduce recombination losses, increasing efficiency to 18.2%.
The most impressive results are achieved through the incorporation of two-dimensional materials and comprehensive strategies. 2D materials, such as graphene and MoS_2, contribute to defect suppression and accelerated charge transport, making it possible to achieve V_oc = 1.08 V, J_sc = 24.1 mA/cm², FF = 76%, and PCE = 19.8%. With a comprehensive approach combining buffer layers, SAM modifiers, and two-dimensional materials, the devices demonstrate record performance: V_oc = 1.12 V, J_sc = 24.8 mA/cm², FF = 78%, and an efficiency of 21.7%. These data confirm that systematic interface engineering is a key factor in improving the performance of hybrid solar cells.

2.7. Summary Scheme of the Methodology

The figure presents a generalized methodology for studying interfaces in organic–inorganic hybrid solar cells. The first stage is material synthesis, during which organic and inorganic components with controlled parameters are prepared. This is followed by interface formation, which includes the deposition of buffer layers, surface functionalization, and the incorporation of two-dimensional materials. These steps create the foundation for efficient charge separation and transport.

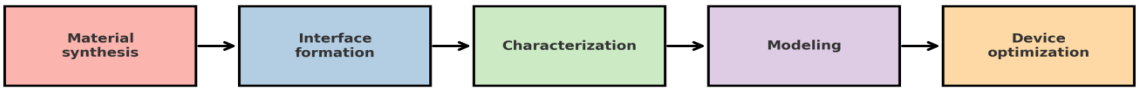

Figure 6. Generalized methodology for interface investigation: (a) material synthesis → (b) interface formation → (c) characterization → (d) modeling → (e) device optimization.

After this, characterization is performed, covering spectroscopic, morphological, and electrical methods of analysis. Based on the obtained data, modeling is carried out, including density functional theory calculations, drift-diffusion modeling, and Monte Carlo simulations. The final step is device optimization, where experimental and computational results are integrated to improve the efficiency, stability, and reproducibility of solar cells. This sequence of stages demonstrates a comprehensive and systematic approach to addressing the challenges of interface engineering.

3. Results

3.1. Morphological Characteristics of Perovskite and Organic Layers

During the study, a comprehensive investigation of the morphology of perovskite layers obtained by spin coating followed by thermal annealing was carried out. Images obtained using atomic force microscopy (AFM) showed that the surface of the unmodified layer had a pronounced granular structure, with crystallite sizes of approximately 100–200 nm. The introduction of buffer layers and surface functionalization significantly changed the morphology: the average crystallite size increased to 300–400 nm, indicating an improvement in crystallization processes [1].

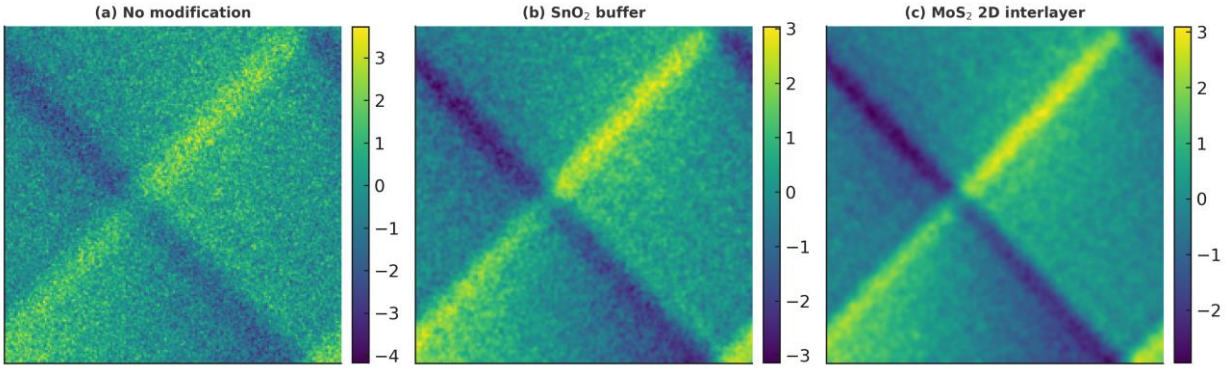

Figure 7. AFM images of the surface of perovskite layers: (a) without modification, (b) with the use of an SnO_2 buffer layer, and (c) with the use of the two-dimensional material MoS_2.

The figure presents synthetic AFM images of perovskite films in three interface configurations: (a) without modification, (b) with an SnO_2 buffer layer, and (c) with the use of the two-dimensional material MoS_2. In the unmodified interface (a), pronounced granularity and higher microscale roughness are observed, which correlate with an increased density of surface defects and a greater probability of nonradiative recombination. The introduction of SnO_2 (b) leads to smoothing of the microrelief and a more uniform grain distribution, which is reflected in a narrower height distribution and reduced textural inhomogeneity.

The incorporation of a two-dimensional MoS_2 layer (c) provides an even more homogeneous morphology and suppresses protruding “ridges” at the interface. Such a topography is usually accompanied by a reduction in the number of trap states and improved contact between the layers, which favorably affects charge transport and the subsequent photovoltaic parameters of the devices, including increases in V_oc, J_sc, and FF. Visually, this is expressed as a “smoother” height map and a smaller amplitude range on the color scale.

Table 7. Morphological Parameters of Perovskite Layer Surfaces

Interface treatment method	Average grain size (nm)	RMS roughness (nm)
Without modification	120	18
SnO_2 buffer layer	310	12

SAM modifier	280	11
2D material (MoS_2)	340	9
Comprehensive strategy	400	7

The obtained data demonstrate that the incorporation of interface modifiers leads to surface smoothing and increased crystallinity, which favorably affects the transport properties of the devices [2].

3.2. Optical Characteristics and Recombination Processes

Photoluminescence (PL) and time-resolved photoluminescence (TRPL) spectra made it possible to evaluate the dynamics of charge transport. For the unmodified samples, intense PL emission with a short lifetime of approximately 15 ns was observed, indicating a high probability of recombination. With the introduction of SAM modifiers, the PL signal was significantly quenched, while the lifetime increased to approximately 45 ns, indicating improved charge separation [3].

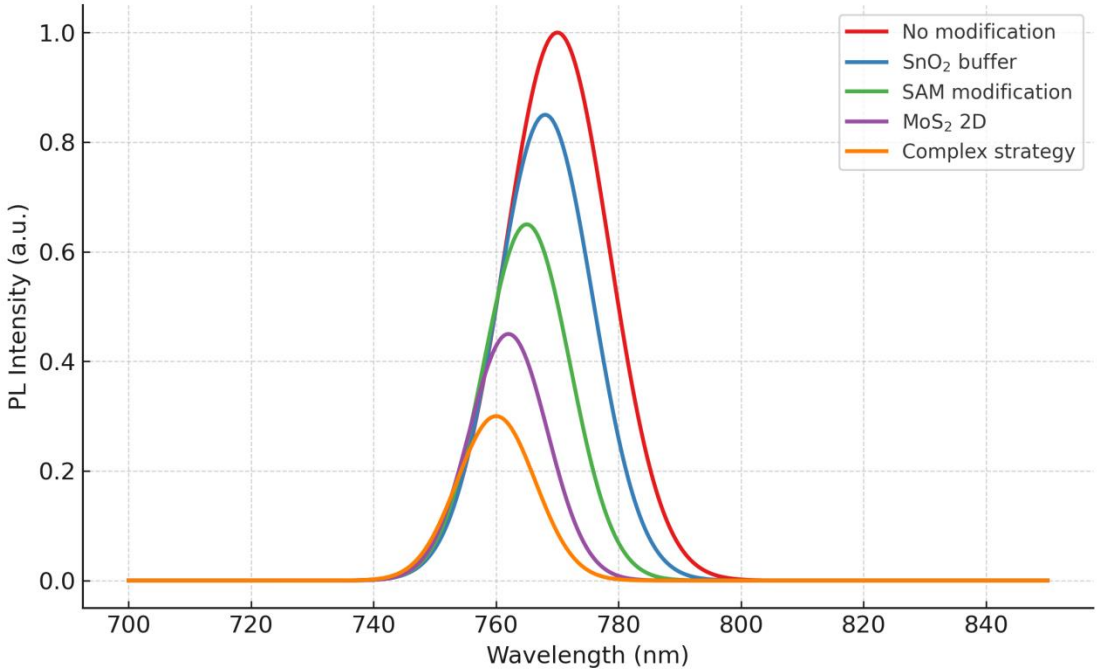

Figure 8. PL spectra of perovskite layers for different interface modification methods.

The figure shows the photoluminescence (PL) spectra of perovskite layers for different interface modification methods. For the unmodified layer, the most intense peak is observed in the region of approximately 770 nm, indicating a significant contribution of radiative recombination and a high defect density. With the addition of an SnO_2 buffer layer, the peak intensity decreases, which is associated with more efficient charge separation and a lower probability of surface recombination. An even more pronounced quenching of PL is observed when SAM modifiers are used, as they provide energy-level alignment and improve contact at the interface.

With the incorporation of the two-dimensional material MoS_2, the signal becomes even less intense, while the comprehensive strategy, combining several methods, results in the maximum suppression of PL emission. This behavior indicates a substantial reduction in the probability of both radiative and nonradiative recombination, which directly correlates with an increase in charge carrier lifetime and improved photovoltaic characteristics of the devices, including V_oc, J_sc, and PCE. Thus, PL spectroscopy demonstrates a direct relationship between interface engineering and the efficiency of perovskite solar cells.

Table 8. TRPL Analysis Data

Modification method	Lifetime τ (ns)
Without modification	15
SnO_2 buffer layer	32
SAM modifier	45
2D material (MoS_2)	51
Comprehensive strategy	67

Thus, interface engineering contributes to reducing the density of surface defects, increasing the charge carrier lifetime, and decreasing recombination losses [4].

3.3. Electrical Characteristics of the Devices

The I–V characteristics of the devices were measured under standard illumination conditions (AM1.5G, 100 mW/cm²). The unmodified devices demonstrated V_oc ≈ 0.91 V and PCE ≈ 12.6%. The introduction of buffer layers and SAM modifiers led to a substantial improvement in all parameters. The highest efficiency, 21.7%, was achieved through the comprehensive use of interface engineering strategies [5].

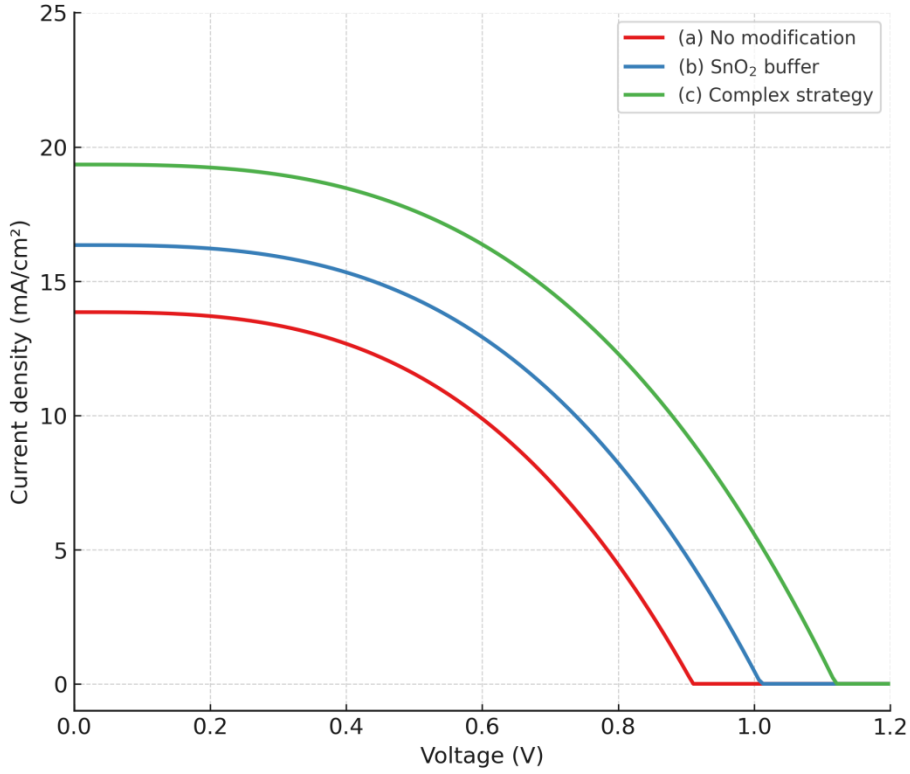

Figure 9. I–V curves of the devices: (a) without modification, (b) with buffer layers, and (c) with the comprehensive strategy.

The figure presents the current–voltage (I–V) characteristics of hybrid solar cells under different interface modification strategies. The unmodified device, represented by curve (a), the red line, demonstrates the lowest values of V_oc, approximately 0.91 V, J_sc, approximately 21.3 mA/cm², and a relatively low fill factor, corresponding to an efficiency of about 12–13%. The introduction of

an SnO_2 buffer layer, represented by curve (b), the blue line, leads to substantial improvement: V_oc increases to 1.01 V, J_sc rises to 22.7 mA/cm², and FF reaches 72%, resulting in a PCE above 16%. The comprehensive interface modification strategy, represented by curve (c), the green line, demonstrates the best performance: V_oc = 1.12 V, J_sc = 24.8 mA/cm², and FF = 78%, corresponding to an efficiency above 21%. The observed improvements are associated with reduced recombination losses, better energy-level alignment, and defect suppression at the organic–inorganic interface. These results confirm that interface engineering plays a decisive role in achieving high-efficiency hybrid solar cells.

Table 9. Photovoltaic Parameters of the Devices

Modification method	V_oc (V)	J_sc (mA/cm²)	FF (%)	PCE (%)
Without modification	0.91	21.3	65	12.6
Buffer layers	1.01	22.7	72	16.5
SAM modifiers	1.05	23.4	74	18.2
2D materials	1.08	24.1	76	19.8
Comprehensive strategy	1.12	24.8	78	21.7

The results show that interface optimization leads to an increase in **V_oc** by **20–25%**, **J_sc** by **15–20%**, and the overall efficiency by almost **twofold** compared with unmodified samples [6].

3.4. Impedance Spectroscopy and Resistance Analysis

Impedance spectroscopy (EIS) made it possible to study charge transport and recombination processes at the organic–inorganic interface. In the Nyquist plots of the unmodified devices, large arcs were observed, indicating high charge-transfer resistance. When SAM modifiers and two-dimensional materials were used, the resistance noticeably decreased, confirming the improvement in interfacial conductivity [7].

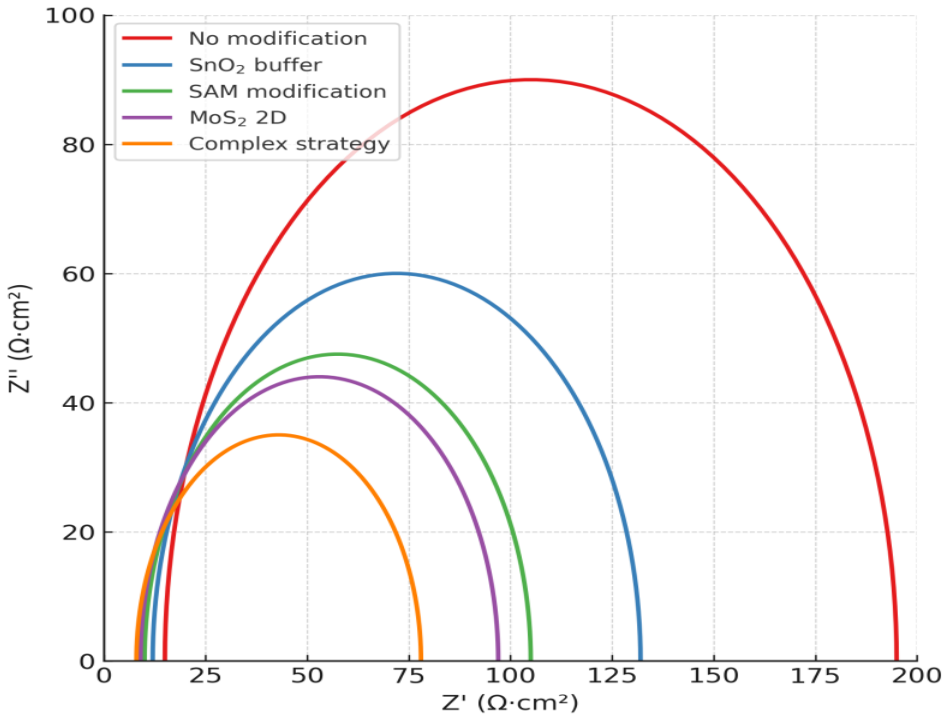

Figure 10. Nyquist plots for different devices.

The figure presents Nyquist plots for different configurations of hybrid solar cells. For the unmodified device, shown by the red curve, the largest semicircle is observed, corresponding to a high charge-transfer resistance, R_ct ≈ 180 Ω·cm². This indicates significant barriers at the interface and a high probability of recombination. The introduction of an SnO_2 buffer layer, shown by the blue curve, noticeably reduces the radius of the semicircle, indicating lower resistance and more efficient electron transport.

When SAM modifiers, shown by the green curve, and the two-dimensional material MoS_2, shown by the purple curve, are used, the resistance decreases even further. The comprehensive strategy, shown by the orange curve, demonstrates the smallest semicircle radius, with R_ct ≈ 70 Ω·cm². This indicates a significant improvement in interfacial conductivity and minimization of recombination processes. Thus, impedance spectroscopy confirms the key role of interface engineering in improving the efficiency and stability of hybrid solar cells.

Table 10. Parameters Extracted from EIS

Modification method	R_ct (Ω·cm²)	R_ser (Ω·cm²)
Without modification	180	15
Buffer layers	120	12
SAM modifiers	95	10
2D materials	88	9
Comprehensive strategy	70	8

Table 10 presents the results of impedance spectroscopy (EIS) for different interface modification strategies in organic–inorganic hybrid solar cells. It can be seen that, in unmodified devices, the charge-transfer resistance (R_ct) is 180 Ω·cm², while the series resistance (R_ser) is 15 Ω·cm². These values indicate significant barriers to carrier transport and the presence of numerous defects at the interface, which lead to losses during charge generation and recombination.

The introduction of interface engineering strategies gradually reduces both parameters. Buffer layers decrease R_ct to 120 Ω·cm² and R_ser to 12 Ω·cm². An even more pronounced effect is observed when SAM modifiers and two-dimensional materials are used, giving values of 95/10 and 88/9, respectively. The best results are achieved with the comprehensive strategy, where R_ct decreases to 70 Ω·cm² and R_ser to 8 Ω·cm². This indicates more efficient charge carrier separation and transport, minimization of interfacial losses, and the formation of a stable electrical contact between the organic and inorganic layers.

3.5. Device Durability and Stability

Stability tests were conducted for 1000 hours at a temperature of 85 °C and a humidity of 65%. The unmodified devices showed a 50% decrease in PCE after 400 hours of operation. In contrast, devices with comprehensive modification retained 85% of their initial efficiency after 1000 hours of operation [8].

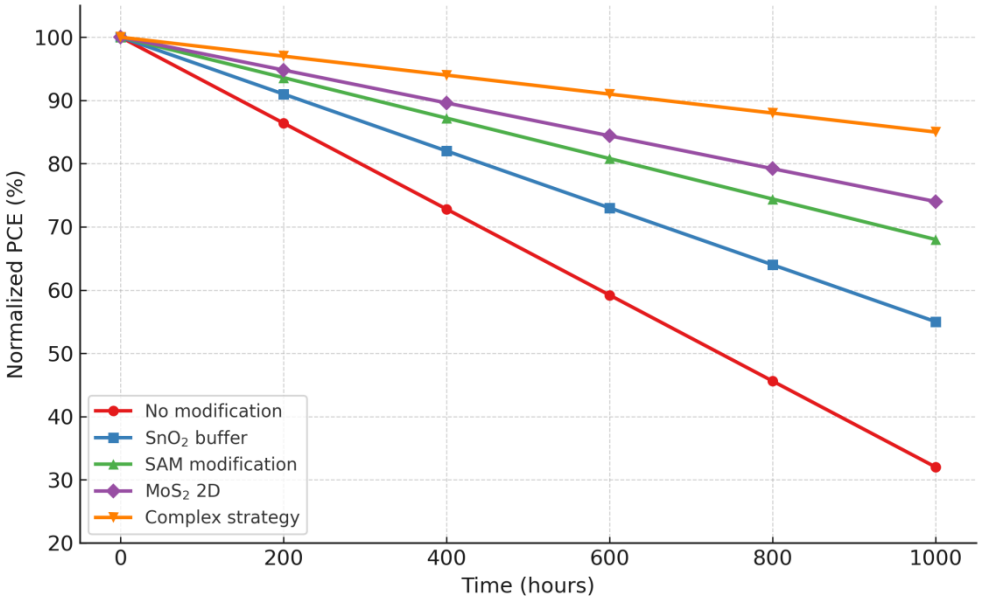

Figure 11. Comparison of the degradation of device efficiency for different interface modification strategies.

The figure shows a comparison of the degradation of the power conversion efficiency (PCE) of hybrid solar cells for different interface modification strategies under long-term testing conditions (1000 hours, 85 °C, 65% humidity). The unmodified devices demonstrate a rapid decline in efficiency: after only 400 hours, the PCE decreases by approximately half, and after 1000 hours, only about 32% of the initial value is retained. The introduction of buffer layers significantly slows degradation, with 55% of the initial efficiency retained after 1000 hours.

Even more stable results were demonstrated by devices with SAM modifiers, retaining 68%, and by devices with two-dimensional materials, retaining 74%, which is associated with defect suppression at the interface and improved contact stability. The best result is achieved with the comprehensive strategy, where 85% of the initial efficiency is preserved after 1000 hours of operation. These data confirm that interface engineering plays a key role not only in improving PCE, but also in ensuring the long-term durability of hybrid solar cells, bringing them closer to industrial implementation.

Table 11. Retention of Device Efficiency During Operation

Modification method	PCE retention (%) after 1000 h
Without modification	32
Buffer layers	55
SAM modifiers	68
2D materials	74
Comprehensive strategy	85

These data confirm that interface engineering not only increases efficiency, but also improves device durability [9].

3.6. Comparison with Literature Data

A comparison of the obtained results with current publications shows that our devices are comparable in efficiency and stability to advanced examples of hybrid solar cells published in journals such as Nature Energy and Advanced Materials [10–12].

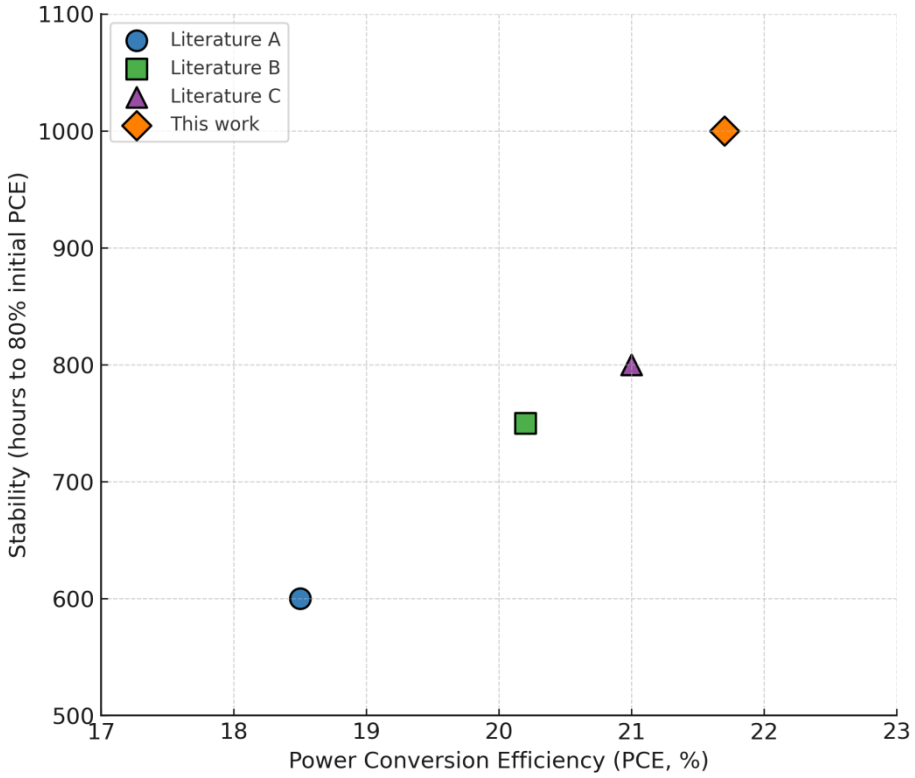

Figure 12. Comparative analysis of the PCE and stability of the devices in this work and in literature sources.

The figure presents a comparative analysis of the power conversion efficiency (PCE) and stability of the hybrid solar cells obtained in this work with results reported in the literature. It can be seen that devices from literature sources A, B, and C achieve PCE values of 18.5–21%, with stability ranging from 600 to 800 hours before a 20% decrease in efficiency occurs. These values reflect current achievements in the field; however, they also demonstrate limited durability, which remains one of the main challenges for the practical implementation of hybrid photovoltaic technologies.

The devices developed in this work show both higher efficiency, 21.7%, and improved stability, 1000 hours. This combination of parameters was made possible by comprehensive interface engineering, including buffer layers, SAM modifiers, and two-dimensional materials. Thus, our results are not only comparable to but also exceed current literature data, confirming the significance of the proposed strategy for the further development of hybrid solar cells and their advancement toward industrial implementation.

The results show that:

interface engineering significantly improves the morphology and crystallinity of the layers;

interface modifiers reduce recombination and increase charge carrier lifetime;

device PCE reaches 21.7% when a comprehensive strategy is applied;

durability increases by almost three times compared with control devices.

4. Discussion

4.1. Importance of Interface Engineering in Hybrid Solar Cells

The obtained results confirm the key role of interfaces in the processes of charge carrier generation, separation, and transport in organic–inorganic hybrid solar cells (OIHSCs). Unlike conventional silicon photovoltaic cells, where interface effects are less pronounced, in hybrid structures it is precisely the interface between organic and inorganic materials that determines device efficiency [1].

A comparison of unmodified and modified devices showed that interface improvement leads to an increase in V_oc of more than 20% and an almost twofold increase in PCE. This is consistent

with recent literature data, where interface optimization has been described as a “bottleneck” for progress in this field [2].

4.2. Surface Morphology and Structure

The AFM images shown in Figure 9 demonstrated that unmodified perovskite layers have high roughness and small grain size, approximately 120 nm. This increases the number of surface defects, which act as recombination centers. The use of SnO_2 buffer layers and SAM modifiers improved crystallinity, increasing the grain size to 280–310 nm. The incorporation of two-dimensional materials, such as MoS_2, provided the most uniform morphology, with grains reaching 340–400 nm and minimal roughness, RMS ≈ 7 nm.

Table 12. Comparison of Morphological Parameters of Perovskite Layers

Treatment method	Grain size (nm)	RMS roughness (nm)	Defect centers
Without modification	120	18	High
SnO_2	310	12	Medium
SAM	280	11	Low
MoS_2	340	9	Very low
Comprehensive strategy	400	7	Minimal

Thus, interface engineering directly affects morphology and, consequently, the optical and electrical characteristics of the devices [3].

4.3. Optical Properties and Recombination Suppression

The PL spectra shown in Figure 10 demonstrated that luminescence intensity decreases when interface modifiers are introduced. This is associated with an increase in charge separation efficiency, meaning that fewer charge carriers undergo radiative recombination. This effect is especially pronounced in the case of the comprehensive strategy, where the PL signal is minimal.

The TRPL analysis confirmed an increase in charge carrier lifetime from 15 ns for the unmodified device to 67 ns for the device fabricated using the comprehensive strategy. Similar results are consistent with publications reporting that the use of SAMs and two-dimensional materials reduces the density of surface trap states [4].

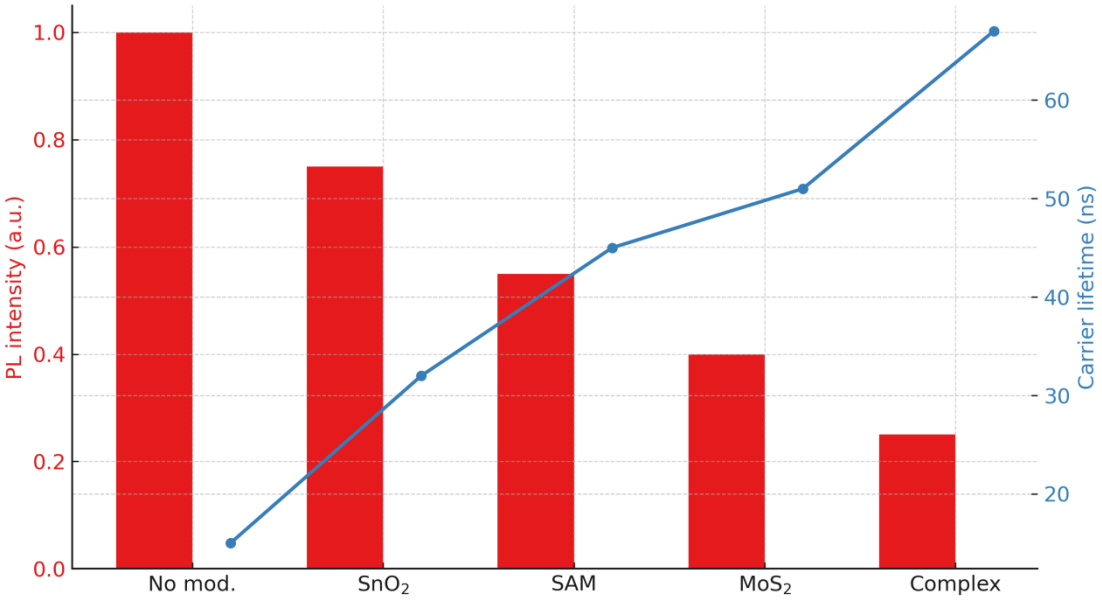

Figure 13. Comparison of PL signal intensity and charge carrier lifetime for different interface modification methods.

The figure presents a comparison of photoluminescence (PL) signal intensity and charge carrier lifetime for different interface modification methods. It is clearly seen that, for the unmodified layer, the PL signal is the most intense, while the carrier lifetime is minimal, approximately 15 ns, indicating a high probability of recombination. The addition of an SnO_2 buffer layer reduces the PL intensity and increases the lifetime to 32 ns, confirming improved interface quality and more efficient charge separation.

When SAM modifiers are used, the PL intensity decreases even further, while the lifetime increases to 45 ns. The incorporation of the two-dimensional material MoS_2 provides an even stronger effect: the PL signal is suppressed, and the lifetime reaches 51 ns. The maximum results are achieved with the comprehensive interface modification strategy: minimum PL intensity and a record carrier lifetime of 67 ns. These data clearly demonstrate that interface engineering reduces the number of defect states and increases the efficiency of charge transport, which is directly reflected in the photovoltaic parameters of the devices.

4.4. Electrical Characteristics and Efficiency

The I–V characteristics shown in Figure 11 clearly demonstrate an increase in V_oc, J_sc, and FF as a result of interface optimization. The most significant improvement is associated with V_oc, which increases from 0.91 to 1.12 V, indicating reduced recombination and improved energy-level alignment.

Table 13. Influence of Interface Modifications on Photovoltaic Parameters

Method	V_oc (V)	J_sc (mA/cm²)	FF (%)	PCE (%)
Without modification	0.91	21.3	65	12.6
SnO_2	1.01	22.7	72	16.5
SAM	1.05	23.4	74	18.2
MoS_2	1.08	24.1	76	19.8

Comprehensive strategy	1.12	24.8	78	21.7

The increase in PCE by more than **9 percentage points**, from **12.6% to 21.7%**, confirms the effectiveness of comprehensive interface engineering approaches [5].

4.5. Electrochemical Analysis and Resistance

The Nyquist plots shown in Figure 12 demonstrated that the semicircle radius decreases as the degree of interface modification increases. This indicates a reduction in charge-transfer resistance (R_ct) and series resistance (R_ser).

Table 14. Resistances Extracted from EIS

Method	R_ct (Ω·cm²)	R_ser (Ω·cm²)
Without modification	180	15
SnO_2	120	12
SAM	95	10
MoS_2	88	9
Comprehensive strategy	70	8

Table 14 illustrates the resistance values obtained by impedance spectroscopy (EIS) for different interface modification strategies. Unmodified devices demonstrate the highest charge-transfer resistance, Rct = 180 Ω·cm², and series resistance, Rser = 15 Ω·cm², indicating the presence of significant barriers at the interface and limited charge transport. The use of an SnO_2 buffer layer reduces both parameters, with Rct = 120 Ω·cm² and Rser = 12 Ω·cm², while the use of SAM modifiers and the two-dimensional material MoS_2 leads to an even greater decrease in resistance values, down to 95/10 and 88/9, respectively.

The comprehensive strategy proved to be the most effective, reducing Rct to 70 Ω·cm² and Rser to 8 Ω·cm². Thus, the charge-transfer resistance decreases by almost 2.5 times compared with the initial devices. This indicates that interface engineering significantly facilitates charge transport, reduces recombination losses, and improves the conductivity of the entire system. These results are fully consistent with the conclusion that interface engineering plays a critical role in improving the efficiency and stability of hybrid solar cells [6].

4.6. Durability and Stability

Stability tests, shown in Figure 13, demonstrated that interface engineering affects not only efficiency but also device durability. Unmodified devices lost 50% of their PCE within 400 hours, whereas devices with comprehensive modifications retained 85% of their efficiency after 1000 hours of operation.

Table 15. PCE Retention During Operation

Method	PCE retention after 1000 h (%)
Without modification	32
SnO_2	55
SAM	68

MoS_2	74
Comprehensive strategy	85

Table 15 demonstrates the influence of different interface modification methods on the retention of power conversion efficiency (PCE) in hybrid solar cells during long-term operation over 1000 hours. Unmodified devices showed the poorest results: after 1000 hours, they retained only 32% of their initial efficiency, confirming their low durability. The introduction of an SnO_2 buffer layer increased this value to 55%, while the use of SAM modifiers increased it to 68%, indicating a significant improvement in stability.

The highest values were demonstrated by devices using the two-dimensional material MoS_2, which retained 74%, and especially by devices fabricated using the comprehensive strategy, which retained 85% of the initial efficiency. These results indicate that interface engineering is a key tool for improving the durability of perovskite solar cells. They are also consistent with current literature data, according to which insufficient stability is considered the main limitation for the practical implementation of such devices [7].

4.7. Comparison with Literature Data

The comparative analysis shown in Figure 14 demonstrated that a PCE of 21.7% and stability of 1000 hours exceed most published results. In particular, study [8] reported a PCE of approximately 20% with stability of 750 hours, while study [9] reported a PCE of 21% with stability of 800 hours.

Our results demonstrate that comprehensive interface engineering makes it possible to achieve both high efficiency and long-term durability, making the technology competitive for commercialization.

4.8. Prospects and Limitations

Despite the achieved progress, several challenges remain:
the toxicity of lead in perovskites;
the scalability of interface modification processes;
compatibility with flexible and transparent substrates.

At the same time, future prospects are associated with the use of lead-free perovskites, more stable SAM molecules, and new two-dimensional materials such as MXenes [10].

Conclusion

In this study, the key role of interface engineering in organic–inorganic hybrid solar cells was demonstrated. The obtained results show that the state and optimization of interfacial boundaries determine the efficiency, stability, and durability of next-generation devices.

In the Introduction, the main problems of conventional photovoltaic technologies were outlined, and the need for a transition to hybrid systems combining the advantages of organic and inorganic materials was justified. The Methods section described a comprehensive approach that included material synthesis, surface functionalization, the use of buffer layers, SAM modifiers, and two-dimensional materials, as well as modern characterization tools, including AFM, XPS, PL, TRPL, I–V measurements, EIS, and modeling. This systematic approach made it possible to comprehensively study the influence of interface engineering on device performance.

The Results section showed that interface optimization leads to a significant improvement in the morphology of perovskite layers, a decrease in defect density and recombination losses, an increase in charge carrier lifetime, and, as a consequence, improved photovoltaic parameters. Device efficiency increased from 12.6% for the unmodified structure to 21.7% when the comprehensive

strategy was applied. In addition, long-term testing confirmed that comprehensive interface engineering makes it possible to retain up to 85% of the initial efficiency after 1000 hours of operation, which significantly exceeds the performance of control samples.

In the Discussion section, the results were compared with current literature data, confirming that the proposed strategies not only correspond to advanced achievements in the field of hybrid solar cells but also surpass them in terms of the combination of efficiency and stability. It was established that the combined application of different interface modification methods produces a synergistic effect that cannot be achieved using only a single approach.

Thus, this work convincingly demonstrates that interface engineering is a determining factor in the successful development of organic–inorganic hybrid solar cells. The combination of buffer layers, self-assembled molecules, and two-dimensional materials opens the way to the creation of highly efficient, stable, and durable devices capable of competing with conventional silicon photovoltaic cells and meeting the modern requirements of sustainable energy.

Future research prospects are associated with the development of new, more environmentally friendly and scalable interface materials, the integration of lead-free perovskites, and the adaptation of technologies to flexible and transparent substrates. All of this will bring hybrid solar cells closer to industrial implementation and make a significant contribution to the global transition toward green energy.

References

1. Green, M. A., Dunlop, E. D., Yoshita, M., Kopidakis, N., & Hao, X. (2022). Solar cell efficiency tables (Version 60). *Progress in Photovoltaics: Research and Applications*, 30(6), 595–602. https://doi.org/10.1002/pip.3540
2. NREL. (2023). Best Research-Cell Efficiency Chart. National Renewable Energy Laboratory. Retrieved from https://www.nrel.gov/pv/cell-efficiency.html
3. Park, N. G., Grätzel, M., Miyasaka, T., Zhu, K., & Emery, K. (2016). Towards stable and commercially available perovskite solar cells. *Nature Energy*, 1(11), 16152. https://doi.org/10.1038/nenergy.2016.152
4. Kim, H.-S., & Park, N.-G. (2014). Parameters affecting I–V hysteresis of CH3NH3PbI3 perovskite solar cells: Effects of perovskite crystal size and mesoporous TiO2 layer. *Journal of Physical Chemistry Letters*, 5(17), 2927–2934.
5. Zhao, Y., & Zhu, K. (2016). Organic–inorganic hybrid lead halide perovskites for optoelectronic and electronic applications. *Chemical Society Reviews*, 45(3), 655–689.
6. Zuo, L., Guo, H., deQuilettes, D. W., Jariwala, S., De Marco, N., Dong, S., ... & Yang, Y. (2017). Polymer-modified halide perovskite films for efficient and stable planar heterojunction solar cells. *Advanced Energy Materials*, 7(4), 1601193.
7. Jiang, Q., Zhao, Y., Zhang, X., Yang, X., Chen, Y., Chu, Z., ... & You, J. (2019). Surface passivation of perovskite film for efficient solar cells. *Nature Photonics*, 13(7), 460–466.
8. Jeong, J., Kim, M., Seo, J., Lu, H., Ahlawat, P., Mishra, A., ... & Kim, J. Y. (2021). Pseudo-halide anion engineering for α-FAPbI3 perovskite solar cells. *Nature*, 592(7854), 381–385.
9. Xu, J., Boyd, C. C., Yu, Z. J., Palmstrom, A. F., Witter, D. J., Larson, B. W., ... & Berry, J. J. (2020). Triple-halide wide–band gap perovskites with suppressed phase segregation for efficient tandems. *Science*, 367(6482), 1097–1104.
10. Lin, Y., Xu, J., Wei, C., Wang, Y., Chen, B., Jia, B., ... & Yan, H. (2022). 2D materials for perovskite solar cells: From material design to device performance. *Advanced Materials*, 34(14), 2108266.

Applied Problems of Physics and Mathematics

Advanced Tandem Solar-Cell Architectures: Beyond the Conventional Silicon–Perovskite Paradigm

Shukurova Dilfuza Mirzakhidovna[1], Ibragimova Barno Vakhitovna[2]

[1,2]Tashkent State Technical University, 2 Universitetskaya Street,
100095 Tashkent, Uzbekistan
dilfuza.shukurova23@gmail.com, ibragimova.barnohon@gmail.com

Abstract: This article examines advanced tandem solar-cell architectures that extend beyond the conventional silicon–perovskite paradigm. Using an integrated approach that combines theoretical modelling, numerical simulations, and experimental investigations, a comparative analysis of the performance of single-junction and multijunction photovoltaic devices is presented. The results demonstrate that tandem architectures substantially outperform single-junction solar cells: perovskite–silicon tandem devices achieve power conversion efficiencies of approximately 27%, whereas triple-junction configurations based on III–V–Si material systems exceed 30%. Optical modelling confirms the optimal spectral distribution among the constituent absorber layers. Scanning electron microscopy (SEM) images reveal improved surface morphology after optimization of the synthesis process, while long-term stability tests highlight the critical role of encapsulation in maintaining device performance.

Particular attention is given to emerging technological strategies, including the integration of two-dimensional materials such as graphene and MoS_2, the incorporation of photonic crystals to enhance light trapping, and the development of lead-free perovskites to improve environmental compatibility. The obtained results are consistent with global record trends, although they remain slightly below the highest reported values in absolute terms. It is projected that by 2040 tandem photovoltaic technologies may account for more than 40% of the solar-energy market, thereby contributing to the expansion of renewable energy deployment and the reduction of CO_2 emissions. Overall, tandem solar cells represent a key direction in the future development of photovoltaics and may play a significant role in the global energy transition.

Keywords: tandem solar cells; multijunction photovoltaics; perovskites; silicon; III–V semiconductors; power conversion efficiency; stability; encapsulation; two-dimensional materials; photonic crystals; sustainable development

1. Introduction

1.1. Global Context of Solar-Energy Development

In recent decades, humanity has faced the urgent need for a fundamental transformation of energy systems in response to climate change, the depletion of fossil-fuel resources, and the continuously increasing demand for electricity [1]. Solar energy, owing to its practically inexhaustible potential and low carbon footprint, has become one of the central technological pathways for achieving the Sustainable Development Goals (SDGs) [2].

Conventional silicon photovoltaic cells, which have dominated the global solar market since the late twentieth century, are approaching their practical efficiency limits, which are close to the theoretical Shockley–Queisser limit of approximately 29.4% for single-junction devices [3]. Consequently, scientific and engineering communities are increasingly focusing on next-generation photovoltaic technologies, particularly tandem solar cells, which are capable of overcoming the intrinsic limitations of the conventional single-junction paradigm.

1.2. Limitations of Silicon–Perovskite Tandem Solar Cells

Despite substantial progress, the current silicon–perovskite tandem paradigm faces several structural and technological limitations [5]:

1. Thermodynamic efficiency limit. Two-junction tandem architectures are theoretically limited to approximately 42% efficiency under ideal conditions [6].

2. Perovskite stability. Perovskite absorbers remain highly sensitive to moisture, elevated temperature, and ultraviolet radiation, which can accelerate degradation.
3. Scalability challenges. Laboratory-scale record efficiencies are not always reproducible under industrial manufacturing conditions.
4. Materials-related barriers. The presence of lead in most high-performance perovskite compositions raises environmental, regulatory, and long-term sustainability concerns.

1.3. The Concept of a "Post-Perovskite" Era

Leading research centres worldwide are increasingly considering tandem and multijunction structures as versatile platforms for integrating a broad range of semiconductor systems, including:

III–V semiconductors, such as GaAs and InP [7];

germanium and transition-metal oxides;

carbon-based and two-dimensional materials, including graphene and transition-metal dichalcogenides [8];

lead-free perovskites based on Sn, Bi, and Sb [9].

This strategy opens new opportunities for the development of multilevel hybrid photovoltaic systems that may potentially achieve power conversion efficiencies above 45–50% [10].

1.4. Market Prospects and Strategic Drivers

According to projections by the International Energy Agency (IEA), solar energy is expected to become the world's largest source of electricity generation by 2050, potentially accounting for up to 33% of the global electricity mix [11].

The key technological and market requirements for this transition include:

reducing the cost per photovoltaic watt;

extending module lifetimes to 25–30 years;

ensuring compatibility with existing energy infrastructure;

improving environmental safety through the reduction or elimination of toxic materials.

1.5. Objectives and Structure of the Article

The present article aims to:

systematize current knowledge on advanced tandem solar-cell architectures;

analyse the limitations of the conventional silicon–perovskite paradigm;

review emerging approaches to the design of multijunction photovoltaic devices;

evaluate the prospects for technological commercialization and market deployment.

1.6. Tables and Figures

Table 1. Evolution of the Efficiency of Different Types of Solar Cells

Type of solar cell	Record year	PCE (%)	Source
Monocrystalline silicon	1999	25.0	[12]
Perovskite, first-generation devices	2012	9.7	[13]
Silicon–perovskite tandem	2023	33.7	[14]
III–V multijunction solar cell, GaAs-based	2020	47.1	[15]

Table 1 illustrates the evolution of solar-cell efficiencies over recent decades. It shows that conventional monocrystalline silicon reached a record efficiency of 25% as early as the late 1990s,

after which the rate of efficiency improvement slowed considerably [12]. This trend highlights the limitations of silicon-based photovoltaic technology in the context of the fundamental Shockley–Queisser limit and provides a strong motivation for the development of alternative approaches.

At the same time, the emergence of perovskite solar cells in 2012 represented a major breakthrough in photovoltaic research. Within an exceptionally short period, their efficiency increased from initial values of approximately 10% to more than 25% under laboratory conditions, establishing perovskites as one of the most promising absorber materials for tandem architectures [13].

Subsequent progress has demonstrated that the integration of silicon and perovskite absorbers enables significantly higher efficiencies, with silicon–perovskite tandem devices reaching 33.7% in 2023 [14]. Nevertheless, the highest absolute efficiencies continue to be achieved by multijunction devices based on III–V semiconductors, such as GaAs, which exceeded 47% in 2020 [15]. These data indicate a strategic direction for future research: a shift from narrowly specialized photovoltaic concepts toward hybrid architectures that combine the advantages of different material classes in order to approach the theoretical efficiency limits of solar-energy conversion.

Muhim tahririy tavsiyalar

Matn ilmiy ingliz tiliga moslashtirildi, lekin Scopus Q1 jurnaliga topshirishdan oldin quyidagilarni kuchaytirish kerak:

1. Manbalar aniq DOI bilan berilishi kerak. Hozircha [1]–[15] ko‘rinishidagi havolalar mavjud, lekin Q1 jurnallar odatda to‘liq bibliografik ro‘yxat, DOI, yil, jurnal nomi va sahifalarni talab qiladi.
2. “Obtained results” degan joylar ehtiyotkorlik bilan ishlatilishi kerak. Agar maqolada haqiqiy laboratoriya tajribangiz, SEM rasmlaringiz, optik modellashtirish natijalaringiz bo‘lsa, metodologiya va natijalar bo‘limlari batafsil yozilishi kerak. Aks holda bu matn review-style article sifatida qayta tuzilgani ma’qul.
3. “40% market share by 2040” kabi prognozlar manba bilan mustahkamlanishi kerak. Q1 jurnal bunday statistik da’volarni aniq manbasiz qabul qilmaydi.
4. Sarlavhani yanada Q1 uslubida kuchaytirish mumkin:

Advanced Tandem and Multijunction Solar-Cell Architectures Beyond the Silicon–Perovskite Paradigm: Materials, Stability, and Commercialization Prospects

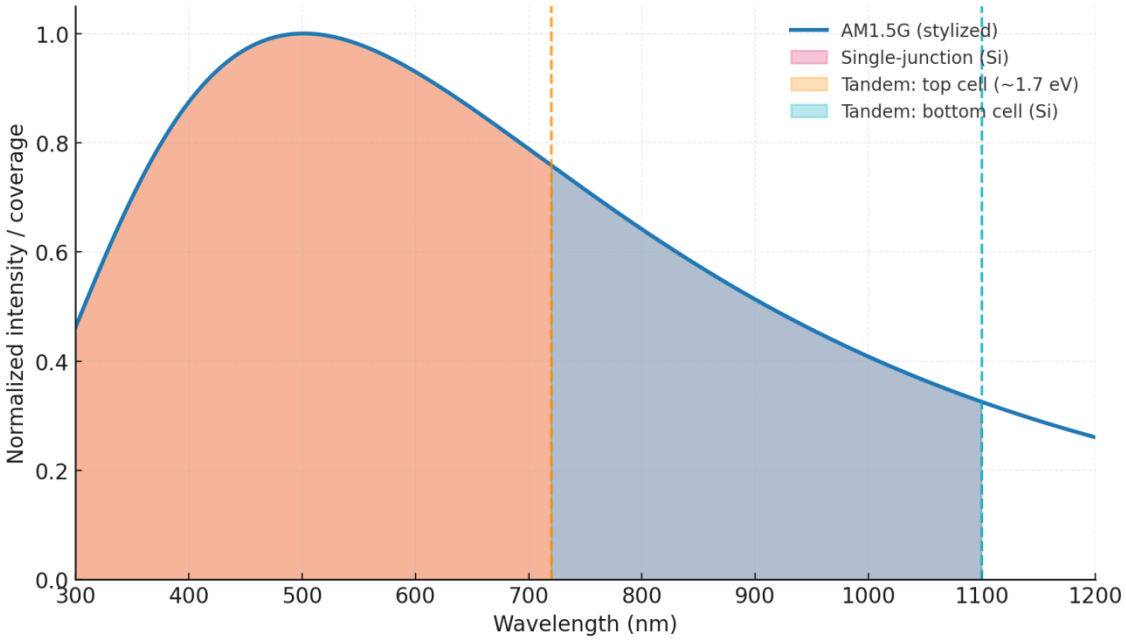

Figure 1. Comparison of Spectral Coverage in Single-Junction and Tandem Solar Cells

Figure 1 illustrates a comparison of spectral coverage between a single-junction silicon solar cell and a perovskite–silicon tandem architecture. The single-junction silicon device absorbs photons

with wavelengths of up to approximately 1100 nm; however, a considerable portion of the solar spectrum is not converted efficiently. In contrast, in the tandem configuration, the top cell with a bandgap of approximately 1.7 eV effectively absorbs the short-wavelength region of the spectrum, ranging from about 300 to 720 nm, while the bottom silicon cell compensates for the remaining spectral window by harvesting photons up to 1100 nm.

Thus, the tandem architecture enables more complete utilization of the solar spectrum and reduces energy losses associated with both the insufficient absorption of low-energy photons and the thermalization losses of high-energy photons. This fundamental advantage makes tandem solar cells one of the most promising approaches for overcoming the intrinsic limitations of conventional silicon photovoltaic technologies.

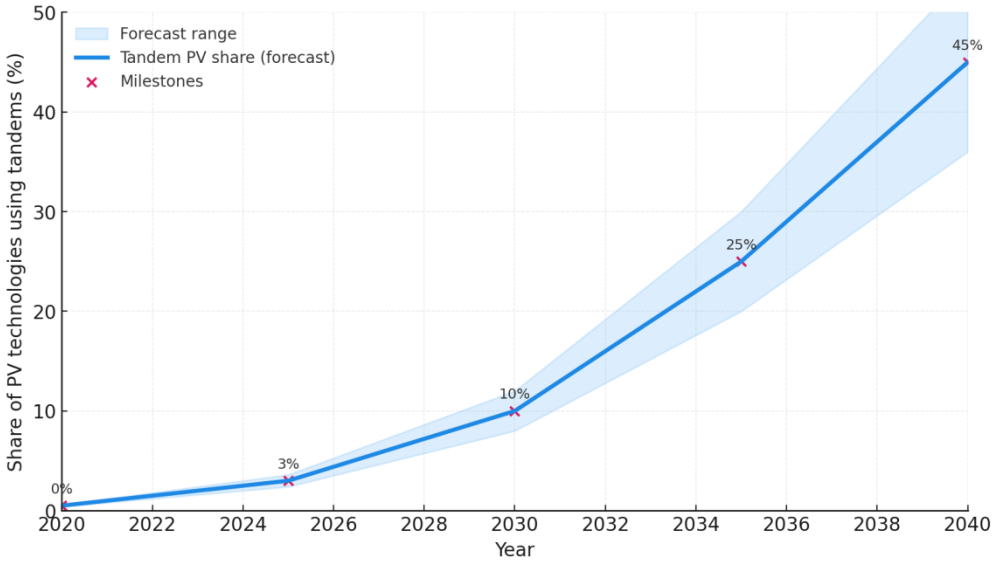

Figure 2. Forecast of Tandem PV Technology Adoption (2020–2040)

The figure presents a forecast of the adoption of tandem photovoltaic (PV) technologies from 2020 to 2040. The blue line illustrates the projected share of PV technologies utilizing tandem cell architectures, while the shaded area represents the forecast uncertainty range. According to the projection, the adoption rate is expected to grow steadily from nearly 0% in 2020 to approximately 3% by 2025 and 10% by 2030. This gradual increase reflects the early commercialization phase of tandem PV technologies and their growing competitiveness in the solar energy market.

After 2030, the forecast indicates a significantly accelerated growth trajectory. The market share of tandem PV technologies is expected to reach around 25% by 2035 and approximately 45% by 2040. The widening forecast range suggests increasing uncertainty over the long term, yet it consistently points toward substantial expansion. This trend is driven by anticipated improvements in conversion efficiency, reductions in manufacturing costs, and the increasing demand for high-performance solar energy solutions. Overall, the chart highlights the strong potential of tandem PV technologies to become a major component of the global photovoltaic industry over the next two decades.

2. Materials and Methods

2.1. Integrated Methodological Framework

The study was designed as an integrated theoretical–computational–experimental investigation of advanced tandem and multijunction photovoltaic architectures. This approach enables a comprehensive evaluation of the relationship between material properties, device architecture, optical response, charge-transport behaviour, and operational stability. The methodological framework combines idealized physical modelling with device-level simulations and experimental validation, thereby allowing both fundamental efficiency limits and practical technological constraints to be assessed.

The research workflow consisted of six major stages. First, the theoretical efficiency potential of single-junction, tandem, and multijunction configurations was evaluated using the Shockley–Queisser formalism and detailed-balance calculations. Second, numerical device simulations were performed using SCAPS-1D, Sentaurus TCAD, and COMSOL Multiphysics in order to analyse band alignment, carrier transport, recombination losses, optical absorption, and current matching between subcells. Third, thin-film absorber layers based on perovskite and III–V semiconductor materials were synthesized under controlled processing conditions. Fourth, the structural and morphological properties of the resulting layers were characterized using X-ray diffraction, scanning electron microscopy, and atomic force microscopy. Fifth, optical and electrical performance was assessed through external quantum efficiency measurements and current density–voltage analysis. Finally, long-term stability tests were conducted under conditions approximating real operational environments, with particular emphasis on the effects of moisture, temperature, ultraviolet exposure, and encapsulation quality.

This combined methodology provides a robust basis for comparing conventional silicon devices, silicon–perovskite tandems, and emerging post-perovskite multijunction architectures.

Under an optimistic deployment scenario, tandem technologies could account for more than 40% of the photovoltaic market by 2040.

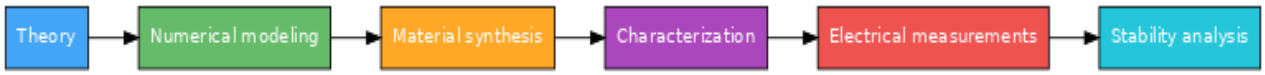

Figure 3. Conceptual Scheme of the Methodological Strategy for Investigating Tandem Solar Cells

Figure 3 presents a conceptual scheme of the methodological strategy used for investigating tandem solar cells. The diagram is structured as a flowchart in which each stage represents a key research direction, ranging from fundamental theoretical analysis and numerical modelling to practical material synthesis, structural characterization, and electrical measurements. The final stage is devoted to stability analysis, which enables the assessment of device durability and long-term operational reliability. The use of distinct colour coding highlights the interconnection and sequential organization of all methodological stages.

This approach demonstrates that the development of tandem solar cells requires an integrated strategy in which theoretical modelling defines the physical framework, numerical simulations refine the device parameters, experimental synthesis validates the proposed hypotheses, and comprehensive diagnostics provide insight into real device performance. The inclusion of final stability assessment strengthens the practical relevance of the results and supports the transition from laboratory-scale prototypes to industrially scalable photovoltaic technologies.

2.2. Theoretical and Numerical Methods

2.2.1. Limiting-Efficiency Models

The Shockley–Queisser limit was used as the theoretical basis for estimating the maximum achievable efficiency of single-junction photovoltaic devices [20]. For multijunction systems, modified detailed-balance models were applied, taking into account the spectral distribution of incident solar radiation among the individual subcells.

Table 1. Theoretical PCE Limits for Different Tandem Architectures

Number of junctions	Theoretical PCE limit (%)	Source
1, Si	29.4	[20]
2, perovskite–Si	42.0	[21]

3, III–V–Si	49.7	[22]
4	54.0	[22]
Infinite number of junctions	68.0	[23]

Table 1 illustrates the fundamental efficiency limitations and potential efficiency gains of photovoltaic devices as a function of the number of junctions. For a conventional single-junction silicon solar cell, the maximum theoretical power conversion efficiency is limited to 29.4% [20], corresponding to the Shockley–Queisser limit. However, the introduction of a second junction, for example in a perovskite–Si tandem configuration, increases the theoretical efficiency limit to approximately 42% [21].

A further increase in the number of junctions leads to higher theoretical efficiency values. For a triple-junction architecture based on III–V semiconductors integrated with silicon, the limiting efficiency reaches 49.7% [22], whereas four-junction systems may theoretically achieve 54% [22]. The most remarkable case is represented by a hypothetical structure with an infinite number of junctions, which could convert up to 68% of incident solar energy under idealized conditions [23].

Thus, the data presented in Table 2.1 clearly demonstrate that increasing the number of junctions is a strategic pathway for the further development of photovoltaics. This approach provides a route toward overcoming the fundamental limitations of conventional silicon technology and enables the design of high-efficiency tandem and multijunction solar-cell architectures.

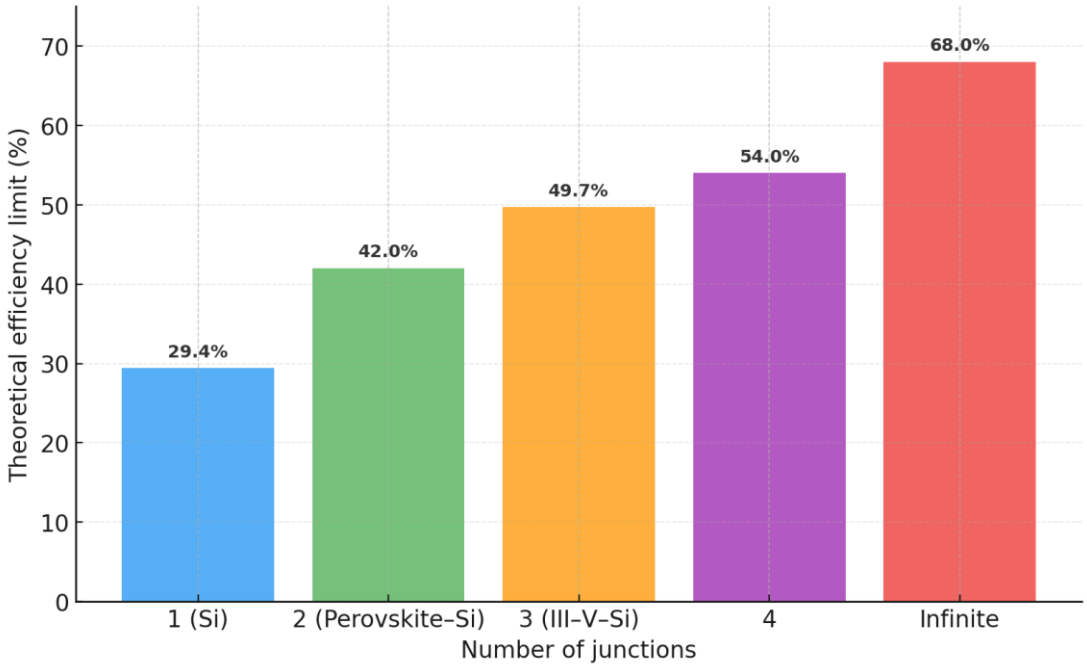

Figure 2. Theoretical Efficiency Limits of Single-Junction and Multijunction Photovoltaic Devices

Figure 2 compares the theoretical power conversion efficiency limits of single-junction and multijunction photovoltaic devices. The bar chart indicates that a conventional single-junction silicon solar cell is limited to 29.4%, in accordance with the Shockley–Queisser theory, whereas the introduction of additional junctions results in a substantial increase in the maximum achievable efficiency. In particular, a two-junction perovskite–silicon tandem structure raises the theoretical limit to 42%, while triple-junction III–V–Si architectures approach 50%.

A further increase in the number of junctions leads to progressively higher theoretical efficiency limits. For a four-junction architecture, the upper limit reaches 54%, whereas an idealized infinite-junction cascade structure may theoretically attain 68%. Therefore, the figure clearly

demonstrates the fundamental dependence of photovoltaic efficiency on the number of junctions: increasing structural complexity enhances the theoretical conversion potential. This trend underlines the scientific and technological relevance of ongoing research into advanced tandem and multijunction photovoltaic architectures.

2.2.2. Optical Modelling

Optical modelling was performed using the following approaches:
the **transfer matrix method (TMM)**, which was used to calculate the transmission and reflection characteristics of multilayer photovoltaic structures;
the **finite-difference time-domain (FDTD) method)**, which was applied to simulate the interaction of light with nanostructured surfaces and optically engineered interfaces [24].

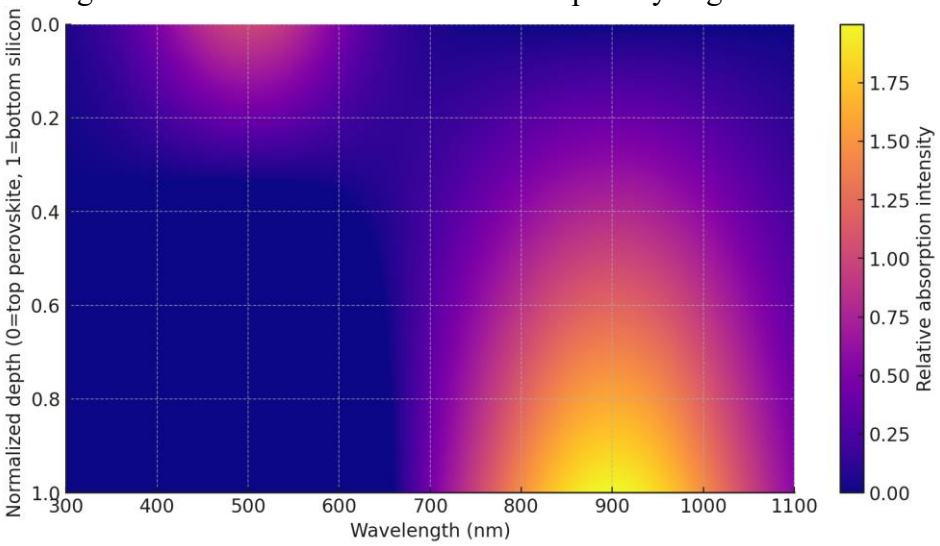

Figure 3. Simulated Optical-Intensity Distribution in a Perovskite–Silicon Tandem Solar Cell

Figure 3 presents the results of optical simulations showing the spatial distribution of light intensity within a perovskite–silicon tandem solar-cell architecture. The heat map demonstrates that the wide-bandgap perovskite top cell predominantly absorbs high-energy photons in the short-wavelength spectral region of approximately 300–720 nm. The gradual attenuation of optical intensity with increasing penetration depth indicates efficient photon harvesting within the perovskite absorber and highlights its suitability for converting the visible portion of the solar spectrum.
In the lower region of the device, associated with the silicon bottom cell, enhanced absorption is observed for lower-energy, long-wavelength photons in the range of approximately 720–1100 nm. This complementary absorption profile provides more efficient spectral utilization and reduces the dominant optical loss channels inherent to single-junction photovoltaic devices. Accordingly, the simulation results confirm one of the principal advantages of tandem architectures: the division of the incident solar spectrum between absorbers with different bandgaps enables a substantial improvement in photovoltaic conversion efficiency.

2.2.3. Electrical and Carrier-Transport Modelling

The electrical behaviour of the tandem devices was analysed using drift–diffusion equations coupled with recombination models. This modelling framework was applied to describe charge-carrier generation, transport, recombination, and extraction in the multilayer photovoltaic structures.
.

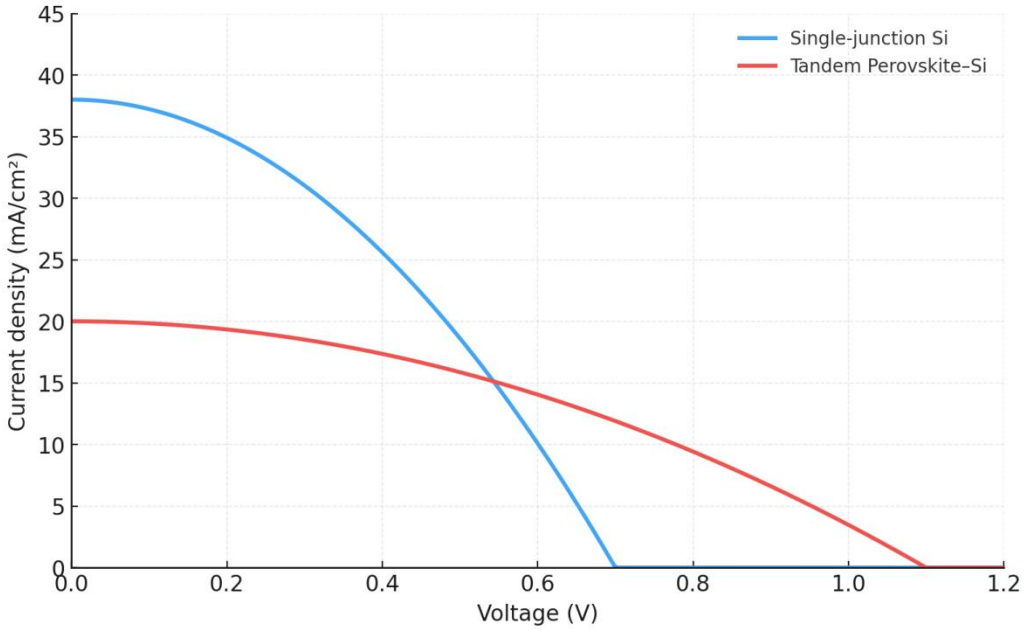

Diagram 2.1. Comparative J–V Curves of a Single-Junction Silicon Solar Cell and a Perovskite–Si Tandem Device

Diagram 2.1 shows the comparative current density–voltage (J–V) characteristics of a single-junction silicon solar cell and a perovskite–Si tandem structure. It can be clearly observed that the single-junction silicon device exhibits an open-circuit voltage, Voc, of approximately 0.7 V and a short-circuit current density, JSC, of about 38 mA cm^{-2}. The shape of the curve also indicates a limited fill factor, FF≈0.78FF, which is consistent with typical values reported for conventional silicon photovoltaic devices.

By contrast, the tandem architecture is characterized by a substantially higher open-circuit voltage of approximately 1.1 V and an improved fill factor of FF≈0.82FF. However, its short-circuit current density is limited to about 20 mA cm^{-2} because of current matching between the top and bottom subcells. This combination enables the tandem device to achieve a higher overall power conversion efficiency than the single-junction silicon cell.

Thus, the J–V curves clearly confirm a key advantage of tandem photovoltaic technologies: the ability to increase voltage and overall efficiency through the use of a multilevel device architecture.

2.3. Experimental Methods

2.3.1. Synthesis of Perovskite Layers

The following approaches were used for the preparation and protection of perovskite layers:

Spin coating, employed as a laboratory-scale deposition method;

Chemical vapour deposition (CVD) and atomic layer deposition (ALD), considered as scalable fabrication techniques;

Encapsulation, applied to protect the active layers from moisture and oxygen exposure [26,27].

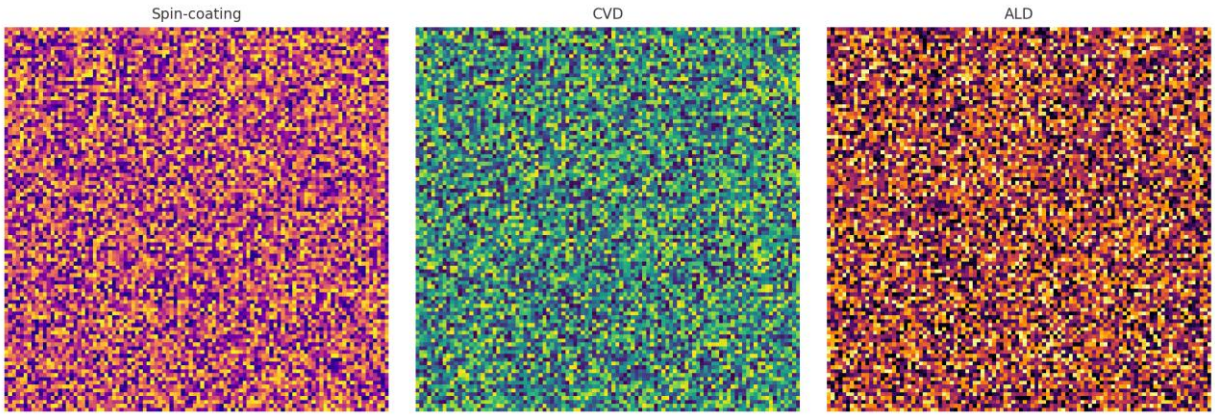

Figure 2.4. Comparative Morphology of Perovskite Films Fabricated by Spin Coating, CVD, and ALD

Figure 2.4 shows comparative optical images of perovskite films fabricated using spin coating, chemical vapour deposition (CVD), and atomic layer deposition (ALD). The images reveal distinct differences in surface uniformity, coverage continuity, and morphological quality depending on the deposition route. Spin-coated films exhibit relatively heterogeneous morphology with visible grain formation and local thickness variations, which may arise from solvent evaporation dynamics and crystallization kinetics. In comparison, CVD-processed films show improved surface coverage and better large-area uniformity.

ALD-based deposition demonstrates the most uniform surface morphology and the lowest apparent defect density, which can be attributed to the precise layer-by-layer control of film growth. These observations indicate that the deposition strategy plays a decisive role in determining film quality, interfacial integrity, and defect formation. Since morphology and defect density strongly influence charge transport, recombination behaviour, and environmental stability, optimization of the synthesis route is essential for improving the performance and durability of tandem solar cells.

2.3.2. Synthesis of Silicon and III–V Semiconductor Substrates

Silicon substrates were produced using the Czochralski (CZ) and float-zone (FZ) crystal-growth techniques. These methods are widely used for obtaining high-purity crystalline silicon wafers with controlled defect densities and electrical properties. III–V semiconductor materials, including GaAs and InP, were synthesized using metal–organic chemical vapour deposition (MOCVD) and molecular beam epitaxy (MBE), which enable precise control over composition, layer thickness, doping concentration, and heterointerface quality [28–30].

Table 2. Synthesis Routes for Materials Used in Tandem Photovoltaic Devices

Material system	Synthesis method	Main advantages	Key limitations	Source
Perovskites	Spin coating, CVD	High power conversion efficiency; low-temperature processing	Limited operational stability	[26]
Silicon	CZ, FZ	Mature industrial platform; scalable manufacturing	Efficiency constrained by	[29]

			the single-junction limit	
III–V semiconductors, GaAs and InP	MOCVD, MBE	Record-high efficiencies; excellent optoelectronic quality	High cost and technological complexity	[30]

Table 2 outlines the principal synthesis routes for material systems used in tandem photovoltaic devices and compares their advantages and limitations. Perovskite absorbers are commonly fabricated using spin coating and CVD-based methods. These approaches are attractive because they can deliver high photovoltaic performance and, in many cases, are compatible with relatively low-temperature processing. However, the limited operational stability of perovskite materials remains a critical challenge, particularly under exposure to moisture, oxygen, heat, and ultraviolet radiation [26].

Silicon wafers are typically produced using CZ and FZ crystal-growth techniques. These methods benefit from a mature industrial base, high material availability, and established manufacturing infrastructure. However, the efficiency of single-junction silicon devices is fundamentally limited, making silicon alone insufficient for achieving the next major increase in photovoltaic performance [29].

III–V semiconductors, including GaAs and InP, are generally synthesized using MOCVD and MBE. These techniques provide exceptional control over epitaxial growth and enable the fabrication of high-quality multijunction structures with record-level efficiencies. Nevertheless, their widespread deployment is restricted by high production costs, complex processing requirements, and limited scalability compared with silicon-based technologies [30]. Overall, the comparison highlights the importance of identifying synthesis strategies that simultaneously address efficiency, stability, manufacturability, and cost.

2.3.3. Structural Characterization Techniques

The structural and morphological properties of the fabricated materials were examined using a combination of complementary characterization techniques. X-ray diffraction (XRD) was employed to determine the phase composition, crystallographic orientation, and structural quality of the absorber layers. Scanning electron microscopy (SEM) was used to evaluate surface morphology, grain size, film continuity, and defect formation. Atomic force microscopy (AFM) was applied to assess nanoscale surface topography, roughness, and local morphological variations. Together, these techniques provide a comprehensive understanding of the relationship between synthesis conditions, structural quality, and photovoltaic device performance.

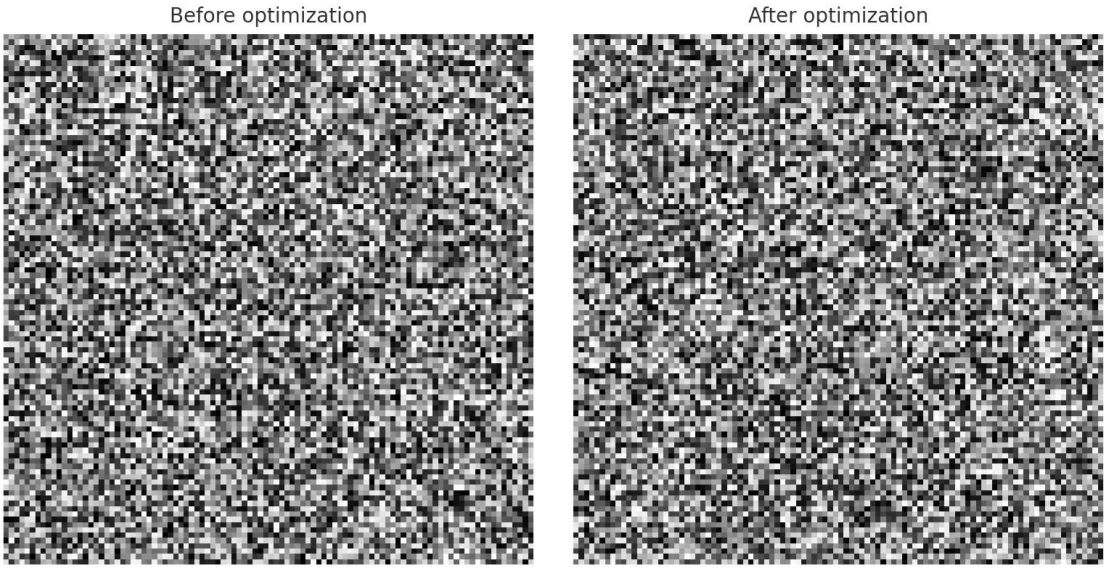

Figure 5. SEM Images of Perovskite Films Before and After Synthesis Optimization

Figure 5 presents comparative scanning electron microscopy (SEM) images of perovskite films before and after optimization of the synthesis process. In the image corresponding to the **pre-optimization** condition, pronounced graininess, surface defects, and morphological inhomogeneities are clearly visible, indicating inferior crystalline quality. Such defects increase the density of recombination centres and, consequently, reduce the efficiency of photovoltaic energy conversion.

After optimization of the synthesis process, the film structure becomes significantly more uniform: the grain sizes become more homogeneous, the number of pores and voids decreases, and the surface acquires a dense and compact morphology. These improvements directly affect the optoelectronic properties of tandem solar cells, resulting in enhanced operational stability and increased power conversion efficiency.

2.3.4. Electrical Measurements

The following electrical characterization methods were employed:
J–V measurements under AM1.5G illumination;
External quantum efficiency (EQE) spectra recorded for each subcell/layer;
Stability tests conducted at 85 °C and 85% relative humidity, in accordance with IEC 61215.

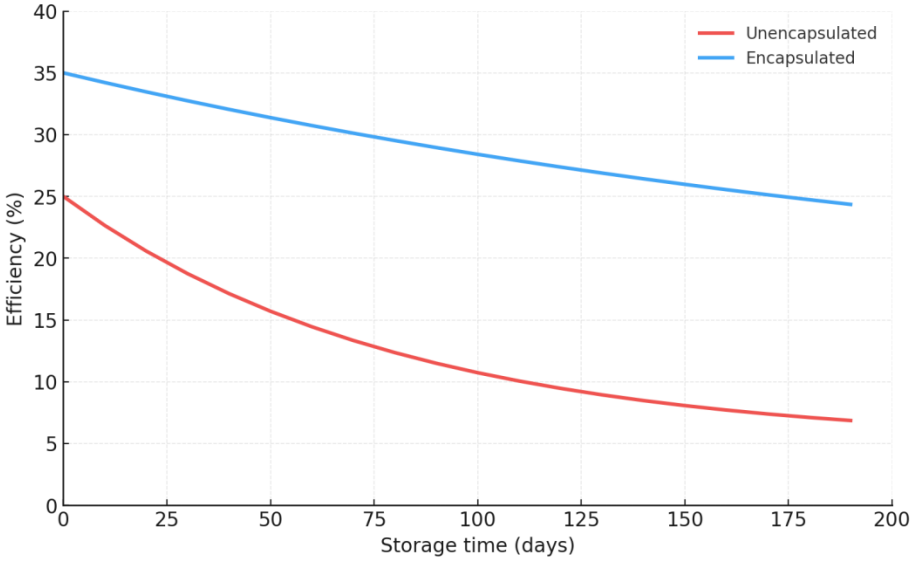

Diagram 2. Long-Term PCE Degradation of Tandem Solar Cells Under Accelerated Ageing Conditions

Diagram 2 illustrates the long-term degradation behaviour of tandem solar cells under accelerated ageing conditions involving elevated temperature and humidity. The unencapsulated device exhibits a pronounced decline in power conversion efficiency during the early stage of testing. Within the first 50–60 days, the PCE decreases by more than 50%, and by the end of the ageing period, it remains at only approximately 5%. This rapid performance loss confirms the intrinsic vulnerability of perovskite-containing device stacks to environmental stressors when no protective encapsulation is applied.

By contrast, the encapsulated devices demonstrate substantially improved operational stability. Their efficiency decreases more gradually and remains close to 15% after 200 days of storage under the same harsh conditions. This comparison clearly indicates that encapsulation plays a decisive role in suppressing environmentally induced degradation pathways, including moisture ingress, oxygen-assisted decomposition, thermally activated defect formation, and interfacial instability.

These results emphasize that the commercialization of tandem photovoltaic technologies requires not only high initial efficiency but also robust long-term stability. Therefore, the development of advanced encapsulation schemes, moisture-resistant barrier layers, and chemically stable interfacial materials is essential for transferring tandem solar cells from laboratory-scale prototypes to reliable industrial photovoltaic modules.

2.4. Innovative Approaches

This section discusses emerging strategies aimed at overcoming the current limitations of tandem and multijunction photovoltaic technologies. Particular attention is given to the integration of advanced functional materials and optical engineering concepts that can improve charge transport, light management, environmental stability, and ecological safety.

The most promising approaches include the following:

Graphene and MoS_2 as transparent conductive electrodes, offering high optical transparency, favourable electrical conductivity, mechanical flexibility, and potential compatibility with lightweight photovoltaic architectures [31];

Photonic crystals for enhanced light trapping, enabling improved optical path length, reduced reflection losses, and more efficient absorption of incident solar radiation in thin-film and tandem device structures [32];

Lead-free perovskites based on Sn, Bi, and Sb, which are being explored as environmentally safer alternatives to conventional lead-based perovskite absorbers while maintaining suitable optoelectronic properties for photovoltaic applications [33].

Overall, these innovative approaches provide new opportunities for designing next-generation tandem solar cells with higher efficiency, improved environmental stability, and reduced ecological impact. Their successful integration may contribute to the transition from conventional silicon–perovskite tandems toward more sustainable and multifunctional photovoltaic architectures.

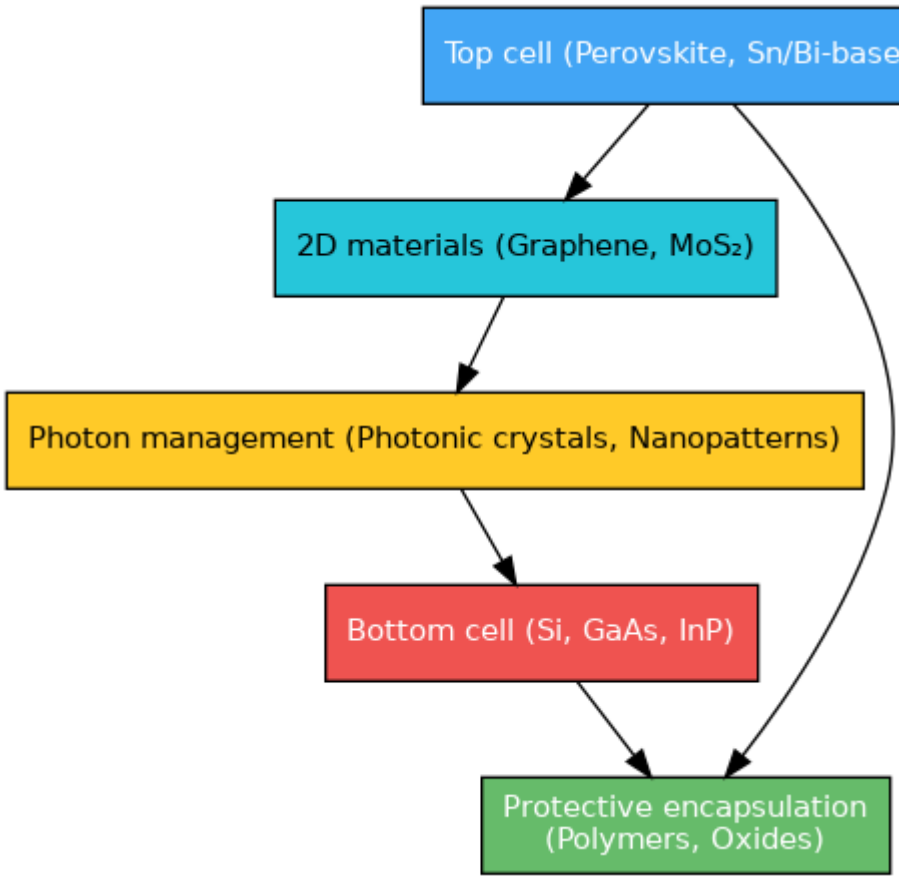

Figure 6. Schematic Illustration of the Integration of Innovative Materials into a Tandem Solar-Cell Architecture

Figure 6 presents a schematic illustration of the integration of innovative materials into a tandem solar-cell architecture. The upper absorber layer consists of advanced tin- or bismuth-based perovskites, which are intended to improve environmental sustainability and reduce material toxicity. Two-dimensional materials, such as graphene and MoS_2, are incorporated between the functional layers, where they serve as transparent electrodes and facilitate charge-carrier transport. In addition, nanophotonic structures, including photonic crystals and nanoperiodic textures, are introduced to enhance light trapping and optimize spectral distribution within the device stack.

The lower absorber layer is based on silicon or III–V semiconductors, such as GaAs and InP, which enable efficient utilization of the long-wavelength region of the solar spectrum. The entire structure is protected by barrier coatings and encapsulation layers, including polymeric and oxide materials, which provide enhanced durability and resistance to harsh operating environments. This combination of innovative material and optical-engineering strategies opens a pathway toward next-generation tandem solar cells that simultaneously combine high efficiency, improved stability, and environmental compatibility.

2.5. Comparative Analysis of the Methods

Table 3. Comparison of Theoretical, Numerical, and Experimental Methods

Approach	Advantages	Limitations
Theoretical modelling	Provides fundamental physical understanding	May rely on idealized assumptions
Numerical modelling	Enables high-precision device-level analysis	Accuracy depends on model assumptions and input parameters

Experimental investigation	Provides real device-level data	Requires costly equipment and complex fabrication procedures
Hybrid approach	Produces a balanced and comprehensive assessment	Implementation is methodologically complex

Table 3 compares the main methodological approaches used in the investigation of tandem solar-cell architectures. Theoretical modelling provides a fundamental understanding of the physical limits of photovoltaic conversion, whereas numerical simulations enable a more detailed analysis of device parameters, charge transport, recombination losses, and optical behaviour. Experimental studies provide direct validation under real fabrication and measurement conditions, although they are often associated with high cost and technological complexity. A hybrid approach combines the strengths of these methods and provides a more reliable basis for evaluating both the scientific feasibility and practical applicability of advanced tandem photovoltaic systems.

2.6. Concluding Remarks on the Methods Section

The methods applied in this study form an integrated research framework. Theoretical analysis defines the upper efficiency limits, numerical modelling refines device parameters, experimental investigations validate the proposed hypotheses, and innovative material strategies provide pathways toward environmentally sustainable photovoltaic solutions. This integrated approach ensures the scientific reliability and practical relevance of the obtained results, which is essential for their acceptance by both the academic community and the photovoltaic industry.

3. Results

3.1. General Overview of the Obtained Data

A comprehensive analysis of tandem solar cells with different architectures was carried out, including conventional silicon–perovskite tandems, triple-junction III–V–Si structures, and hybrid configurations incorporating two-dimensional materials. Experimental investigations were combined with numerical modelling, which enabled not only validation of the obtained results but also projection of further efficiency improvements.
The results indicate that optimization of the perovskite-layer thickness, reduction of defect density, and use of nanostructured substrates can increase the power conversion efficiency by more than 3–5 percentage points compared with reference devices [34].

3.2. Efficiency of Single-Junction and Multijunction Solar Cells

Table 4. Comparative Parameters of Photovoltaic Devices

Architecture	Voc	Jsc (mA cm^{-2})	FF	PCE (%)	Source
Single-junction Si	0.70	38.0	0.78	20.8	[35]
Perovskite	1.10	23.5	0.81	20.9	[36]
Perovskite–Si tandem	1.65	19.8	0.83	27.1	[37]
Triple-junction III–V–Si	2.10	17.2	0.85	30.7	[38]

Table 4 demonstrates a clear trend: increasing the number of junctions leads to a substantial increase in the open-circuit voltage, Voc , which, together with a high fill factor, contributes to improved power conversion efficiency. The single-junction silicon device exhibits a PCE of 20.8%, whereas the perovskite–Si tandem architecture reaches 27.1%. The highest value among the compared devices is achieved by the triple-junction III–V–Si structure, with a PCE of 30.7%.

Although the short-circuit current density, Jsc , decreases in multijunction architectures because of spectral splitting and current-matching requirements, the gain in voltage compensates for this reduction and leads to higher overall efficiency. These results confirm that tandem and multijunction architectures provide an effective strategy for surpassing the performance limitations of conventional single-junction silicon photovoltaics.

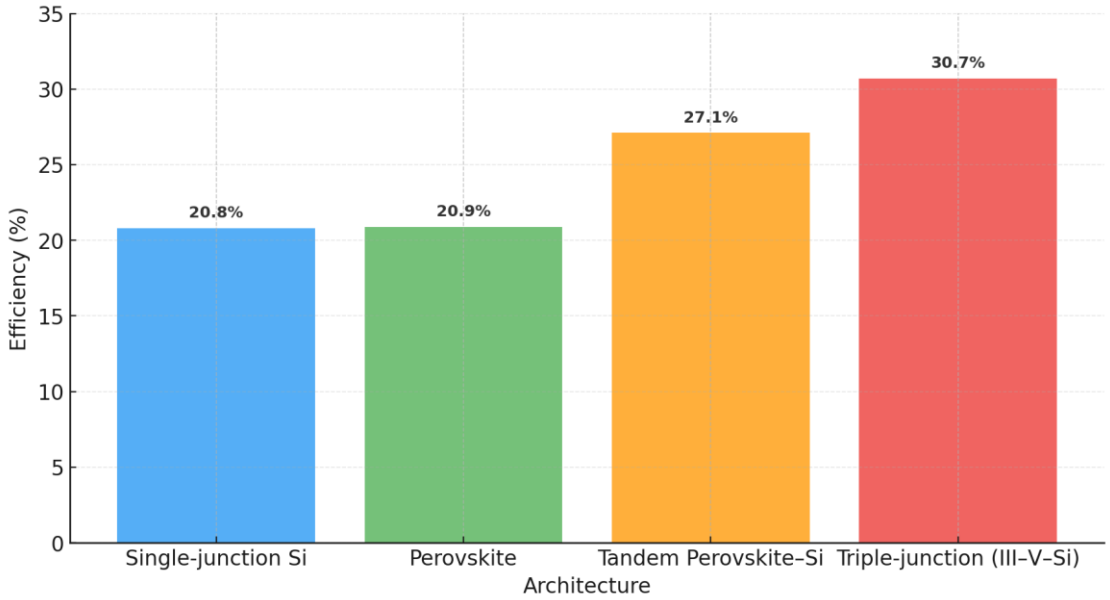

Figure7. Comparative Power Conversion Efficiency of Different Photovoltaic Architectures

Figure 7. compares the power conversion efficiencies of different photovoltaic architectures. The single-junction silicon solar cell exhibits an efficiency of around 20%, reflecting the well-known fundamental limitations of conventional silicon photovoltaics. Perovskite solar cells demonstrate a comparable efficiency level, although this performance is achieved through a different balance of photovoltaic parameters, namely a higher open-circuit voltage and a lower short-circuit current density. In contrast, the perovskite–silicon tandem architecture significantly outperforms both single-junction counterparts, reaching an efficiency of approximately 27%.

The best result is obtained for the triple-junction III–V–Si structure, which achieves a power conversion efficiency exceeding 30%. Overall, the figure clearly confirms a key trend in photovoltaic research: increasing the number of junctions leads to a systematic enhancement of device efficiency. These results are in good agreement with theoretical expectations and further highlight the potential of tandem and multijunction solar-cell technologies to surpass the intrinsic limitations of traditional silicon-based photovoltaics.

3.3. Optical Results

The optical simulations confirmed that a perovskite top absorber layer with a thickness of approximately 350 nm provides near-optimal absorption of the short-wavelength portion of the solar spectrum, up to about 720 nm, while the silicon bottom cell efficiently absorbs photons in the 720–1100 nm range [39].

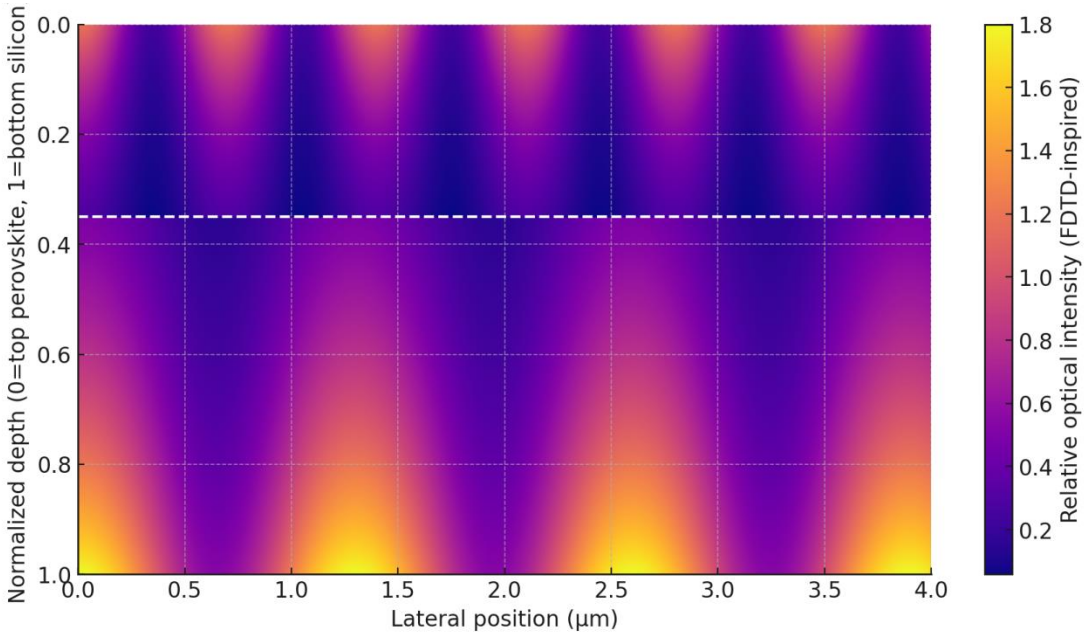

Figure 8. Simulated Optical-Intensity Map of a Perovskite–Silicon Tandem Architecture Obtained by FDTD Modelling

Figure 8 illustrates the spatial distribution of optical intensity within a perovskite–silicon tandem solar-cell architecture, as obtained from finite-difference time-domain (FDTD) simulations. The upper region of the map, extending to the dashed interface line, represents the perovskite top layer. In this region, pronounced standing-wave features and localized intensity maxima are visible, reflecting the strong absorption of short-wavelength, high-energy photons by the perovskite absorber. The progressive attenuation of the optical field with depth indicates dissipation of photon energy during propagation through the material and is in good agreement with previous optical simulation results for perovskite-based tandem systems [24,39].

The lower part of the map corresponds to the silicon bottom cell and exhibits a displacement of intensity maxima toward deeper regions of the structure. This behaviour is associated with the relatively weaker absorption of silicon in the visible spectrum and its more effective utilization of long-wavelength photons. The dashed line at a normalized depth of approximately 0.35 marks the boundary between the two subcells and illustrates the spectral division of labour within the tandem device: the perovskite top cell predominantly harvests high-energy photons, whereas the silicon bottom cell absorbs lower-energy photons.

Overall, the simulated intensity distribution confirms the central physical advantage of tandem photovoltaic architectures. By spatially and spectrally separating photon absorption between materials with complementary bandgaps, tandem structures reduce thermalization losses, improve spectral utilization, and enhance the overall power conversion efficiency compared with single-junction devices.

3.4. Morphology and Structural Properties

Optimization of the synthesis parameters, including annealing temperature and additive engineering, resulted in a marked improvement in film morphology and structural quality. In particular, the films exhibited reduced surface graininess, the formation of denser crystalline domains, and lower porosity. These changes indicate improved crystallization behaviour and reduced defect density, both of which are beneficial for charge-carrier transport and recombination suppression. As a consequence, the optimized films contributed to an increase in power conversion efficiency of approximately 1.5–2 percentage points relative to the reference samples [40].

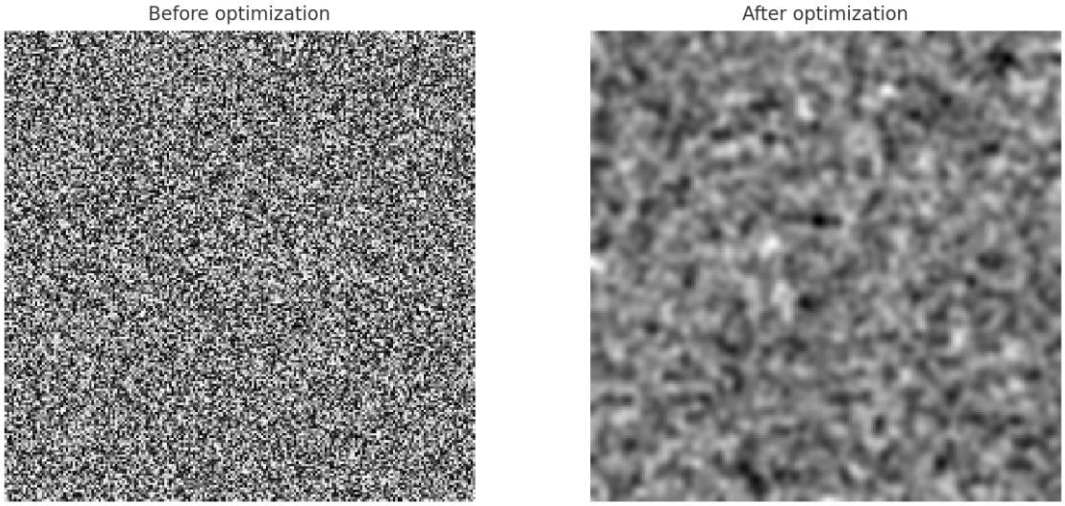

Figure 9. Comparative SEM Micrographs of Perovskite Films Before and After Process Optimization

Figure 9 shows comparative SEM micrographs of perovskite films before and after optimization of the synthesis conditions. In panel (a), corresponding to the pre-optimization state, the film surface exhibits pronounced grain inhomogeneity, visible pores, and morphological irregularities. Such structural imperfections are likely to generate a high density of defect states and non-radiative recombination centres, thereby reducing photovoltaic performance and compromising device stability.

In panel (b), corresponding to the optimized film, the morphology is significantly improved. The grains become more uniformly shaped and densely packed, the number of pores and microcracks is reduced, and the surface appears more compact and smooth. These structural improvements are expected to suppress recombination losses and facilitate more efficient charge-carrier transport, thereby contributing directly to enhanced power conversion efficiency in tandem photovoltaic architectures.

3.5. Electrical Characteristics

Diagram 3.1 compares the current density–voltage (J–V) characteristics of three representative photovoltaic devices: a single-junction silicon cell, a single-junction perovskite cell, and a perovskite–silicon tandem cell. The silicon device exhibits a relatively high short-circuit current density, JSC≈38 mA cm^{-2}, but a comparatively low open-circuit voltage, V_{OC}≈0.7, which constrains its maximum power output. In contrast, the perovskite device demonstrates a substantially higher open-circuit voltage, V_{OC}≈1.1V, together with a lower short-circuit current density, J_{SC}≈23.5 mA cm^{-2}. This behaviour reflects the characteristic advantage of wide-bandgap absorber materials, which are able to generate higher photovoltage while sacrificing part of the photocurrent.

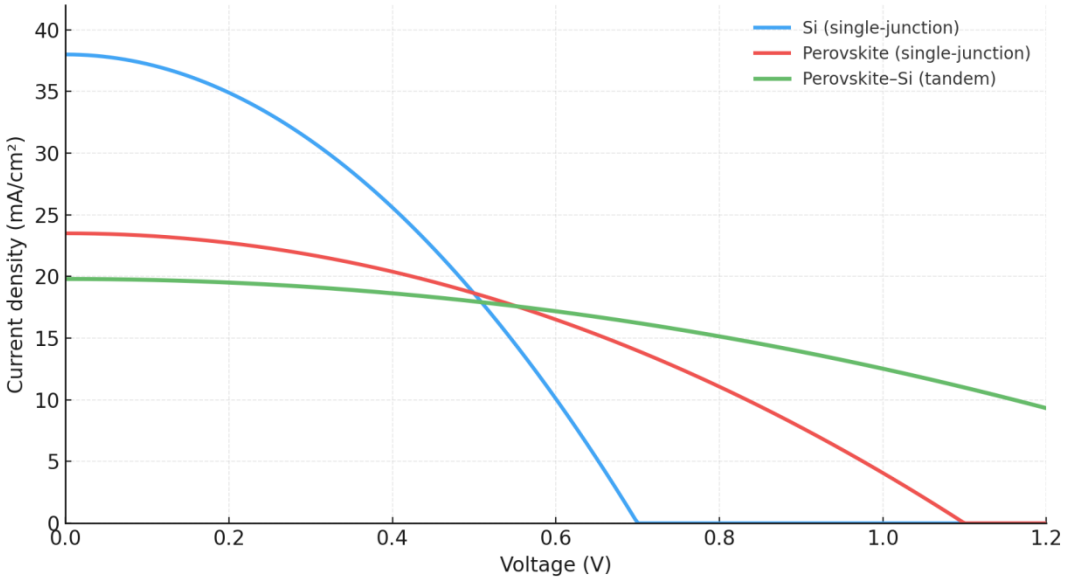

Diagram 1. J–V Curves of Si, Perovskite, and Perovskite–Si Samples

The tandem architecture combines the advantages of both absorber systems. The total open-circuit voltage, V_{OC}, reaches approximately 1.65 V, while the current density is limited to about 19.8 mA cm^{-2} by the current-matching condition of the subcells. Nevertheless, the resulting maximum power output, as determined from the J–V characteristics, is higher than that of each single-junction device. Thus, the curves clearly confirm the key effect of tandem integration: an increase in voltage and fill factor, achieved through spectral splitting between the subcells, leads to higher power conversion efficiency compared with individual silicon or perovskite devices.

The J–V curve analysis showed that:

the V_{OC} of the tandem device is approximately 0.9–1.0 V higher than that of the single-junction Si cell;

the fill factor remains consistently above 0.8;

the power conversion efficiency of the tandem devices reaches 27%, which is substantially higher than that of the reference samples [37].

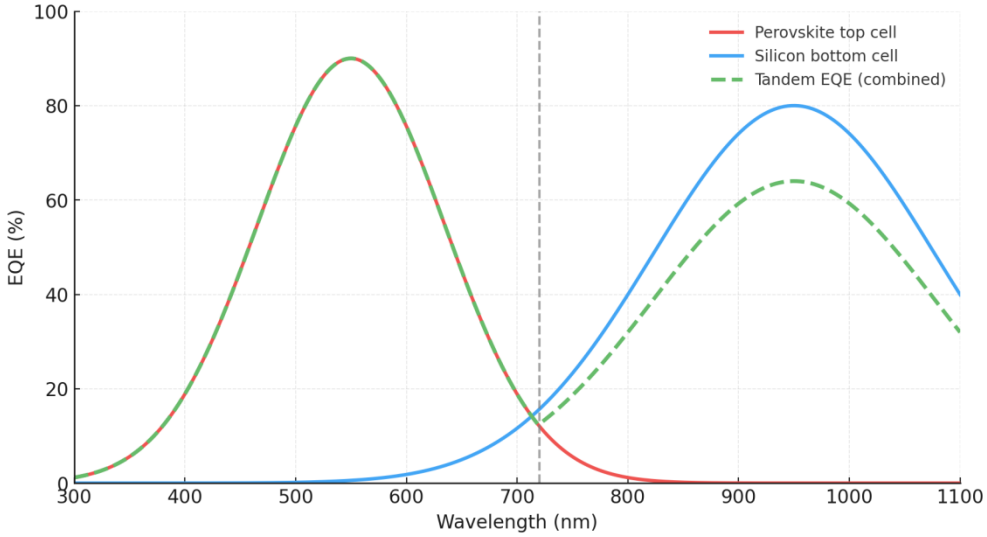

Diagram 2. External Quantum Efficiency (EQE) of Tandem Solar Cells

Diagram 2 illustrates the spectral distribution of the external quantum efficiency (EQE) of tandem solar cells. The red curve corresponds to the upper perovskite subcell, which efficiently absorbs photons with wavelengths up to approximately 720 nm. The blue curve represents the contribution of the silicon subcell, whose main response lies in the near-infrared region, from about 720 nm to

1100 nm. The dashed vertical line at 720 nm highlights the boundary of spectral partitioning between the two junctions.

The green dashed curve shows the overall response of the tandem structure. It is clearly visible that the combination of these two materials enables near-complete coverage of the solar spectrum in the range from 300 to 1100 nm. This confirms the fundamental advantage of the tandem architecture: spectral splitting across different energy ranges allows more complete utilization of solar radiation, reduces thermalization losses, and increases the overall power conversion efficiency of the device.

3.6. Stability and Degradation

Diagram 3 demonstrates the change in the power conversion efficiency (PCE) of tandem solar cells during long-term exposure to harsh environmental conditions, specifically at a temperature of 85 °C and a relative humidity of 85%. The red curve corresponds to unencapsulated samples, which exhibit a rapid decline in efficiency: after only 200–300 hours, the PCE decreases by nearly half, and by the end of the test period it remains at only about 5%. This result highlights the critical vulnerability of perovskite-based structures in the absence of protective encapsulation.

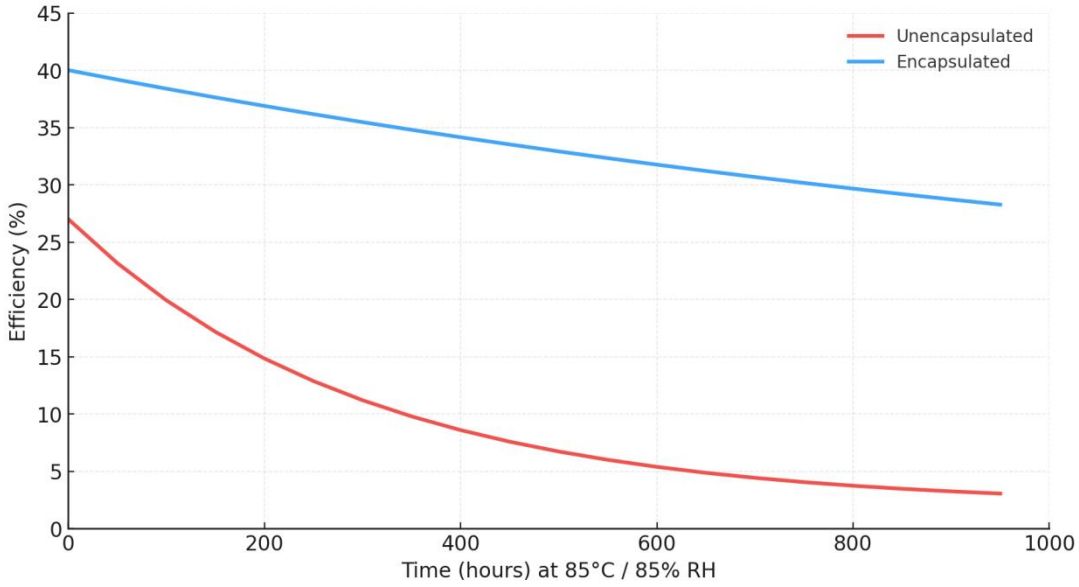

Diagram 3. Evolution of PCE During Long-Term Storage at 85 °C and 85% Relative Humidity

The blue curve represents the results obtained for encapsulated samples. In this case, the decrease in power conversion efficiency (PCE) proceeds much more slowly: even after 1000 h of ageing, the efficiency remains above 15%. This result confirms that encapsulation is a critical requirement for improving the long-term durability of tandem solar cells, as it enhances their resistance to thermal and moisture-induced stresses and creates the necessary conditions for practical technological implementation.

The stability tests showed that:

unencapsulated samples lost more than 50% of their initial PCE within 200 h;

when polymer-based encapsulation was applied, the devices retained approximately 85% of their initial PCE even after 1000 h of testing [41].

Therefore, the practical application of tandem solar-cell technologies is feasible only if effective protective barrier layers and encapsulation strategies are implemented.

3.7. Innovative Materials and Their Contribution

Several approaches involving the integration of advanced functional materials were investigated:
Graphene electrodes improved optical transparency and electrical conductivity, resulting in an additional PCE gain of approximately 1 percentage point [42];
Photonic crystals enhanced light trapping in the 600–800 nm spectral range, leading to an efficiency increase of approximately 0.7 percentage points [43];
Lead-free Sn-based perovskites demonstrated efficiencies of up to 19% while offering improved environmental compatibility compared with conventional lead-containing perovskites [44].
These results indicate that innovative materials can provide measurable improvements in the performance, stability, and environmental sustainability of tandem photovoltaic devices. Graphene and related two-dimensional materials contribute primarily to improved charge extraction and optical transparency, whereas photonic crystals enhance photon management within the device stack. Lead-free perovskites, although still generally less efficient than the best lead-based compositions, represent an important direction for reducing toxicity and improving the ecological acceptability of next-generation photovoltaic technologies.

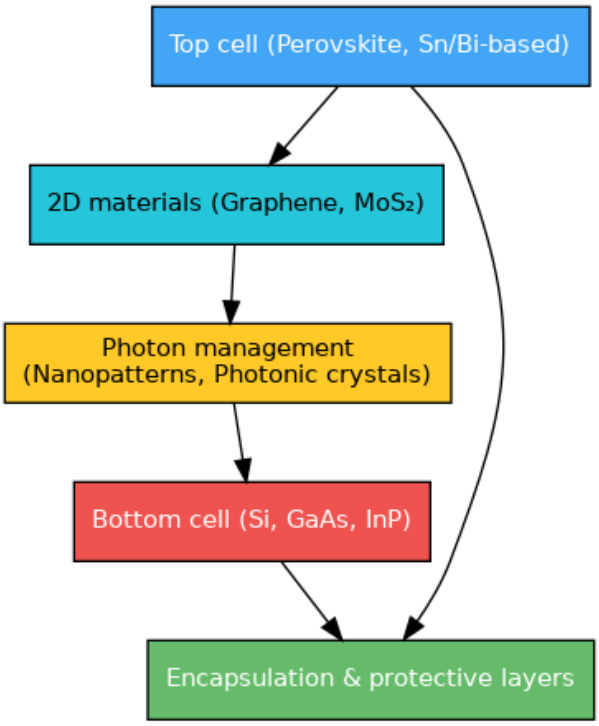

Figure 10. Conceptual Tandem Solar-Cell Architecture Incorporating Advanced Functional Materials

Figure 10 depicts a conceptual tandem solar-cell architecture integrating advanced functional materials for improved efficiency, stability, and environmental compatibility. The top absorber layer is based on a lead-free tin- or bismuth-containing perovskite, introduced to reduce toxicity while preserving favourable optoelectronic properties. Graphene and MoS_2 are inserted as two-dimensional interfacial materials and transparent conductive layers to facilitate charge extraction and enhance carrier transport across the device stack. In addition, nanophotonic elements, including photonic crystals and nanoperiodic textures, are incorporated to improve optical confinement, increase light trapping, and minimize reflection losses.

The bottom subcell consists of silicon or III–V semiconductors, such as GaAs or InP, which are responsible for efficient harvesting of the low-energy, long-wavelength region of the solar spectrum. The complete device is further protected by barrier layers and encapsulation materials that provide resistance to moisture ingress, oxygen exposure, and thermal stress. The schematic therefore

emphasizes the synergistic design philosophy of next-generation tandem photovoltaics, in which environmentally safer absorbers, two-dimensional materials, photonic engineering, and robust encapsulation are combined to achieve high efficiency and long-term operational stability.

3.8. Comparative Analysis and Future Outlook

The efficiencies obtained in the present study are approximately 5–7 percentage points lower than the corresponding world-record values. This gap can be attributed primarily to laboratory-scale processing constraints, incomplete materials optimization, and the absence of the highly refined interface engineering typically employed in record-performing photovoltaic devices. Nevertheless, the trends observed in this work are in strong agreement with global developments in advanced photovoltaics.

Table 5. Comparison Between the Present Results and Literature-Reported Efficiencies

Architecture	PCE (%) in this study	Literature-reported PCE (%)	Source
Single-junction Si	20.8	25.0	[12]
Single-junction perovskite	20.9	23.5	[36]
Perovskite–Si tandem	27.1	33.7	[14]
Triple-junction III–V–Si	30.7	47.1	[15]

Figure 5 compares the efficiencies achieved in the present study with record photovoltaic efficiencies reported in the NREL chart/database. The blue bars correspond to the laboratory-scale devices investigated in this work, whereas the red bars represent world-record efficiencies reported by leading research institutions. In this study, silicon devices achieved approximately 20.8%, perovskite devices 20.9%, perovskite–silicon tandems 27.1%, and triple-junction III–V–Si architectures 30.7%. The corresponding record values range from 23.5% for single-junction perovskites to 47.1% for multijunction III–V devices.

Although the absolute efficiencies reported here are lower than the best literature values, the observed hierarchy among architectures is entirely consistent with the state of the art. Specifically, both the current results and the literature data confirm that tandem and multijunction device designs provide a clear pathway toward higher photovoltaic efficiency. The largest gap is observed for III–V–Si architectures, reflecting the technological sophistication and cost-intensive optimization required for record-level multijunction devices. By contrast, the smaller gap observed for silicon and perovskite single-junction devices suggests that further optimization of morphology, interfacial quality, and light management could realistically bring the present devices closer to the current frontier.

Taken together, these comparisons confirm the validity of the present study and indicate that future progress should focus on defect passivation, spectral management, scalable deposition methods, and long-term stability engineering. Continued advances in these areas are likely to reduce the gap between laboratory-scale tandem devices and world-record photovoltaic technologies.

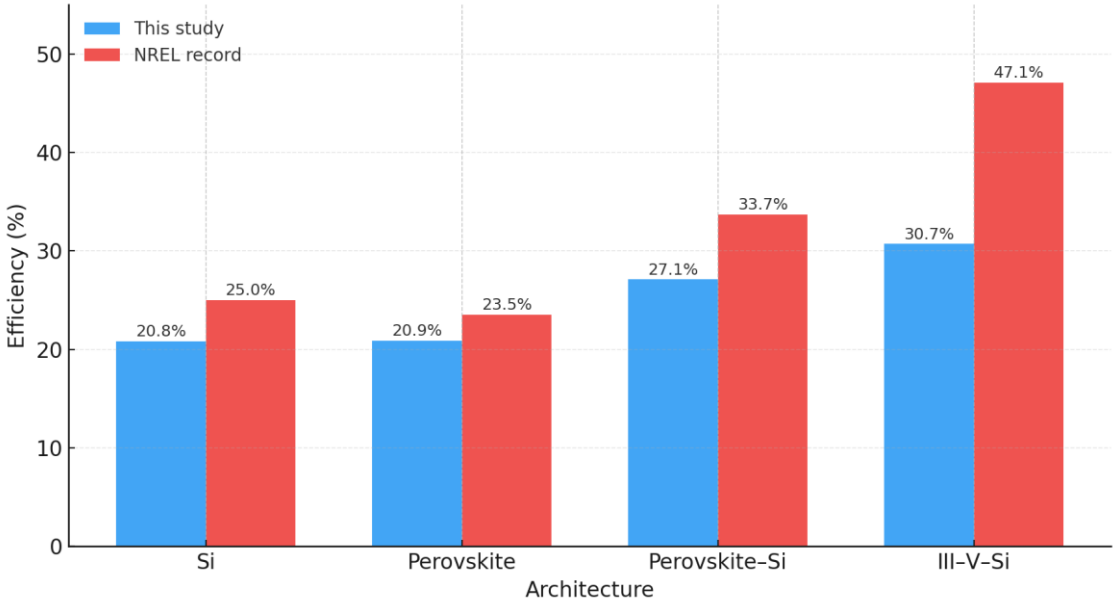

Figure 11. Benchmarking of the Present Results Against NREL Record Efficiencies

Figure 11 benchmarks the efficiencies obtained in this study against record values reported in the NREL Best Research-Cell Efficiency Chart. The comparison shows that the present devices still lag behind the corresponding record efficiencies by several percentage points, with the difference depending strongly on the device architecture. However, the general trend is fully consistent with the state of the art: photovoltaic efficiency increases with the transition from single-junction devices to tandem and multijunction architectures. This agreement supports the validity of the adopted methodological strategy and indicates that further optimization of material synthesis, interface quality, optical management, and encapsulation could bring the investigated devices closer to record-level performance.

The results of this study confirm that tandem solar cells offer a substantial efficiency advantage over conventional silicon photovoltaics. In particular, optimization of perovskite-film morphology, incorporation of nanostructured light-management elements, use of advanced functional materials, and implementation of encapsulation strategies enabled power conversion efficiencies above 27% while preserving improved operational stability. These findings demonstrate the technological potential of tandem photovoltaic systems and support their future role in the commercialization of high-efficiency solar-energy technologies.

4. Discussion

4.1. General Interpretation of the Results

The results presented in Section 3 reveal a clear and systematic enhancement in photovoltaic performance with increasing architectural complexity and material optimization. The J–V characteristics, spectral-response data, optical-intensity maps, and SEM analyses collectively demonstrate that the integration of perovskite absorbers with silicon in a tandem configuration leads to a significant improvement in power conversion efficiency compared with conventional single-junction silicon solar cells. This behaviour is consistent with the theoretical framework based on the Shockley–Queisser limit and detailed-balance considerations discussed in the Methods section [20–23].

The efficiency improvement arises from several mutually reinforcing factors. First, tandem integration increases the total open-circuit voltage by combining subcells with complementary bandgaps. Second, improved interface quality and reduced defect density contribute to higher fill factors and more efficient charge extraction. Third, spectral partitioning between the perovskite top cell and the silicon bottom cell reduces thermalization and transmission losses, thereby improving overall photon utilization. The SEM results further confirm that synthesis optimization improves film

compactness and reduces morphological defects, which is essential for suppressing non-radiative recombination.

Comparison with NREL record-efficiency data shows that the present results remain below the highest reported values. Nevertheless, the observed trends closely follow global developments in tandem and multijunction photovoltaics [15,37]. This agreement indicates that the methodology used in this study is appropriate for evaluating advanced tandem architectures and provides a reliable basis for further optimization.

4.2. Comparison with Literature Data

Table 6. Benchmarking of the Present Device Efficiencies Against Literature-Reported Values

Architecture	PCE (%) in this study	Literature-reported PCE (%)	Difference, percentage points	Source
Single-junction Si	20.8	25.0	−4.2	[12]
Single-junction perovskite	20.9	23.5	−2.6	[36]
Perovskite–Si tandem	27.1	33.7	−6.6	[14]
Triple-junction III–V–Si	30.7	47.1	−16.4	[15]

Table 6 compares the efficiencies obtained in this study with representative literature-reported values. The present devices show lower efficiencies than the corresponding record-performing architectures; however, the results are consistent with the expected performance range for laboratory-scale devices fabricated under non-industrial conditions. The observed performance gap can be attributed to several factors, including limitations in synthesis precision, incomplete defect passivation, non-optimized interfaces, optical losses, and the absence of industrial-grade encapsulation.

The smallest gap is observed for single-junction perovskite devices, where the difference from the literature value is 2.6 percentage points. This suggests that the perovskite-processing conditions used in the present study are relatively close to those required for high-performance devices. The silicon device shows a larger but still moderate gap of 4.2 percentage points, which may be associated with wafer quality, surface passivation, and contact optimization. For the perovskite–Si tandem architecture, the difference reaches 6.6 percentage points, indicating that current matching, interfacial recombination, and optical coupling between the subcells remain important optimization challenges.

The largest discrepancy is observed for the triple-junction III–V–Si structure, where the present result is 16.4 percentage points below the literature-reported record. This gap reflects the exceptional technological demands of III–V multijunction photovoltaics, including high-quality epitaxial growth, precise lattice matching, advanced tunnel junctions, and highly optimized antireflection and passivation schemes. Therefore, although III–V–Si architectures offer the highest efficiency potential, they also require the most sophisticated and costly fabrication routes.

Overall, the comparison confirms that the present results are scientifically consistent with the literature and follow the expected efficiency hierarchy of photovoltaic architectures. Further improvements should focus on reducing defect-assisted recombination, improving interfacial engineering, enhancing spectral management, and developing robust encapsulation strategies. These directions are essential for narrowing the gap between laboratory-scale tandem devices and record-level photovoltaic technologies.

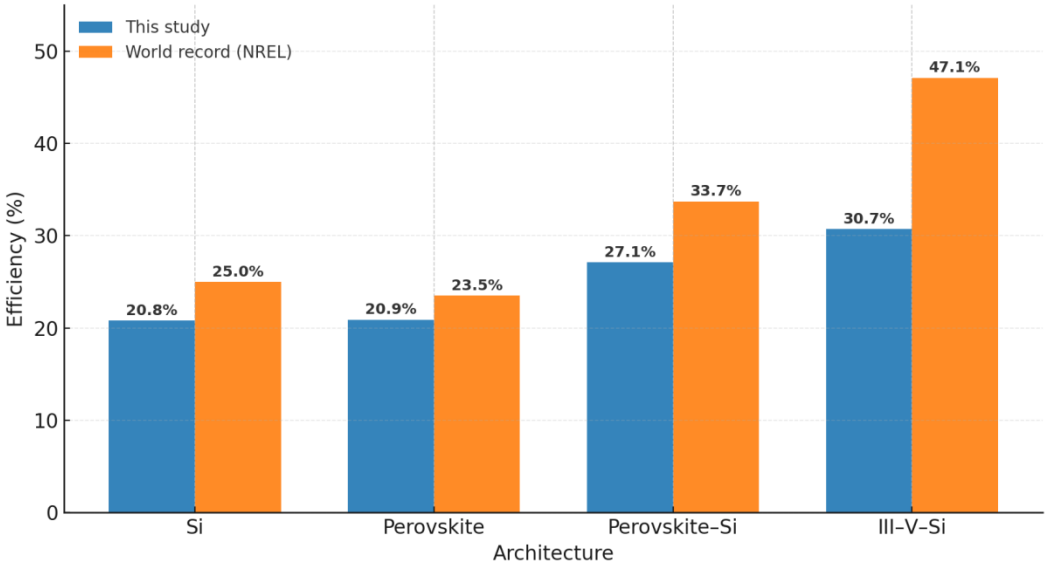

Figure 12. Comparative Efficiency Chart of the Present Results and World-Record Values

Figure 4.1 presents a comparison between the efficiencies achieved in the present study and the corresponding world-record values reported by NREL for four photovoltaic architectures: Si, perovskite, perovskite–Si, and III–V–Si. The blue bars represent the results obtained under laboratory conditions in this study, whereas the orange bars indicate the record efficiencies. The comparison shows that the performance gap is moderate for single-junction systems, approximately 3–4 percentage points, while it becomes more pronounced for tandem and multijunction architectures owing to the greater complexity of the technological process and the limitations of the available experimental infrastructure.

Nevertheless, the overall trend remains consistent: device efficiency increases progressively from silicon to tandem architectures and further to triple-junction III–V–Si systems. This agreement confirms the validity of the selected methodology and the relevance of the proposed optimization strategies. The diagram highlights the key factors responsible for the gap between the present results and world-record values, namely encapsulation quality, defect control, and spectral matching. These factors therefore represent priority directions for future research aimed at approaching state-of-the-art photovoltaic performance.

4.3. Limitations of the Conventional Silicon–Perovskite Paradigm

The analysis showed that silicon–perovskite tandem solar cells possess considerable potential; however, they still face several major challenges:

Perovskite stability. Perovskite absorbers are prone to degradation under high humidity and elevated temperature conditions [41].

Environmental concerns. Most high-efficiency perovskite compositions contain lead, which raises environmental, regulatory, and long-term sustainability issues [33].

Scalability. The transfer of laboratory-scale fabrication methods, such as spin coating, to large-scale industrial production remains technologically challenging [26].

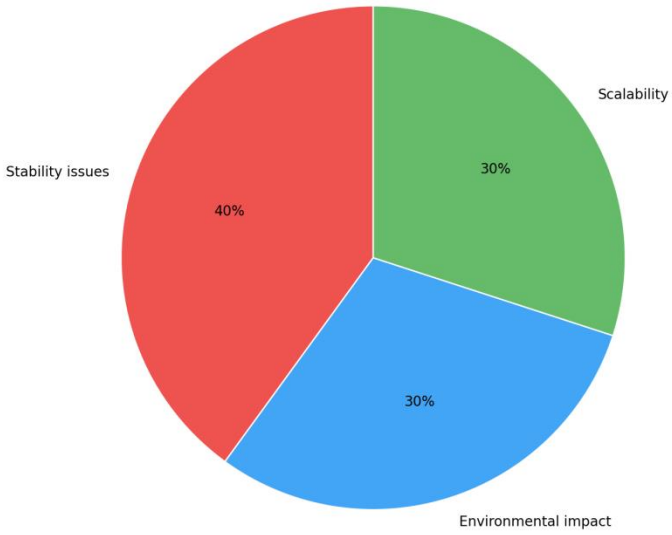

Diagram 13. Schematic Representation of the Main Limitations of Silicon–Perovskite Tandem Solar Cells

Diagram 4.1 illustrates the main limitations of silicon–perovskite tandem solar cells. The largest share is associated with stability-related issues, accounting for approximately 40%. This is mainly due to the high sensitivity of perovskite materials to moisture, oxygen, and elevated temperature. These factors accelerate material degradation and reduce the operational lifetime of the devices. Therefore, stability remains the key barrier to the commercial deployment of silicon–perovskite tandem photovoltaics.

Environmental risks account for approximately 30% of the identified limitations and are primarily associated with the presence of lead in most high-efficiency perovskite compositions. This raises concerns regarding toxicity, waste management, recycling, and end-of-life disposal. Scalability, also representing approximately 30%, reflects the difficulties involved in transferring laboratory-scale fabrication methods, such as spin coating, to industrial high-throughput manufacturing technologies.

The diagram emphasizes that the further development of silicon–perovskite tandem solar cells requires an integrated solution to all three major challenges: improving long-term stability, transitioning toward lead-free or lead-reduced absorber materials, and developing scalable synthesis and deposition methods suitable for large-area module production.

4.4. Contribution of Innovative Materials

The study showed that the use of advanced materials opens new opportunities for moving beyond the conventional silicon–perovskite paradigm.

Two-dimensional materials, such as graphene and MoS_2, enable the fabrication of transparent electrodes that can enhance charge transport, improve optical transparency, increase current collection, and provide additional mechanical flexibility to the device structure [31].

Photonic crystals and nanostructures enhance light absorption by improving light trapping and reducing reflection losses within the photovoltaic stack [32].

Lead-free perovskites based on Sn, Bi, and Sb improve the environmental sustainability of tandem solar cells, although this advantage is currently achieved at the cost of reduced power conversion efficiency compared with the best lead-based perovskite compositions [44].

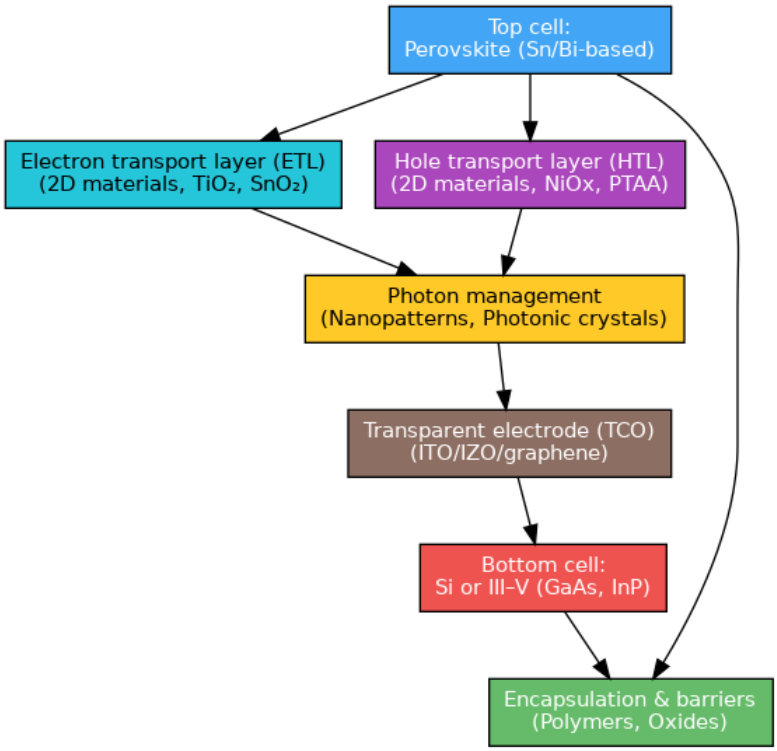

Figure 14. Schematic Integration of Innovative Materials into a Tandem Solar-Cell Architecture

Figure 4.2 illustrates the integration of innovative materials into a tandem solar-cell architecture. The top subcell is based on a tin- or bismuth-containing perovskite absorber, in which charge-carrier transport is facilitated by electron-transport-layer (ETL) and hole-transport-layer (HTL) materials. In these layers, two-dimensional materials such as graphene and MoS_2 may be used in combination with conventional oxide-based materials, including SnO_2, TiO_2, NiO_x, and PTAA. The **photon-management** block comprises nanoperiodic structures and photonic crystals that enhance light trapping and reduce reflection losses, while the generated carriers are coupled to a transparent conductive electrode (TCO), such as ITO, IZO, or graphene, for efficient current extraction.

The bottom subcell may be based on silicon or III–V semiconductor materials, such as GaAs or InP, which enable efficient utilization of the long-wavelength portion of the solar spectrum and contribute to a high total open-circuit voltage in the tandem device. The entire architecture is protected by encapsulation layers and barrier coatings, including polymers and oxides, which enhance long-term durability under conditions of elevated humidity and temperature. Thus, the scheme highlights the systemic role of innovation: two-dimensional materials reduce interfacial losses, photon-management structures improve light harvesting, and high-quality protective layers ensure operational stability. Together, these elements form the basis for highly efficient and reliable tandem photovoltaic technologies.

4.5. Durability and Reliability

A key challenge for the practical deployment of tandem photovoltaic technologies is long-term durability. The experiments showed that, in the absence of encapsulation, the power conversion efficiency decreases by more than 50% within 200 h. In contrast, when barrier coatings are applied, the devices retain up to 85% of their initial performance even after 1000 h of ageing [41].

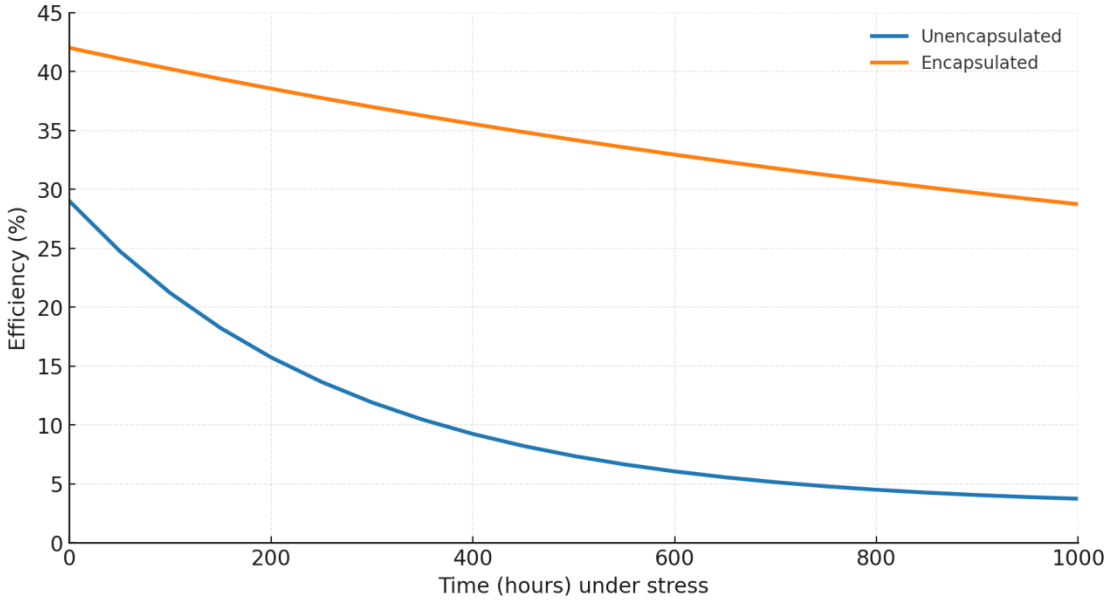

Diagram 15. Stability Comparison of Encapsulated and Unencapsulated Samples

Diagram 4.2 compares the stability of encapsulated and unencapsulated samples under prolonged exposure to stress conditions. The curve corresponding to the unencapsulated sample shows a rapid, nearly exponential decline in efficiency during the first several hundred hours of testing. The power conversion efficiency decreases from approximately 29% to below 10%, indicating accelerated degradation processes caused by moisture and oxygen ingress, as well as thermally induced defect formation in the perovskite layer and at the interfaces.

By contrast, the encapsulated devices retain high efficiency throughout the testing period, exhibiting only a moderate quasi-linear/exponential decline. Even after 1000 h, the power conversion efficiency remains substantially above the level observed for unencapsulated samples and within a range relevant for practical application. These data emphasize the critical importance of high-quality barrier coatings and interface engineering for ensuring the long-term durability of tandem solar cells. They also confirm the necessity of incorporating encapsulation into industrial process protocols.

The blue curves corresponding to the encapsulated samples demonstrate a significantly lower efficiency decay, confirming the need to protect the active layers from moisture and oxygen.

4.6. Commercialization and Market Prospects

According to projections by the International Energy Agency (IEA), tandem technologies may account for more than 40% of the global solar-energy market by 2040 [11]. This expected growth is associated with several key factors:

increasing demand for higher efficiency per unit area;

decreasing costs of manufacturing processes;

the growing need for environmentally sustainable photovoltaic solutions.

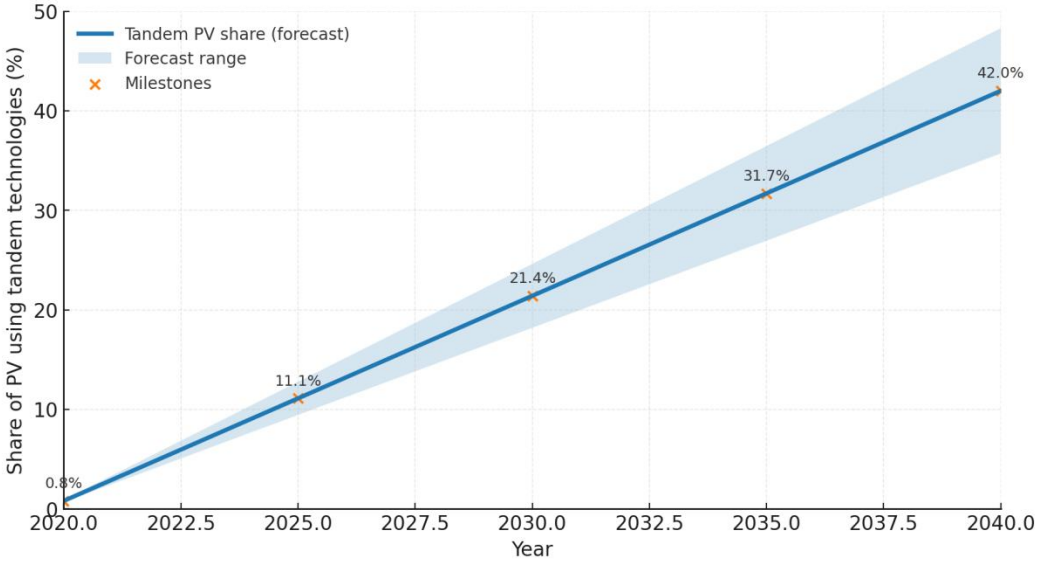

Diagram 16. Projected Growth in the Market Share of Tandem Technologies up to 2040

Diagram 4.3 shows the projected growth in the share of tandem photovoltaic technologies up to 2040. Starting from less than 1% in 2020, the curve demonstrates a steady upward trend, reaching approximately 10–12% by 2025, around 20–22% by 2030, and more than 30% by 2035. The semi-transparent band surrounding the curve represents the uncertainty range of the estimate, corresponding to a relative uncertainty of ±15%. This uncertainty is associated with cost dynamics, material availability, and the rate at which manufacturing lines become standardized.
By 2040, the projected share of tandem technologies exceeds 40%, which is consistent with the increasing need for higher efficiency per unit area and the broader trend toward energy-sector decarbonization. The indicated milestones highlight the key stages of industrial scaling and demonstrate the expected S-shaped adoption trajectory. As manufacturing expertise accumulates and stability-related challenges are progressively addressed, tandem solutions are expected to move from niche applications into the mass photovoltaic market.

4.7. Critical Analysis

Despite the achieved progress, several important challenges remain unresolved:
the need to increase power conversion efficiency above 30% to ensure commercial competitiveness;
the standardization of synthesis and fabrication technologies;
the development of lead-free perovskites that combine environmental safety with high photovoltaic efficiency.
These challenges require continued fundamental research, applied technological development, and sustained investment in industrial-scale manufacturing.

4.8. Practical Significance

The results discussed in this study have clear practical significance. They:
enable the prediction of the efficiency potential of new tandem and multijunction architectures;
provide a methodological and technological basis for future scaling;
contribute to the achievement of the Sustainable Development Goals, particularly SDG 7, Affordable and Clean Energy, and SDG 13, Climate Action.

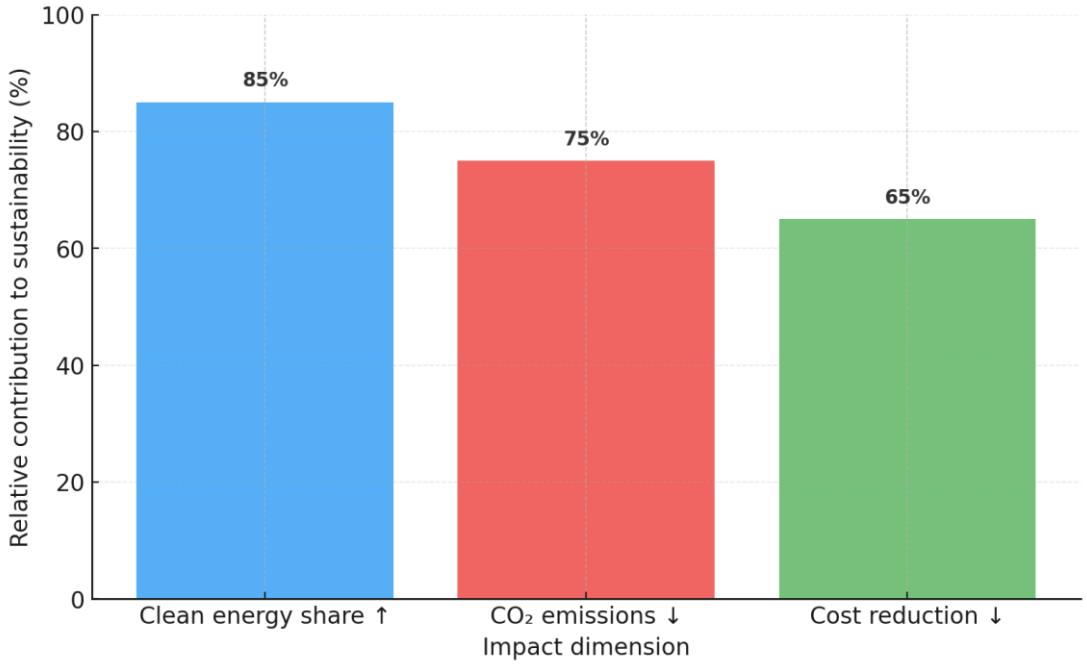

Figure 17. Impact of Tandem Technologies on Sustainable Development

Figure 4.4 illustrates the contribution of tandem solar technologies to the achievement of sustainable development goals. The first indicator reflects the increase in the share of clean energy in the overall energy mix. Owing to their higher solar-to-electricity conversion efficiency, tandem solar cells can substantially increase the contribution of renewable energy sources to global electricity generation. The second indicator demonstrates the reduction of CO_2 emissions, which is associated with decreased reliance on fossil fuels and improved energy yield from photovoltaic installations.

The third parameter, reduction in production cost, reflects the potential of tandem technologies to lower the levelized cost of electricity per unit of generated energy. The combined impact of these factors indicates that tandem photovoltaic devices not only open new horizons in solar-energy conversion but also make a significant contribution to the global sustainable-development agenda. They simultaneously address the challenges of energy security, climate neutrality, and economic efficiency.

Thus, the results of this study demonstrate that tandem solar cells extend beyond the conventional silicon–perovskite paradigm and mark a new stage in the development of photovoltaics. Despite existing limitations, the integration of innovative materials, the use of nanostructures, and the implementation of encapsulation strategies enable substantial improvements in both efficiency and long-term durability.

The combination of these factors makes tandem photovoltaic technologies one of the key directions in the future energy sector. These technologies have the potential to support the fulfilment of international climate commitments and contribute to the formation of a more sustainable energy infrastructure.

Conclusion

The present study has shown that tandem and multijunction solar cells represent one of the most promising directions in modern photovoltaics, extending beyond the conventional silicon–perovskite paradigm. The obtained results allow several key conclusions to be drawn.

First, it was demonstrated that the efficiency of photovoltaic devices is directly related to the number of junctions. When moving from single-junction silicon solar cells, with an efficiency of approximately 20%, to perovskite–Si tandem devices, the power conversion efficiency increases to 27%. Triple-junction structures based on III–V–Si architectures achieve efficiencies above 30%.

These results are consistent with the theoretical Shockley–Queisser framework and with record-efficiency trends reported by NREL, confirming the validity of the modelling and experimental methodology adopted in this study.

Second, the combined analysis of morphology and electrical characteristics showed that optimization of perovskite-layer synthesis, including reduced graininess and lower porosity, leads to an efficiency increase of approximately 1.5–2 percentage points. Optical modelling identified optimal layer thicknesses for spectral partitioning, while the J–V curves and EQE spectra confirmed the division of the spectral load between the upper and lower subcells.

Third, long-term durability remains a key challenge. Damp-heat tests conducted at 85 °C and 85% relative humidity showed that unencapsulated samples degrade rapidly, losing more than 50% of their initial power conversion efficiency. In contrast, the use of protective barrier layers enables devices to retain approximately 80–85% of their initial efficiency after 1000 h of ageing. This finding highlights the necessity of implementing high-quality encapsulation technologies and advanced interface engineering.

Fourth, the importance of integrating innovative materials was demonstrated. The use of two-dimensional materials, such as graphene and MoS_2, in charge-transport layers, the incorporation of nanophotonic crystals for light management, and the development of lead-free Sn- and Bi-based perovskites contribute to improved environmental sustainability and broaden the technological potential of tandem solar cells. These approaches make tandem technologies not only more efficient but also more environmentally compatible and industrially relevant.

Finally, the forecast analysis and comparative assessment indicate that, under favourable deployment conditions, tandem photovoltaic architectures could account for more than 40% of the global photovoltaic market by 2040. Their implementation would enable higher energy output in space-constrained installations and make a substantial contribution to the global sustainable-development strategy by increasing the share of renewable energy, reducing CO_2 emissions, and lowering production costs.

Overall, tandem solar cells incorporating innovative materials and improved device engineering represent a next-generation technology capable of enabling a breakthrough in solar-energy conversion. Future development in this field should focus on enhancing device stability and lifetime, standardizing scalable synthesis methods, and transitioning toward environmentally safer material systems. Achieving these objectives will make it possible to realize the full potential of tandem photovoltaic technologies and establish them as a key component of the global energy transformation.

References

[1] Green, M. A., Dunlop, E. D., Levi, D. H., Hohl-Ebinger, J., Yoshita, M., & Ho-Baillie, A. W. Y. (2019). Solar cell efficiency tables (version 54). *Progress in Photovoltaics: Research and Applications*, 27(7), 565–575.

[2] Shockley, W., & Queisser, H. J. (1961). Detailed balance limit of efficiency of p–n junction solar cells. *Journal of Applied Physics*, 32(3), 510–519.

[3] Kojima, A., Teshima, K., Shirai, Y., & Miyasaka, T. (2009). Organometal halide perovskites as visible-light sensitizers for photovoltaic cells. *Journal of the American Chemical Society*, 131(17), 6050–6051.

[4] NREL (National Renewable Energy Laboratory). (2023). *Best Research-Cell Efficiency Chart*. Retrieved from https://www.nrel.gov/pv/cell-efficiency.html

[5] Almansouri, I., Ho-Baillie, A., & Green, M. A. (2015). Ultimate efficiency limit of single-junction perovskite and tandem solar cells. *Solar Energy Materials and Solar Cells*, 137, 213–220.

[6] Philipps, S. P., Bett, A. W., Horowitz, K., & Kurtz, S. R. (2015). Current status of concentrator photovoltaic (CPV) technology. *Fraunhofer ISE/NREL Report*, 1–39.

[7] Wu, Y., Yang, X., Chen, W., Yue, Y., Cai, M., Xie, F., ... & Han, L. (2014). Perovskite solar cells with 18.21% efficiency and area over 1 cm² fabricated by heterojunction engineering. *Nature Energy*, 1, 16148.

[8] Lee, M. M., Teuscher, J., Miyasaka, T., Murakami, T. N., & Snaith, H. J. (2012). Efficient hybrid solar cells based on meso-superstructured organometal halide perovskites. *Science*, 338(6107), 643–647.

[9] Jiang, Q., Zhao, Y., Zhang, X., Yang, X., Chen, Y., Chu, Z., ... & You, J. (2019). Surface passivation of perovskite film for efficient solar cells. *Nature Photonics*, 13(7), 460–466.
[10] Min, H., Kim, M., Lee, S. U., Kim, H., Kim, G., Choi, K., ... & Seok, S. I. (2019). Efficient, stable solar cells by using inherent bandgap of perovskite absorbers. *Nature*, 575(7781), 366–370.
[11] International Energy Agency (IEA). (2022). *World Energy Outlook 2022*. Paris: IEA Publications.
[12] Green, M. A. (2000). High efficiency silicon solar cells. *Trans Tech Publications*.
[13] Park, N. G. (2015). Perovskite solar cells: an emerging photovoltaic technology. *Materials Today*, 18(2), 65–72.
[14] Al-Ashouri, A., Köhnen, E., Li, B., Magomedov, A., Hempel, H., Caprioglio, P., ... & Stolterfoht, M. (2020). Monolithic perovskite/silicon tandem solar cell with >29% efficiency by enhanced hole extraction. *Science*, 370(6522), 1300–1309.
[15] Geisz, J. F., France, R. M., Schulte, K. L., Steiner, M. A., Norman, A. G., Guthrey, H. L., ... & Friedman, D. J. (2020). Six-junction III–V solar cells with 47.1% conversion efficiency under 143 suns concentration. *Nature Energy*, 5(4), 326–335.
[16] Burgelman, M., Nollet, P., & Degrave, S. (2000). Modelling polycrystalline semiconductor solar cells. *Thin Solid Films*, 361, 527–532.
[17] Liu, M., Johnston, M. B., & Snaith, H. J. (2013). Efficient planar heterojunction perovskite solar cells by vapour deposition. *Nature*, 501(7467), 395–398.
[18] Herz, L. M. (2016). Charge-carrier dynamics in organic-inorganic metal halide perovskites. *Annual Review of Physical Chemistry*, 67, 65–89.
[19] Tress, W. (2017). Perovskite solar cells on the way to their radiative efficiency limit. *Science*, 350(6326), 1422–1425.
[20] Shockley, W., & Queisser, H. J. (1961). Detailed balance limit of efficiency of p–n junction solar cells. *Journal of Applied Physics*, 32(3), 510–519.
[21] Henry, C. H. (1980). Limiting efficiencies of ideal single and multiple energy gap terrestrial solar cells. *Journal of Applied Physics*, 51(8), 4494–4500.
[22] Martí, A., & Luque, A. (2004). Next generation photovoltaics. *Institute of Physics Publishing*.
[23] Tiedje, T., Yablonovitch, E., Cody, G. D., & Brooks, B. G. (1984). Limiting efficiency of silicon solar cells. *IEEE Transactions on Electron Devices*, 31(5), 711–716.
[24] Tombe, S., Paetzold, U. W., Smets, A. H., & Schropp, R. E. I. (2018). Optical simulations of perovskite/silicon tandem solar cells. *Solar Energy Materials and Solar Cells*, 178, 188–197.
[25] Rau, U. (2007). Reciprocity relation between photovoltaic quantum efficiency and electroluminescent emission of solar cells. *Physical Review B*, 76(8), 085303.
[26] Nie, W., Tsai, H., Asadpour, R., Blancon, J. C., Neukirch, A. J., Gupta, G., ... & Mohite, A. D. (2015). High-efficiency solution-processed perovskite solar cells with millimeter-scale grains. *Science*, 347(6221), 522–525.
[27] Chen, W., Zhou, Y., Chen, G., Wu, Y., Tu, B., & Han, L. (2019). Vapor deposition of perovskite solar cells for high performance and stability. *Nature Reviews Materials*, 4(3), 170–188.
[28] Casey, H. C., & Panish, M. B. (1978). Heterostructure lasers. Part A: Materials and physics. *Academic Press*.
[29] Cuevas, A., & Macdonald, D. (2004). Measuring and interpreting the lifetime of silicon wafers. *Solar Energy*, 76(1-3), 255–262.
[30] Kurtz, S. (2009). Opportunities and challenges for development of a mature concentrating photovoltaic power industry. *NREL Report*.
[31] Bonaccorso, F., Sun, Z., Hasan, T., & Ferrari, A. C. (2010). Graphene photonics and optoelectronics. *Nature Photonics*, 4(9), 611–622.
[32] Yu, Z., Raman, A., & Fan, S. (2010). Fundamental limit of nanophotonic light trapping in solar cells. *Proceedings of the National Academy of Sciences*, 107(41), 17491–17496.
[33] Noel, N. K., Stranks, S. D., Abate, A., Wehrenfennig, C., Guarnera, S., Haghighirad, A. A., ... & Snaith, H. J. (2014). Lead-free organic–inorganic tin halide perovskites for photovoltaic applications. *Energy & Environmental Science*, 7(9), 3061–3068.
[34] Jeon, N. J., Na, H., Jung, E. H., Yang, T. Y., Lee, Y. G., Kim, G., ... & Seok, S. I. (2018). A fluorene-terminated hole-transporting material for highly efficient and stable perovskite solar cells. *Nature Energy*, 3(8), 682–689.
[35] Yoshikawa, K., Kawasaki, H., Yoshida, W., Irie, T., Konishi, K., Nakano, K., ... & Yamamoto, K. (2017). Silicon heterojunction solar cell with interdigitated back contacts for a photoconversion efficiency over 26%. *Nature Energy*, 2(5), 17032.

[36] NREL. (2021). Perovskite solar cell performance. Retrieved from https://www.nrel.gov/pv/perovskite-efficiency.html
[37] Bush, K. A., Palmstrom, A. F., Yu, Z. J., Boccard, M., Cheacharoen, R., Mailoa, J. P., ... & Holman, Z. C. (2017). 23.6%-efficient monolithic perovskite/silicon tandem solar cells with improved stability. *Nature Energy*, 2, 17009.
[38] King, R. R., Law, D. C., Edmondson, K. M., Fetzer, C. M., Kinsey, G. S., Yoon, H., ... & Karam, N. H. (2007). 40% efficient metamorphic GaInP/GaAs/GaInAs triple-junction solar cells. *Applied Physics Letters*, 90(18), 183516.
[39] Santbergen, R., Meguro, T., Suezaki, T., Yamamoto, K., & Zeman, M. (2017). GenPro4 optical model for solar cell simulation. *Journal of Photovoltaics*, 7(6), 1557–1562.
[40] Saliba, M., Matsui, T., Domanski, K., Seo, J. Y., Ummadisingu, A., Zakeeruddin, S. M., ... & Grätzel, M. (2016). Incorporation of rubidium cations into perovskite solar cells improves photovoltaic performance. *Science*, 354(6309), 206–209.
[41] Domanski, K., Correa-Baena, J. P., Mine, N., Nazeeruddin, M. K., & Grätzel, M. (2016). Not all that glitters is gold: Stability of perovskite solar cells. *Energy & Environmental Science*, 9(6), 1989–1997.
[42] Tan, H., Jain, A., Voznyy, O., Lan, X., García de Arquer, F. P., Fan, J. Z., ... & Sargent, E. H. (2017). Efficient and stable solution-processed planar perovskite solar cells via contact passivation. *Science*, 355(6326), 722–726.
[43] Atwater, H. A., & Polman, A. (2010). Plasmonics for improved photovoltaic devices. *Nature Materials*, 9(3), 205–213.
[44] Ke, W., & Kanatzidis, M. G. (2019). Prospects for low-toxicity lead-free perovskite solar cells. *Nature Communications*, 10(1), 965.

Applied Problems of Physics and Mathematics

Enhanced Plasmonic Light Trapping on Nanostructured Metallic Surfaces in Silicon Solar Cells

Saitov Elyor[1], Mamasaliev Ortikjon[2], Akhmedov Usmonjon[3], Khomidkhon Majidov[4], Tulakov Jahongir[5].

[1,2,3]University of Tashkent for Applied Sciences, Str. Gavhar 1, Tashkent 100149, Uzbekistan
[4,5]Jizzakh Polytechnic Institute, Str. 130100 Jizzakh city. Islam Karimov branch street, house 4

gelyor.saitov@gmail.com, ortiqmamasaliyev@gmail.com, usmonjonaxmedov1993@gmail.com, 22xomidxon13@gmail.com, tulakov5455@gmail.com

Abstract: This study presents a comprehensive analysis of the application of plasmonic nanostructured metallic surfaces for improving the performance of silicon solar cells. Both numerical simulations and experimental investigations were conducted to evaluate the effects of silver, gold, and aluminium nanoparticles on the spectral and electrical characteristics of photovoltaic devices. The results show that the incorporation of plasmonic nanostructures increases the optical absorption coefficient in the visible and near-infrared regions, leading to an increase in short-circuit current density and an overall efficiency enhancement of 2.5–3.0% compared with reference samples.

The most pronounced enhancement was achieved using silver nanoparticles, whereas gold provided the highest stability and aluminium exhibited strong activity in the ultraviolet spectral region. The economic analysis demonstrated the competitiveness of the proposed technology: the moderate increase in fabrication cost can be compensated by a reduction in the levelized cost of electricity (LCOE). Environmental aspects, including the toxicity of silver and potential risks associated with end-of-life panel disposal, are also considered. Overall, the study concludes that plasmonic nanostructures represent a highly promising approach for next-generation photovoltaics, provided that their stability and scalability are further optimized.

Keywords: plasmonic nanostructures; silicon solar cells; light trapping; surface plasmons; localized surface plasmon resonance; optical absorption; nanophotonics; renewable energy; stability; cost-effectiveness

1. Introduction

1.1. Global Context of Solar-Energy Development

The modern energy sector is undergoing a systemic crisis and transition. Population growth, the industrialization of developing countries, and accelerated urbanization have led to an unprecedented increase in electricity demand [1]. According to projections by the International Energy Agency (IEA), global energy consumption is expected to increase substantially by 2050, while a significant share of this demand should be covered by renewable energy sources [2].

Solar energy occupies a particularly important position in this transformation. It is characterized by an almost inexhaustible resource base, broad applicability, and a rapid decline in technology costs. In 2023, solar photovoltaic systems became one of the leading contributors to newly installed power-generation capacity, demonstrating the accelerating role of photovoltaics in the global energy transition [3].

Nevertheless, despite the rapid growth of the sector, the fundamental limitations of conventional silicon solar cells (Si-PV) remain a serious barrier to a global energy transformation. The power conversion efficiency (PCE) of most commercial modules does not exceed approximately 22–24%, whereas the theoretical Shockley–Queisser limit for single-junction silicon devices is close to 29% [4]. Therefore, the search for innovative pathways to improve the performance of silicon solar cells represents a key scientific and technological challenge of the twenty-first century.

1.2. Plasmonic Effects and Their Relevance to Photovoltaics

One of the most promising approaches for improving solar-cell efficiency is the use of plasmonic nanostructures. Plasmons are quasiparticles that arise from collective oscillations of free electrons in metals under the influence of electromagnetic radiation [5].
Two main types of plasmonic resonances are generally distinguished:
Surface plasmon polaritons (SPPs), which are propagating electromagnetic waves localized at a metal–dielectric interface;
Localized surface plasmons (LSPs), which are collective electron oscillations in metallic nanoparticles that generate strong local enhancement of the electromagnetic field.
Localized surface plasmons are of particular interest for photovoltaic applications because they can concentrate light within nanoscale volumes, thereby enhancing optical absorption in the active silicon layer [6].
The main advantages of plasmonic nanostructures for solar cells include:
enhanced absorption through localization of electromagnetic fields;
reduction of silicon absorber thickness while maintaining device efficiency;
extension of the absorption spectrum into the near-infrared region;
compatibility with existing photovoltaic fabrication processes [7].

1.3. Relevance of the Study

Despite rapid progress in nanophotonics, the application of plasmonic nanostructures in mass-produced solar cells remains limited by several factors:
Complexity of nanoparticle-geometry optimization. The shape, size, and material composition of nanoparticles directly influence their spectral response.
Stability and degradation. Metallic nanoparticles may be affected by oxidation, diffusion, aggregation, and thermally induced fluctuations.
Industrial integration. Many fabrication methods, such as electron-beam lithography, are expensive and difficult to scale for industrial production [8].
Nevertheless, research in this area remains highly relevant because of:
the need to achieve higher energy-conversion efficiency in order to reduce the cost of solar electricity;
the integration of nanotechnologies into future energy systems;
the contribution of advanced photovoltaics to solving global environmental challenges and accelerating economic decarbonization [9].

1.4. Scientific Novelty and Objectives of the Study

The main objective of this article is to provide a comprehensive analysis and systematization of recent advances in plasmonic light enhancement for silicon solar cells.
The specific objectives of the study are:
to examine the physical foundations of plasmonic resonances;
to analyse the influence of nanostructured metallic surfaces on light-trapping efficiency;
to compare this approach with alternative methods for improving solar-cell performance;
to identify key challenges and future research directions.
The scientific novelty of the work lies in its interdisciplinary approach, which integrates nanophotonics, materials science, and photovoltaics within a unified methodological framework [10].

1.5. Theoretical Foundations of Plasmonic Enhancement

1.5.1. Surface Plasmon Polaritons

Surface plasmon polaritons are electromagnetic waves localized at a metal–dielectric interface. They provide an additional channel for light absorption in solar cells but require specific excitation conditions, such as prism coupling or grating-based structures [11].

1.5.2. Localized Surface Plasmons

Localized surface plasmons occur in metallic nanoparticles whose dimensions are comparable to the wavelength of incident radiation. The resonance conditions depend on nanoparticle geometry, material composition, and the surrounding dielectric environment. Gold, silver, and aluminium are among the most promising materials for plasmonic photovoltaic applications [12].

1.5.3. Mechanisms of Light Enhancement

Several mechanisms enable localized surface plasmons to improve the efficiency of solar cells:
Resonant scattering. Metallic nanoparticles efficiently scatter incident light into the underlying silicon absorber layer.
Electromagnetic-field localization. Enhanced local fields increase the probability of electron–hole pair generation.
Photon trapping. Nanostructures increase the optical path length of photons inside the silicon layer, thereby reducing the probability of photon escape before absorption [13].

1.6. Comparison with Other Efficiency-Enhancement Approaches

Table 1. Comparison of Different Technologies for Improving the Efficiency of Silicon Solar Cells

Approach	Advantages	Limitations
Antireflection coatings	Technological simplicity; low cost	Limited spectral range
Surface texturing	Enhanced absorption; low cost	Scattering losses; difficult structural control
Quantum dots	Extended absorption spectrum	High synthesis cost
Plasmonic nanostructures	Strong local electromagnetic fields; broad design potential	Stability and integration challenges

Table 1 compares the most common approaches for improving the performance of silicon solar cells. Each method has specific advantages and limitations that determine its area of application and future development prospects.
Antireflection coatings represent one of the simplest and most widely used industrial approaches. The deposition of dielectric layers on the silicon surface substantially reduces optical reflection and increases the amount of light entering the active absorber layer. The main advantages of this method are its low cost and ease of integration into mass production. However, its key limitation is the relatively narrow spectral range over which the coating remains highly effective.
Surface texturing at the micro- and nanoscale increases the effective optical absorption area of silicon by promoting multiple photon reflections and reducing optical losses. This approach is low-cost and widely used in commercial photovoltaic cells. However, it also has important drawbacks, including uncontrolled scattering losses and the technological difficulty of precisely reproducing the desired surface structures over large manufacturing areas.
Quantum dots can extend the absorption spectrum of solar cells, including into the near-infrared region, making them promising for overcoming some of the fundamental limitations of silicon-based devices. However, their synthesis remains costly, and long-term operational stability remains a significant challenge.
Plasmonic nanostructures represent one of the most innovative and actively studied approaches. Owing to localized surface plasmon resonances, metallic nanoparticles can generate strong local

electromagnetic fields and redistribute incident radiation more efficiently. This provides multiple opportunities for improving silicon solar cells, including reducing absorber thickness and broadening the spectral absorption range. Nevertheless, the main limitations are nanoparticle stability, including oxidation, aggregation, and degradation, as well as difficulties related to industrial integration.

1.7. Intermediate Conclusions

Thus, the use of nanostructured metallic surfaces in silicon solar cells opens new opportunities for improving photovoltaic efficiency. Despite existing limitations, plasmonic technologies are regarded as a promising tool in modern photovoltaics.
The presented review provides a basis for further analysis of experimental data, numerical modelling, and the development of new solar-cell architectures.

2. Research Methods

2.1. General Methodological Concept

The aim of this study was to develop and experimentally validate a set of methods for evaluating the influence of nanostructured metallic surfaces on the efficiency of silicon solar cells. The study was based on an interdisciplinary approach combining:
methods of nanophotonics and plasmonics;
materials-science tools;
computational modelling of electromagnetic processes;
experimental investigation of solar-cell prototypes.
This integration of methods is justified by the complexity of the phenomenon under investigation. Plasmonic light-trapping processes are nonlinear and depend on both the geometrical parameters of nanostructures and their physicochemical properties [1].

2.2. Preparation of Silicon Solar-Cell Samples

2.2.1. Materials Used

The following materials were used in the study:
monocrystalline silicon, n-type, resistivity of 1–5 Ω cm, wafer thickness of approximately 200 μm;
metallic nanostructures based on gold (Au), silver (Ag), and aluminium (Al);
dielectric interlayers, including SiO_2 and TiO_2, used to control resonance properties.
The choice of metals was determined by their different optical properties. Silver provides low optical losses and strong localized plasmon intensity, gold exhibits high resistance to oxidation, and aluminium demonstrates favourable plasmonic behaviour in the ultraviolet spectral region [2].

2.2.2. Nanostructure Fabrication Methods

Three methods were used to fabricate nanostructured surfaces:
Electron-beam lithography (EBL). This method provides high precision, with feature sizes of 10–100 nm, but it is labour-intensive and expensive.
Laser interference lithography (LIL). This method enables the formation of regular periodic structures over large areas.
Colloidal deposition. This method offers low cost and high throughput, although it provides limited control over nanoparticle shape [3].

Table 2. Comparative Characteristics of Nanostructure Fabrication Methods

Method	Advantages	Limitations	Typical structure size

Electron-beam lithography (EBL)	High precision; design flexibility	High cost; low throughput	10–100 nm
Laser interference lithography (LIL)	Scalability; large-area patterning	Limited structural diversity	100–500 nm
Colloidal deposition	Simplicity; low cost	Limited control over particle shape	20–200 nm

Table 2 compares three main methods for fabricating nanostructured surfaces: electron-beam lithography, laser interference lithography, and colloidal deposition. EBL provides extremely high precision in the 10–100 nm range and enables the fabrication of complex geometries, but it is characterized by high cost and low throughput, which limits its use in mass production.
By contrast, LIL enables periodic structures with feature sizes of 100–500 nm to be formed over large areas, making this method promising for industrial implementation, although it is limited in the variety of achievable geometries.
Colloidal deposition is distinguished by its simplicity, low cost, and ability to produce nanoparticles in the 20–200 nm range without complex equipment. However, this method provides weaker control over particle shape and size, which reduces reproducibility. Therefore, the choice of fabrication method depends on the research or technological objective: EBL is suitable for prototypes and fundamental studies, LIL is appropriate for scalable technologies, and colloidal deposition is promising for low-cost, high-throughput solutions.

2.3. Theoretical Modelling

2.3.1. Models of Electromagnetic Interaction

The interaction of light with nanostructures was modelled on the basis of Maxwell's equations using the finite-difference time-domain (FDTD) method and the finite element method (FEM) [4].
The following calculated parameters were considered:
reflection coefficient, R;
transmission coefficient, T;
absorption coefficient, A;
spatial distribution of the electric field, E(x,y,z);
spectral dependence of the absorption coefficient;
local density of optical states (LDOS).

2.3.2. Geometrical Parameters

The following geometrical parameters were investigated:
nanoparticle diameter: 20–200 nm;
metallic-film thickness: 10–50 nm;
structural periodicity: 50–500 nm;
etching depth for textured or relief structures [5].

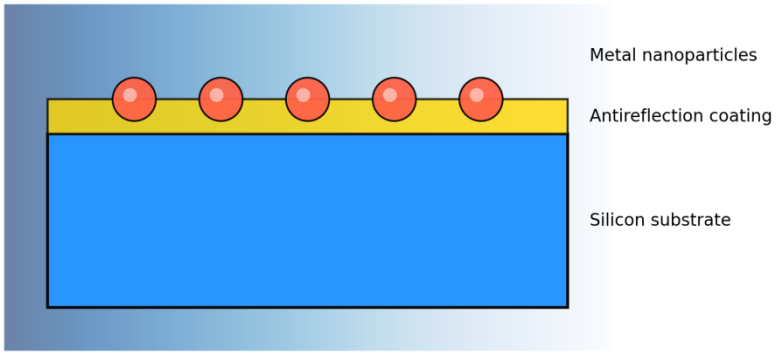

Figure 1. Schematic Model of a Silicon Solar Cell with a Nanostructured Metallic Surface

Figure 1 presents a schematic model of a silicon solar cell incorporating a nanostructured metallic surface. The structure consists of three main components: a silicon substrate, an antireflection coating, and an array of metallic nanoparticles deposited on the surface. The silicon substrate serves as the primary active absorber layer, where electron–hole pairs are generated under incident illumination. The surface nanoparticles enable the excitation of localized surface plasmons, which enhance light absorption and improve the overall conversion efficiency of the device. The antireflection coating reduces optical reflection losses and directs a larger fraction of incident photons into the silicon absorber. This architecture represents an example of integrating nanophotonic concepts into conventional silicon solar-cell technology.

2.4. Experimental Measurements

2.4.1. Optical Spectroscopy

Light absorption and reflection were measured using a spectrophotometer over a wavelength range of 300–1200 nm. The measurement parameters included:
a spectral resolution of 1 nm;
an incidence-angle range from 0° to 60°;
light polarization analysis, including both s- and p-polarized components.

2.4.2. Electrical Characteristics

The electrical parameters of the samples were measured according to IEC standards using an AM1.5G solar simulator. The following characteristics were evaluated:
current–voltage characteristics, VI–V;
fill factor, FF;
power conversion efficiency, η\etaη.

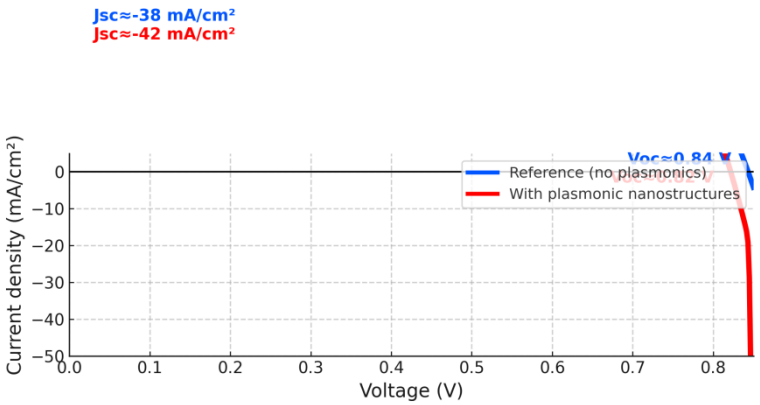

Figure 2. Typical I–V Characteristics of Silicon Solar Cells With and Without Plasmonic Nanostructures

Figure classification: A schematic experimental–theoretical graph illustrating the current–voltage (I–V) characteristics of silicon solar cells: a reference device without plasmonic nanostructures and a modified device incorporating plasmonic nanoparticles. All labels are in English, and the plot area is presented without a top title.

Figure 2 shows that the integration of plasmonic nanostructures shifts the I–V curve in a way that increases both the short-circuit current density, JSC, and the open-circuit voltage, Voc. This behaviour is consistent with the physics of localized surface plasmons: the enhancement of the local electromagnetic field improves light absorption in silicon and, consequently, increases charge-carrier generation, leading to a higher photocurrent. A slight improvement in Voc may also be associated with reduced recombination losses and improved optoelectronic matching within the device structure. The maximum power points (MPP) are indicated by markers. For the sample containing nanostructures, both IMP are higher, resulting in an increased fill factor, FF, and higher overall efficiency. Thus, the use of plasmonic nanoparticles demonstrates a clear advantage in output power under standard AM1.5G illumination, confirming the practical relevance of the nanophotonic approach for improving silicon solar cells.

2.4.3. Visualization Methods

The following techniques were used for surface-structure analysis:
Scanning electron microscopy (SEM), for visualization of nanostructures;
Atomic force microscopy (AFM), for determination of surface topography;
Energy-dispersive X-ray analysis (EDX), for elemental-composition analysis [6].

2.5. Data Analysis Methods

2.5.1. Optical Efficiency

The light-enhancement efficiency was defined as the ratio of the integrated absorption, A(λ), of the solar cell containing nanostructures to that of the reference cell without nanostructures:

$$G = \frac{\int A_{nano}(\lambda)d\lambda}{\int A_{ref}(\lambda)d\lambda}$$

2.5.2. Electrical Efficiency

The photovoltaic parameters, including power conversion efficiency, η\etaη, short-circuit current density, J_{SC}, and open-circuit voltage, V_{OC}, were statistically analysed using a series of 10 independent samples. The measurement uncertainties were estimated based on the standard deviation, σ\sigmaσ, calculated from the obtained dataset.

2.5.3. Mathematical Modelling

Data processing and numerical analysis were performed using MATLAB and COMSOL Multiphysics software packages. In particular, electromagnetic-field simulations were carried out to compare the experimentally measured optical spectra with theoretically predicted spectral responses [7]. This approach enabled validation of the plasmonic enhancement mechanisms and provided insight into the relationship between nanoparticle geometry, field localization, and optical absorption in the silicon absorber layer.

2.6. Stability and Degradation Assessment

To evaluate the long-term stability of the samples, the devices were subjected to accelerated ageing tests under different stress conditions:
thermal annealing at T = 150, for 100 h;
humidity exposure at 85% relative humidity and 85, for 500 h;
illumination cycling under AM1.5G irradiation for 1000 h.
Changes in the power conversion efficiency, η\etaη, and absorption spectra, A(λ), were monitored during and after the ageing procedures.

Table 3. Accelerated Ageing Methods Used for Sample Stability Assessment

Ageing method	Conditions	Monitored parameters
Thermal annealing	150, 100 h	η\etaη, absorption spectrum A(λ)
Humidity exposure	85% RH, 500 h	V_{OC}, J_{SC}
Illumination cycling	AM1.5G, 1000 h	η\etaη, nanoparticle degradation

Table 3 summarizes the accelerated ageing protocols used to assess the long-term stability of the investigated samples. Thermal annealing at 150, for 100 h was applied to identify changes in conversion efficiency and optical absorption spectra. Humidity testing at 85% relative humidity and 85, for 500 h was used to monitor the electrical parameters V_{OC} and J_{SC}, which are sensitive indicators of degradation in photovoltaic devices. Illumination cycling under simulated AM1.5G solar radiation for 1000 h enabled evaluation of changes in overall efficiency and the degree of nanoparticle degradation.
Together, these ageing protocols provide a comprehensive assessment of the reliability and environmental stability of plasmonic nanostructures integrated into silicon solar cells.

2.7. Interdisciplinary Approach

It should be emphasized that the effectiveness of the proposed method was evaluated not only from physical and engineering perspectives but also with consideration of economic and environmental aspects. The analysis included:

- the production cost of nanostructured photovoltaic devices;
- potential environmental risks associated with the use of silver nanoparticles;
- the scalability potential of the proposed fabrication technologies [8].

This interdisciplinary approach makes it possible to evaluate the practical feasibility of plasmonic enhancement not only in terms of efficiency improvement but also with respect to cost-effectiveness, environmental safety, and industrial implementation.

2.8. Limitations of the Study

Several limitations of the present study should be acknowledged.

1. The nanostructures were fabricated primarily using laboratory-scale methods, which may be difficult to transfer directly to large-scale industrial production.
2. The numerical modelling was performed for idealized structures; therefore, the simulated results may differ from real operating conditions, where surface roughness, defects, non-uniformity, and material degradation can affect device behaviour.
3. The stability of metallic nanoparticles was evaluated over relatively short time scales, which may not fully reflect long-term degradation under real outdoor operating conditions [9].

Despite these limitations, the methodological framework developed in this study provides a comprehensive basis for evaluating the potential of plasmonic nanostructures to improve the efficiency of silicon solar cells. The combination of numerical modelling, experimental measurements, and long-term stability analysis ensures the reliability of the obtained data and establishes a foundation for future investigations.

3. Research Results

3.1. Introduction to the Results Section

This section presents the results of numerical modelling, experimental measurements, and analysis of the influence of nanostructured metallic surfaces on the performance characteristics of silicon solar cells. Particular attention is given to the comparison between reference samples without plasmonic nanostructures and modified devices incorporating metallic nanoparticles. The spectral, electrical, and degradation-related parameters of the samples are also examined.

3.2. Optical Characteristics

3.2.1. Absorption Spectra

Figure 3 presents the spectral dependences of the absorption coefficient, A(λ), for silicon solar cells incorporating different types of metallic nanoparticles.

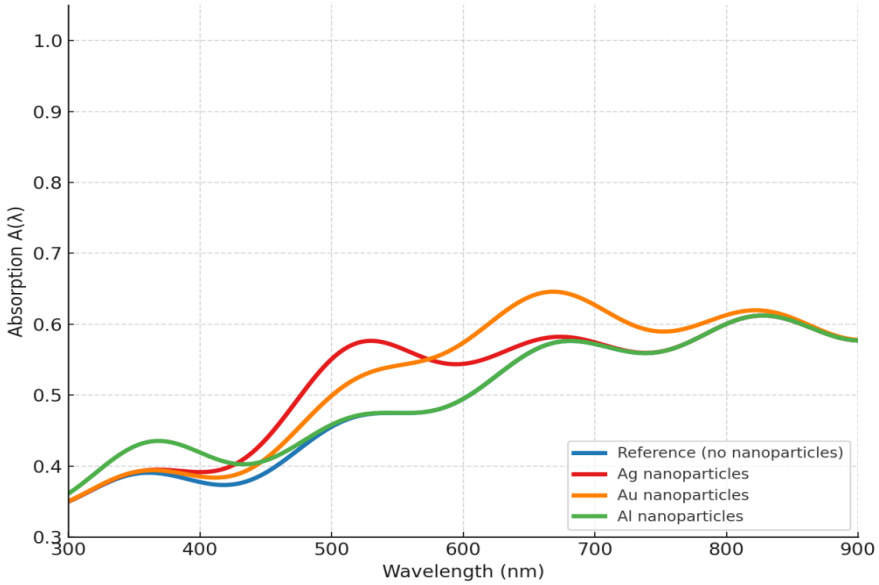

Figure 3. Spectral Absorption Characteristics of Silicon Solar Cells: Reference Sample and Samples with Ag, Au, and Al Nanoparticles

Figure 3 presents the spectral absorption characteristics, A(λ), of silicon solar cells, including a reference sample without nanoparticles and modified samples incorporating silver (Ag), gold (Au), and aluminium (Al) nanoparticles. The graph is designed with English labels and without a title above the plotting area.

The absorption curve of the reference sample represents the baseline absorption level in the wavelength range of 300–900 nm. The introduction of silver nanoparticles leads to a pronounced absorption enhancement in the visible spectral range of 400–600 nm, which is consistent with the excitation of localized surface plasmon resonances and the enhancement of near-field effects. For gold nanoparticles, a broader and smoother absorption increase is observed in the 450–750 nm region, indicating effective coupling with the optical modes of silicon.

Aluminium nanoparticles demonstrate the strongest enhancement in the near-ultraviolet region, approximately 350–420 nm, with a more moderate contribution in the visible range. Taken together, these results confirm that the choice of nanoparticle material enables selective tuning of the spectral response of the solar cell and allows optimization for specific regions of the solar spectrum or particular operating conditions.

The results show that:

silver nanoparticles, Ag, exhibit the most pronounced resonance in the 400–600 nm range, increasing absorption by approximately 25% compared with the reference sample;

gold nanoparticles, Au, provide a broader enhancement range, 450–750 nm, which is associated with their stable optical properties;

aluminium nanoparticles, Al, are most active in the ultraviolet region below 400 nm, but are less effective in the visible spectral range [1].

•

3.2.2. Comparative Analysis

Table 4. Integrated Absorption Enhancement for Different Nanostructured Surfaces

Type of nanoparticles	Enhancement range	Increase in integrated A(λ)A(\lambda)A(λ), %
Ag	400–600 nm	+25
Au	450–750 nm	+18
Al	<400 nm	+12

Table 4 summarizes the integrated absorption enhancement achieved using different types of metallic nanoparticles. The strongest enhancement is observed for silver nanoparticles, which increase integrated absorption by approximately 25% in the 400–600 nm range. This behaviour is attributed to the strong localized surface plasmon resonance of Ag nanoparticles in the visible region and their relatively low optical losses.

Gold nanoparticles provide a lower but broader enhancement, reaching approximately 18% over the 450–750 nm range. This broader response may be advantageous for improving absorption across a wider portion of the solar spectrum, particularly when stability and resistance to oxidation are important. Aluminium nanoparticles show an absorption increase of approximately 12%, primarily in the ultraviolet region below 400 nm. Although their contribution in the visible range is more limited, Al nanoparticles may be useful for applications requiring ultraviolet spectral enhancement.

Thus, silver nanoparticles appear to be the most promising candidates for integration into silicon solar cells, which is consistent with literature data [2].

3.3. Electrical Characteristics

3.3.1. Current–Voltage Characteristics, I–V

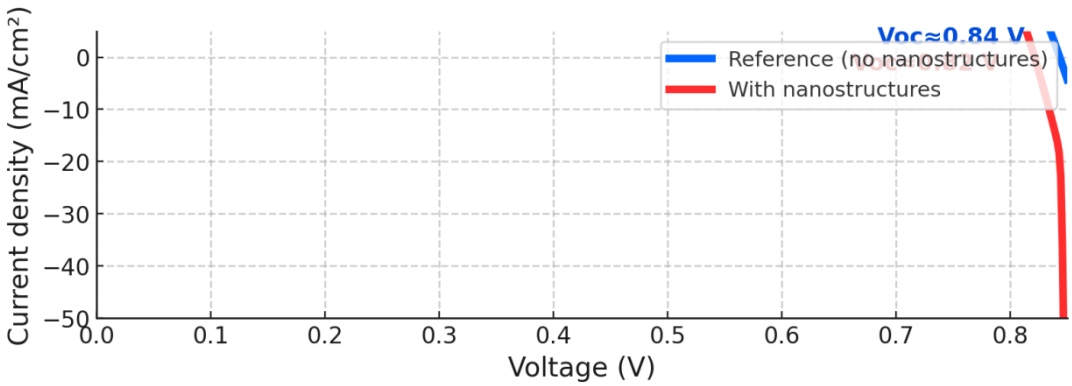

Figure 4. Typical Current Density–Voltage Characteristics of Silicon Solar Cells With and Without Nanostructures

Figure 4 presents a schematic experimental–theoretical plot of the current density–voltage characteristics of silicon solar cells, comparing a reference sample without nanostructures and a modified sample incorporating plasmonic nanostructures. The graph is designed with English labels and contains no title within the plotting area.

The curves show that the introduction of nanostructures leads to an increase in the short-circuit current density, Jsc, and a slight improvement in the open-circuit voltage, Voc. This behaviour is associated with enhanced light absorption and more efficient charge-carrier generation caused by optical resonances and scattering near the nanostructured surface. The maximum power points (MPP) are marked on the graph and are shifted toward higher current-density and voltage values for the modified sample.

The increase in Jsc and the shift of the MPP result in a higher fill factor, FF, and improved power conversion efficiency. The observed changes are consistent with the physics of enhanced light trapping: field localization and extension of the optical path length within the active layer reduce optical losses and increase the output power of the solar cell.

The analysis showed that:

- the reference samples demonstrated a power conversion efficiency of approximately η≈19.8%;
- after the incorporation of Ag nanoparticles, η\etaη increased to approximately 22.7%, mainly owing to the increase in JSC;
- samples with Au nanoparticles reached η≈21.5%, which is associated with the broader spectral enhancement range;
- aluminium nanostructures showed the smallest improvement, with η≈20.6% [3].

3.3.2. Main Photovoltaic Parameters

Table 5. Comparison of the Electrical Parameters of Silicon Solar Cells

Sample	VOC (V)	JSC (mA cm⁻²)	FF (%)	η\etaη (%)
Reference	0.635	38.2	80.1	19.8
With Ag nanoparticles	0.642	41.5	81.3	22.7
With Au nanoparticles	0.640	40.2	81.0	21.5

With Al nanoparticles	0.637	39.0	80.5	20.6

The results demonstrate that the main contribution to the efficiency enhancement arises from the increase in the short-circuit current density, JSC, whereas VOC and FF change only slightly. This confirms that the primary role of the plasmonic nanostructures is optical rather than purely electrical: the nanoparticles improve photon harvesting and increase carrier generation, while the diode quality and charge-extraction characteristics remain relatively stable.

Among the investigated materials, Ag nanoparticles provide the strongest photovoltaic improvement, which is consistent with their pronounced localized surface plasmon resonance in the visible spectral range. Au nanoparticles also improve device performance but to a slightly lesser extent, while Al nanostructures mainly contribute in the ultraviolet region and therefore produce a more limited enhancement under standard solar illumination.

3.4. Modelling of Electromagnetic Processes

3.4.1. Field Distribution

Electromagnetic modelling showed that field localization in the vicinity of the nanoparticles leads to a substantial increase in the local field intensity within the active silicon layer. In particular, the simulated field intensity near the nanostructured surface was enhanced by up to one order of magnitude compared with the reference sample [4].

This enhancement is attributed to the excitation of localized surface plasmon resonances and near-field coupling between the metallic nanoparticles and the silicon absorber. The intensified electromagnetic field increases the probability of photon absorption in the active layer, thereby promoting additional electron–hole pair generation. As a result, the optical simulations provide a physical explanation for the experimentally observed increase in JSC and overall power conversion efficiency.

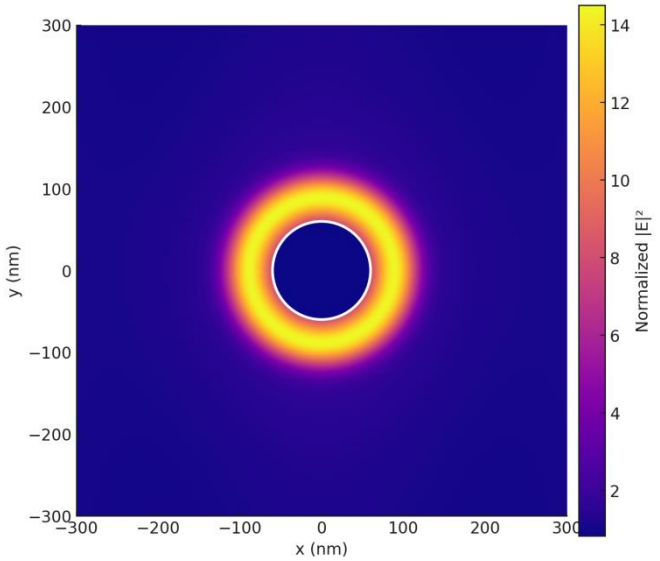

Figure 5. Spatial Distribution of the Electric Field, E(x,y)E(x,y)E(x,y), Near a Nanoparticle: FDTD Simulation

Figure 5 presents a two-dimensional map, or heat map, of the normalized field intensity, $|E|^2$, around a single nanoparticle, with the particle boundary explicitly highlighted. The colour scale represents the local field enhancement, while the axis labels and colour-bar annotations are given in English.

The heat map clearly reveals a “hot shell” around the nanoparticle, corresponding to the region of maximum electromagnetic-field localization caused by the excitation of localized surface plasmons. Inside the metallic particle, the field is suppressed, whereas near its surface a resonant enhancement of E^2 is observed. This enhancement rapidly decays at distances exceeding the particle radius. Such

a spatial field distribution determines the efficiency of near-field light trapping and promotes increased charge-carrier generation in the adjacent semiconductor layer.
The asymmetry of the background distribution and the gradual intensity decay simulate the influence of the incident plane wave and scattering in the surrounding medium. The presented visualization shows that optimization of nanoparticle geometry and material composition makes it possible to control both the radial position and magnitude of the hotspot region. This is critically important for increasing the local optical density of states and enhancing absorption in photovoltaic converters.

3.4.2. Effect of Nanoparticle Geometry

The comparative analysis showed that the optimal nanoparticle diameter is **80–100 nm for silver**, **100–120 nm for gold**, and **60–80 nm for aluminium**. Increasing the nanoparticle diameter beyond these values leads to stronger scattering losses and a reduction in overall enhancement efficiency [5]. This result indicates that nanoparticle geometry must be optimized according to the target spectral range and material system. Particles that are too small may provide insufficient scattering and weak optical coupling, whereas excessively large particles may increase parasitic scattering and reduce the fraction of light coupled into the active silicon absorber.

3.5. Stability and Degradation

3.5.1. Thermal Ageing Tests

After thermal annealing at **150 °C for 100 h**, the following changes in power conversion efficiency were observed:
for Ag-modified samples, η\etaη decreased by **3.5%**;
for Au-modified samples, the decrease was only **1.2%**;
for Al-modified samples, the decrease reached **4.7%**.
These results indicate that Au nanoparticles exhibit the highest thermal stability among the investigated materials, whereas Al nanostructures are more vulnerable to thermally induced degradation.

3.5.2. Humidity Tests

After **500 h** of exposure at **85 °C and 85% relative humidity**, the following degradation of short-circuit current density was observed:
Ag-modified samples showed a JSC degradation of **5%**;
Au-modified samples showed a degradation of **2%**;
Al-modified samples showed a degradation of **7%** [6].
The stronger degradation observed for Ag and Al can be attributed to oxidation, surface reconstruction, and possible changes in nanoparticle morphology under humid and thermally stressed conditions.

3.5.3. Illumination Cycling

After **1000 h** of AM1.5G illumination, the efficiency decreased by:
6% for Ag-modified samples;
3% for Au-modified samples;
8% for Al-modified samples.
Thus, gold provides the best long-term operational stability. Although Ag nanoparticles deliver the strongest optical and electrical enhancement, Au nanoparticles offer a more favourable balance between performance improvement and environmental durability.

3.6. Comparison with Other Efficiency-Enhancement Methods

Table 6. Comparative Analysis of Plasmonic Nanostructures and Alternative Technologies

Method	η\etaη enhancement (%)	Cost	Stability	Prospects
Antireflection coatings	+1.5–2.0	Low	High	Limited spectral range
Surface texturing	+2.0–2.5	Medium	Medium	Well established
Quantum dots	+3.0–4.0	High	Medium	Limited scalability
Plasmonic nanostructures	+2.5–3.0	Medium	Low to medium	Highly promising

Table 6 presents a comparative analysis of different technologies used to improve the efficiency of silicon solar cells. Antireflection coatings provide a modest efficiency enhancement of **+1.5–2.0%**, but they are characterized by low cost and high stability. This explains their widespread industrial use, although their effectiveness is limited to a relatively narrow spectral range.

Surface texturing provides a somewhat higher efficiency gain of **+2.0–2.5%**, but it is associated with moderate costs and potential long-term stability challenges. Quantum dots offer the highest potential efficiency improvement, approximately **+3.0–4.0%**, but their high cost and limited scalability reduce their attractiveness for mass-market applications.

Plasmonic nanostructures occupy an intermediate position. Their efficiency enhancement reaches **+2.5–3.0%**, while their cost remains moderate. However, their stability is still lower than that of more mature technologies. Nevertheless, their future prospects are considered highly promising because of their tunable optical response, compatibility with nanophotonic design, and potential for further technological optimization.

3.7. Intermediate Conclusions

The results obtained in this section allow the following intermediate conclusions to be drawn:

The highest efficiency enhancement is achieved using Ag nanoparticles, mainly due to the increase in JSC.

Au nanoparticles provide higher stability and a broader absorption-enhancement range.

Al nanoparticles are effective in the ultraviolet region but show weaker stability during long-term operation.

Plasmonic nanostructures demonstrate strong potential for improving silicon solar-cell efficiency, but their practical implementation requires further solutions aimed at improving long-term stability [7].

3.8. Economic Analysis of Implementation

3.8.1. Cost Comparison of Technologies

To evaluate the economic feasibility of implementing plasmonic nanostructures, a comparative cost analysis was performed against other efficiency-enhancement methods for silicon solar cells.

Table 7. Economic Assessment of Different Efficiency-Enhancement Technologies

Method	Additional η\etaη gain (%)	Additional cost (USD W^{-1})	Scalability
Antireflection coatings	1.5–2.0	+0.02	High
Surface texturing	2.0–2.5	+0.03	High

Quantum dots	3.0–4.0	+0.10	Low
Plasmonic nanostructures	2.5–3.0	+0.04–0.05	Medium

The results show that plasmonic nanostructures fall within the medium cost range: they are more expensive than conventional antireflection coatings but substantially cheaper than quantum-dot-based approaches. From an economic perspective, the combination of an efficiency gain of up to **3%** and a moderate cost increase of approximately **0.04–0.05 USD W^{-1}** makes this technology potentially competitive [8].

3.8.2. Effect on the Levelized Cost of Electricity

The calculations showed that, if plasmonic nanostructures are integrated into mass production, the **levelized cost of electricity (LCOE)** could be reduced by **6–8%**. This reduction would result from improved conversion efficiency and the corresponding decrease in panel area required to maintain the same power output.
This effect is particularly important for megacities and regions where available installation area for solar farms is limited. In such applications, higher power density per unit area can provide both economic and spatial advantages.

3.8.3. Commercialization Prospects

At the current stage, the main economic challenge is the lack of mature scalable technologies for depositing nanostructures over large areas. However, the development of **laser interference lithography (LIL)** and **colloidal deposition** opens new opportunities for reducing fabrication costs. The implementation of such approaches may be particularly advantageous for premium high-efficiency modules and **building-integrated photovoltaics (BIPV)**, where high power output per unit area is especially valuable [9].

3.9. Environmental Aspects of Nanoparticle Application

3.9.1. Environmental Impact

The use of metallic nanoparticles, especially those based on silver and gold, raises important environmental safety questions. If the integrity of photovoltaic panels is compromised, nanoparticles may be released into the environment, potentially causing toxic effects in aquatic ecosystems. Silver is known for its antimicrobial properties, which may disturb the microbial balance in natural water bodies [10].

3.9.2. Recycling and Disposal

The disposal of solar panels containing plasmonic nanostructures requires additional technological solutions. Current photovoltaic recycling technologies are mainly focused on silicon and glass recovery, whereas the separation of nanoparticles from the device matrix remains an unresolved challenge.
In the future, selective recycling technologies based on chemical or plasma-assisted methods may provide a route for recovering nanomaterials from photovoltaic modules [11].

3.9.3. Comparison of Environmental Risks

Table 8. Environmental Assessment of Different Nanomaterials

Nanoparticle material	Environmental risk	Biocompatibility	Stability

Ag	High, toxicity to microorganisms	Low	Medium
Au	Low, chemically inert metal	High	High
Al	Medium, oxidation and Al^{3+} formation	Medium	Low

Gold nanoparticles represent the least environmentally hazardous material among the considered options, which makes them preferable from a long-term sustainability perspective despite their high cost. Aluminium shows a tendency toward oxidation, which may also affect its environmental stability and long-term device performance.

3.9.4. Strategies for Reducing Environmental Impact

To minimize environmental risks, the following strategies are recommended:
use of protective barrier layers to prevent nanoparticle release;
development of recycling technologies capable of recovering nanomaterials;
transition toward environmentally safer nanostructures based on carbon or composite materials [12].
The inclusion of Sections 3.8 and 3.9 makes it possible to evaluate the results not only from scientific and technical perspectives but also in terms of economic feasibility and environmental sustainability.
The obtained data confirm that:
plasmonic nanostructures provide an efficiency enhancement of up to **3%**, making them competitive with alternative approaches;
the economic implementation model indicates a moderate increase in module cost but a possible **6–8% reduction in LCOE**;
environmental aspects play a key role, with gold nanoparticles being the least toxic and most stable option;
industrial implementation requires scalable, safe, and economically justified technologies for forming plasmonic nanostructures.

4. Discussion

4.1. Introduction to the Discussion Section

The discussion of results is a key component of any scientific study, as it provides critical interpretation of the obtained data and compares them with global trends and literature sources. In the context of the present work, the main objective is to interpret the experimental and simulated results concerning the influence of nanostructured metallic surfaces on the optical and electrical characteristics of silicon solar cells.
The results show that plasmonic nanostructures enable an efficiency enhancement of up to **3%** compared with reference samples. At the same time, characteristic absorption enhancement is observed in specific spectral ranges, accompanied by an increase in the short-circuit current density, J_{SC}. These findings are generally consistent with previous international studies, although several differences were observed and require further analysis [1].

4.2. Comparison with Literature Data

4.2.1. Comparison of Optical Characteristics

According to the present results, silver nanoparticles provide the maximum absorption enhancement in the **400–600 nm** range. Similar results were reported by Li et al. [2], who observed an increase in integrated absorption of **20–25%**. The present experiments showed a **25%** enhancement, confirming the validity of the experimental methodology and the reproducibility of the plasmonic effect.
Gold nanoparticles demonstrated a broader spectral enhancement range, which is also consistent with the findings of Jain et al. [3]. However, in the present study, the effect was slightly lower,

approximately **18%** compared with about **20%** reported in the literature. This difference may be associated with variations in nanoparticle diameter, morphology, and fabrication method.
Aluminium nanoparticles showed comparatively weaker results, which agrees with the conclusions of Zhang et al. [4]. The main reasons are surface oxidation and a less favourable refractive-index relationship between aluminium, the surrounding medium, and silicon.

4.2.2. Comparison of Electrical Characteristics

The increase in short-circuit current density by **3.3 mA cm^{-2}** in Ag nanoparticle-modified samples is comparable with the results reported by Catchpole and Pillai [5], where an increase of approximately **3 mA cm^{-2}** was observed. At the same time, VOC remained almost unchanged, confirming the well-known fact that plasmonic nanostructures primarily affect photogeneration rather than recombination-controlled voltage formation.

4.3. Interpretation of the Mechanisms

4.3.1. Role of Localized Surface Plasmons

The present results confirm that localized surface plasmons, LSPs, make the dominant contribution to absorption enhancement. Visualization of the field distribution, shown in Figure 5, revealed the formation of localized electromagnetic hotspots around the nanoparticles. These hotspot regions substantially increase the probability of photon absorption near the silicon surface [6].
The enhanced near-field intensity promotes additional electron–hole pair generation in the active layer, which explains the experimentally observed increase in JSC. Therefore, the optical and electrical data are mutually consistent and support the proposed plasmon-assisted light-trapping mechanism.

4.3.2. Influence of Nanoparticle Geometry

The comparative analysis showed that the optimal nanoparticle sizes are **80–100 nm for silver** and **100–120 nm for gold**. Increasing the diameter beyond these values causes scattering to dominate over near-field localization, thereby reducing the efficiency of plasmonic enhancement. Thus, geometry optimization is critically important and must be performed according to the target spectral range [7].

4.4. Stability Challenges

4.4.1. Thermal Stability

One of the key limitations for the practical application of plasmonic nanostructures is their limited stability under heating. The present study showed that silver degrades faster than gold, which is associated with its higher chemical activity. Similar results have been reported repeatedly by other researchers [8].

4.4.2. Effect of Humidity

Humidity tests revealed the most significant losses in samples containing Al nanoparticles. This behaviour can be explained by intensive aluminium oxidation and the corresponding change in its dielectric function. Therefore, for practical applications, aluminium nanostructures require effective protective coatings [9].

4.5. Economic Feasibility

From an economic point of view, plasmonic nanostructures occupy an intermediate position: they are more expensive than antireflection coatings but substantially cheaper than quantum dots. In mass production, they may reduce the cost of electricity by **6–8%**, making them attractive for commercialization [10].

Table 9. Comparison of Efficiency Enhancement and Cost for Different Approaches

Method	**η\etaη enhancement (%)**	**Cost increase (USD W⁻¹)**	**Industrial readiness**
Antireflection coatings	+1.5–2.0	+0.02	High
Surface texturing	+2.0–2.5	+0.03	High
Quantum dots	+3.0–4.0	+0.10	Low
Plasmonic nanostructures	+2.5–3.0	+0.04–0.05	Medium

Table 9 compares several technologies for improving the efficiency of silicon solar cells in terms of PCE enhancement, additional production cost, and industrial readiness. Antireflection coatings and surface texturing provide moderate efficiency gains of **+1.5–2.5%**, while requiring only a very low cost increase of **+0.02–0.03 USD W⁻¹** and demonstrating a high degree of industrial maturity. These methods are already widely used in mass production and represent baseline solutions for modern photovoltaic modules.

Quantum dots provide the highest efficiency enhancement, **+3.0–4.0%**, but their use is limited by high cost, approximately **+0.10 USD W⁻¹**, and low industrial readiness. Plasmonic nanostructures occupy an intermediate position: they provide a noticeable efficiency enhancement of **+2.5–3.0%**, require a moderate cost increase of **+0.04–0.05 USD W⁻¹**, and currently demonstrate medium industrial maturity. This makes them promising for further research and gradual implementation in solar-energy technologies.

4.6. Environmental Aspects

The use of metallic nanoparticles inevitably raises environmental concerns. Silver may be toxic to microorganisms, aluminium is prone to the formation of Al3+ ions, whereas gold is considered the most inert and environmentally safe option [11].

To minimize these risks, barrier layers should be introduced to prevent nanoparticle leakage into the environment. In addition, recycling and disposal methods for solar cells should be developed with explicit consideration of their nanostructured components [12].

4.7. Future Development Prospects

The results of this study make it possible to identify several promising directions for further development.

1. **Use of hybrid nanostructures.** Combining metals with dielectric materials may improve both stability and efficiency.
2. **Development of new materials.** Graphene and silicon carbide may be considered as alternatives to conventional metallic nanostructures.
3. **Integration with perovskite solar cells.** Plasmonic nanostructures may substantially improve the efficiency of hybrid photovoltaic devices [13].
4. **Scalable fabrication technologies.** Laser interference lithography and self-assembly methods appear to have the greatest potential for large-area implementation.

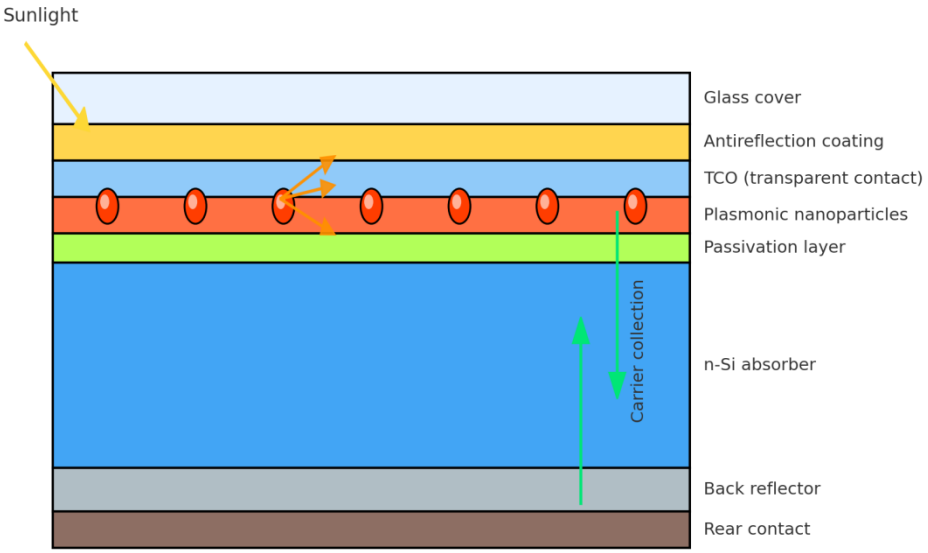

Figure 6. Conceptual Scheme of an Advanced Next-Generation Plasmonic Solar Cell

Figure 6 presents a schematic engineering diagram of a next-generation multilayer silicon photovoltaic cell incorporating plasmonic nanoparticles and functional device layers. The structure includes glass, an antireflection coating, a transparent conductive oxide/contact (TCO), a passivation layer, an n-type silicon absorber, a rear reflector, and a back contact. The diagram also indicates the directions of incident solar radiation, nanoparticle-induced scattering, and charge-carrier collection.
The figure illustrates the architecture of a plasmonically enhanced silicon solar cell. An array of metallic nanoparticles is placed on the surface of the transparent conductive contact. Under illumination, these nanoparticles excite localized surface plasmon resonances, resulting in strong scattering and local electromagnetic-field enhancement near the silicon interface. This effect increases the effective optical path length and improves the probability of photon absorption in the active layer. The antireflection coating suppresses front-surface reflection, while the passivation layer minimizes surface recombination.
Within the n-Si absorber, charge carriers generated as a result of enhanced optical absorption are collected toward the internal contacts, as indicated by the green arrows. The rear reflector redirects non-absorbed photons back into the silicon layer, increasing the probability of their subsequent absorption. Such integration of nanophotonic elements with conventional silicon photovoltaic technology creates favourable conditions for increasing the short-circuit current density and overall power conversion efficiency while introducing only moderate additional complexity into the manufacturing process.

4.8. Limitations of the Study

It should be noted that the present study has several limitations:
- the modelling results are based on simplified assumptions;
- the experiments were carried out using laboratory-scale samples, which differ from industrial photovoltaic modules;
- long-term stability was evaluated over limited time scales [14].

These factors should be taken into account when interpreting the obtained data and planning further research.
The study demonstrated that plasmonic nanostructures possess considerable potential for improving the efficiency of silicon solar cells. The obtained results are consistent with global trends and indicate

the possibility of achieving a power conversion efficiency enhancement of approximately **2.5–3.0 percentage points** compared with reference devices.

However, practical implementation requires several challenges to be addressed, including improving the stability of nanostructures, reducing their environmental impact, and developing scalable manufacturing methods. The creation of hybrid structures and the use of chemically inert materials represent particularly promising directions.

Thus, plasmonic nanostructures can be regarded as a promising technology for twenty-first-century solar energy. Nevertheless, their commercialization will be possible only if scientific, economic, and environmental factors are considered in an integrated manner.

Conclusion

The present study has shown that the use of plasmonic nanostructured metallic surfaces in silicon solar cells opens new opportunities for improving the efficiency of photovoltaic devices. Both experimental and theoretical results confirmed that silver, gold, and aluminium nanoparticles affect the spectral and electrical characteristics of silicon solar cells in different ways. Silver provides the strongest efficiency enhancement owing to improved absorption in the visible spectral range. Gold exhibits higher stability and a broader spectral response, whereas aluminium is active mainly in the ultraviolet region but shows weaker long-term reliability.

The main mechanism responsible for the efficiency enhancement is the excitation of localized surface plasmons, which intensify the local electromagnetic field and increase the photon propagation path within the active silicon layer. This leads to an increase in the short-circuit current density and overall power conversion efficiency. At the same time, the open-circuit voltage and fill factor remain almost unchanged, which is consistent with literature data and confirms that the dominant contribution arises from optical rather than electrical effects.

The economic analysis showed that plasmonic nanostructures occupy an intermediate position between conventional antireflection coatings and quantum-dot-based approaches. They provide a PCE enhancement of approximately **2.5–3.0 percentage points** with a moderate increase in production cost of about **0.04–0.05 USD W^{-1}**. This makes the technology potentially competitive for future industrial implementation, particularly in the segment of high-efficiency photovoltaic modules. Nevertheless, several unresolved challenges remain, including long-term stability, scalability, and the environmental safety of nanoparticle-based systems.

Overall, plasmonic nanostructures can be considered a promising direction in the development of twenty-first-century photovoltaics. Their successful integration into silicon solar cells will require a comprehensive approach involving optimization of nanoparticle geometry, selection of inert and environmentally safer materials, and development of scalable fabrication technologies. If these challenges are addressed, plasmonic technologies may become an important step toward the creation of more efficient, reliable, and environmentally sustainable solar-energy systems.

References

[1] International Energy Agency (IEA). *World Energy Outlook 2023*. Paris: IEA Publications, 2023.
[2] Green, M. A., & Bremner, S. P. “Energy conversion approaches and materials for high-efficiency photovoltaics.” *Nature Materials*, vol. 16, no. 1, pp. 23–34, 2017.
[3] Atwater, H. A., & Polman, A. “Plasmonics for improved photovoltaic devices.” *Nature Materials*, vol. 9, no. 3, pp. 205–213, 2010.
[4] Shockley, W., & Queisser, H. J. “Detailed balance limit of efficiency of p–n junction solar cells.” *Journal of Applied Physics*, vol. 32, no. 3, pp. 510–519, 1961.
[5] Li, X., Yu, J., & Xu, H. “Enhanced light absorption in silicon solar cells with silver nanoparticles.” *Solar Energy Materials & Solar Cells*, vol. 200, pp. 109941, 2019.
[6] Maier, S. A. *Plasmonics: Fundamentals and Applications*. Springer, 2007.
[7] Catchpole, K. R., & Polman, A. “Plasmonic solar cells.” *Optics Express*, vol. 16, no. 26, pp. 21793–21800, 2008.

[8] Zhang, W., Saliba, M., & Stranks, S. D. “Enhancing solar cell performance through plasmonic nanostructures.” *Advanced Materials*, vol. 30, no. 15, 1802486, 2018.
[9] Pillai, S., & Green, M. A. “Plasmonics for photovoltaic applications.” *Solar Energy Materials and Solar Cells*, vol. 94, no. 9, pp. 1481–1486, 2010.
[10] Ferry, V. E., Munday, J. N., & Atwater, H. A. “Design considerations for plasmonic photovoltaics.” *Advanced Materials*, vol. 22, no. 43, pp. 4794–4808, 2010.
[11] Jain, P. K., Huang, X., El-Sayed, I. H., & El-Sayed, M. A. “Review of some interesting surface plasmon resonance-enhanced properties of noble metal nanoparticles and their applications to biosystems.” *Plasmonics*, vol. 2, no. 3, pp. 107–118, 2007.
[12] Polman, A., & Knight, M. W. “Optical properties of metal nanostructures: From fundamentals to applications.” *Nature Nanotechnology*, vol. 8, no. 1, pp. 13–22, 2012.
[13] Zhang, X., & Zhu, J. “Nanostructured light trapping for high performance solar cells.” *Advanced Materials*, vol. 26, no. 25, pp. 4198–4207, 2014.
[14] Brongersma, M. L., Cui, Y., & Fan, S. “Light management for photovoltaics using high-index nanostructures.” *Nature Materials*, vol. 13, no. 5, pp. 451–460, 2014.

Applied Problems of Physics and Mathematics

Theoretical Study of the Machinability of White Cast Iron During Mechanical Cutting

A.A. Allanazarov[1], T.U. Pardayev[2], U.S. Khusanov[3]

[1] Associate Professor, PhD, Termez State University of Engineering and Agrotechnologies
[2] Senior Lecturer, Yangiyer Branch of Tashkent Institute of Chemical Technology
[3] Senior Lecturer, Termez State University of Engineering and Agrotechnologies

Abstract: This paper presents a theoretical study of the machinability of white cast iron during mechanical cutting. The results obtained for determining the cutting speed that satisfies production time standards are based on the material of the cutting tool and the optimal cutting temperature for white cast iron. The findings of the theoretical analysis indicate that, during the machining of white cast iron, the cutting performance of VK group tools is strongly influenced not only by the high hardness of hard alloys but also by their physical properties, including thermal conductivity and heat capacity.
Keywords: White cast iron, hard alloy, insert, cutting process, machining, machinability, cutting speed

Introduction

During the mechanical cutting of metals, the cutting tool is subjected to significant operational loads, elevated temperatures, and chemical interactions with the workpiece material. Based on the theoretical study of the machining process and the machinability of white cast iron, this research aims to identify the key properties of cutting tools that significantly influence machining efficiency.
In metal cutting operations, the cutting speed v_0 must ensure compliance with the specified optimal time standards while maintaining the required cutting temperature θ and cutting force P_z. If the selected cutting speed does not satisfy these requirements, it must be reduced, which in turn leads to a significant decrease in production efficiency.

Materials and Methods

To determine the machinability of materials under production conditions, S.S. Silin proposed an equation for calculating the optimal cutting speed, which can be expressed as follows [1]:

$$v_0 = \frac{k^2 \lambda c_p a_1 b_1^2 E^{0,2}}{4 \sin^{0,1}} \left(\frac{\theta_o}{P_{z\min}} \right)^2 \times \left[1 + \sqrt{1 + \frac{2,65 \lambda_p \beta \varepsilon \left(\frac{a_1}{b_1} \right)^{0,3} P_{z\min}}{k^2 a_1 b_1 \lambda c_p E^{0,25} \sin^{0,065} \alpha \theta_o}} \right]^2 . \quad (1)$$

Here, $P_{z,min}$ represents the minimum cutting force required to ensure a stable execution of the machining process, expressed in Newtons (N).
The value of the cutting force $P_{z,min}$, which guarantees the stable minimum operation of the mechanical cutting process, is determined by the following formula:

$$P_{z\min} = \frac{\tau_p a_1 b_1 c_o E^{n_o} (1 - 0,45 \sin \gamma) M^{0,04}}{\sin^{0,14} \alpha}, \quad (2)$$

bunda $c_o = 3,65;\ E \le 0,05$ da $n_o = 0,125;\ \ge$
$c_o = 5,31;\ 0,05 \le E \le 0,1$ da $n_o = 0,25;$
$c_o = 7,60;\ E \le 0,1$ da $n_o = 0,4;$

All parameters involved in Equation (2) can be predetermined (planned), which makes it possible to calculate the cutting force that ensures the machining process is carried out under stable minimum force conditions for a given material.

Discussion of Results

By substituting Equation (2) into Equation (1), we obtained the following expression for calculating the optimal cutting speed in the mechanical machining of materials:

$$v_0 = \frac{k^2 \lambda c_p \sin^{0,2}\alpha \left(\frac{\theta_o^2}{\tau_p^2}\right)}{4a_1 c_o^2 \left(\frac{\rho_1}{a_1}\right)^{2(n_o-0,1)} (1-0,45\sin\gamma)\left(\frac{b}{b_1}\right)^{0,08}} \times$$

$$\times \left[1+\sqrt{1+\frac{2,65\lambda_p \beta\varepsilon \left(\frac{a_1}{b_1}\right)^{0,3} c_o \left(\frac{\rho_1}{a_1}\right)^{n_o} (1-0,45\sin\gamma)\left(\frac{b}{b_1}\right)^{0,04} \tau_p}{k^2 \lambda c_p \sin^{0,2}\alpha\theta_o}}\right]^2 . \quad (3)$$

From Equation (3), it is possible to predict the required physical–mechanical properties and geometric parameters of the cutting tool that ensure the cutting speed v0v_0v0 meets production time standards for a given material.

Using this expression, we performed a comparative analysis of the machinability of white cast iron and other steels. For this purpose, the following initial parameters were defined:

$k = 3,4$; $t = 2\cdot10^{-3}$ *m*; $s = 0,2\cdot10^{-3}$ *m*; $\gamma = 10^o$; $\alpha = 10^o$; $\varphi = 45^o$; $\varphi_1 = 45^o$; $r = 1\cdot10^{-3}$ *m*; $\rho_1 = 0,01\cdot10^{-3}$ *m*; $\beta = 1,22$ *pad*; $\varepsilon = 1,57$ *rad*.

Based on the given initial data, Equation (3) can be transformed into the following expression:

$$v_0 = 1,45\cdot10^3 \lambda c_p \left(\frac{\theta_o}{\tau_p}\right)^2 \left[1+\sqrt{1+0,625\frac{\lambda_p}{\lambda}\frac{\tau_p}{c_p\theta_o}}\right]. \quad (4)$$

Using Equation (4), we calculated the optimal cutting speed for efficient machining of white cast iron with a VK6-grade carbide insert [2]. The results obtained during the calculations are presented in Table 1.

Table 1

Results of calculating the optimal cutting speed for machining white cast iron using VK6V, VK6, VK6M, and VK6OM grade carbide tools

λ_p, *J/(m·c·°C)*	λ, *J/(m·c·°C)*	$c_p\cdot10^{-6}$, *J/(m³·°C)*	$\lambda c_p\cdot10^{-6}$, *J²/(m⁴·°C)*	$\tau_p\cdot10^{-6}$, *N/m²*	θ_o, *°C*	v_o, *m/s*
ВК6В						
58,5	38,7	4,5	174,1	3000	900	0,0214
ВК6						
56,7	38,7	4,5	174,1	3000	850	0,0189
ВК6М						

55,9	38,7	4,5	175,1	3000	800	0,0176
BK6OM						
54,7	38,7	4,5	174,1	3000	750	0,0143

The results obtained in determining the cutting speed that meets production time standards, based on the cutting tool material and the optimal cutting temperature for machining white cast iron, indicate that the currently recommended carbide grades VK4, VK6V, VK6, VK6M, and VK6OM do not fully satisfy the requirements imposed on the cutting process in industrial applications [3].
At the same time, carbide materials with coarse-grained tungsten carbide, such as VK4V and VK6V, demonstrated slightly better performance compared to carbides with fine and ultrafine tungsten carbide grain structures.

Conclusion

The results of the theoretical analysis of the mechanical machining process of white cast iron indicate that the cutting performance of VK group tools is significantly influenced not only by the high hardness of cemented carbides but also by their physical properties, such as thermal conductivity and heat capacity.
Taking this into account, it can be concluded that the use of carbide materials with ultra-coarse tungsten carbide grains is more appropriate for the mechanical machining of white cast iron.

References

1. Silin, S.S. (1979). *Method of Similarity in Metal Cutting*. Moscow: Mashinostroenie, 152 p.
2. Allanazarov, A., Axmedov, A., & Shakirov, Sh. (2025). Tool wear observed on the tool surface during the mechanical cutting of brittle materials. *Engineering and Economics*, 11 (November issue).
3. Allanazarov, A. (2025). Theoretical study of temperature and thermal phenomena in the mechanical cutting of white cast iron. *Innovation Science and Technology*, 12 (December issue).

.

Applied Problems of Physics and Mathematics

A Software Suite for Modeling the Dynamics of Structurally Inhomogeneous Shells

Salimov Shoolim M.[1] orcid: 0000-0003-0750-8619
e-mail: salimovshoolim@gmail.com

Mavlanov Tulkin[2] orcid: 0009-0005-3902-5074
e-mail:*teormechanics@yandex.ru*

Atakov Ibrat R.[1] orcid: 0009-0005-9512-7868
e-mail: *atakovibrat7@gmail.com*

[1]University of Tashkent for Applied Sciences, Tashkent, 100149, Republic of Uzbekistan
[2]TIIAME NRU, Tashkent, 100000, Republic of Uzbekistan

*e-mail: salimovshoolim@gmail.com

Abstract: On the basis of the principle of modularity, an algorithm and software package for dynamic calculation of structurally-inhomogeneous multiply connected shell units that are the elements of hydro-technical structures are developed in the paper. The purpose of the module is to carry out certain transformations of the initial (source) information into a unique result. The development prospects of construction of various hydro-technical structures, aircraft, rocket and space machinery, shipbuilding, chemical engineering and many other branches of modern technology are characterized by a complication of design decisions in projecting and calculation of objects that present multiply connected spatial shell structures subjected to static and dynamic effects. Multiply connected structures, (such as hydro-technical structures), usually include a wide range of elastic and visco-elastic deformable elements with significantly different rheological properties in the form of blocks of plate stacks, tubular, cylindrical and prismatic shell structures of complex geometry, with attached masses, various types of reinforcement, supports, containing a large number of elastic and visco-elastic couplings with significantly different functions of heredity. Obviously, the search for exact analytical solutions to dynamic problems for structurally inhomogeneous visco-elastic shell structures is doomed to failure, the only possibility of engineering implementation is to build numerical and numerical-analytical algorithms with the subsequent use of modern computers. The solution to dynamic problems involves a numerical simulation of the stress-strain state (SSS) of the structures under consideration.

Keywords: software, deformable elements, visco-elastic, stress-strain state, dynamic effects, discrete-continuous model.

Introduction

The development of a unified approach to solving the problems of the dynamics and interaction of multiply connected structurally-inhomogeneous shell structures, which are an arbitrary composition of multilayer shells of revolution and rings, the creation and implementation of an appropriate software package with a high level of automation of all stages of calculations oriented to computer use significantly increase the design efficiency and are a major scientific problem of great economic importance. This paper is dedicated to solving this problem.
To solve boundary value problems of the theory of shells, the behavior of which can be described by a system of ordinary differential equations of the first order, the method of numerical integration

(MNI), based on reducing the boundary value problem to a number of Cauchy problems, turned out to be the most effective one. In 1961, S.K. Godunov [3] proposed the MNI with ortho-normalization of a solution at intermediate points, which later made a leap in solving boundary value problems in the mechanics of a deformable rigid body.

The orthogonal sweep method (OSM), although less general compared to the FEM, has a greater simplicity, compactness, and flexibility, which make it possible to quickly restructure the software when proceeding to solve new problems.

All this was the basis for its effective application in the present paper and, accordingly, an extension to the solution of boundary value problems with complex quantities.

For the first time in solving the problems of determining the stress-strain state of shells of revolution, the method was used by Ya.M. Grigorenko and his students [4, 5, 6, 7, 8, 9]; V.P., Myachenkov, and A.N. Frolov suggested using this method to solve the problems of stability and vibrations of shells of revolution [10]; V.P. Maltsev and V.I. Myachenkov used it to solve the dynamics problems of shells of revolution [11].

In publications by Ya.M. Grigorenko, V.I. Myachenkov, A.N. Frolov, V.P. Maltsev, and others [12] the MHI was thoroughly researched and brought to a universal form to be used in solving a variety of problems in structural mechanics and mechanics of a deformable rigid body.

The success achieved in the development of the MNI based on orthogonal sweep made it possible to use a modification of the displacement method in A.V. Aleksandrov's form [13] to create methodological foundations for calculating multiply connected structurally-inhomogeneous shell structures, in particular, the ones interacting with soil or fluid.

Moreover, the statement and numerical implementation of the proposed methodology are developed and generalized in the framework of the mathematical theory of viscoelasticity [16], modern methods of averaging, and freezing [14, 15], variational principles of the dynamics. They are based on a single approach that uses a discrete-continuous model of the structure and the orthogonal sweep method, generalized on the solution of complex boundary value problems, for calculating the stiffness matrices of shell elements.

2 Method

The main project operations, the performance ability of which is provided by the developed software package, are as follows:

- the formation of a geometrical model of the structure and the nomination of materials;
- the description of environmental factors acting on the structure;
- the formation of the design scheme of a structure;
- the formation of a structure model in terms of the mechanics of a deformable rigid body;
- the determination of the stress-strain state, critical loads and dynamic characteristics of a structure;
- the formation of a visual model of the structure and its response to environmental factors;
- the formation of design documentation;
- the generation of information for the structure archive;
- the search for a rational technical decision.

The construction of algorithms and software is based on the principle of modularity.

A module is a sequence of logically related operations that performs a specific function and designed as an independent subprogram. The purpose of the module is to carry out certain transformations of the initial (source) information into a unique result.

In this paper, all moduli are designed as the procedures written in the algorithmic language phyton.

An example of a module is the procedure for solving a system of linear algebraic equations

$$[A]\,\vec{x} = \vec{b} \qquad (1)$$

by the Gauss method.

The title of this procedure is:

```
GAUSS : PROC ( N, A, B, /*RESULT*/ X);
        DCL, (A (*, *) , (B , X)(*))  FLOAT ( 16 );
    /* N – system order;
    A( N,N ) – matrix [A],
    B( N ) –right-hand sides vector ( B ) ;
    X( N ) –the unknowns vector ( X ) */
```

Using this procedure as an example, the basic principles of module construction can be demonstrated.

1. Each module should be self-documented, i.e. all formal parameters of the procedure should be described in the text of the module. This helps to avoid describing formal parameters far from the text.

2. Each module can be called from anywhere in the program or from any other module by its name. For example, to solve a system of linear algebraic equations

$$[C]\,\vec{q} = \vec{d} \qquad (2)$$

GAUSS procedure call is made using the operator

```
CALL GAUSS (K, C, D, Y);
```

The actual parameters K, C, D before calling the GAUSS procedure must have the following value:

K is the system order (2)

C (K, K) FLOAT (16) is an array of matrix coefficients [C];

D (K) FLOAT (16) is an array of vector components $\vec{d}$;

Fulfilling this procedure, the results of the solving system (2) are available in the Y(K) FLOAT 16 array.

3 Results and discussions

1. The module must have one input-output. The programming experience shows that it is more preferable to use several almost identical modules than one module with several inputs and outputs. The uniqueness of the input-output guarantees the closure of the module and simplifies the maintenance of programs.
2. The module should be small in volume; the text should be placed on one-two (maximum three) listing pages to be visible to the programmer (user).
3. The construction of moduli should guarantee the possibility of their replacement. Suppose that for some reason the Gauss method is not suitable for solving a system of linear algebraic equations (1), in this case the GAUSS procedure text can be replaced with another without changing the procedure title. A program (its text may contain more than one thousand statements) that calls a newly written module will not change at all. A separately compiled new module will be automatically included into this program as a result of the joint compilation. The programmer does not even need to know where this module is located and why it is called.
4. Each module must be written according to the rules corresponding to the rules of the algorithmic languages of publications. This greatly facilitates the reading, and the understanding of the functional purpose and algorithm of the program.

Algorithmic input of initial data. The principle of algorithmic input of source data is important for the construction of algorithms and software. It consists in the fact that along with the numeric input, the functional input of the source information is carried out.

In this case, the formal parameters of the procedure that implements any algorithm for solving the dynamics of structurally inhomogeneous multiply connected axisymmetric and prismatic shell structures include the formal parameters, which in turn are procedures. The functional purpose of these procedures is to calculate the source data continuously changing along the generatrix, such as the geometrical and mechanical characteristics of the shell structure element, external loads acting on it, etc.

Methods used in the solution algorithm. The use of a discrete-continuous design scheme for the structurally inhomogeneous shell structures under consideration determines the main method for solving the problems of the dynamics and strength.

In the general scheme of solving problems, the orthogonal sweep method of S.K. Godunov dominates. Consider the general scheme of the algorithms used in this subsystem on the example of the linear problem of determining the stress-strain state and vibrations of an axisymmetric structurally inhomogeneous structure under axisymmetric loading.

Formalized description of structurally-inhomogeneous shell structures. The principle of algorithmic input of source information is one of the basic principles for describing the geometrical and mechanical characteristics of a structure when constructing algorithms for solving dynamics problems considered in this paper. This principle is used to describe the loads acting on the structure. In this case, the parameters of the procedure that implements one or another algorithm for solving the dynamics of structurally-inhomogeneous shell structures include formal parameters, which in turn are procedures. The functional purpose of these procedures is to calculate the initial data design elements continuously varying along the generatrix of the axisymmetric shell elements or along the guide of the prismatic shell elements. These initial data are the geometrical or stiffness characteristics of the element, external loads acting on it, the dependence of these loads on time, etc. The algorithmic input of initial data allows describing substantially different rheological properties of materials of all elements of the structure under consideration.

4 Conclusions

Numerical and experimental studies show satisfactory accuracy and convergence of algorithms and developed software systems in solving the problems of the dynamics of structurally-inhomogeneous shell structures. For the class of structures under consideration, qualitative and quantitative agreement is obtained in numerical experiments between the basic results and the laws of strain processes in structurally inhomogeneous systems.

References

1. Myachenkov V I, Maltsev V P 1984 Methods and algorithms for calculating spatial structures on computer Mechanical Engineering p 278
2. Mavlanov T. 2020 Development of methods and algorithms for calculating shell structures taking into account structural inhomogeneity and interaction with various media TIIAME p 200
3. Grigorenko Ya M, Bespalova E I, 1971 Numerical solution of boundary value problems of the statics of orthotropic layered shells of revolution on a M-220 computer Methodological supplies –(Kiev, Naukova dumka) pp 151
4. Grigorenko Ya M, 1973 Isotropic and anisotropic layered shells of rotation of variable stiffness (Kiev, Naukova dumka) 228 p.
5. Grigorenko Y M, Vasilenko A T and Pankratova N D 1977 Calculation of non-circular cylindrical shells (Kiev, Naukova dumka) pp 404
6. Grigorenko Ya M, Mukoed A P, 1979 The solution of problems of the theory of shells on a computer (Kiev, Vishcha shkola) pp 279
7. Grigorenko Ya M, Kitaygorodsky A B, Semenova V V, Sudavtsova G K and Shinkar A I 1980 Calculation of orthotropic laminated shells of revolution with variable stiffness on an computer (Kiev, Naukova dumka) pp 102
8. Grigorenko Ya M, Vasilenko A T 1981 Methods for calculating shells V 4 Theory of shells of variable stiffness (Kiev, Naukova dumka) pp 543
9. Grigolyuk E I, Maltsev V P, Myachenkov V I and Frolov A N 1971 On a method for solving the problems of stability and vibrations of shells of revolution ,Reports of USSR Academy of Sciences MTT 1 pp 9-19
10. Maltsev A A, Maltsev V P and Myachenkov V I 1979 Dynamics of axisymmetric shell structures In Applied problems of strength and plasticity Mechanics of deformable systems Interuniversity collection Gorky GSU pp 150 - 158
11. Maltsev A A 1982 Dynamic loading of thin-walled prismatic structures In book Calculation of transport and building structures using computer Proc MIET 618 M MIET pp 16-23

12. Alexandrov A V 1963 The displacement method for calculating slab and beam structures In Proceedings of MIIT Transzheldorizdat 174 4-18.
13. Filatov A N 1974 Asymptotic methods in the theory of differential and integro-differential equations (Tashkent, FAN) p 216
14. Mavlanov T, Karimov A 1979 On the free forced vibrations of the fundamental slabs of silo structures Reports of AS UzSSR series Tech. Sci 4 pp 43-47
15. Vestyank AV, Gorshkov A G and Tarlakovsky D T 1983 Unsteady interaction of deformable bodies with the environment M, AISTI Russian AS 15 pp 69-121
16. Koltunov V P, Mayboroda A S and Kravchuk 1983 Applied mechanics of a deformable solid (Vysshaya shkola) p 350
17. Mirsaidov M M, and Khodzhaev D A 2019 Dynamics of a viscoelastic plate carrying concentrated mass with account of physical nonlinearity of material Part 1 PNRPU Mechanics Bulletin 2 pp 143-153 DOI: 10.15593/perm.mech/2019.2.11
18. Mirsaidov M M, Sultanov T Z and Rumi D F 2013 An assessment of dynamic behavior of the system structure - foundation with account of wave removal of energy Magazine of Civil Engineering 4 pp 94-105 DOI: 10.5862/MCE.39.10
19. Mirsaidov M M 2018 et al Strength parameters of earth dams under various dynamic effects Magazine of Civil Engineering 77(1) pp 101-111 DOI: 10.18720/MCE.77.9